2003

High resolution studies of the HI in the western magellanic bridge

Erik Muller
University of Wollongong

High resolution studies of the HI in the Western Magellanic Bridge

A Thesis submitted in fulfilment of the requirements for the award of the degree

Doctor of Philosophy

from

UNIVERSITY OF WOLLONGONG

by

Erik Muller, BMedPhys

Department of Engineering Physics

2003

CERTIFICATION

I, Erik Muller, declare that this thesis, submitted in fulfilment of the requirements for the award of Doctor of Philosophy, in the Department of Engineering Physics, University of Wollongong, is wholly my own work unless otherwise referenced or acknowledged. The document has not been submitted for qualifications at any other academic institution.

Erik M. Muller

2^{nd} May 2003

Contents

List of Tables

List of Figures

Acknowledgements

There are always many people and institutions involved in pounding any thesis into shape. In my case, two institutions are were deeply involved in the development of this thesis: of course the people and staff at the University were always an encouragement and always able to lend a hand or suggestions when necessary. Through my University Supervisor, Bill Zealey, the department somehow scraped together enough funding to send me overseas on probably far too many occasions. Bill is particularly to thank for facilitating the access of these funds when I know things are tight for the impoverished department! The ATNF and in a wider perspective, the CSIRO, are also to thank for accepting me into the student scholarship program. Through this I was given access to telescopes, computers, software and people, as well as opportunities for involvement in organisation of symposia, and even supervising the running of the Mopra telescope. ATNF was an amazing place to be, I am glad that I was able to be involved there.

On a more individual level: My joint supervision at ATNF originally started with Dr Raymond Haynes, whom I thank for getting me going on the Magellanic Bridge before he retired to the tasmanian end of Australia. I imagine that my ATNF supervisor, Lister Staveley-Smith is acknowledged in countless theses, so enthusiastic and complete is his commitment to students at ATNF. I was unbelievably lucky to have Lister as one of my supervisors. He has read, re-read, approved, disapproved, suggested, encouraged, enthused and inspired so much of this thesis (not so much disapproving I hope).

The very Idea for the content and focus of this thesis came from Snezana Stanimirović, whom I have had the pleasure of badgering with inane, and what were probably perceived as exasperating discoveries, re-discoveries and re-re-discoveries of various bits and pieces of the HI in the Magellanic Bridge. It is Snezanas HI dataset from which I started. All 8 Cds worth and she deserves enormous thanks for unconditionally giving it all to me. I hope that I was able to do the dataset the justice she intended. I hope that I will be able to continue to do the dataset justice.

An enormous thanks goes to so many people for various reasons: Vince Mcintyre for helping so seflessly with many computer hardware/software issues. Also to Malte Maquarding for assistance and suggestions for data analysis techniques, as long as they were related to AIPS++!. Finally, I hope Richard Gooch, creator of KARMA will still be talking to me after my incessant emails asking for changes or updates to his incredible software.

I must also acknowledge the support and patience of my friends and family, particularly my parents who after phenomenal thesis editing efforts, I think are becoming more astronomy-

savvy than makes me comfortable. My long term wonderful friend Annie who has shown me that the only thing that really matters is that you are doing something that you enjoy. My housemate Mark who, without really knowing, has been an incredible support by letting me expound and preach my ideas on bits of the thesis, life in general and Sydney bus drivers. Finally, so much thanks must go to my housemate Angela, who has kept me focussed, driven, consoled and motivated with timely advice and especially for playing frisbee.

Abstract

The Magellanic Bridge is a region of predominantly neutral hydrogen, connecting the Small and Large Magellanic Clouds (SMC and LMC respectively). We present here wide-field observations of this region in the 21cm transition of HI. These observations are made using the ATCA and Parkes telescopes. The resulting dataset encompasses a spatial range of 98″- 7° and are at a velocity resolution of $\sim$1.63 km s^{-1}. This dataset has formed the basis for a series of analyses which are the subject of this thesis.

The HI in the Bridge is seen to have a complex and filamentary structure across the entire range of observed spatial and velocity scales. A census of the expanding shell population, which were parameterised using a strict selection criteria, has resulted in the detection of a shell population with a mean kinematical age of 6.2 Myr. This is in general agreement with the shell population of the SMC, although is was shown that the strict shell selection criteria was insensitive to fragmenting or incomplete shells. A strict selection criteria led to the detection of a region in the Bridge where an apparently older shell population exists. The HI of this region, found at Right Ascensions greater than approximately $2^{\rm h}\,20'$, appears relatively quiescent. It appears that shells in this region may left to develop for a longer time before they are ruptured and distorted by ambient turbulence.

A study of the spatial power spectrum has shown that distribution of structure in the Bridge is quite inhomogeneous. Two apparently different morphological regions are detected in the Bridge: the northern part is at a higher velocity and shows very little small scale variation and the southern, lower velocity and significantly brighter part shows an approximately Kolmogorov power spectrum. The power law index of the southern part is consistent with power indices derived from HI in the SMC. The power spectrum of both the northern and southern part are well fit using a single component, and show no indication for a dominant scale. Visually, the southern part of the Bridge appears to suggest a east-west elongation in the structure. This is not apparent in a quantitative test of the

Fourier transform of the image data. A smaller-scale analysis using the Spectral Correlation Function, which provides a measurement of the variation of spectra as a function of spatial lag, suggests that the spectra do in fact vary more slowly in the East-West direction, i.e. approximately along the line joining the SMC and LMC.

Several large scale features found in the Bridge show evidence for large energy deposition events. Part of the HI in the Bridge appears to be distinctly offset in velocity and position and a comparison of numerical N-Body simulations of the Magellanic System, where the SMC is modelled as a spiral galaxy, shows excellent agreement with the observed HI distribution, both in position and in velocity. From these simulations, it appears that the velocity offset part of the Bridge is in fact a distant arm of the SMC while the closer arm comprises a link between the LMC-SMC. The observed filamentary nature of the lower velocity component is consistent with severe turbulent mixing which may be generated by the tidal interaction of the SMC and LMC.

The brighter, lower velocity part of the Bridge is shown to have a bimodal spectral profile. The bimodality is contiguous in position and in velocity with a shell complex in the SMC. The observed bimodality in the Bridge indicates that the Bridge formed *after* the formation of the SMC shell complex, however the kinematical ages for the shell complex are a factor of $\sim$15 younger than the predicted age of the Bridge structure.

A large radii ($\sim$1.6 kpc) loop filament is observed off the North-Eastern corner of the SMC. The velocity structure of the loop is reminicent of an expanding region, although the energy requirements for this shell are so extreme that no current hole or shell formation theories can satisfactorily account for its development. Such a feature would require an unseen massive stellar association to generate the necessary energy output. To form the observed feature by a high velocity cloud collision would require the impinging mass to have velocities and densities which are entirely inconsistent with the observed HVC population. Finally, the idea that the loop occurs at the first gravitational Lagrange point of the LMC-SMC system is inconsistent with Numerical simulations in that the simulations suggest that the loop is in fact located in the distant spiral arm of the SMC and therefore not in the correct location for a L1 point. Furthermore, the simulations do not show any evidence for the formation of this feature as observed. As such, the formation mechanism for this significant, large-scale loop is still uncertain.

A survey of Hα emission regions throughout the Bridge, using a new and untested Hα

dataset, has isolated several new Hα emission regions. In general, these Hα regions appear to be spatially associated with UV sources from the FAUST catalogue, although in some cases the Hα emission region show a morphology which is characteristic of formation by collisional heating. Some of the Hα features which show a ring-like morphology are compared with the HI dataset. In this way, an estimate of the age of the shell can be made. Due to calibration difficulties, and a lack of continuum information, this part of the thesis comprises only a list of positions of the Hα features and a discussion of possible ionisation mechanisms.

A search for ^{12}CO(1-0) emission regions in the Bridge has resulted in the first detection of this molecule in the Magellanic Bridge. The CO emission region appears to be embedded in an HI cloud and has a S_{60}/S_{100} which is similar to those found in the SMC. The narrow line width of the Bridge CO detection is consistent with a low metallicity, indicating that the HI in the Bridge is less evolved than that of the SMC or the Magellanic Stream. From empirical models based on analyses of CO emission regions in the SMC, an upper limit of the radius of this region is estimated at $\sim$16 pc.

Chapter 1

Introduction

"It's a what??... where???"- Maureen Muller, 2000

This Thesis focusses on analysis of observations of a predominantly gaseous region between the Small and Large Magellanic Clouds (SMC and LMC respectively). This region has been named the 'Magellanic Bridge' (Hindman et al. 1961) and at a distance of ∼60 kpc, it is the closest extragalactic example of a large-scale feature formed through tidal forces.

The Small and Large Magellanic Clouds are two nearby dwarf irregular galaxies. The Clouds are easily discernable optically. However, observations at the 1.4GHz (∼21 cm) spin-flip transition of neutral hydrogen (HI), reveal a different and far more extended morphology to that suggested by their optical appearance (Kerr, Hindman & Robinson, 1954).

Aside from the two Clouds themselves, the Magellanic System includes at least three other components visible at the HI transition. The Magellanic Stream, the Leading Arm and the Magellanic Bridge show evidence of being kinematically and geometrically inter-related, although the boundaries between the components are not well-defined. Figure 1.1 shows the Magellanic System as it appears in HI from early observations (Mathewson, Cleary & Murray, 1974): the LMC and the SMC themselves are seen as the most dense members of the Magellanic System while the other components are considerably more tenuous and filamentary.

The Figure shows the Magellanic Bridge as the HI emission region between the clouds. This region is the focus of this Thesis; however, since the evolution of the system as a

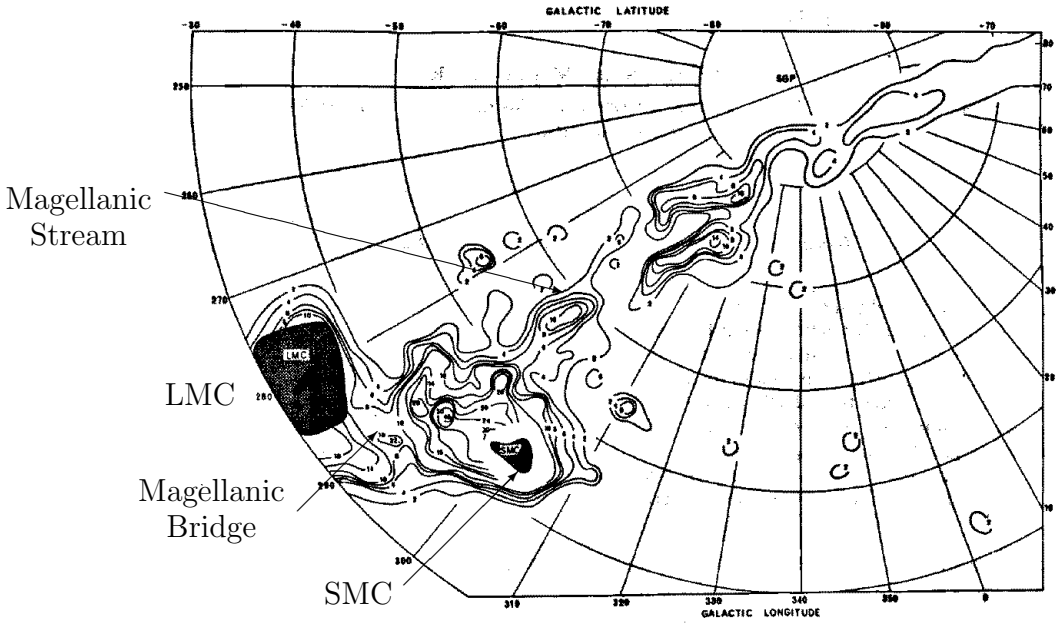

Figure 1.1: Map of HI in the direction of the Magellanic System, by Mathewson, Cleary & Murray in 1974 using a 18m reflector at Parkes. Compare with Figure 1.2 to note the improvements in resolution and sensitivity for modern observations

whole is a fundamental consideration in its analysis, a review of past and recent studies of each of the Magellanic components will be presented here, with an emphasis on studies of the HI transition.

1.1 Early observations

The proximity of the Magellanic System presents an opportunity for detailed, high spatial resolution studies of astrophysical phenomena. The centres of the LMC and SMC are at around $5^h\,19^m$ -$68^\circ\,44^m$ and $0^h\,58^m$ -$72^\circ\,51'$ (J2000) respectively in the Equatorial coordinate system. The radial distance to the Clouds has been the subject of considerable study. Most of the techniques used to estimate the distances of the Magellanic Clouds employ observations of RR Lyrae variables (e.g. Clementini et al. 2003; Feast 1988) or Mira variables (e.g. Feast 1989, See Westerlund, 1990 for a review). Westerlund (1990) also presents some comparable measurements from observations of O or B type stars and red giant stars. The general consensus of the radial distances is that the LMC and the SMC are at a distance of approximately 50 kpc and 60 kpc respectively [1] (Welch et al.

[1]These distances will be assumed throughout this Thesis

1987).

The clouds are separated by ∼21 degrees, which corresponds to a projected spatial separation of 22 kpc (e.g. Staveley-Smith et al. 1998). At these radial distances, the Parkes telescope (for example) is capable of achieving spatial resolutions of ∼260pc at λ=21cm. Nowhere else outside the Galaxy are such high spatial resolutions possible. The Magellanic System therefore, offers a unique opportunity for astronomy and astrophysics in general. As such, the history of study of this system is long and at times, colourful.

Both clouds have been exhaustively observed at the 21cm wavelength. After being first detected in HI by Kerr, Hindman and Robinson (1954) with a 36ft parabolic reflector, subsequent HI surveys by Hindman et al. (1961), Hindman et al. (1963) and also Hindman, Kerr & McGee (1963) observed an 'intercloud' region of neutral hydrogen. Detailed maps of the HI within the Magellanic System were finally produced by Mathewson, Cleary &Murray (1974) using an 18m antenna (shown in Figure 1.1). This investigation led to the discovery of the Magellanic Stream; the long, northerly-projecting ribbon of neutral hydrogen. A subsequent vigorous debate regarding the mechanisms involved in the development and structure of the Magellanic features ensued.

The construction of the 64 m Parkes telescope allowed high resolution observations of the Magellanic System. With a beamwidth of ∼15′ at 21cm, the first high resolution observations of the System were made by Mathewson, Schwarz & Murray (1977). The authors of this paper were (fiercely) opposed to the 'tidal stream' scenario for the formation of the Magellanic Stream (see also Mathewson & Schwarz, 1976) and this study focussed primarily on the clumpy structure of the trailing Magellanic Stream, with a view to examining its compatibility with a 'Turbulent Wake' evolutionary hypothesis. Mathewson had previously submitted a presentation to the Royal Greenwich Observatory (Mathewson, 1976) which made an outright rejection of the tidal theory, on the basis of a lack of comparability with some theoretical considerations; in particular, no stellar population had ever been observed in the Stream and the observed radial velocities were too high to be explained without unreasonably large geometries and densities of the Galactic Halo.

The complete Parkes HI dataset of the Magellanic Stream were not published until 1984 (Mathewson & Ford, 1984). The new data revealed the true extent of the faint and filamentary nature of the HI envelope surrounding the Magellanic Clouds. By this time, numerical N-Body simulations (Fujimoto, 1979; Murai & Fujimoto, 1980; Gardiner &

Noguchi, 1996) of the Magellanic System had begun to provide substantial support for the Tidal theory for the formation of the Stream. The simulations showed that the basic morphology of the Magellanic System can be reproduced to some degree, solely from gravitational considerations of the LMC-SMC-Galaxy system. More importantly, these simulations also predicted a close-encounter collision of a few kpc between the two Clouds approximately 2×10^8 years ago.

McGee & Newton (1986) used the Parkes telescope in a more dedicated study to make measurements at 217 positions throughout the Magellanic Bridge. They found the HI profiles throughout much of the Bridge were in some cases extremely complex, suggesting a turbulent structure both in position and in velocity.

The development of a thirteen beam focal plane receiver array for the Parkes telescope during 1997 allowed observations at significantly higher sensitivity than ever before. The first observations of the Magellanic Stream with this new instrument were made by Putman et al. (1998). This study made use of the high sensitivity and fast tracking modality of the new multi-beam system to observe a 2,400 square degree area around the SGP. Since the development of the Multibeam system, observations of the HI in and around the Clouds have progressed rapidly and the components of the Magellanic System have come to be regarded as structures in their own right.

Figure 1.1 shows the measurements made during the initial observations with the 18m telescope (Mathewson et al. 1974). Most of the main features are visible, including the Clouds, the Bridge and the Stream. The Leading Arm is absent from this figure however, since these observations did not extend far enough to the north. Figure 1.2 shows the improvements in sensitivity and resolution of the more recent observations by Putman et al. (2003), made using the 64m Parkes Multibeam telescope. In these higher ($\times$ 3.5) resolution data, the filamentary nature of Magellanic HI is clear in both the Clouds and the Bridge. The Leading arm can be seen extending southward in the opposite direction to the Stream.

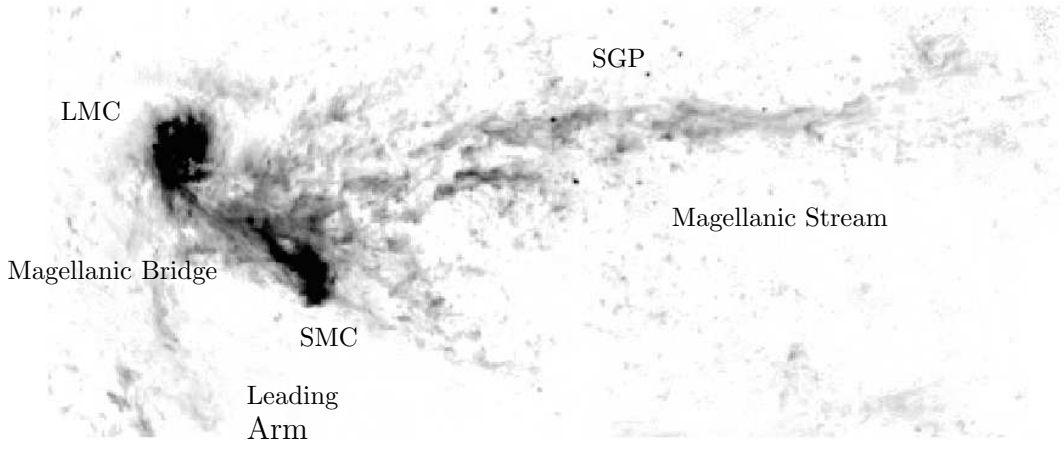

Figure 1.2: The Magellanic System in HI. This image is taken with the Parkes 64m antenna in a Survey by Putman et al. (2003).

1.2 The Cool and Warm ISM of the Magellanic System

The Magellanic system has been described above as being composed of a number of kinematically and geometrically related HI structures. The Magellanic Bridge is an important member of the Magellanic System and to understand how this feature has evolved and developed, it is necessary to have an understanding of the entire System. The rest of this section will review the literature which have explored various aspects of the different components of the Magellanic System. A dedicated review of the literature regarding the Magellanic Bridge is given in Section 1.3

1.2.1 The Small Magellanic Cloud

The HI component of the SMC has been studied across a wide range of spatial scales. The first HI observations of the Magellanic System by Kerr, Hindman & Robinson (1954) revealed that the spatial extent of each Cloud was significantly larger than previously thought. The total HI mass of the SMC as measured by these authors is $4{\times}10^8 M_\odot$.

Later, more sensitive observations by Hindman et al. (1963) using a 21ft antenna and a subsequent interpretation by Hindman, Kerr & McGee (1963) led to suggestions of a second HI mass component within the SMC which was later dubbed the 'Mini-Magellanic Cloud' by Mathewson (1984). The velocity separation of the two components was estimated to be 25-30 km s^{-1}.

Much later observations of the SMC, at significantly higher spatial and velocity resolution by Staveley-Smith et al. (1997) were taken with the Australia Telescope Compact Array (ATCA). With a minimum spatial resolution of $\sim 98''$, the SMC was seen to be filamentary and 'frothy' - dominated by holes and shells. These authors undertook a survey for expanding HI shell structures and were able to statistically analyse a population of 500 expanding HI spherical shell structures. A general result from this survey was that the ages of the shells were found to be extremely young, with a mean kinematic age of 5.4 Myr and a tightly confined deviation of 2.1 Myr. Under the assumption that the mechanism for energy deposition into the SMC ISM was through stellar wind action, these authors noted a discrepancy between the calculated kinematic age of the HI expanding shells and the ages of OB stars within the SMC. It was also suggested that the apparent young and well confined shell ages may be due to a recent period of star formation, possibly triggered by the gravitational effects of the Galaxy. At that time these observations were made only with the ATCA and hence lacked large scale structural information. The 'Mini-Magellanic Cloud' hypothesis was re-interpreted by Staveley-Smith et al. (1997) as the super-position of a large conglomeration of HI expanding shells.

A complete analysis of HI in the SMC was possible after the addition of zero-spacing information from the Parkes Multibeam survey by Stanimirović et al. (1999a). The combined SMC ATCA-Parkes datacube was re-surveyed for larger-scale expanding structures and a number of 'supershells' were located and parameterized. 'Supershells' were those shells with radii larger than ~ 1 kpc and represent the extreme upper-end of shell sizes within the SMC.

With now a larger and more complete range of spatial scales, Staveley-Smith et al. (1998) and Stanimirović et al. (1999a) undertook the first analysis of the spatial power spectrum applied to an entire galaxy. The power spectra is a measure of the relative power emitted across a range of spatial scales and in the case of the SMC, the HI power spectrum can be fit extremely well with a power law of the form $P_k(k) \propto k^{\gamma}$ (Staveley-Smith et al.

1998; Stanimirović et al. 1999a; Stanimirović et al. 1999b; Stanimirović & Lazarian, 2001), indicating that the SMC contains a non-preferential distribution of spatial scales and that there are no processes active in the SMC that result in a dominant scale. From this, Stanimirović & Lazarian (2001) concluded that the SMC was essentially a 'three-dimensional' structure, i.e. the line of sight thickness of the SMC was comparable to its extent in the other two dimensions.

The Hα features of the Small Magellanic Cloud have been studied and catalogued in a detailed study of the Magellanic Clouds by Davies, Elliott & Meaburn (1976). Although current observation techniques have produced a new Hα dataset of superior sensitivity, the original work by Davies, Elliott & Meaburn (1976) remains the active authority on Hα features of the SMC and LMC. In general, Davies, Elliott & Meaburn (1976) found a significant Hα component distributed throughout the SMC. In many cases, an OB association was found in proximity to an Hα emission region, although these authors note that in one instance, surprisingly little Hα was detected near a particularly bright OB association. These authors also found that Hα regions were generally associated with HI column densities $>10^{21}$cm^2.

Numerous studies of the stellar population of the SMC have built up a considerable resource for this topic (e.g. Kunkel, Demers & Irwin, 2000; Demers, Kunkel & Irwin, 2000; Morgan & Hatzidimitriou, 1995; Tucholke, de Boer & Seitter, 1995). A study which is important to this Thesis is that made by Zaritsky et al. (2000), who made a statistical analysis of the distributions of the stellar population. This research uncovered a spatial shift in the centre of the young stellar population relative to that of the older population. To date, this research is the only real evidence for large-scale event which may have caused a displacement of SMC gas and thereby a relative shift in the raw material in which the youngest stars form.

The SMC has been searched thoroughly at a range of molecular transition lines. Detections of ^{12}CO and ^{13}CO in particular have led to a great deal of information regarding conditions in the SMC (e.g. Israel et al. 1993 and papers of that series). The general consensus resulting from these studies is that the SMC appears to be CO deficient (Israel et al. 1993 and papers of that series; Rubio, et al. 1991; Rubio, Cohen & Montani, 1984). The SMC also appears to be significantly less metallic than the Galaxy (Rolleston et al. 1999; Israel et al. 1993 and papers of that series; Rolleston et al. 1993), although this is

a state that is rather typical for dwarf irregular galaxies (e.g. Madden, 2002; Galliano et al. 2002)

The cool component of HI in absorption has been examined by Dickey et al. (2000), who discovered a cool HI fraction which was abnormally low compared with that of the Galaxy. They conclude that the reason for the lower fractional cool component may be due to a number of effects, including a low metallicity, leading to a reduced cooling volume.

1.2.2 The Large Magellanic Cloud

At 0ptical wavelengths, the LMC shows evidence for a 'Bar' and otherwise has a generally irregular structure. In a dramatic contrast, HI studies of the LMC (e.g. McGee & Milton, 1966) have shown a striking spiral-like structure, which extends far beyond the radius suggested by optical observations.

Recent high resolution observations of the HI in the LMC have been made by Kim et al. (1997), who have shown the complex small-scale and filamentary HI structure is dominated by holes and loops, similar to that of the SMC, although on a much larger scale. These observations were made using the ATCA only, although they have since been complemented with zero-spacing observations from the Parkes telescope (Staveley-Smith et al. 2003).

Of particular interest to this Thesis are the studies of the Power Spectrum and of the 'Spectral Correlation Function' (SCF) as applied to the LMC HI dataset. The former analysis, made by Elmegreen, Kim & Staveley-Smith (2001) was able to show evidence for a *characteristic length*, indicated by a feature in the power spectrum at $\sim$100pc. This contrasts with the featureless power spectrum of the SMC (e.g. Staveley-Smith et al. 1998; Stanimirović et al. 1999a; Stanimirović et al. 1999b) and Elmegreen, Kim & Staveley-Smith (2001) have suggested the excess power at this scale was due to the thickness of the LMC disk. A subsequent analysis with the SCF by Padoan et al. (2001) showed a spatial decorrelation at slightly larger scales of $\sim$180 pc, which was nonetheless also regarded as further evidence for the thickness of the disk.

The CO survey of the LMC, as part of a Magellanic CO SEST Key survey program, was undertaken by Israel et al. (1993) which showed that the general spatial coincidence of IRAS sources and CO emission regions found in the SMC was true also for the LMC. The

CO emission regions in the LMC spanned a slightly larger velocity dispersion range and a significantly larger integrated intensity (I_{CO}) range, although the isotopic ratios of I_{12}/I_{13} were slightly lower for the LMC. There were however, no real conclusions that the authors could make from differences in CO intensities and isotopic ratios between the SMC and the LMC.

An exhaustive survey of CO regions in the LMC was finally made with the 4m NANTEN telescope (e.g. Mizuno et al. 2001; Mizuno et al. 2002). This survey covered the entire LMC HI surface and found in most cases, excellent correlation of CO regions with both HI and with 100μm excess emission. This survey is ongoing and has now been expanded to include the Magellanic Bridge and the SMC.

As the LMC is the closest of our more substantial galactic neighbours, it has also been the subject of extensive optical studies. The supernova event SN 1987A, catalysed a continuing storm of research (Manchester et al. 2002) and added to the armory of distance estimating techniques (Mitchell et al. 2002).

Recently, a luminosity study of red clump stars from randomly chosen fields across the LMC found evidence for a warp of the LMC disk (Olsen & Salyk, 2003). The authors suggest that the warp may have been caused by the close interaction between the SMC and LMC during the last close encounter $\sim$200 Myr ago (e.g. Murai & Fujimoto, 1980), although they also speculate that the gravitational forces from the Galaxy may be contributing at least in part.

1.2.3 The Magellanic Stream, Leading arm and HVCs

Projecting northward from the Magellanic Bridge and Magellanic Clouds is the Magellanic Stream, a larger ribbon of hydrogen extending approximately 100° across the sky past the SGP (Mathewson, Cleary & Murray, 1974). Although the mechanism responsible for forming the Stream has been contentious in the past, the Stream is now commonly regarded as evidence of the gravitational effect of the Galaxy on the Magellanic System (e.g. Putman et al. 1998).

The HI in the Stream is found to have a complex morphology, although it is concentrated in two long filaments for a significant part of its length (Morras 1985; Putman, 2000). The geometry of the HI of the Magellanic System suggests that the Stream may in fact

have been extruded from the tenuous gas of the Bridge. However, measurements of the metallicity of the Stream (Gibson et al. 2000) show that the Stream gas has a metallicity that is much higher than that of the Bridge and is more consistent with those found in the SMC. Recent numerical models by Maddison, Kawata & Gibson (2002) confirm that the Stream has probably originated from the SMC halo.

The periphery of the HI disk-like structure of the of the LMC is found to be dominated by wisps and tendrils, the largest of which extend out towards the SMC and also in a direction opposite to that of the Magellanic Stream (Brüns, 2002; Staveley-Smith et al. 2003). One of the more dominant and obvious extensions is that of the Leading arm (Putman et al. 1998). This extension of the LMC is thought to be the tidal counterpart of the Stream and its discovery largely put competing theories for the tidal formation of the Stream to rest.

Clustered around the LMC and nearby the interface between the SMC and Bridge, are found what appear to be fragments or debris of HI. Many of these objects are shown kinematically to be members of the Magellanic System (e.g. Brüns, 2003), although since distance measurements to the features are so difficult, it is unknown whether these objects are truly Magellanic in origin. The exhaustive studies by Brüns (2003) therefore, were not able to conclusively determine a density for these objects. Kinematically, many of these objects are classed as High Velocity Clouds (HVCs). Absorption line measurements for one of these objects appear to indicate metallicities which reflect an extra-Galactic, or Magellanic origin (Sembach et al. 2002; Gibson et al. 2000).

1.3 Observational status of the Magellanic Bridge

The Magellanic Bridge exists as a region of chiefly neutral hydrogen lying between the two Magellanic clouds (Hindman 1963, Mathewson, Cleary & Murray, 1974). The Bridge has been shown to contain young blue stars, as well as a population of older red stars (Irwin, Kunkel& Demers, 1985; Demers & Battinelli, 1998; Demers et al. 1993, Bica & Schmitt, 1995). A study of the kinematic information of the neutral hydrogen of the Bridge, as well as its geometry, suggest that the Bridge is closely related to the Magellanic Clouds and shows particularly strong continuity with the SMC (Mathewson & Ford, 1984). Numerical simulations (e.g. Murai & Fujimoto, 1980, Gardiner & Noguchi, 1996) suggest that the

development of the Bridge was initiated after the Magellanic Clouds had suffered a close encounter ∼150-200 Myr ago, where they were separated by ∼3 kpc. As such, there is extremely strong support for the tidal scenario for the origin of the Bridge.

The smooth velocity continuity of the HI Bridge into the SMC makes a precise demarkation of the spatial extent of the Bridge difficult. However, throughout this Thesis, we will refer to the Magellanic Bridge as the region extending from the SMC, at around $1^{\rm h}\,30^{\rm m}$ towards the LMC, where the LMC and the Bridge merge at around $4^{\rm h}\,40^{\rm m}$, although this is by no means a rigid definition of the extent of the Magellanic Bridge. This Thesis examines only the western half of the Bridge, including the highest HI column densities of the Bridge ranging from 10^{21} to $< 10^{18}$ cm^{-2}.

Numerical simulations of the formation of the Magellanic System are not capable of estimating the exact fractional composition of SMC and LMC gas within the Magellanic Bridge or the level of metal enrichment. The kinematics, proximity and geometry of the Bridge relative to the SMC suggest that it is realistic to assume that at least part of the original SMC matter is entrained within the Bridge. Furthermore, numerical simulations confirm that this is the case (e.g. Gardiner, Sawa & Noguchi, 1994).

1.3.1 HI observations

The first detections of the HI line from the Magellanic Bridge were made by Kerr, Hindman & Robinson (1954). These observations were made using using a 36 ft parabolic dish at an angular resolution of ∼1° and included part of a wider Magellanic HI survey. It was the later observations by Mathewson & Ford (1984) however, which demonstrated the existence of smooth spatial and velocity HI connectivity between the SMC and the Bridge. A more recent and dedicated survey at higher velocity resolution was conducted by McGee & Newton (1986) at a resolution of ∼15′. This study exposed the intricate and complex spatial and velocity structure of the HI. A Gaussian component fitting analysis showed that the HI profiles were in general quite complex. An even more recent survey conducted using the Multibeam facility on the Parkes telescope (Putman, Gibson & Staveley-Smith, 1999) at a still finer velocity resolution, has revealed the spatial connectivity of the HI between the Magellanic Bridge and the other components of the Magellanic System down to very low sensitivities.

At this stage, there have been no attempts to quantify and analyse the kinematics and morphology of neutral hydrogen in the Bridge in the context of the rest of the Magellanic system. This Thesis attempts to redress this deficiency and undertakes a comparative study of HI in the Bridge with that of the SMC, as well as other exemplary HI systems.

1.3.2 Stars

The optical component of the Bridge has received considerable attention, in particular, the study of the distributions and ages of the stellar population (e.g. Westerlund & Glaspey, 1971; Kontizas et al. 1988; Demers & Battinelli, 1988; Grondin, Demers & Kunkel, 1992 and papers of that series). An automated process was used to generate a catalogue of a few hundred thousand stars by scanning plates from the UK-Schmidt telescope containing observations of the Bridge (Demers & Irwin, 1991; Battinelli & Demers, 1992). The absolute age and age variation has been of principal interest, since this can provide constraints on modelling the Magellanic System. Age estimates for OB associations within the Magellanic Bridge range between 7 Myr to $\sim$100 Myr (Hambly et al. 1994; Grondin, Demers & Kunkel, 1990). More recent work by Demers & Battinelli (1998) found that the stars in the Bridge may have formed during a period of starburst, between 10-25 Myr ago. Initially, there were suggestions of a systematic variation of stellar age along the length of the Bridge (e.g. Kunkel, 1992), which would indicate an episode of star formation triggered by the propagation of a shockwave. However, later more complete studies of the OB population in the Bridge (e.g. Grondin, Demers & Kunkel, 1992) have showed that no gradient existed.

Some research has been conducted into the older stellar population of the Magellanic Bridge. Demers, Irwin & Kunkel (1993) conclude that the distribution of red stars (B-V>1.75) can be used to define the perimeter of the LMC Halo. A small number of red stars are found outside this well-defined boundary however, which these authors suggest could in fact be fore-ground stars associated with the Galaxy.

The area in the Bridge included in a cluster analysis by Battinelli & Demers (1992) (from the dataset of Demers & Irwin, 1991) spans only half the area under study in this Thesis. However, this catalogue has recently been extended further west towards the SMC by Bica &Schmitt (1995) which covers the entire area relevant to this Thesis. This catalogue by Bica & Schmitt, (1995) is used extensively throughout this Thesis.

1.3.3 Molecular observations and metallicity

As the Bridge represents a tidal structure (Mathewson & Cleary, 1974), of very low metallicity (e.g. Hambly et al. 1994; Rolleston et al. 1993; Rolleston et al. 1999, Lehner et al. 2001), the process of star formation in the Bridge is of particular interest, since star formation under these conditions is largely unobserved. The exact mechanism of star formation within the Bridge is still poorly understood as only one molecular region in the Bridge has been found (Lehner, 2002), despite the relatively young stellar age range ($\sim$10-25 Myr, Grondin, Demers & Kunkel).

Star formation regions are usually traced by detection of molecular transitions, indicating a local molecular condensation and the possible imminent (or current) collapse of a molecular cloud. Observations for emission lines of molecular transitions have been confined almost exclusively to the Clouds themselves (e.g. Israel et al. 1993 and papers of that series). The only search for CO emission within the Bridge has resulted in a non-detection down to an RMS of $\sim$60 mK (Smoker et al. 2000). Selection of candidate CO emission regions for this survey were based on findings by Rolleston et al. (1999) who had suggested that CO in emission was commonly associated with cold HI clouds. This unsuccessful search was focussed on a region of cold HI detected by Kobulnicky & Dickey (1999) at RA = $3^{\rm h}\,11^{\rm m}\,54.75^{\rm s}$ (J2000), Dec.= $-76^\circ\,51'51.6''$ (J2000), a position slightly south of the area under study throughout this Thesis.

A further search for molecular transition lines was conducted by Lehner et al. (2001) who were able to detect evidence of many molecular and atomic species and isotopes in absorption towards a star at RA = $2^{\rm h}\,57^{\rm m}\,12.94^{\rm s}$ (J2000), Dec. = $-72^\circ\,52'5\ 4''$, just outside the area observed for this Thesis. This study corroborated the conclusions by Rolleston et al. (1999) regarding the very low metallicity of the Bridge, which was found to be $\sim$0.1 dex lower than the SMC (Rolleston et al. 1999). The SMC is itself a much lower metallicity than the Galaxy (Gibson et al. 2000). Finally, Lehner (2002) detected traces of molecular absorption lines (particularly H_2 and O VI) in two different locations in the Bridge towards two bright and massive stars.

1.3.4 Hα observations

Evidence for sources capable of ionising local hydrogen was first found from Hα observations by Johnson, Meaburn & Osman (1982). Later follow-up observations in the Very-Wide-Field Ultraviolet Sky Survey, conducted on Spacelab 1 by Courtés et al. (1984) and later by Marcelin, Boulesteix & Georgelin (1985) confirmed that ionisation of hydrogen was an active process within the Bridge.

Hα plates of the Magellanic System were taken during 1976 by the UK-Schmidt survey for a study of the Hα in the SMC and LMC (Davies, Elliott & Meaburn, 1976). These were re-examined by Meaburn (1986) for coherent Hα structures within the Bridge. Meaburn made some preliminary measurements of a few 'nebulous' regions. Most of these were irregularly shaped clumps of emission, however one Hα ring, evidence for an ionised shell, was clearly apparent. Meaburn (1986) suggested that the ionising source responsible for the Hα emission region might be a supernova, or more likely, a single O8 type star. The same object was examined by Parker (1998), who found that the object FAUST 392 was coincident with the ring. Parker suggested that FAUST 392 may be a white dwarf object, although he conceded that the Hα structure may also be a supernova remnant. Later Hα spectroscopic observations of this shell by Graham et al. (2001) were able to identify Hα emission corresponding to the approaching and receding sides of the shell, with an expansion velocity of $\sim$37 km s^{-1}. These measurements refined the previous age estimates by Meaburn (1986) to 5.29$\pm$0.26 Myr. These authors discovered that the most likely origin of the ionisation source was a blue star, with B-V magnitude consistent with a Wolf-Rayet star.

At this time, there has not been a thorough analysis of Hα from the Magellanic Bridge.

1.4 Evolution of the Magellanic System

Theories of the origin of the Magellanic Stream and the evolution of the Magellanic System have been the source of vigorous debate following the HI detection of the Stream by Mathewson, Cleary & Murray (1974). Initial suggestions included a ram-pressure stripping model, a 'turbulent wake' model, a tidally stripped model, or a hybridisation of a few of these concepts (Mathewson 1976; Mathewson & Schwarz, 1976; Mathewson, Schwarz & Murray, 1977). One of the more powerful arguments used throughout this

debate were that the Stream does not appear to have a stellar component. This conflicts with a tidally stripped model where the stellar component is accelerated at the same rate as the gaseous part and should be extracted at the same rate. Also, the radial velocities of the tip of the stream were too large to be explained without the presence of a dense Galactic Halo. At this time, a stellar population has still not been convincingly detected in the Magellanic Stream. Recent sophisticated N-body simulations have been able to simulate the evolution of a Magellanic which lacks a stellar component (Maddison, Kawata & Gibson, 2002). Following the recent discovery of the Leading arm which is considered to be the tidal counterpart to the Stream (Putman, Gibson & Staveley-Smith, 1999), and reasonably successful several simulation developments (e.g. Yoshizawa & Noguchi, 1999), it is widely accepted that the Magellanic System is significantly tidally interacting with the Galaxy. The Stream and the Leading Arm are the result of the differential tidal forces involved.

A brief review of the various models follows:

1.4.1 Ram pressure

Ram pressure, a process by which fluid drag presents a resistive force to a moving body, has been invoked to explain the existence of the Magellanic Stream (Moore & Davis, 1994). In this case, the effect of the Magellanic System moving through the Galactic Halo causes the more tenuous component to be stripped from the clouds, leaving a wake of gas of roughly constant density which should be devoid of the heavier and denser components. Both of these properties have been shown to be the case for the Magellanic Stream. A necessary component of the ram pressure stripping scenario is that of a dense Galactic halo at large distances. Moore & Davis (1994) model the Galaxy with an ionised disk and an extended halo ($>$ 50-65 kpc) to supply the necessary drag force and restore the infalling gas to the observed velocities. Murali (2000) argues that heating caused by the Cloud's motion through the halo is more likely to cause the stream to evaporate within a short time at the densities predicted by Moore & Davis (1994). The densities which Murali (2000) calculates are necessary to produce the stream through ram pressure stripping are not consistent with observations.

The ram pressure model has difficulty explaining the presence of the counter tidal arm, which extends from the LMC in the opposite direction to the Stream, although it may be

somewhat successful in accounting for the 'finger-like' projections emanating away from the Bridge in the same direction as the Stream.

1.4.2 Tidal stripping

A tidal stripping scenario suggests that the Magellanic Stream is the result of the Galaxy's gravitational effects of the primordial gas of the Magellanic Clouds.

Until recently, the major deficiency of this theory is its predictions of the presence of stars within the stream, yet despite numerous independent searches (Brück & Hawkins, 1984; Brück & Hawkins, 1983; Tanaka & Hamajima, 1982), no conclusive evidence of any stellar population had been found. More recent simulations incorporating full hydrodynamics by Maddison, Kawata and Gibson (2002), have been successful in reproducing the formation of the Stream by tidal stripping without containing a stellar population.

The Tidal theory also predicts a counter arm feature, extending in the opposite direction of the stream. No feature was observed until improvements in telescope sensitivity finally led to its detection in HI by Putman, Gibson & Staveley-Smith (1999).

At this stage, the formation of the Magellanic System and in particular the Magellanic Stream, is thought to be dominated by the gravitational influence of the Galaxy. Although it is unclear to what extent the tidal stripping scenario affects the evolution of the Magellanic Bridge.

1.4.3 Turbulent wake

The turbulent wake model, proposed by Mathewson, Schwarz & Murray (1977), suggests that the stream is a signature of the passage of the Magellanic Clouds through the Galaxy Halo. The perturbed Halo gas becomes thermally unstable, cools and falls as clumps towards the Galaxy as they lose buoyancy. Mathewson assumed that at 100 kpc, the Halo had a density of $\rho \approx 5\times10^{-4}$-$10^{-3}$ cm^{-3}and a temperature of T$\approx 5\times10^{5}$ K. Mathewson, Schwarz & Murray (1977) estimated the volume particle density for a clump closest to the SMC as 2×10^{-2}cm^{-3}. From this, a cooling time of $\sim10^{8}$ was derived for this cloud. This model supposes that the Halo at Magellanic distances is sufficiently hot and does not significantly oppose or distort the infalling cool clouds.

1.4.4 Numerical simulations

A large number of attempts have been made to numerically simulate the current appearance of the Magellanic System. Most of the simulations have focussed more on mechanisms involved in the evolution of the Magellanic Stream (e.g. Gardiner & Noguchi, 1996; Gardiner, Sawa & Fujimoto, 1994; Murai & Fujimoto, 1980). The preliminary simulations were primarily based on N-body routines, i.e. simulating gravitational forces only (Fujimoto, 1979).

As computer speed has improved, the complexity of the simulated system have also advanced and additional physical processes and parameters are included. Simulations by Yoshizawa & Noguchi (1999) was one such simulation where the morphology of the Stream was reproduced almost completely devoid of a stellar population; however this simulation did not take into account any non-gravitational large scale forces. The most recent attempts at modelling the formation of the Magellanic System have been quite involved. Maddison, Kawata & Gibson (2002) have compared simulations where only gravitational forces were considered with those where star-formation and other elaborate feed-back mechanisms were included. In this case, the more sophisticated simulations resulted in a severely disrupted SMC and a stream without a stellar population. This finding suggests that the gas comprising the stream was tidally stripped from the outer regions of the SMC.

1.5 The Interstellar Medium

The Interstellar Medium (ISM) is an extremely important and very prevalent and important component of the Galaxy and Universe. It is largely this component that we detect with HI observations. A short review of the composition of the ISM will be presented here.

The ISM is the name given to the lumpy, inhomogeneous raw matter in which stars and everything else condense, interact and die. It has been likened to an 'ocean of the galaxy, composed largely of a cool fluid confined by gravity to a thin layer and serving as a reservoir for all of the material in stars and planets that will ever form, evolve and disperse.' (Elmegreen, 1992).

Its composition is in general, a mixture of hydrogen, helium and a small contribution from heavier elements and dust. The literature does not agree on an exact fractional composition, but there appears to be some consensus around 60-90% Hydrogen, 30-10% Helium and $< 1\%$ dust (e.g. Bowers & Deeming, 1984; Metzger, 1975). The important detail is that by number, the ISM is chiefly hydrogen, with a significant contribution of Helium and an almost negligible quantity of heavier elements, such as O, C, Ne as well as dust. Another important detail is its extreme rarity. Bowers and Deeming (1984) quote gas densities of 0.025 $M_\odot\,pc^{-3}$, with a dust density of $\sim$0.002 $M_\odot\,pc^{-3}$. The ISM comprises a relatively small (5-10%) mass fraction of a standard spiral galaxy (Metzger, 1975), although figures up to 40% have been cited (Lequeux, 1983). In volume and in its role however, the ISM is a significant and important structure and HI observations are used to provide a first insight into the morphological structure of the ISM across a wide range of scales. The HI information is typically supplemented with observations at other wavelengths to help obtain a fuller understanding of the physical and chemical status of the region under study.

Models have been proposed in an effort to understand and predict some of the properties and functions of the ISM. For some time, the 'two-phase' model, offered by Field, Goldsmith & Habing (1969) was the simplest and most effective model. This model predicted that a thermally stable two-phase configuration of the ISM existed. In this case, a hot gas (T$\approx 10^4$ K) dominated the ISM and was interspersed with cooler clouds of T $\leq 10^4$ K, where both the components would be in pressure equilibrium. The validity of this prediction was highly dependant on the assumed value of the cosmic ray flux. The two-phase model has largely become superseded by a three-phase model, proposed by McKee & Ostriker (1977). This study used estimates of SNe frequency to conclude that under the two-phase model, the tenuous ISM would quickly become compressed and shocked by violent SN events. The ISM has now started to be considered as a much more complex assortment of components (e.g. Burke & Graham-Smith, 1998, Stanimirović, 1999). Here the ISM is pre-divided into two phases existing in pressure equilibrium (or close to it), with concomitant low and high temperature ranges. The *Neutral medium* includes matter that exists in a cool, electrically neutral state, or low pressure environment. The counterpart is the *ionised medium*, which exists at a range of higher temperatures. Table 1.1 has been reproduced from Burke & Graham-Smith (1998) and shows the respective parts of the ISM, along with the associated temperature ranges. Burke & Graham-Smith

State	Regime	Temperature range
Ionised Medium	Warm Ionised Medium (WIM)	T ∼10,000 K
	Hot Ionised Medium (HIM)	T > 50,000 K
Neutral Medium	Warm Neutral Medium (WNM)	T ∼100- 1000 K
	Cool Neutral Medium (CNM)	10 K < T < 100 K
	Cold Neutral Medium	T < 10 K
	(also Neutral Medium - NM[1])	

[1] Stanimirović (1999)

Table 1.1: Table compiled from Burke & Graham-Smith (1998). Detailing composition of the ISM, along with temperature regime for each component.

Temperature (K)	Primary coolant
10	CO
10^2	H_2,C^+
10^3	Metastable ions
10^4	H,H^++e

Table 1.2: Table from Dyson & Williams, (1997). This shows the important ISM coolant molecules and ions over a range of temperatures.

(1998) are careful to point out that the temperature regime as quoted is not well defined, particularly at the low temperature range.

The molecular component shown in Table 1.2 is an important element in the ISM, since it is this along with the ionic component, that is primarily responsible for cooling the ISM (e.g. Dyson & Williams 1997), depending on the temperature and density of the ISM. The most active coolants in the ISM are shown in Table 1.2.

The Magellanic System provides an un-matched, front-seat view of inter-galactic, large-scale processes which are active in a developing and tidally affected dwarf galaxy system. This Thesis presents and discusses observations of the HI in the ISM of the Magellanic Bridge. Where appropriate, studies at additional transitions are examined. This Thesis is broken into the following chapters;

- The present Chapter contained a review of the literature regarding observations of the Magellanic System. The observational history of the Magellanic System, with an emphasis on the Magellanic Bridge was also discussed, as well as a brief revision of ISM models.

- Chapter 2 includes an introduction and discussion on the fundamental processes that allow observations of Neutral hydrogen (HI), Carbon Monoxide (CO) and the first emission line of Hydrogen, (Hα). The remainder of this chapter will cover the theory for observational techniques for single dish and interferometric observing.

- The procedures used to observe the HI datacube which forms the subject of analysis for much of this Thesis are detailed in Chapter 3. This chapter describes observations with both the Narrabri Interferometer and the Parkes 64m single-dish Telescope. Some preliminary observations and discussion of the cube are also presented in this chapter.

- A detailed analysis of an HI expanding shell survey is presented in Chapter 4. This chapter also contains a discussion and comparison of the collated statistics with those of other systems, in particular with the adjacent SMC.

- Chapter 5 contains a statistical analysis of the HI of the Magellanic Bridge. In particular, an analysis of the Spatial Power Spectrum and the behaviour of the Spectral Correlation Function is presented here. A comparison with similar studies of other systems is also made in this chapter.

- The large scale features of the Magellanic Bridge are discussed in Chapter 6. In particular, a Gaussian decompositon of the HI dataset, a large loop-shaped void, a velocity discontinuity and a velocity bifurcation form the subject of this chapter.

- Chapter 7 contains a catalogue of Hα observations of the Magellanic Bridge. This Chapter represents a new catalogue of Hα features and related possible ionisation mechanisms in the Magellanic Bridge.

- Chapter 8 contains observations at the CO(1-0) transition and the ramifications of such a detection for the Magellanic Bridge. The topics of star-formation rates and its consequences on the Bridge are discussed here.

- A summary and conclusions are made in Chapter 9.

Chapter 2

Review of observation and physical theory

"Yeah...I think you have told me about all this before...quite a few times actually." - Angela Edwards, 2003

2.1 Theory of physical processes

This Chapter contains a review of the physical processes responsible for the atomic and molecular lines examined in this Thesis. The molecular and atomic transitions most relevant to this Thesis are: the spin-flip transition the of lowest energy state of atomic hydrogen,HI ; the highest electric energy transition in the Balmer series of atomic hydrogen H(3-2), Hα ; and the first rotational transition of diatomic Carbon Monoxide, CO(1-0). The last part of this chapter will present the theoretical operations of single dish and interferometric observing. Much of what is discussed in the following can be found in a number of textbooks (e.g. Bourke & Graham-Smith, 1998; Taylor, Carilli & Perley, 1999).

2.1.1 HI theory

Neutral hydrogen accounts for up to 10% of the total Galactic mass. As such, the study of the neutral hydrogen component is an important and powerful probe into the morphology and kinematics of the ISM.

The hyperfine transition between spin states of the single electron in the hydrogen atom

is responsible for the much-studied 21cm emission. As this is the lowest energy transition for atomic hydrogen, it is referred to as the *HI transition*. The frequency of the energy emitted (or absorbed) during a transition between the parallel and anti-parallel spin states has been measured in laboratories at 1.420405753 GHz (e.g. Kerr, 1968). A transition between spin states has an Einstein probability co-efficient of A_{10}=2.85 $\times$ 10^{-15} sec^{-1}, which amounts to a transition rate of one event in 11 million years. The small transition probability results in a line which is intrinsically very narrow. Consequently this transition is ideal for making measurements of velocities and velocity dispersions.

Following Verschuur, Kellermann & Brunt (1974), the number density of neutral hydrogen can be inferred from HI observations, starting from the solution for the equation of transfer. The intensity for a given frequency I_ν, from an element at a radial position x is given by:

$$I_\nu = \int_0^\infty j_\nu e^{-\int_o^r k_\nu \mathbf{dr}} \mathbf{dx}$$

where j_ν and k_ν are the specific co-efficients of emission and absorbtion.

In the Rayleigh-Jeans approximation, the brightness temperature: T_B and the emission co-efficients are related to the Intensity I_ν and co-efficient of the specific emission j_ν, by:

$$T_B = \frac{I_\nu}{2k\lambda^2} \; and \; J_\nu = \frac{j_\nu}{2k\lambda^2}$$

We also use the Boltzman distribution to describe the relative population of the ith state with:

$$\frac{n_i}{n_0} = \frac{g_i}{g_0} e^{-(h\nu_i^0)/kT_s}$$

where n_i/n_0 is the statistical probability of transition from the ith state to the 0th state and T_s is the *Spin Temperature*, which describes a temperature that relates the relative populations of the parallel and anti parallel spin states. For HI , g_1=3 and g_0=1

The last three equations can be combined to give:

$$T_B = \int_0^\infty T_s K_\nu e^{-\tau_\nu} \tag{2.1}$$

with $\tau_\nu = \int_0^x K_\nu dx$ is the *optical depth* arising from any absorptive material for the frequency ν along the line from 0 to x.

Finally, using a the radio approximation ($h\nu \ll kT_s$) to simplify a relation for the absorptive co-efficient $K\nu$:

$$K_\nu = a_\nu n_0 \frac{h\nu}{kT_s}$$

where

$$a_\nu = A_{01}\frac{c_2}{8\pi\nu^2}\frac{g_1}{g_0}f(d\nu)$$

and $f(d\nu)$ describes the density of emission events per frequency interval $d\nu$, we arrive at an estimate for the number density of emitters per square cm (for units of km s^{-1}):

$$N_H = 1.8 \times 10^{18} \int T_B s \ dv \ cm^{-2}$$

This is one of the fundamental relations used to estimate the masses and densities of HI regions. For many cases in the Galaxy, the HI is assumed to be optically thin and the optical depth can be checked with absorption measurements.

2.1.2 CO theory

Molecular gas comprises a significant fraction of the Galactic mass, entrained in large features called *Giant Molecular Clouds*. Molecular clouds represent an important component of the process of gas fragmentation and star formation. Figure 2.1 shows a part of the feedback processes where molecular clouds play an important part.

It can be seen that such clouds are integral to the evolution of galaxies and for star formation. The study of such structures is therefore a useful technique to probe the dynamics of these objects.

Carbon Monoxide (CO) is a diatomic molecule with a small dipole moment. Consequently, the frequency corresponding to the excitation energy for the first rotational transition (1-0) is ν=115.271GHz and the lifetime for this transition is large: 1.7×10^7s (e.g. Steinberg & Lequeux, 1963). CO is generally more easily found in a high density, low temperature environment, shielded from high energy radiation, which otherwise might cause its dissociation. Such a scenario also describes a region that is beginning the first stages of star formation. As such, CO is typically used as a tracer for sites of star formation and for molecular gas.

The high ISM density found in star forming regions produces a local over-abundance of carbon, oxygen and also dust. The carbon and oxygen may separately impact and adhere

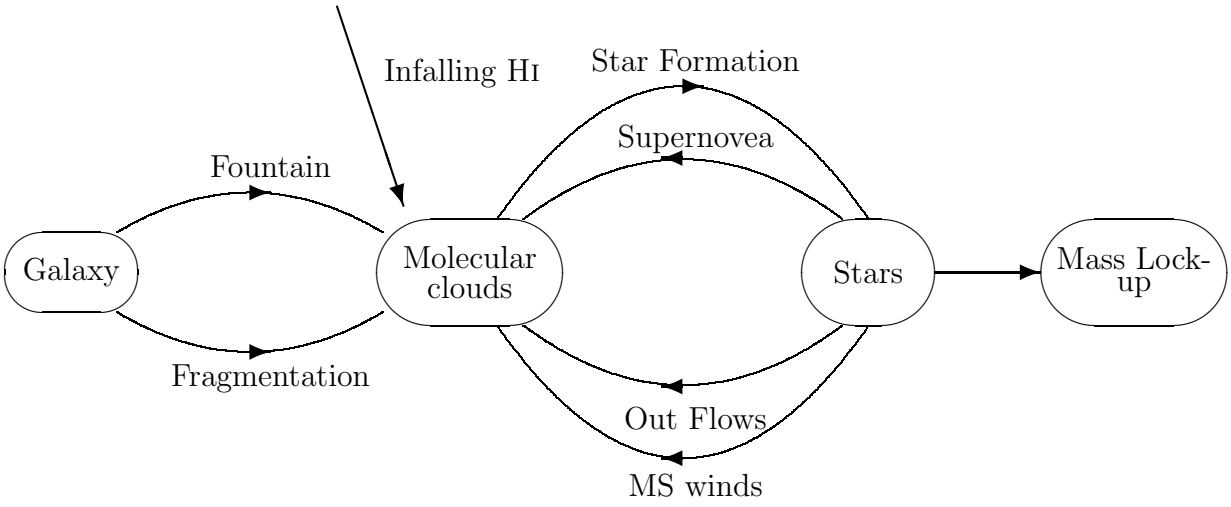

Figure 2.1: Flowchart of mass transfer for a molecular cloud system. After *Burton, Elmegreen & Genzel, 1991*

onto the surface of the dust. The atoms are free to move about on the dust surface and may eventually interact and combine through some reaction scheme. The reaction may be a rapid exothermic neutral exchange, e.g. CH + O → CO + H, or a scheme involving more complex path, e.g.:

$$C^+ + H_2O \rightarrow HCO^+ + H$$
$$HCO^+ + e \rightarrow H + CO$$

(e.g. Burton, Elmegreen & Genzel, 1991). The mechanism for ejection of the new molecule from the dust surface is not well known, though the energy released during the combination is one such process through which the new CO molecule can re-join the ISM. Other processes such as shocks or *radiative sputtering* are also possible ejection mechanisms.

As CO is commonly used as a tracer for molecular gas, the relationship of $I_{CO}/N(H_2)$ is a topic of great interest (e.g. Shull & Beckwith, 1982; Young & Scoville, 1981; Pak & Jaffe, 1999). In the case of the Galaxy and other large spiral galaxies, it appears that the X ratio ($X = N(H_2)/I_{co}$) is reasonably constant within the disk (e.g. Sanders, Scoville & Solomon, 1985). Maloney & Black (1998) have shown that the X factor is an sensitive function of the kinetic temperature of the ISM, and is not as thoroughly constant, even within the Galaxy, as assumed. Indeed, the Galactic X value is not necessarily preserved in low metallicity galaxies such as those comprising the Magellanic System: Israel & Burton, (1986) have found a surprisingly low CO luminosity in a sample of Dwarf Galaxies and

suggest that the low metallicity or H_2 content may be in fact responsible for the apparent relatively low CO content (e.g. Israel et al. 1993 and papers of that series for similar studies on the Magellanic Clouds). These findings suggest that the Galactic X factor underestimates the amount of CO present in the dwarf systems.

UV radiation with a wavelength of $911.75 < \lambda < 1117.8$Å, is is important in the destruction of CO by photodisassociation. The effectiveness of shielding against radiation within this band is therefore of importance to measurements of the abundance of interstellar CO. Van Dishoeck & Black (1985) have made a theoretical examination of the effects of self and mutual shielding to photoionisation. Shielding by dust, and in particular by H and H_2 are also significant factors in shielding efficiency considered by van Dishoeck & Black: the H and H_2 lines effectively offer total shielding from radiation in the wavelength range 1062-1064Å. These species afford partial protection from radiation at the 1076Å, 939 and 941.5Å bands of ^{12}CO.

2.1.3 Hα theory

Emission at the Hα transition occurs during a electron transition from the n=3 to n=2 energy states for hydrogen (i.e. the third to second excited states). This transition regime falls within the Balmer series and has an equivalent wavelength 6563.1 Å. The energy dissipated (or absorbed) during the Hα transition is $\sim$1.890 eV, or 3.029×10^{-12} ergs.

Detection of the emission of Hα, being a recombination transition and a relaxation of an excited hydrogen population, indicates the presence of an efficient process which acts to ionise the ISM to at least the third (n=3) excited state. Therefore, the detection of this relaxation transition has been used throughout the literature a tracer for large-scale energy transfer processes. Hot stars or regions of vigorous gas dynamics which can impart sufficient excitation to the ISM are commonly identified through the detection of Hα emission.

Forming stars, newly formed stars or other energetic bodies which emit large amounts of radiation, a significant quantity of which is emitted in the UV, are capable of exciting hydrogen into the n=3 or higher energy states (a star may form an *HII region*, referring to the ionisation level of the hydrogen atom). Detection of Hα can therefore be used

an indicator for regions of recent star formation, or to indicate the presence of some other hot body. Scenarios such as these can typically be distinguished from other ionising processes (i.e. collisional) after measurements of the continuum emission which can reveal the thermal origin of the radiation.

A second important mechanism leading to the ionisation of the ISM is by collisional heating. An impinging flow may compress a hydrogen region, imparting the kinetic energy of the flow to the electronic excitation of the hydrogen. To ionise the hydrogen to the n=3 energy level, the minimum necessary for Hα emission, the impact or collapse velocity of the neutral hydrogen must be $\gtrsim$19 km s^{-1}. Such a process can be found for example, in the blast wave from a Supernova which can compress and heat the neutral ISM and give rise to Hα emission; a stellar wind streaming past and impinging on a clump of material can generate the same compression and transfer of kinetic energy. Similarly, a collision between hydrogen clouds will result in a propagating shockwave in each cloud which may also lead to the subsequent ionisation of the hydrogen. Since these are largely exchanges of kinetic energy, these processes are not bright sources of continuum emission.

As Hα emission occurs from the recombination of excited gaseous Hydrogen, Hα features do not necessarily assume any characteristic shape or morphology. A particular Hα structure however, can occasionally be attributed to some specific process; Hα emission associated with a supernova or planetary nebula remnant will generally assume a circular, or arc-like appearance. Gas clouds centrally heated may appear in Hα with a diffuse or clumpy morphology. Hα emission which has been collisionally pumped may be observed with a 'bow-shock' structure. Stellar associations are continuum sources and will therefore be apparent in continuum observations and non-thermal processes, such as cloud collisions are not sources of continuum emission. Theoretically, Hα regions heated by a stellar source can be differentiated from collisionally excited emission regions by comparing the distribution of the Hα emission to that of the continuum emission.

2.2 Radio Observation theory

As data collected for this Thesis was obtained from both a single-dish instrument and from a multi-element interferometer, theory of the operation of these two modalities will be discussed in some detail in the following sections. For a more complete review, see Burke &

Graham-Smith (1997) or Taylor, Carilli & Perley (1999). The data discussed in this Thesis comprises observations sensitive to a large range of spatial scales ($\sim$7° -98″) observed over a large spatial area ($\sim$7° $\times$7°). The Parkes 64 m Telescope, operated by the Australia Telescope National Facility (ATNF), was used to obtain total power measurements across large spatial scales, while the Narrabri interferometer (the Australia Telescope Compact Array, ATCA[1]) was used to observe across the smaller spatial scales. As the region of interest covers an area much larger than the size of the interferometer primary beam, a *mosaicing* technique is used to combine multiple ATCA pointings. The following sections detail the general theory of single dish and interferometric observing. The mosaicing technique and the methods used to generate and combine the interferometric and total power datasets are described in Chapter 3.

2.2.1 Single dish observing

The single dish data used in this Thesis were collected using the CSIRO Parkes 64 m dish in Parkes, Australia. This section will contain only a general description of the single-dish observing modality. A more detailed description of the Parkes telescope and the processing methods involved in collecting and processing the HI dataset is presented in Chapter 3.

2.2.1.1 Configuration

A single dish telescope may be regarded as simply a large power collector. Typically a single dish comprises a metal reflector to focus and incoming voltage, $\vec{E}$, onto the actual detecting element. In most cases, the pointing of a single dish is controlled by physically changing the attitude of the metal reflector so that the direction of maximum response is towards the source. In less conventional cases, the shape of the reflector may be modified or the receivers themselves may be moved instead.

A few parameters of the dish are inherent in its design and construction; typically one property of the telescope is enhanced at the expense of the efficiency of another. Defining characteristic parameters of a single dish telescope include its beam pattern (point spread

[1]The Australia telescope Compact Array and the Parkes Telescope are part of the Australia Telescope, which is funded by the Commonwealth of Australia for operation as a National Facility managed by CSIRO.

function PSF) and its diameter D. These affect other important characteristics such as the efficiency ε, beamwidth θ and the Gain, G.

Most telescopes use a reflecting metal dish shaped to a parabola by revolution (paraboloid), or some similar profile. For a paraboloid, the path-length for all reflected radiation to the focal point is equal. Thus the information that arrives at the focal point from the source is phase-correlated. The *Full Width at Half maximum* or FWHM (also called the Full Width at Half Power, FWHP) of the point spread function of the telescope (also called the *Beamwidth*) is closely related to the *resolution*. The FWHM (in degrees) is given by $\sim\lambda$/D, where λ is the observing wavelength and D is the diameter of the dish. Phase correlation is lost for any radiation that reflects with an angle greater than this.

2.2.1.2 Beam Pattern

The beam pattern of the telescope defines the response of the telescope as a function of sky position and is characteristic of the hardware design. In addition to the shape and size of the reflecting dish and subsequent sub-reflectors, ultimately the receiver horn shape also has a significant effect on the beam pattern. The general response of the dish to incoming radiation can be found by integrating the contributions from excitation currents across its two-dimensional surface:

$$F(\theta,\phi) = \int\int g(\xi,\eta)e^{-2\pi i(\xi\theta+\eta\phi)}d\xi d\eta$$

(Burke & Graham-Smith, 1997) where g(θ,ϕ) describes the excitation current density distribution. Figure. 2.2 shows how the beam pattern is generally distributed on a single dish telescope. The main beam can be seen in Figure 2.2 as the large and forward pointing lobe and the *sidelobes* are those shown pointing to offset angles.

One of the important trade-offs in telescope design is the extent to which the side-lobes will contribute to the received signal. This can be modified to some extent by altering the shape of the receiver horn and reflecting dish surface, although these modifications come at the expense of effective collecting area (and therefore of gain and beamwidth). Signal entering the receiver through these lobes will lead to spurious power measurements (note that some power from the backward direction is observed by the receiver). As such, single dish measurements must be flux calibrated with observations of a well-known and preferably extended source. In this Thesis, the flux calibration is performed during

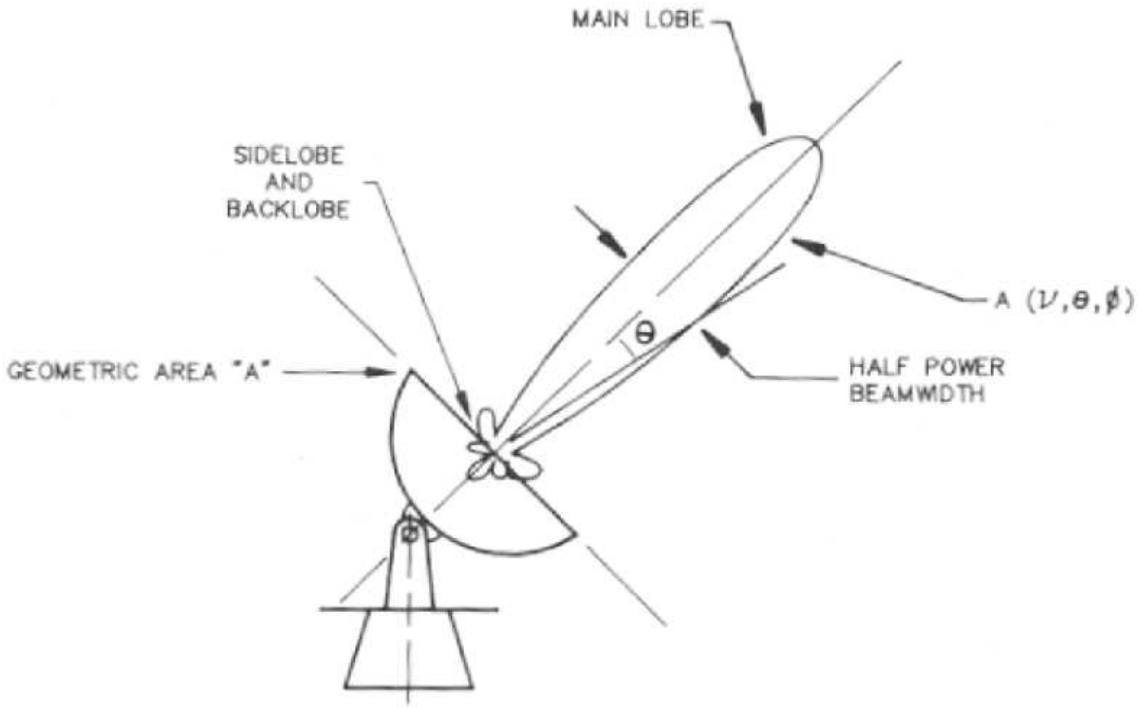

Figure 2.2: Reception pattern of a single dish telescope (After After *Napier, 1999*), as a function of elevation and azimuth angle: θ, ϕ. The main lobe is the direction of maximum reception, although spurious signal can also enter through the smaller side-lobes.

merging with Interferometer data. This procedure is discussed in Chapter 3.

Single dish information was used in this Thesis to supply the *zero spacings* information, that is, structure that corresponds to lags which are $\geq$ zero in the fourier domain. The procedure used to merge the single dish data with interferometric data is also covered in Chapter 3.

2.2.2 Interferometric observing

An interferometer combines and correlates time-integrated voltage outputs from antenna pairs and ultimately generates an intensity map of the sky, $I_\nu(\mathbf{x},\mathbf{y})$. All interferometric data used in this Thesis has been collected and pre-processed at the Australia Telescope Compact Array (ATCA) at the Paul Wilde Observatory, Australia. The specifics of this instrument are discussed later in Chapter 3 and the following presents a more general description of the theory of interferometric observing and of the image processing procedure.

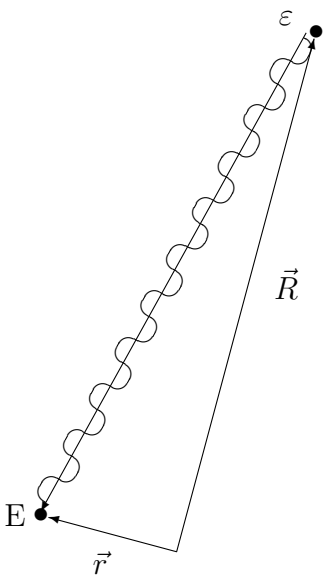

Figure 2.3: Simple scenario for observer-source configuration. The source is located at $\vec{R}$ and has an output voltage of $\vec{\varepsilon}$, which is detected by an observer at $\vec{r}$ who measures a voltage. $\vec{E}$.

2.2.2.1 Detection

With reference to Figure 2.3; in the most simple case, a detecting element located at $\vec{\mathbf{r}}$, is used to observe a source of voltage ε (assumed to be time invariant for simplicity) which is located at $\vec{R}$. Following Clarke (1999), the voltage output of the element will be:

$$E(r)_\nu = \int \varepsilon_\nu(\mathbf{R}) \frac{e^{2\pi i\nu|\mathbf{R}-\mathbf{r}|/\mathbf{c}}}{|\mathbf{R}-\mathbf{r}|} dS \tag{2.2}$$

where dS is the surface element on the sky. For two arbitrarily located detecting elements at $\mathbf{r}_1$ and $\mathbf{r}_2$, the correlated signal is:

$$E_\nu(\mathbf{r_1}, \mathbf{r_2}) = \langle E_\nu(\mathbf{R_1}) E^*_\nu(\mathbf{R_2}) \rangle \tag{2.3}$$

This value will become zero for $\mathbf{R_1} \neq \mathbf{R_2}$ and bearing in mind that the power emitted by the source is proportional to E^2, substituting Equation 2.2 into Equation 2.3 gives the spatial coherence, or *Visibility*:

$$V_\nu(\mathbf{r_1}, \mathbf{r_2}) \approx \int I_\nu(\mathbf{s}) e^{-2\pi i\nu \mathbf{s}\cdot(\mathbf{r_1}-\mathbf{r_2})/\mathbf{c}} d\Omega \tag{2.4}$$

where $dS = R^2 d\Omega$ and $\mathbf{s}$ is the unit vector in the direction of ε and where $I_\nu = |R^2| \langle \varepsilon \rangle$ is

the measured signal intensity. From equation 2.4 it is apparent that the cross-correlated voltage is dependant on the projected vector difference of $\vec{r_1} - \vec{r_2}$ (i.e. the apparent separation of the two detecting elements as viewed from the source) and the product V_ν will be a time varying quantity, but will be a maximum for $\vec{r_1} - \vec{r_2} = 0$. i.e. when the direction to the source is perpendicular to the joining the detecting elements. Typically, the visibility is discussed in a reference frame where the vector separation is referred to in units of wavelengths; $\vec{r_1} - \vec{r_2} = \lambda(u, v, 0)$. This plane is called the *UV plane*. We also make a co-ordinate transfer to the cosines of $\vec{s}$, so that $\vec{s} = (l, m, \sqrt{1 - l^2 - m^2})$,and $d\Omega = \frac{1}{\sqrt{1-l^2-m^2}} dldm$:

$$V_\nu(\mathbf{u}, \mathbf{v}) \approx \int\int I_\nu(\mathbf{s}) \frac{e^{-2\pi i \nu \cdot (\mathbf{ul}+\mathbf{vm})}}{\sqrt{1 - l^2 - m^2}} dldm \tag{2.5}$$

However, in general it can be assumed that the direction cosines l and m are typically small, so that the visibility relation becomes:

$$V_\nu(\mathbf{u}, \mathbf{v}) = \int\int I_\nu(l, m) e^{-2\pi i(\mathbf{ul}+\mathbf{vm})} dldm \tag{2.6}$$

Finally, the Fourier inversion of the visibility in equation 2.6 yields the spatial Intensity distribution:

$$I_\nu(l, m) = \int\int V_\nu(\mathbf{u}, \mathbf{v}) e^{2\pi i(ul+vm)} \mathbf{dudv} \tag{2.7}$$

which is the desired distribution.

2.2.2.2 The Interferometer

The voltage detected by the telescope elements is modulated by its direction-dependent effective area $\vec{A}$(l,m). As such, the Equation 2.6 will become:

$$V_\nu(\mathbf{u}, \mathbf{v}) \approx \int\int A(l, m) I_\nu(l, m) \frac{e^{-2\pi i \nu \cdot (\mathbf{ul}+\mathbf{vm})}}{\sqrt{1 - l^2 - m^2}} dldm$$

The Fourier inversion will be:

$$A(l, m) I_\nu(l, m) = \int\int V_\nu(\mathbf{u}, \mathbf{v}) e^{2\pi i(ul+vm)} \mathbf{dudv}$$

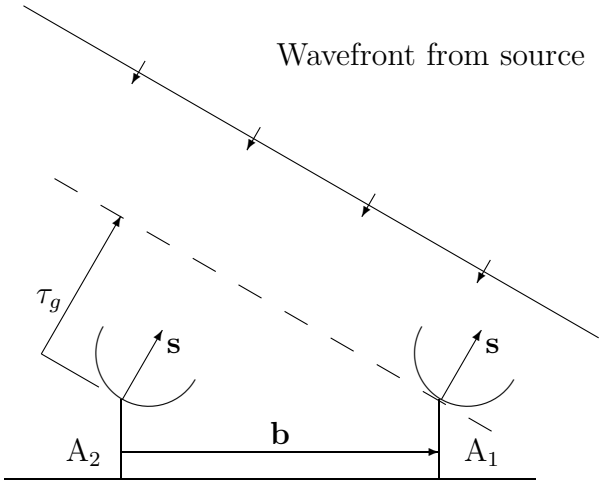

Figure 2.4: Example scenario where for a non-zero $\tau_g = \mathbf{b}\cdot\mathbf{s}/c$. The phase difference between the signal arriving at the elements is given by $2\pi\tau_g/\lambda$. As such, in order to return a phase-correlated output, the signal from A_1 must be delayed by τ_g

Interferometers use a number of detecting elements to increase spatial resolution and sensitivity (see Figure 2.4). From Equation 2.4 it was shown that the V_ν would vary with time as the observed source moves relative to the telescopes and that coupled with the telescopes direction-dependant effective area, V_ν would be maximised when the direction of the source of interest perpendicular to the line joining the telescope elements. The position of maximum response is called the *phase centre*.

As maximum response is achieved when the position of the source is coincident with the phase centre, it would be convenient to have some means of moving the position of the phase centre as the source moves relative to the telescope. This is achieved by inserting an artificial delay between the telescope and correlator in order to compensate for the different arrival times of the wavefront for each telescope. Figure 2.4 shows a typical two element interferometer. The difference in arrival times of the wavefront is given by $\tau_g = \mathbf{b}\cdot\mathbf{s}/c$. By inserting an artificial delay τ, the phase centre will track over the sky as the source moves, thereby maintaining the position of peak sensitivity concurrent with the source. This procedure is known as *Phase Tracking*.

Interferometer observations represent a series of time-averaged observations from a number of descrete telescopes. The function representing the distribution of sampling by all baseline pairs, over the time of observations in the UV plane is the *sampling function:* $S(u, v)$.

The effect of observing at a collection of points in the UV plane modulates the visibility function and Eq. 2.7 becomes:

$$I'_\nu(l,m) = \int\int S(u,v)V_\nu(u,v)e^{2\pi(\mathbf{ul+vm})}\mathbf{dudv}$$

Or, equivalently, using the convolution theorem:

$$I'_\nu(l,m) = I_\nu(l,m) \otimes B(l,m)$$

Where B(l,m) is the fourier transform of the Sampling function and I' is called the *Dirty Image*, referring to the fact that finite sampling of the UV plane typically leads to a rather messy intensity map.

On occasion, it may be necessary to survey a region which occupies a larger spatial area than that of the interferometer primary beam. In these cases, it is necessary to *mosaic* a number of interferometer observations into a large datacube. This technique was followed to achieve the high-resolution observations used in this Thesis and a description of mosaicing and its application in the current Thesis is left until Chapter 3.

Chapter 3

HI Dataset

"And how is all this this supposed to end world poverty?.." - Stephen Muller, 1999

This Chapter outlines the methods involved in collecting and processing observations of the HI line in the direction of the Magellanic Bridge, followed by a presentation and brief discussion of the final results. The first part in each section describes the specifics of the instrument and procedures used to obtain and process the output dataset.

The observations are discussed in Chapter 3.1. Section 3.1.1 presents the methodology of observations and subsequent data reduction and processing of data obtained with the Australia Telescope Compact Array (ATCA). Section 3.1.5 presents the methodology involved in the same type of observations and data processing for data obtained with the Parkes Telescope. Data combination techniques are presented in Section 3.1.6 and some preliminary discussion of the morphology of the resulting datacube is presented in Chapter 3.2

3.1 HI Data Collection

This section presents the techniques and methods used to collect and process HI data of the Magellanic Bridge using the ATCA and the Parkes Telescope.

3.1.1 Interferometric Observations.

Interferometric observations for this Thesis were made with the Australia Telescope Compact Array (ATCA). The ATCA is a six-element interferometer at the Paul Wild observatory at Narrabri, N.S.W. Australia (*lat. 149.5 E long. 30.27 S*). Five of the elements are moveable among a number of discrete locations along a linear east-west track, allowing for a variety of pre-determined configurations and therefore some opportunity to observe the UV plane thoroughly. The sixth telescope is located approximately 3km west of the other five and has a much more limited freedom in position. Each of the dishes themselves have a 22m diameter non-parabolic main dish with a pseudo-hyperbolic sub-reflector. The reflectors and receivers are arranged on an alt-azimuth mounting.

The receivers are on-axis and capable of measuring both polarisations simultaneously at L (20 cm), S (13 cm), C (6 cm) or X (3 cm) bands. Typically, data is collected in both narrow-band and continuum modes and at two orthogonal polarisations, although this is user-dependent. System temperature measurements and calibrations are made by the periodic (30 Hz) measurement of a noise diode.

3.1.2 Observations with the ATCA

Observations of the 21 cm HI line were made over a 7x6 degree field using the 375 m configuration of the ATCA. These observations were made over three sessions: 1997 April 13, 15-16, 18; 1997 October 9-15; and 2000 January 29 to February 2. Pointing centres are shown overlaid on a Parkes Multibeam map (Brüns, 2003) in Figure 3.1. The area is broken into 12 'blocks', each containing 40 pointings. Each pointing is visited for twenty seconds, approximately once every 15 minutes. The total integrated time for each pointing is thus $\sim$16 minutes.

Most of the blocks were observed at this rate over 12 hours for complete UV sampling. Five of the blocks were not observed for a full 12 hours, although these are incomplete by only 6% and significant artifacts do not exist in the final image data. The UV coverage of the central pointing (pointing #20) for block 4 is shown in Figure 3.2 as an example of the UV sampling for these observations.

The ATCA observations were made using a 4 MHz bandwidth, with 1024 channels at a central frequency of 1.420 GHz, resulting in a channel spacing of 0.83 km s^{-1} before

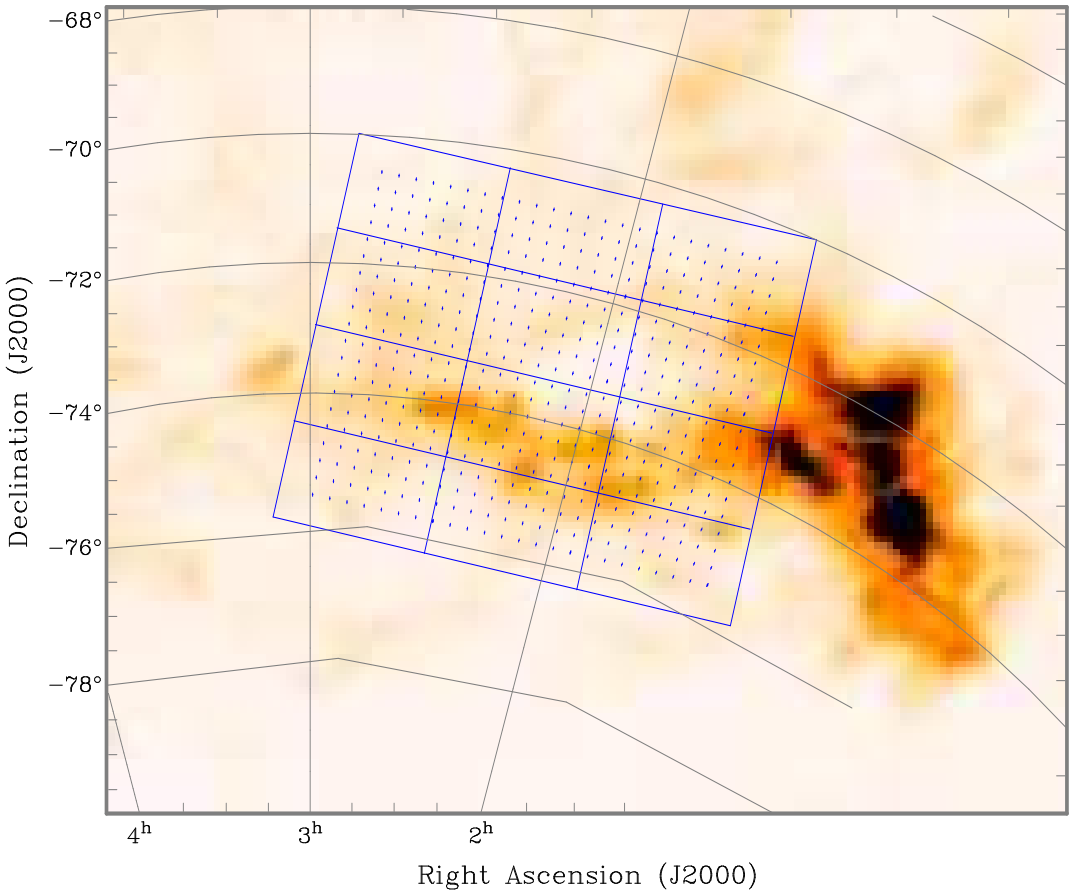

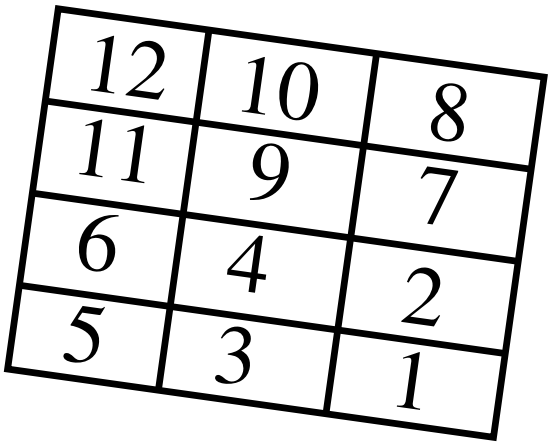

Figure 3.1: *Top:* Pointing centres for ATCA observations to be mosaiced and combined with short-spacings data. These are overlaid on an HI peak pixel map of the SMC and western Magellanic Bridge (Brüns, 2003). Overlaid grid defines boundaries of 'blocks'. There is a total of 480 centres over the entire field. *Bottom:* Block numbering, used for planning of observations.

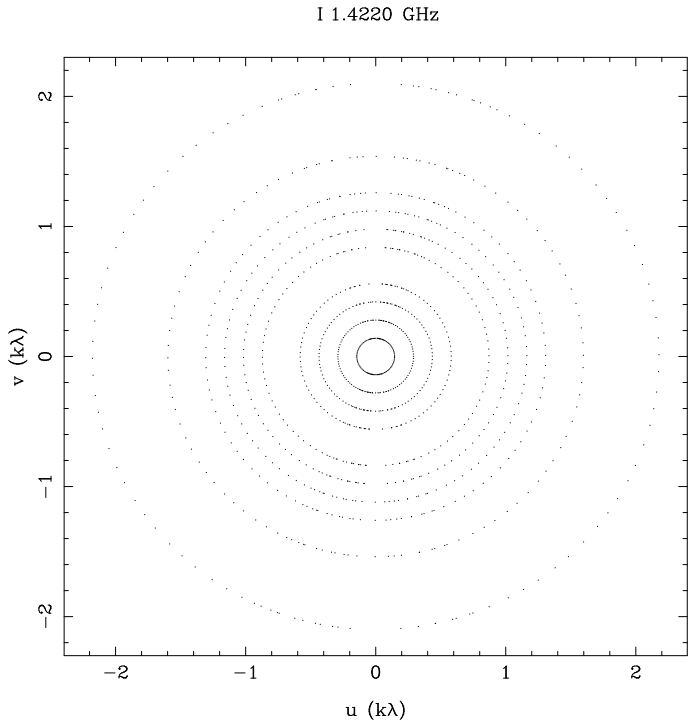

Figure 3.2: UV coverage for pointing #20 of 'block 4', centred at RA $02^{\rm h}\,06^{\rm m}\,07.6^{\rm s}$, Dec. $-74^\circ\,39'55.1''$. This is a typical example of the UV coverage for these observations.

Hanning smoothing.

The calibrator PKS B1934-638 was observed as a flux standard. This is assumed to be 14.9 Jy at 1.42 GHz. Where this could not be observed, PKS B0407-658 was observed instead, this is assumed to be 14.4 Jy at 1.42 GHz. PKS B0252-712 was used for phase calibration where possible, otherwise PKS B0454-810 was used. At 1.42 GHz, PKS B0252-712 is scaled to 5.7 Jy and PKS B0454-810 is scaled to 1.10 Jy.

The primary flux calibrator was observed before (and after, where possible) each observing session, none of which lasted for more than twelve hours. The phase calibrators were observed approximately every fifteen minutes.

3.1.3 ATCA data reduction

The *MIRIAD* data reduction suite was exclusively used for processing and reduction of the ATCA visibility data. Basically, there are three stages involved in converting raw data to a useful dataset. The first step is the rather labour intensive data reduction and calibration. This involves searching through the raw data to remove and 'flag' interference

spikes or other obviously spurious data. Only unflagged data contribute to the final datacube. Once flagging is complete, the calibration measurements are applied to the unflagged data to convert observed amplitudes into brightness temperatures. The third stage involves converting the edited and calibrated visibilities into a brightness map.

This section elaborates on the details of the flagging, calibration and image conversion steps. The *MIRIAD* data reduction suite was used for standard editing and calibration methods as well as the image inversion step (e.g. Stanimirović, 1999). Figure 3.3 shows the iterative procedure followed in reducing and calibrating the dataset. This will now be briefly described.

During the observing the telescope operating software may automatically flag any data associated with a detected telescope malfunction as bad data. Following observing, the data is also examined by the observer who may flag and exclude any other obvious interference. Prior to any calibration, the data are Hanning smoothed using the *MIRIAD* task ATLOD to a channel spacing of $\sim$1.63 km s^{-1}. The calibration can be somewhat iterative, as interference is not always obvious from the raw data. The calibration can begin once the necessary flagging is complete.

The calibration process was as follows:

1. Observations of the Primary Calibrator (PKS1934-638) are selected out from the dataset and scaled to a flux level of 14.9 Jy.

2. Observations of the Phase Calibrator (usually PKS0252-712) are selected out from the dataset scaled according to the Primary calibrator set and checked for flux and phase consistency.

3. Flux levels of source data are bootstrapped according to corrections derived from the Primary and Phase calibrator dataset.

3.1.4 Interferometer Image generation

The mosaicing method most commonly used to create a brightness image of the observed source is computed from a linear combination of images formed from the individual pointings:

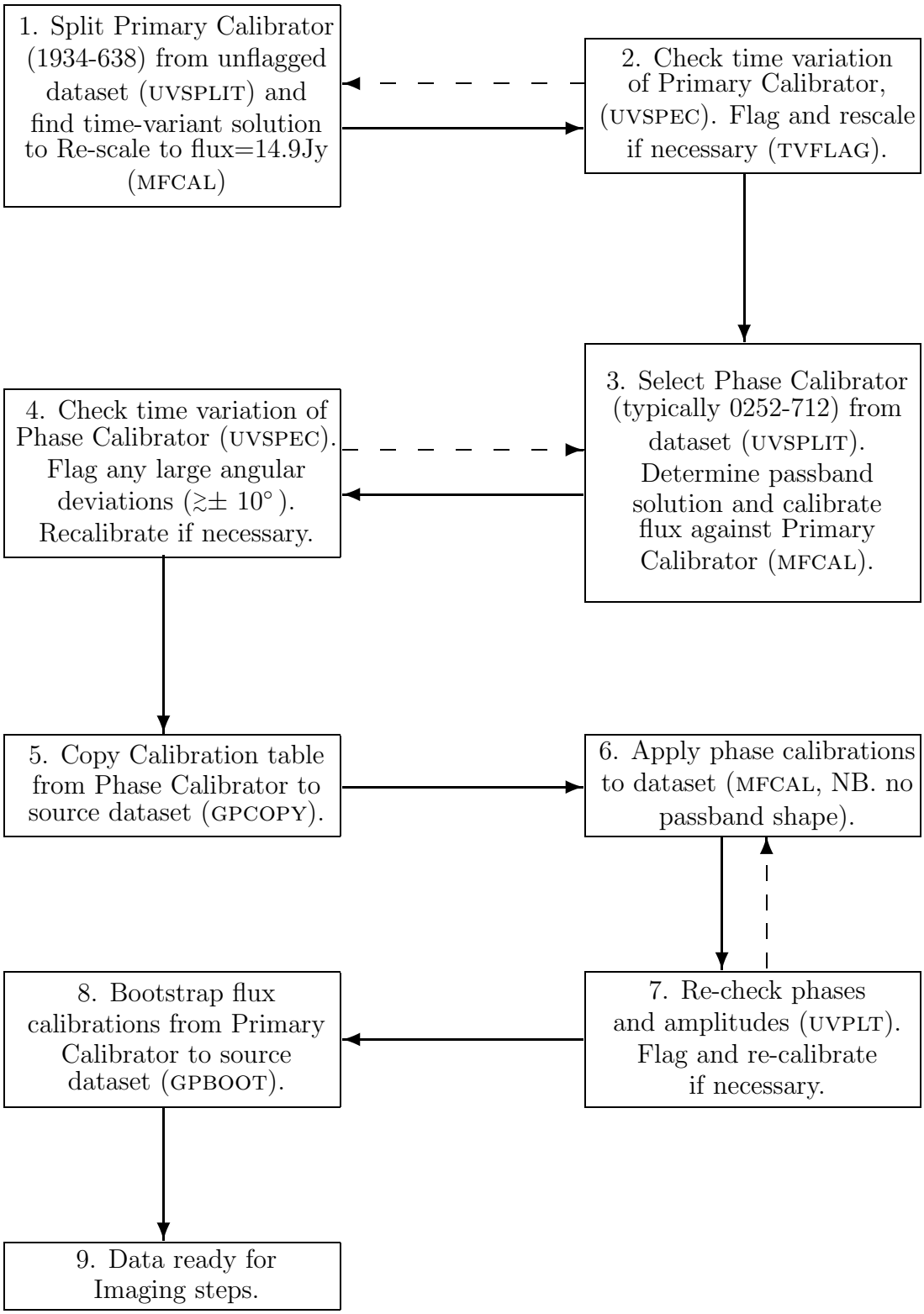

Figure 3.3: Flow chart of procedure followed for calibration of ATCA data. Brackets indicate the *MIRIAD* tasks used to complete the indicated process. The input (*at top*) takes visibilities after flagging and editing. The output is ready for line subtraction.

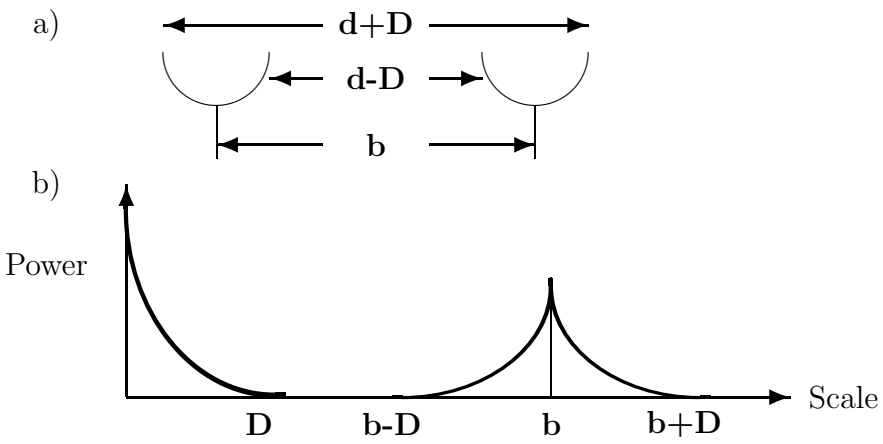

Figure 3.4: *a) Top* The full physical diameter of each interferometer element can reduce the minimum baseline *b* to *b-D*. *b) Bottom* The corresponding coverage in one direction in UV. After *Holdaway 1999*

$$I(x) = \frac{\sum_p A(\mathbf{x} - \mathbf{x_p}) I_p(x)}{\sum_p A^2(\mathbf{x} - \mathbf{x_p})}$$

where I_p is the pth individual image with an noise variance σ and A describes the beam pattern [1].

One advantage to be gained from this approach to mosaicing is that the entire dish surface contributes to the UV dataset. As such, for mosaicing, the smallest baseline available from the interferometer is found by $l_{min} - D$, where D is the diameter of the interferometer element. This is shown more clearly in Figure 3.4.

Figure 3.5 shows the deconvolution procedure followed after flagging and calibration of the dataset. A baseline of second order was fitted to the spectral data and subtracted. The data were then re-binned into 20 second integrations and the Stokes I parameter was selected. The dataset were then converted from visibilities with a standard MIRIAD recipe:

1. INVERT was used to linearly create a dirty image mosaic from the visibilities, using

[1] Sault, Staveley-Smith & Brouw (1996) use a more specific weighted form:

$$\mathbf{I}(\mathbf{x}) = W(x) \frac{\sum_p A(\mathbf{x} - \mathbf{x_p}) I_p(x)/\sigma_p^2}{\sum_p A^2(\mathbf{x} - \mathbf{x_p})/\sigma_p^2}$$

where σ_p is the variance at p and $W(x)$ is a weighting function, designed to vary the importance of power as a function of baseline. This gives an even distribution of noise across the combined image.

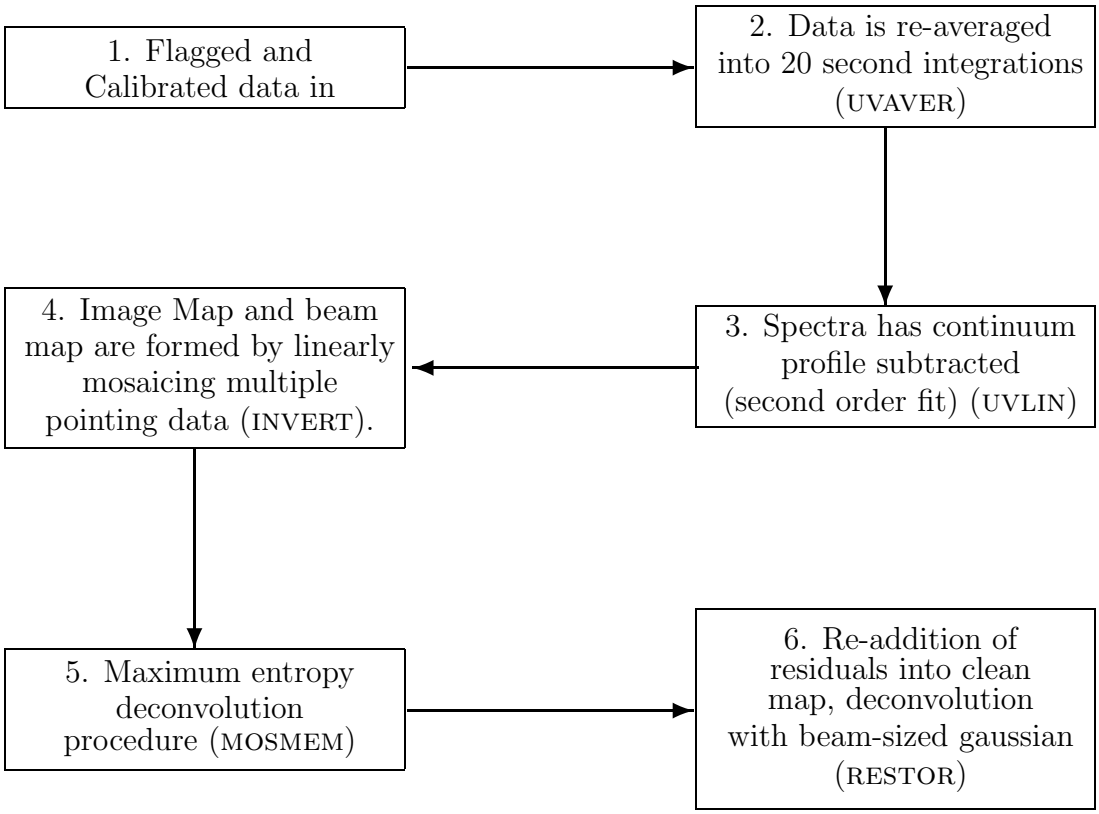

Figure 3.5: Flowchart of baseline substraction and deconvolution procedure, immediately following data calibration procedure. Brackets indicate the *MIRIAD* tasks used to complete the indicated process.

a robustness parameter of zero to down-weight the longer baselines. This has a final sensitivity of 0.9 K.

2. MOSMEM Performs the deconvolution via a maximum entropy minimising routine to deconvolve the dirty image cube.

3. RESTOR was used to add back in the residuals and convolve the data with a 98″ Gaussian function.

3.1.5 Parkes Observations

The Parkes telescope is a 64m telescope, located near Parkes, N.S.W., Australia (/emphlat. 148.3 E long. 33.00 S). The reflector is a parabolic surface on an alt-azimuth mount. The inner 17 m of the dish is a solid surface, with a perforated aluminium plate out to 45m, followed by 5/16 inch (77 mm) mesh to the remaining 64 m. It has an

efficiency (main beam flux/total flux) of $\sim$0.7.

The Parkes telescope has recently been upgraded with a new 13 beam focal-plane array for observations across the L-band, called the *Multibeam*. At this band, each beam has a FWHM width of $\sim$14.1′. This tool is now one of the most commonly used receivers at the Parkes facility and has unprecedented sensitivity at very high scanning speeds.

Observations were made using the Multibeam receiver during 1999 November 2nd-8th. Due to computer processing limitations, only the seven inner receivers of the Multibeam array were used. Forty-eight overlapping scans were made in Declination, using the on-the-fly mapping mode at $1^\circ\,\mathrm{min}^{-1}$ in Declination. The scans were centred on RA $02^\mathrm{h}\,00^\mathrm{m\,s}$, Dec. $-72^\circ\,20'$ (J2000) and extended 8° in RA and in Declination, large enough to fully encompass the area observed with the ATCA. The scans were interleaved with a spacing of 1.11° with a continuously rotating receiver so as to maintain a relative angle of 19.1° of the scan tracks to the sky. The final spacing between adjacent beam tracks was $\sim$6.7′. The tracks made by the centre beam on the sky are shown plotted on a Parkes HI map of the SMC (Brüns, 2003) in Figure 3.6.

For these observations, an 8 MHz bandwidth was used, with 2048 channels and centred on 1.42 GHz. This gave a channel spacing of 0.83 km s^{-1}. These observations were frequency-switched with a frequency throw of +3.5MHz (equivalent to $\sim$896 channels and $\sim$739.5 km s^{-1}).

3.1.5.1 Single dish Data reduction

The data were reduced and bandpass calibrated using the AIPS++ online data reduction system LIVEDATA. LIVEDATA was also used to apply velocity corrections. The cube was gridded using the 'sdfits2cube' algorithm (SLAP package, Staveley-Smith, L. priv. comm.), resulting in a beam FWHM of 15.7′.

3.1.6 Merging single dish and interferometer data

The merging of single dish and interferometric data can be accomplished through a variety of methods. See Stanimirović, (1999) for a review and comparison of alternatives.

Stanimirović (1999) concluded that for telescopes where there is significant overlap in

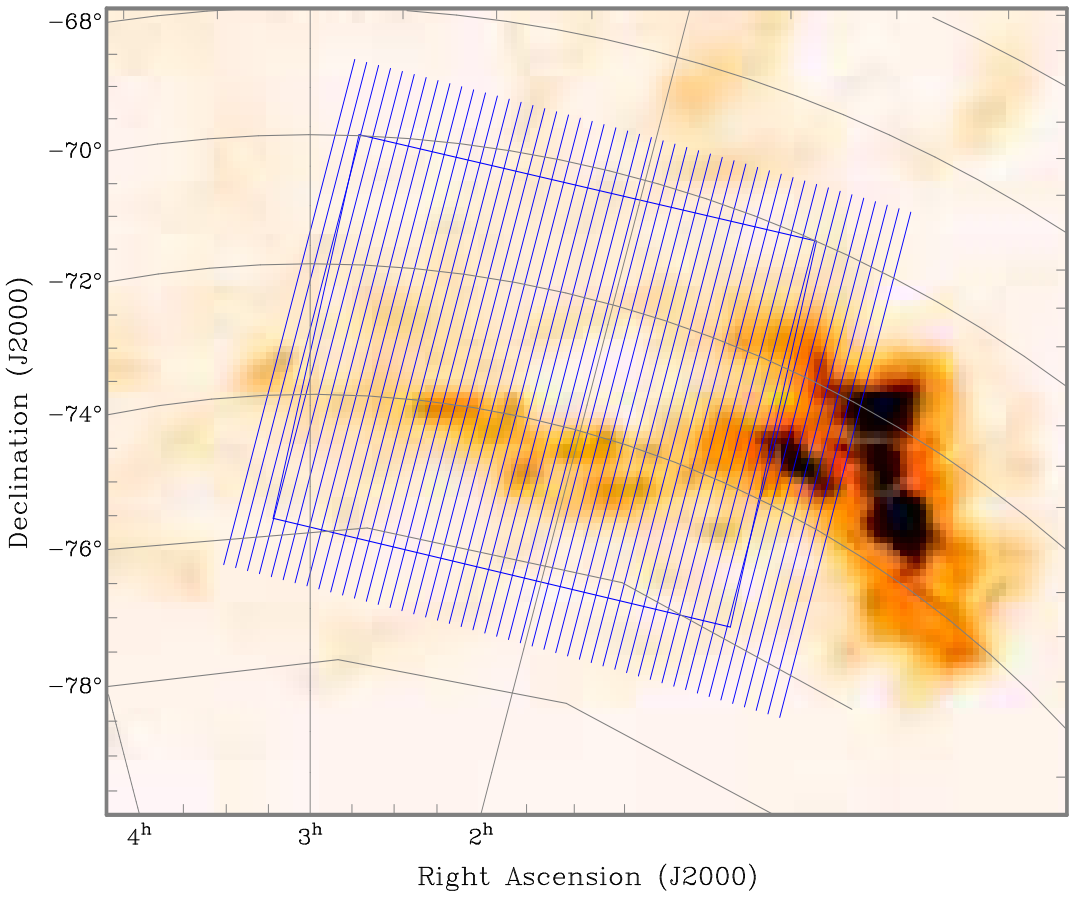

Figure 3.6: Tracks made by the centre beam on the sky, shown overlaid on an HI peak pixel map of the SMC and western Magellanic Bridge (Brüns, 2003). The square region defines the final perimeter of the dataset.

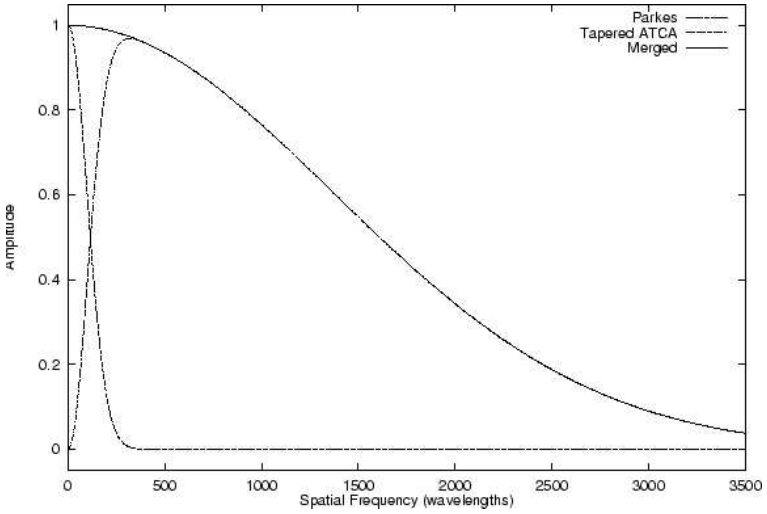

Figure 3.7: Target amplitude vs spatial frequency as returned by IMMERGE. The flux of the Parkes data is scaled accordingly so that the combined dataset returns this distribution (From MIRIAD manual). In the ideal case, the scaling factor is $\sim$1.

the UV plane (i.e. $D_{singledish} >>$ shortest baseline), the differences between merging methods, where single dish data is added to interferometric data before, during, or after deconvolution are usually minimal. As such, a linear, post-deconvolution method was employed here for its simplicity. The ATCA and Parkes data cubes were combined using the *MIRIAD* task IMMERGE. The Parkes data were first Hanning smoothed to the same velocity resolution as the ATCA data and regridded to the same spatial and velocity dimensions using the *MIRIAD* task REGRID.

IMMERGE scales the Parkes data by comparing data that is common to both datasets in the Fourier plane. It linearly adds the two data sets and weights the low spatial resolution data (i.e. the Parkes dataset) so the combined amplitude-spatial frequency response curve returns to a Gaussian form, in this case, with a width equal to that of the ATCA data. An idealised representation of the target Spatial Power Spectrum is shown in Figure 3.7 (*MIRIAD* manual, Sault, Killeen 1999). For perfectly calibrated and stable telescopes the low resolution data scaling factor should be equal to 1, however, data quality varies over time and from telescope to telescope and this factor is determined more accurately using IMMERGE. A scaling factor of $\sim$1.15 for the Multibeam dataset is used during combination of the Parkes data from these observations.

The combined cube is converted to brightness temperature using the relation; $S = 2k\Omega T_B/\lambda^2$, where Ω is the beam area of the combined cube ($=\Omega_{ATCA}$). For this ATCA

configuration, S=63.07 K/Jy.

The combined cube covers a velocity range of -100 km s^{-1} to 350 km s^{-1} with 152 channels. It has a velocity channel spacing of 1.65 km s^{-1} and an RMS of 0.8 K beam^{-1} as measured in line free channels of the cube. This corresponds to a column density of 1.7×10^{18} cm^2 for each velocity channel, assuming the mass is optically thin. The final angular resolution is 98″.

The resulting datacube is presented in the next section.

3.2 The complete HI cube.

Figures 3.8a and 3.8b show the integrated intensity maps of the RA-Dec and RA-Velocity projections of the combined ATCA/Parkes data cube, while the Velocity-Declination projection is shown in Figure 3.9. Lines of constant velocity (38 km s^{-1} and 8 km s^{-1}) in the Galactic rest frame are included on the RA-Velocity map. The conversion from Heliocentric to Galactic rest-frames (GSR) is made with the relation:

$$V_{GSR} = V_{Hel} + 232\sin(l)\cos(b) + 9\cos(l)\cos(b) + 7\sin(b)$$

(e.g. Paturel et al. 1997).

A number of features are immediately obvious in the RA-DEC map (Fig.3.8a):

1. Parts of the Magellanic Bridge show very complex HI. We see structure in the form of loops, filaments and clumps distributed over all observed spatial scales, down to the projected size of the ATCA beam of ∼28 pc. A survey of apparently expanding spherical HI regions is detailed in Chapter 4 and a statistical analysis of the structure of the observed HI is presented in Chapter 5.

2. Brighter HI emission appears to be confined to a central filament within the observed region that runs almost parallel to the lines of constant Declination. The HI column density is higher than the background diffuse component by a factor of ∼20. The highest column density in this east-west strip is 5.5×10^{21} cm^{-2} and is located at RA $1^{\rm h}\,23^{\rm m}\,59^{\rm s}$, Dec. $-73^\circ\,07'43''$(J2000). However, this point is actually inside the SMC, found on the eastern edge of the observed region. Excluding the SMC (i.e.

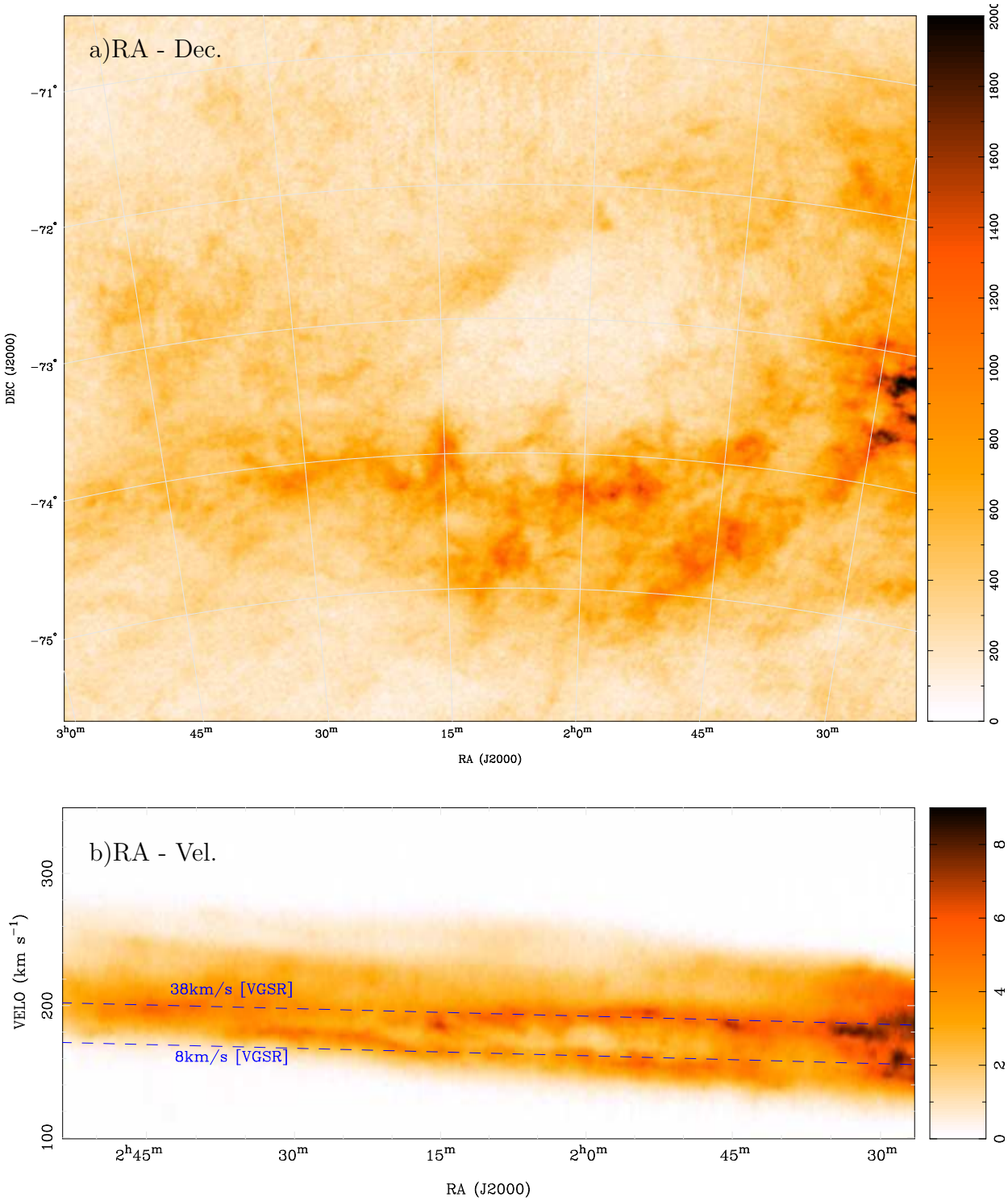

Figure 3.8: Integrated intensity maps of Right Ascension-Declination and Right Ascension-Velocity projections of combined ATCA-Parkes datacube. Colourscale is a linear transfer function as shown on the intensity wedge with units in K·km s^{-1}. A conversion to column density (atm/cm^{-2}) can be made by multiplying the integrated intensity by $1.8{\times}10^{18}$ (Equation 2.1). Shown here are *Top:* a) RA-Dec. projection. *Bottom:* b) Velocity-Dec. projection (see Figure 3.9 for RA-Velocity projection). Velocities are in the Heliocentric rest frame and Right Ascension scale in b) is correct only for the centre Declination of the dataset, at $-73°\,27'59''$. The upper and lower lines in b) denote velocities of 38 and 8 km s^{-1} respectively, relative to Galactic Standard of Rest.

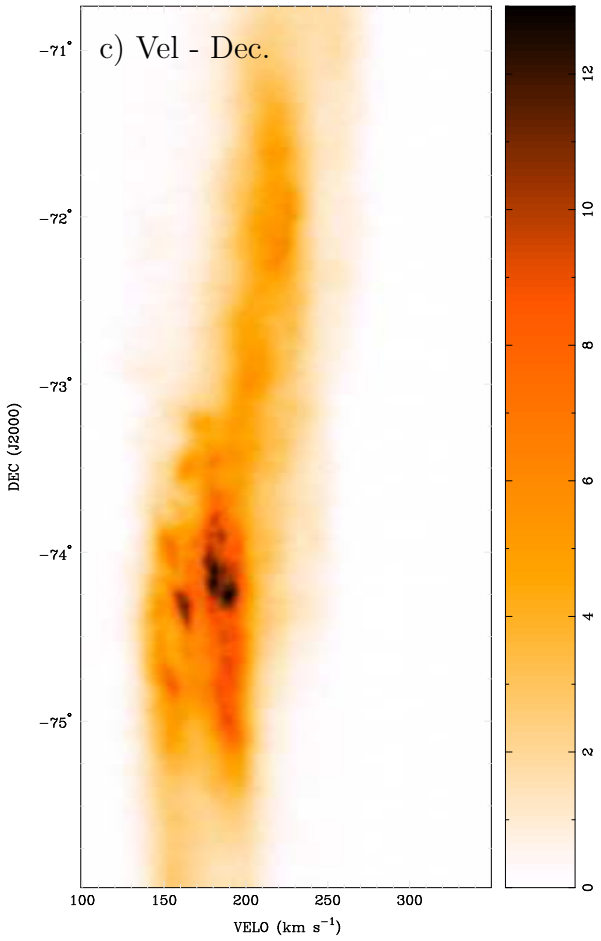

Figure 3.9: Integrated intensity maps of Velocity-Declination projection of combined ATCA-Parkes datacube. Greyscale is a linear transfer function as shown on the wedge and units are K·km s^{-1}. Declination scaling is correct only at the centre RA of the dataset, at $2^{h}\,08^{m}\,7.6^{s}$.

east of $\sim 1^{\rm h}\,35^{\rm m}$), the highest column density is $\sim 2.8\times10^{21}$ cm^{-2} at RA $01^{\rm h}\,58^{\rm m}\,09^{\rm s}$, Dec. $-74^\circ\,17'28''$(J2000).

3. A loop filament, centred at approximately $\sim$RA $\sim 02^{\rm h}\,09^{\rm m}\,59^{\rm s}$, Dec. $-73^\circ\,21'56''$ (J2000) appears to be a truly rim-brightened region. The column density of the loop varies between $\sim$0.5-1$\times10^{21}$ cm^{-2}, while the mean column density of the interior of the loop is $\sim 0.2\times10^{21}$ cm^{-2}. The radius of the loop is $\sim 1^\circ$, corresponding to a projected diameter of $\sim$1.1 kpc. Possible formation mechanisms involved in creating this loop are discussed in Chapter 6.

From the Velocity-position maps (Figures. 3.8b and 3.9) we see that:

1. An apparent velocity bimodality can be seen in the RA-Vel plot of Figure 3.8b and to a lesser extent in Figure 3.9. Closer to the SMC, the velocity profile appears to be trimodal and this will also be discussed later in Chapter 6. The separation of the velocity peaks is $\sim$30 km s^{-1}, which appears to be roughly constant in RA from the SMC up to RA $2^{\rm h}\,17^{\rm m}$, where it suddenly converges to a single velocity of 180 km s^{-1} (heliocentric). This is also a large-scale feature of the Bridge which will be discussed in Chapter 6.

2. The heliocentric velocity increases smoothly from the SMC, there also appears to be a much smaller velocity gradient with respect to GSR.

Figure 3.9 also reveals interesting velocity structure.

1. The bimodality seen in Figure 3.8b manifests as an elongated and inverted 'U'.

2. There appears to be a large volume of gas in the more northern part of the Bridge, with a substantially higher velocity. In this projection, this region covers the declinations $\sim -74^\circ\,21'$ to $-73^\circ\,19'$, the relative shift in velocity is $\sim$+40 km s^{-1}. This feature is discussed in the context of numerical simulations in Chapter 6.

Intensity maps of the RA-Dec projection of the cube, integrated over groups of five channels (intervals of $\sim$8 km s^{-1}) are shown in Figure 3.10. The SMC appears in the first few frames on the western edge of the observed area. The large loop filament is particularly obvious in the higher velocity frames centred on V_{Hel}=194-227 km s^{-1}.

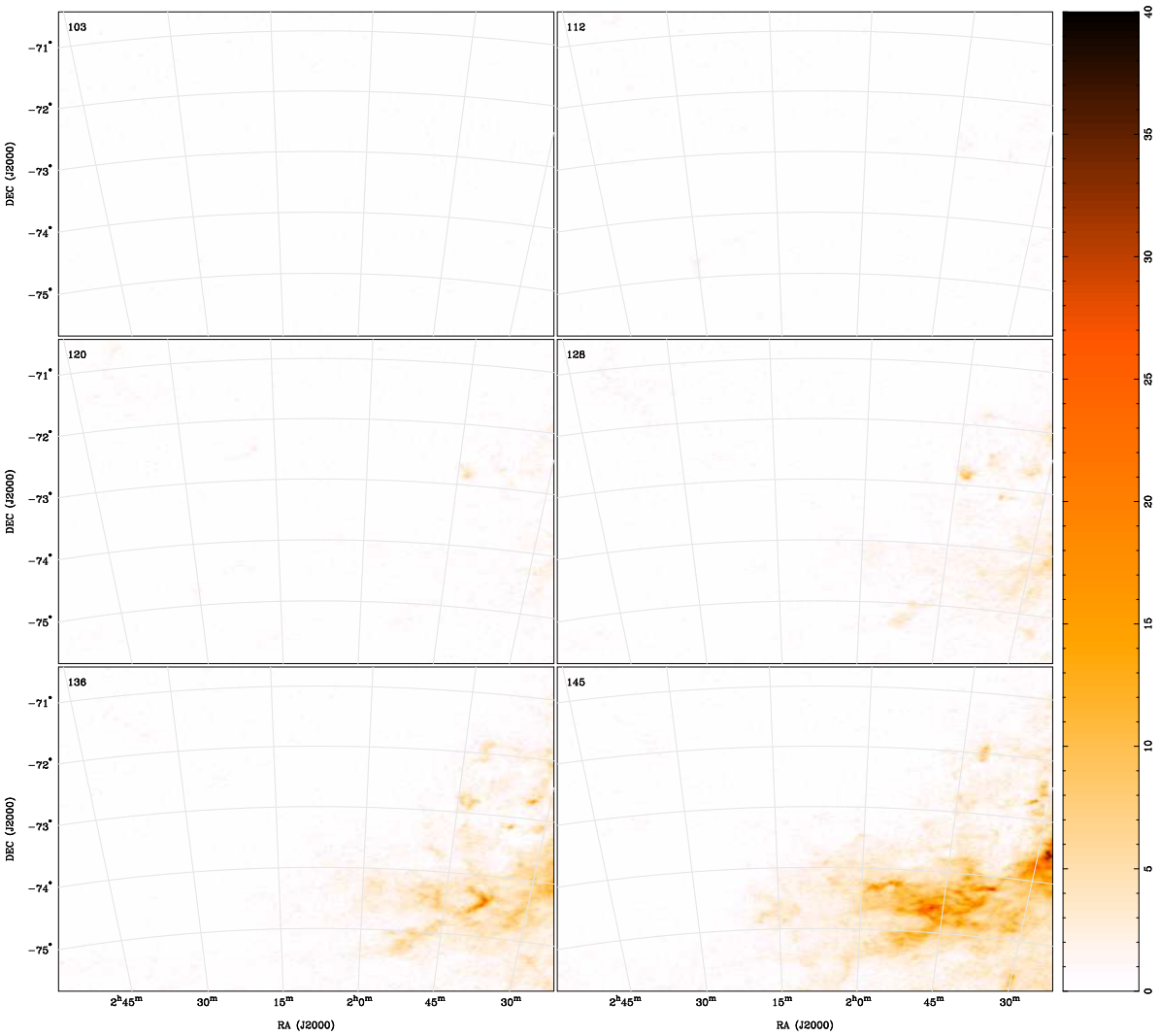

Figure 3.10: RA-Declination projection maps for the ATCA-Parkes HI observed dataset in the direction of the Magellanic Bridge. Each map is averaged over five channels ($\sim$8 km s^{-1}) of the original datacube. The velocity of the centre channel is shown in the top left of each map. Units are in Kelvin, with a linear transfer function.

Figure 3.11 shows thin integrated slices of the Right Ascension-Velocity projection of the combined datacube. These maps are integrated across 9′ in declination. The velocity bifurcation can be seen between $\sim -76^\circ\,08'$ to $-73^\circ\,27'$.

Finally, shown in Figure 3.12 are intensity maps, averaged over thin $\sim$10.5′ intervals of the Velocity-Declination projections of the cube. These plots also show the higher velocity HI mass at low declinations mentioned earlier.

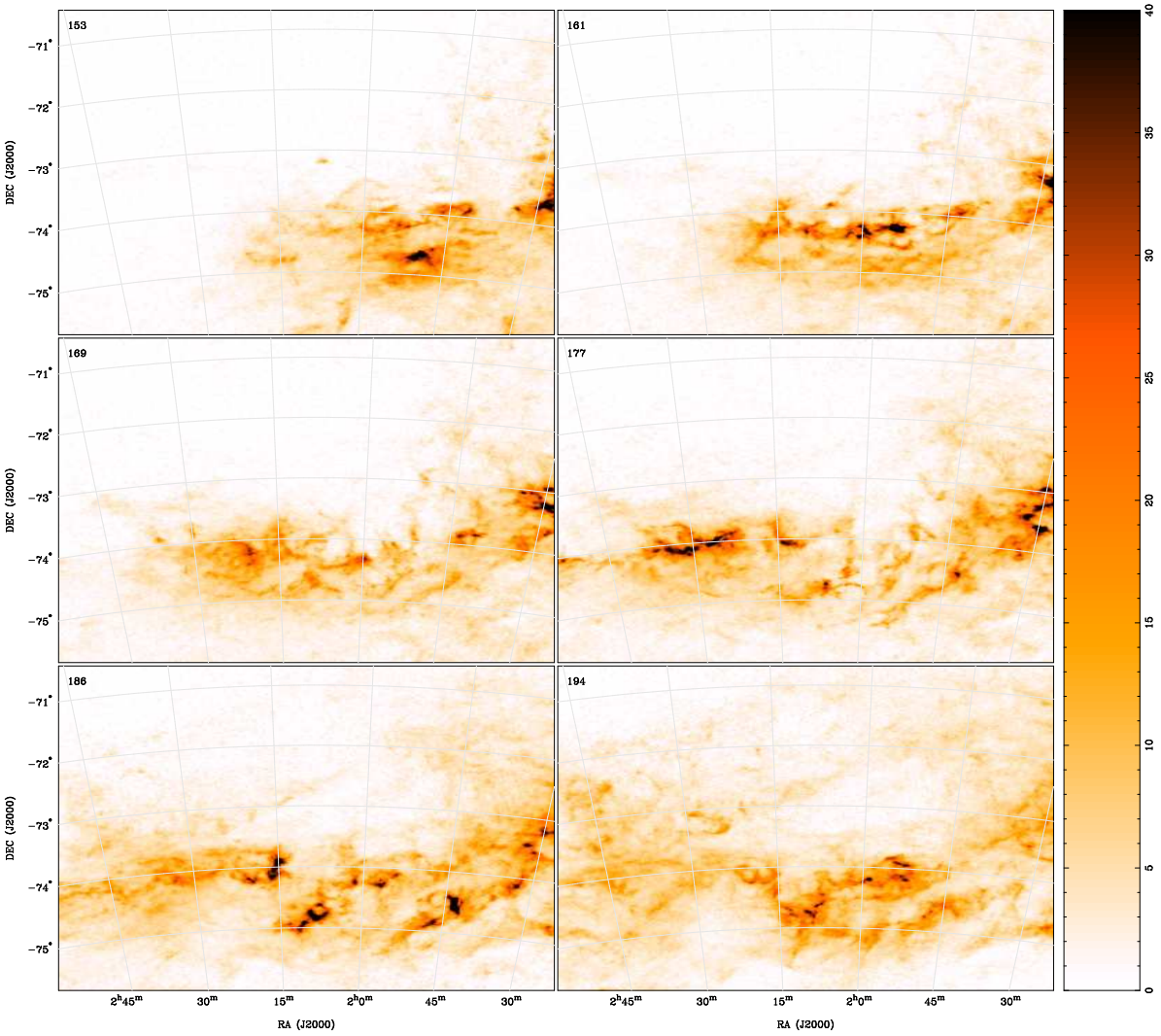

Figure 3.10: *cont.* RA-Declination projection maps for the ATCA-Parkes HI observed dataset in the direction of the Magellanic Bridge. Each map is averaged over five channels ($\sim$8 km s^{-1}) of the original datacube. The velocity of the centre channel is shown in the top left of each map. Units are in Kelvin, with a linear transfer function.

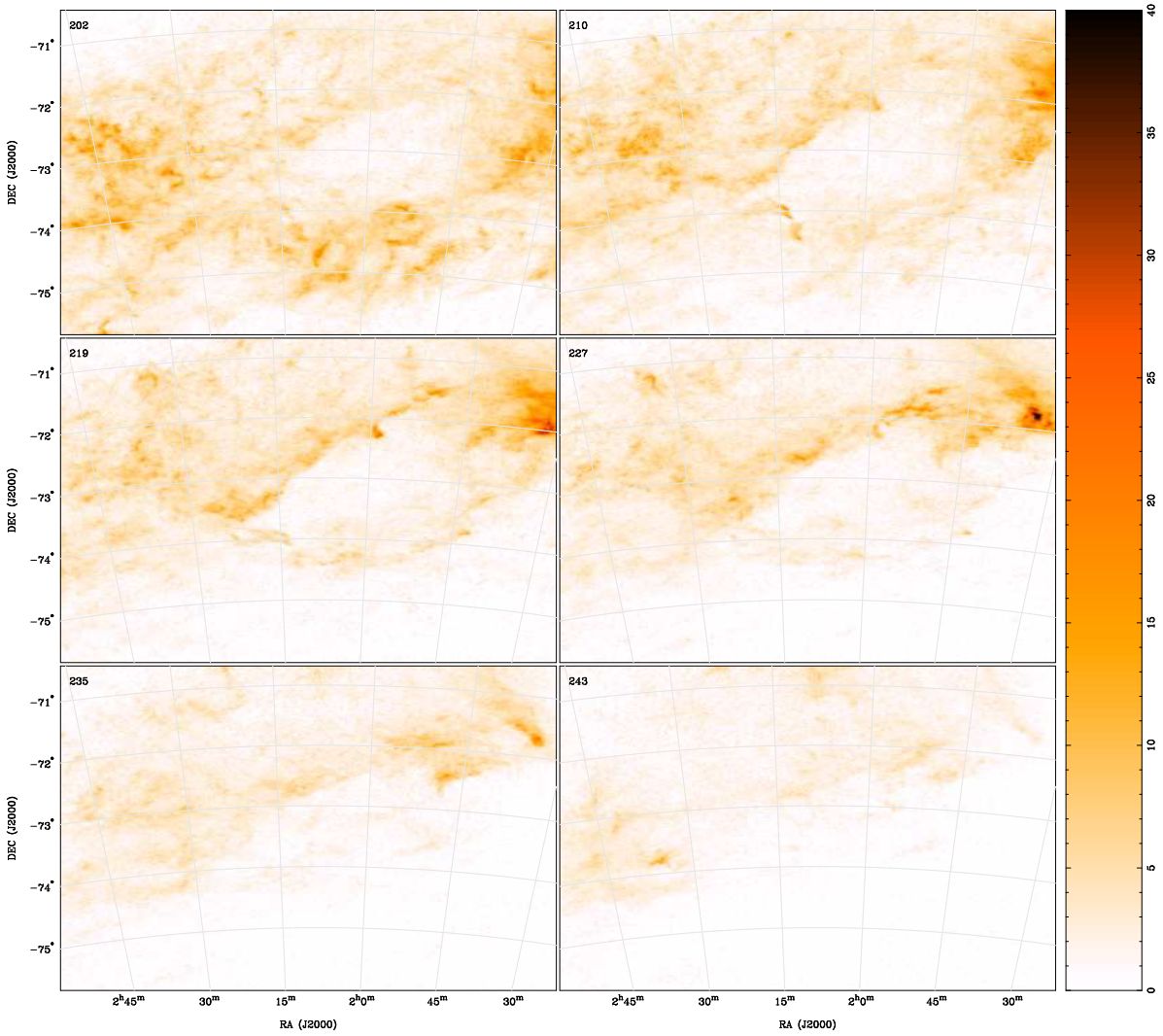

Figure 3.10: *cont.* RA-Declination projection maps for the ATCA-Parkes HI observed dataset in the direction of the Magellanic Bridge. Each map is averaged over five channels ($\sim$8 km s^{-1}) of the original datacube. The velocity of the centre channel is shown in the top left of each map. Units are in Kelvin, with a linear transfer function.

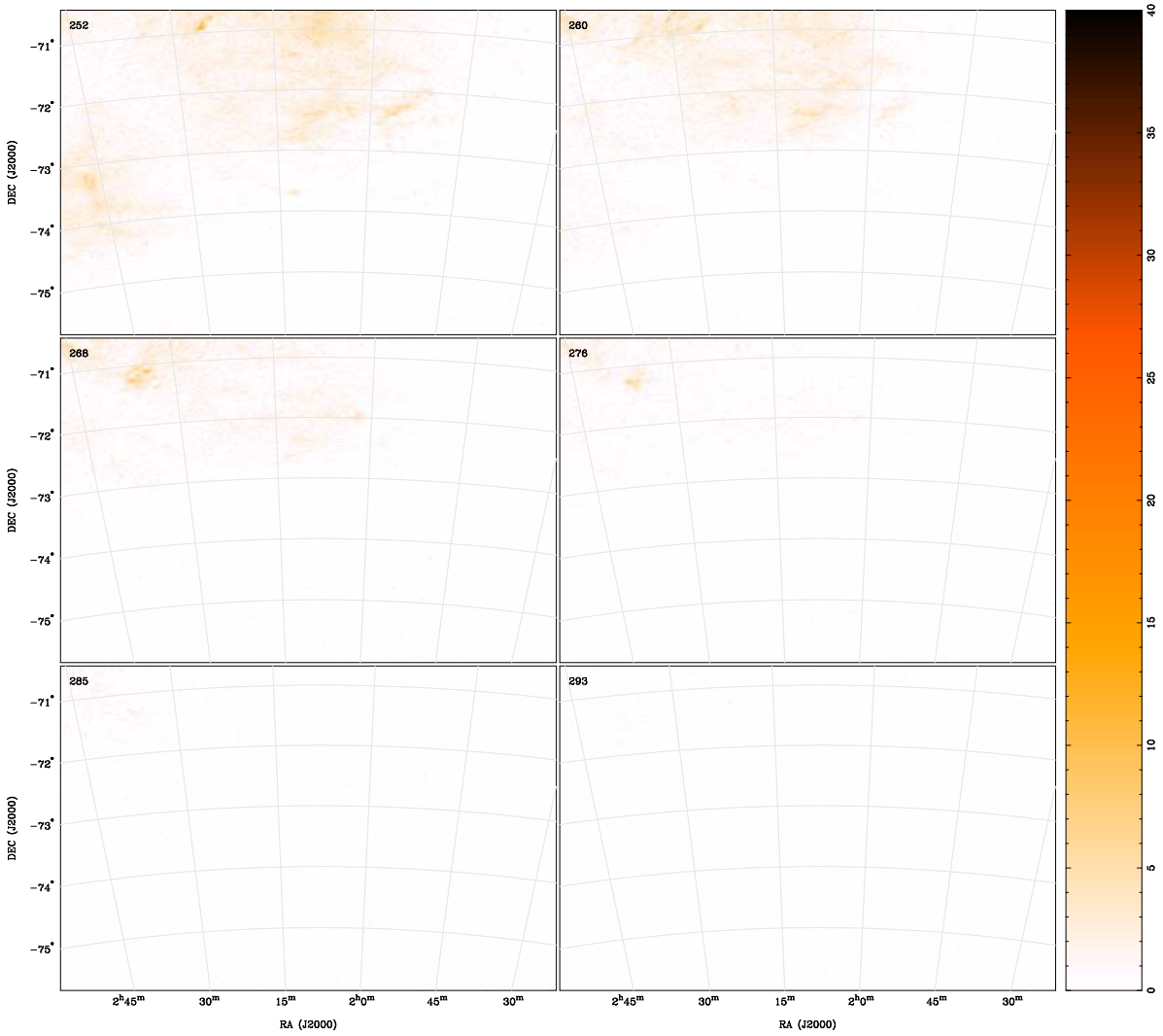

Figure 3.10: *cont.* RA-Declination projection maps for the ATCA-Parkes HI observed dataset in the direction of the Magellanic Bridge. Each map is averaged over five channels ($\sim$8 km s^{-1}) of the original datacube. The velocity of the centre channel is shown in the top left of each map. Units are in Kelvin, with a linear transfer function.

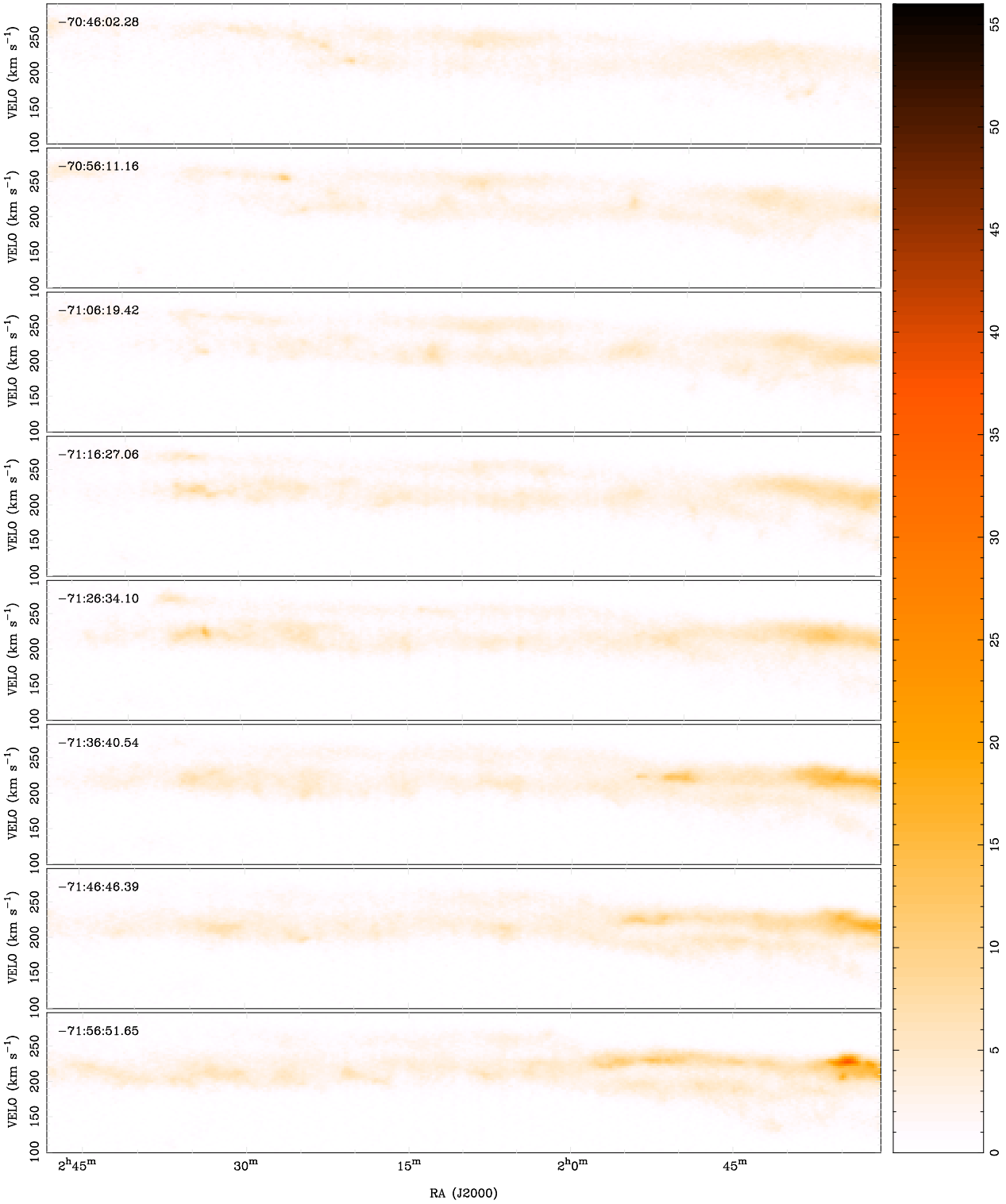

Figure 3.11: Channel maps of the RA-Velocity projection of the combined datacube integrated across 9′ in declination. The declination of the centre channel is shown in the top left of each map. Units are in Kelvin, with a linear transfer function.

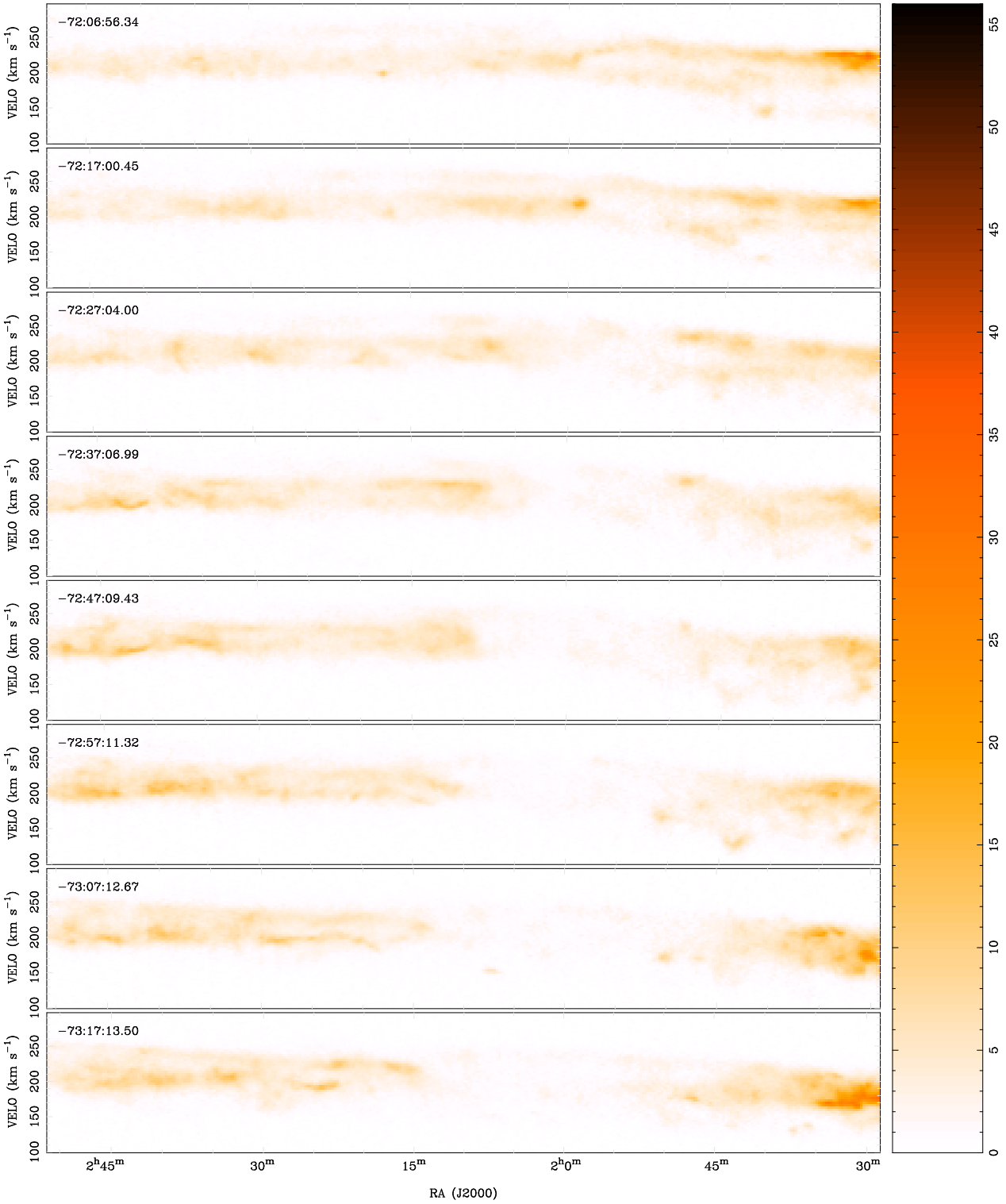

Figure 3.11: *cont.* Channel maps of the RA-Velocity projection of the combined datacube averaged across 9′ in declination. The declination of the centre channel is shown in the top left of each map. Units are in Kelvin, with a linear transfer function.

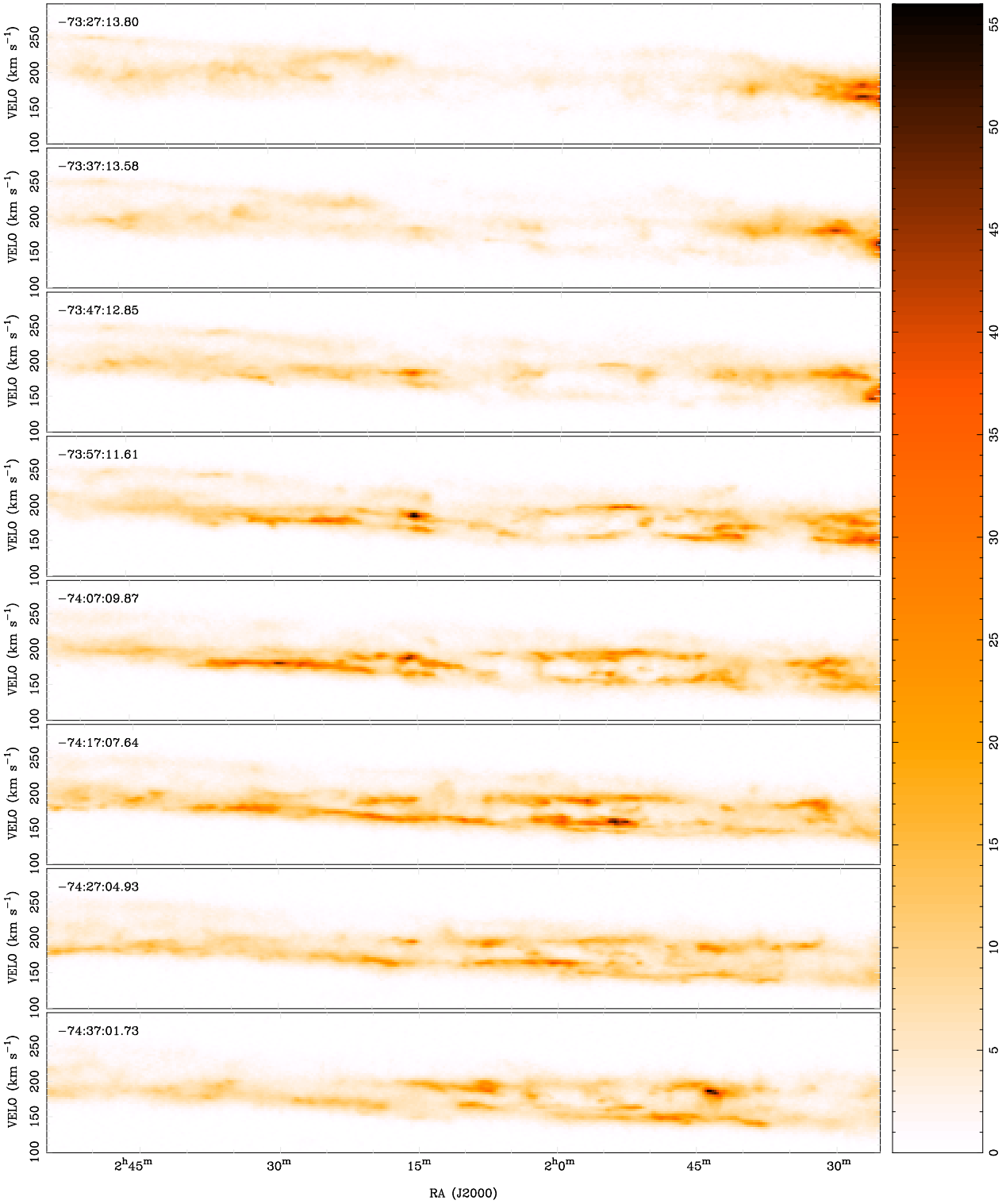

Figure 3.11: *cont.* Channel maps of the RA-Velocity projection of the combined datacube averaged across 9′ in declination. The declination of the centre channel is shown in the top left of each map. Units are in Kelvin, with a linear transfer function.

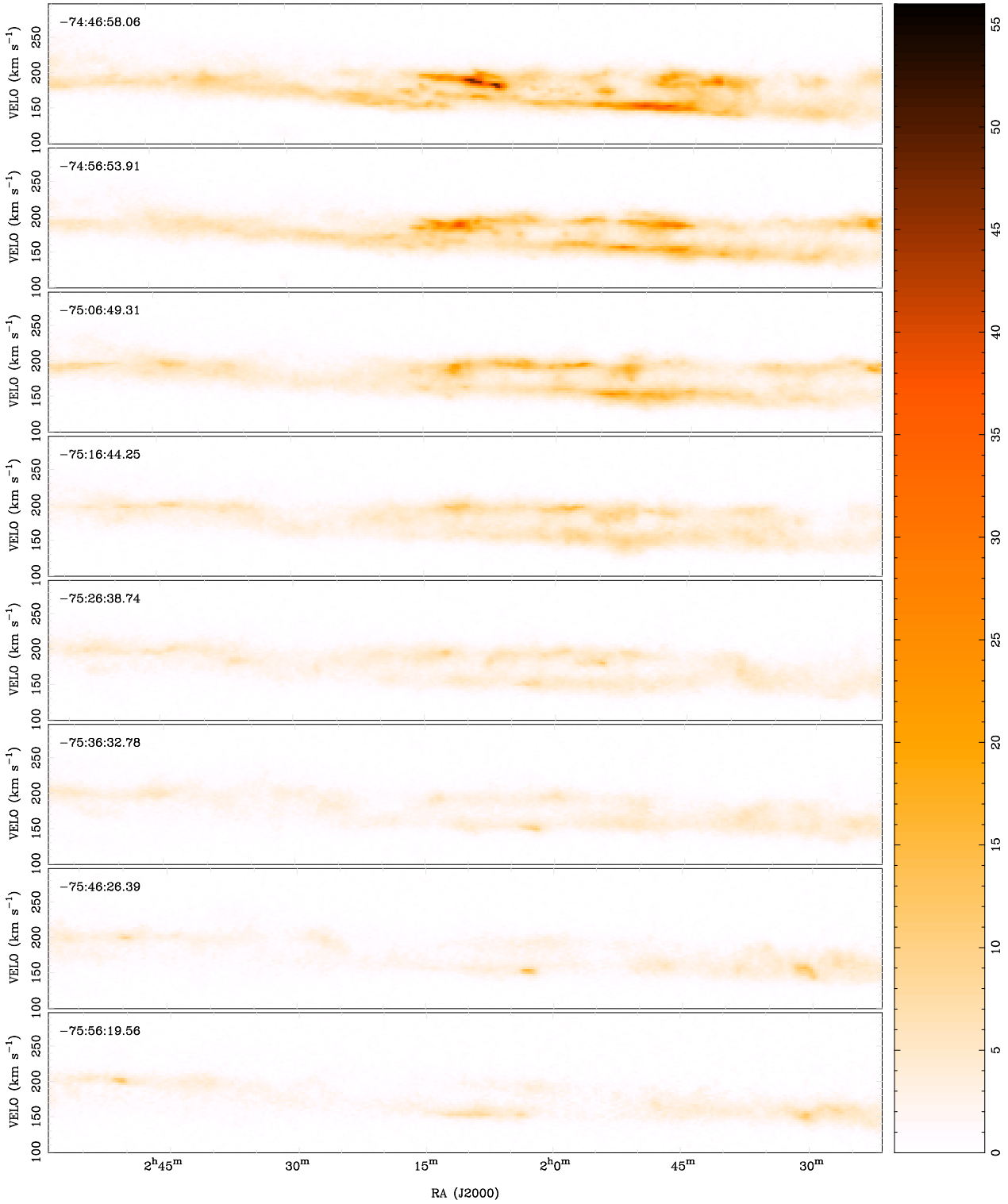

Figure 3.11: *cont.* Channel maps of the RA-Velocity projection of the combined datacube averaged across 9′ in declination. The declination of the centre channel is shown in the top left of each map. Units are in Kelvin, with a linear transfer function.

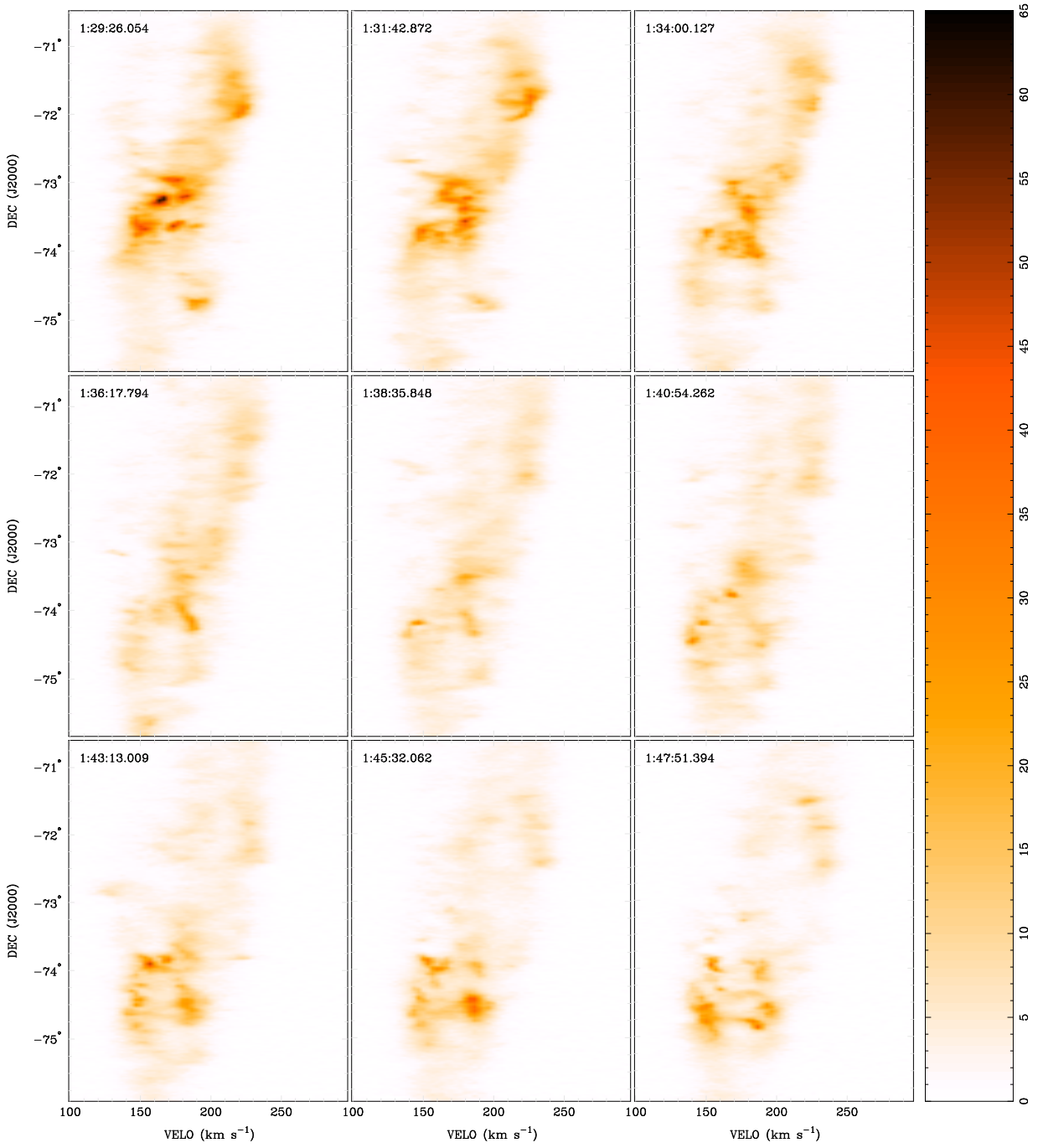

Figure 3.12: Channel maps of the Velocity-declination projection of the combined datacube averaged over thin $\sim$10.5′ intervals. The Right ascension of the centre channel is shown in the top left of each map. Units are in Kelvin, with a linear transfer function.

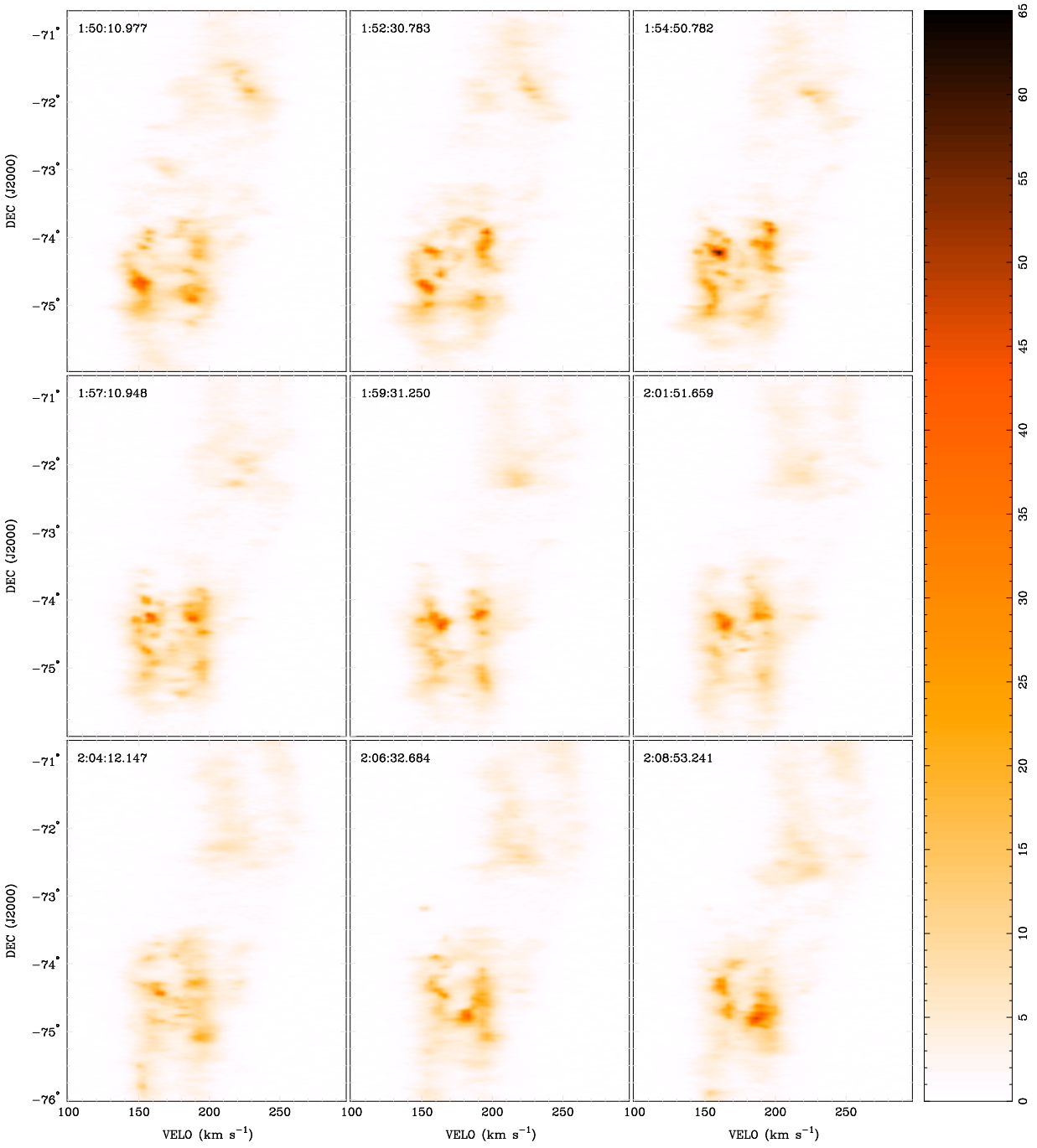

Figure 3.12: *cont.* Channel maps of the Velocity-declination projection of the combined datacube averaged over thin $\sim$10.5′ intervals. The Right ascension of the centre channel is shown in the top left of each map. Units are in Kelvin, with a linear transfer function.

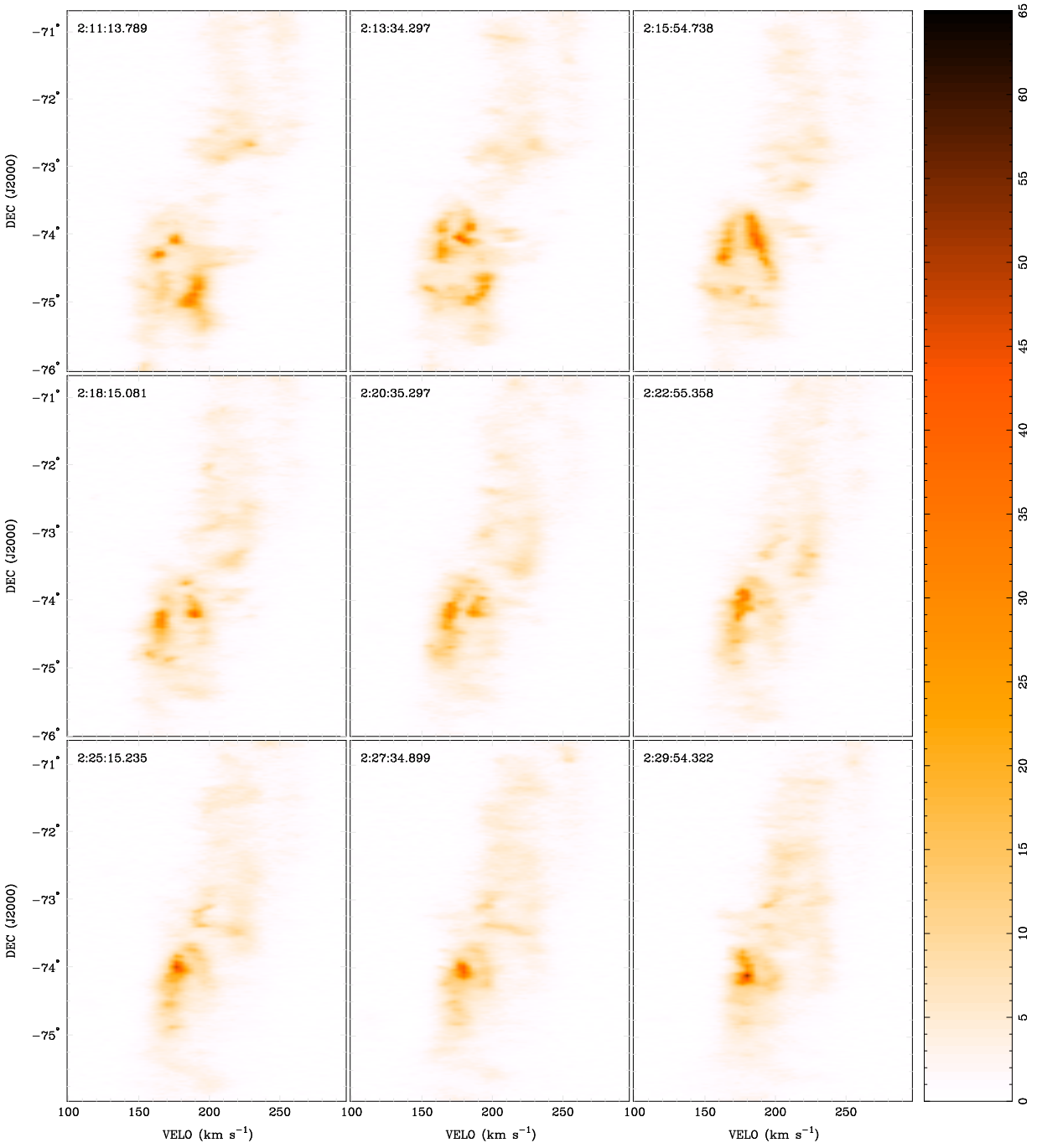

Figure 3.12: *cont.* Channel maps of the Velocity-declination projection of the combined datacube averaged over thin $\sim$10.5′ intervals. The Right ascension of the centre channel is shown in the top left of each map. Units are in Kelvin, with a linear transfer function.

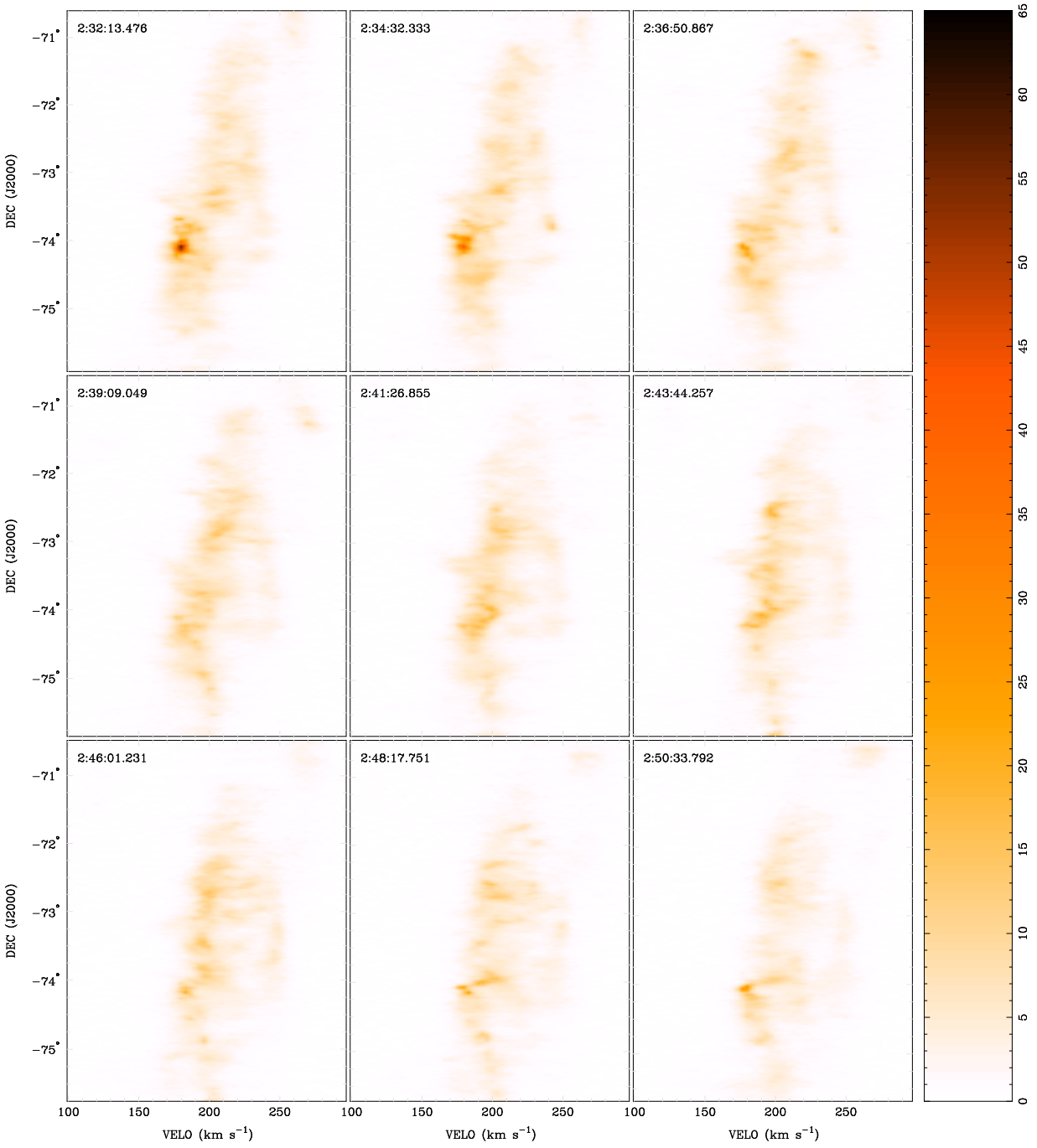

Figure 3.12: *cont.* Channel maps of the Velocity-declination projection of the combined datacube averaged over thin $\sim$10.5′ intervals. The Right ascension of the centre channel is shown in the top left of each map. Units are in Kelvin, with a linear transfer function.

3.2.1 Mass and density calculations

The mass of the observed region excluding the SMC in the western edge of the observed area (west of $\sim 1^{\rm h}\,35^{\rm m}$) and a $35''$ margin around the edge of the image (which is relatively undersampled) is $\sim 1.5\times10^{8}$ $M_{\odot}$. However, Figure 3.8b shows that the central region contains the brightest HI and we will see later that the the expanding shell population appears to be more prevalent in this area (see Chapter 4). If we examine only the central higher-column density filament, bounded by -75.5° to -73.5° in declination and $1^{\rm h}\,34'$ to $2^{\rm h}\,46'$ in RA (corresponding to a height of $\sim$2.1kpc and a length of $\sim$5kpc, see Figure 3.8a), we find an enclosed mass of approximately 7.4×10^{7} $M_{\odot}$ with a surface mass distribution of ~ 7 $M_{\odot}\,pc^{-2}$. There are two reasonable approaches to calculate the density of this region:

1. We can assume that the mass of this region is contained within a cylinder of radius 2.1kpc/2 = 1.1kpc and height 5 kpc, then the approximate volume density is $n_o \sim 0.2$ cm^{-3}.

2. Demers & Battinelli (1998) have inferred a depth of the Bridge of $\sim$5 kpc by measuring a difference in distance modulus of two adjacent (separated by $\sim$7') O associations. If the high density region of the Bridge is modelled as a slab, with a width of 5 kpc, a length of $\sim$5 kpc and a thickness of $\sim$2.1 kpc, the number density of HI is ~ 0.06 cm^{-3}.

These figures are derived from the central high-density region and the estimate will represent a maximum value for the observed area. The more tenuous gas to the north of the central region has column densities which are a factor $\sim$0.3-0.5 of the central high density region (Figure 3.8a). As the latter value of n=0.06 cm^{-3} is derived using real depth measurements, we use this value throughout this study.

3.2.2 Correction for HI self absorption.

To estimate the extent of HI self absorption in the Bridge, we use tabulated HI self-absorption correction factors derived for the SMC by Stanimirović (1999). Table 4.2 in this study shows that column densities within the range 25-65$\times10^{20}$ cm^{-2} require a correction of $\sim$1.1 and if we note that the the HI integrated intensity in the Bridge (east of

$\sim 1^{h}\,34^{s}$) peaks at 27×10^{20} cm^{-2}and has an average of 6.47×10^{20} cm^{-2}, we may conclude that a correction for HI self-absorption will have a negligible effect on this Magellanic Bridge HI data. This dataset therefore has no corrections made for HI self-absorption.

Chapter 4

HI shells in the Magellanic Bridge

"Oh no, Not again..." - Sperm Whale, 1980's

We have seen that much of the HI in the Magellanic Bridge is complex and filamentary. Parts of the brighter HI is arranged in many apparent loop or crescent-like features. In this Chapter, we present the results of an HI expanding shell survey of the Magellanic Bridge HI dataset with reference to the observed OB stellar population. The results of the survey are compared with those of similar studies on the SMC and the HI-rich Magellanic-type galaxy, HoII.

4.1 HI expanding shells

A shell or bubble within a gas cloud can be generated through a variety of mechanisms. The most commonly assumed scenario involves a series of stellar winds and Supernova events (SNe) which deposit energy into the medium (Weaver et al. 1977; Cox, 1972; Chevalier 1974). Alternative shell formation mechanisms such as Gamma ray bursts (Efremov, Elmegreen and Hodge, 1998) and HVC-disk collisions (Tenorio-Tagle, 1981; Tenorio-Tagle et al. 1986; Tenorio-Tagle et al. 1987; Tenorio-Tagle & Bodenheimer, 1988) may also produce elliptical structures with similar appearance. In general however, it is very difficult to determine the process by which a particular shell has been formed.

Expanding shells leave a characteristic imprint in HI column density maps as a relatively bright ring in spatial co-ordinates and, depending on the expansion velocity of the shell, as an ellipse in position-velocity space. A survey for expanding shell features is difficult and

can be quite a subjective process. In most cases, the ring shape is distorted or fragmented and accurately parameterising the radii or expansion velocity can be very difficult. The rest of this section will present a review of existing shell formation theories.

4.1.1 Stellar wind

Shell formation by a stellar wind starts with a young energetic star or cluster, which ionises the surrounding gas into a hot, high pressure region and thereby produces a spherical, high-density shockwave which propagates into the ambient neutral gas (Shu, 1992). In addition to ionisation, the young star constantly sheds mass in a stellar wind which impinges on the local gas. The overall result is a relatively low density sphere enclosed by a higher density hydrogen shell, the outer edge of which is neutral and moves at supersonic velocities into the ambient gas (McCray & Snow, 1979). This scenario is described in detail by Weaver et al. (1977) and Castor, McCray & Weaver (1975).

Weaver et al. (1977) and Castor, McCray & Weaver (1975) derive various expressions describing the evolution of various parameters of shells formed by stellar wind as a function of ambient gas density and time. The models by Weaver et al. (1977) were among the first to incorporate wind momentum transfer and thermal effects into a shell expansion theory. Weaver et al. (1977) describe the evolution of an expanding shell as it moves through three stages:

i. The first is a brief adiabatic expansion phase, where the expansion is too fast to settle into thermal equilibrium with the surrounding gas. This phase has been shown to be the briefest for all phases (Avedisova, 1972).

   For this phase, Weaver et al. (1977) describes the shell as having a layered morphology. As shown in Figure 4.1, the innermost layer (layer *a*, at radius R_1 from the star in Figure 4.1) is the supersonic stellar wind, comprising mass and ionising radiation shed isotropically into the ambient medium by the star. The shocked part of the wind forms layer *b* (which is assumed to be thin and approximately isobaric) with an external radius of R_c, while the shocked ISM forms layer *c* and has an external radius of R_2. The external and unaffected ISM comprises layer *d*.

ii. The second stage describes a period of radiative loss, where the swept-up region begins to cool and collapse into a thin spherical neutral shell. Weaver et al. (1977)

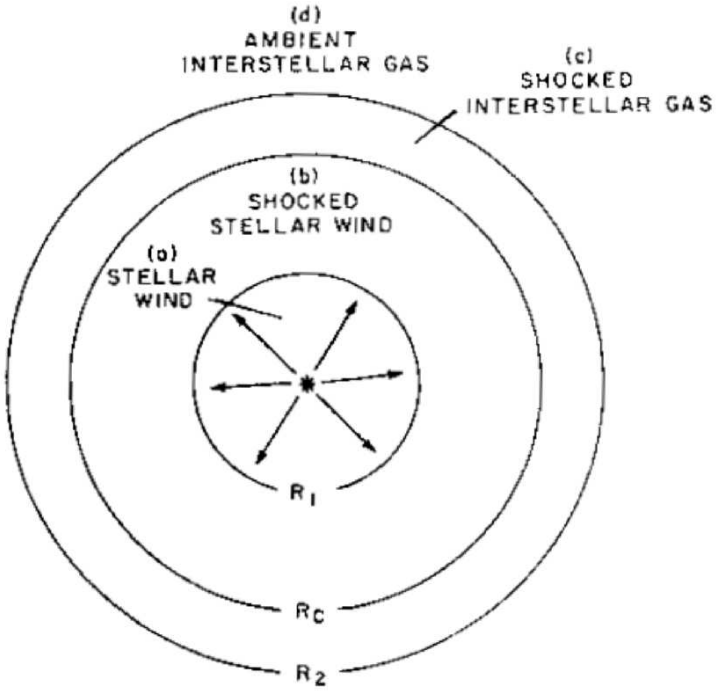

Figure 4.1: Canonical description of the internal structure for the first phase of a stellar-wind driven expanding shell (after *Weaver et al. 1977*). The gas within the shell is arranged in layers. The swept up ISM is collected at the outmost layer.

show that the outermost radius of the shell varies with time as (Equation 21, Weaver et al. 1977):

$$R_2 = \left(\frac{250}{308\pi}\right)^{1/5} L_w^{1/5} \rho_o^{-1/5} T^{3/5}$$

where L_w is the total energy output (luminosity) of the central star required to generate the observed shell, in ergs s^{-1}, ρ is the ISM density and T is the time since $R_2 \approx 0$.

Typically, this relation is expressed as a function of the observable parameters: the shell radius and expansion velocity:

$$L_s = 1.5 \times 10^5 \left(\frac{r}{100pc}\right)^5 \left(\frac{T}{10^6 yr}\right)^{-3} \left(\frac{n_o}{1cm^{-3}}\right) L_\odot erg \tag{4.1}$$

where $L_\odot$ is the solar luminosity (3.8×10^{33} erg $\cdot s^{-1}$). Weaver et al. (1977) also show that the age of the shell can be estimated from the shell radius R_s, the expansion velocity v_{exp} and ambient density ρ :

$$T_s = \frac{3}{5}\left(\frac{R_s}{v_{exp}}\right) Myr \tag{4.2}$$

The parameter T_s is commonly referred to as the *Dynamic* or *Kinematic age*.

- iii. The last stage describes the least dynamic phase of the evolution of the shell. At the beginning of this phase the mass of the swept shell is roughly equal to that which has been shed by the star. The internal region is now cold, having shed the energy through expansion and radiation. The shell, which by this stage may have suffered significant fragmentation, continues drifting under its own momentum and becomes more and more tenuous until it becomes indistinguishable from the ISM.

There are two key assumptions made Weaver et al. (1977) regarding the evolution of a shell expanding in the ambient HI. Firstly, it is assumed that the the energy deposition into the ISM by the association is constant in time. The second assumption is that the distribution of the ambient density is invariant over space, i.e. that there are no significant voids or clumps.

It should be noted that Shull & Saken (1995), have shown that the dynamic age can be wrongly estimated for stellar associations which do not show co-evolution, i.e. for associations populated with stars of a range of ages and at different stages of evolution. Higher mass members of the association which are evolving off the main sequence cause a variation in the rate of energy deposition into the forming shell. Ultimately, this scenario violates one of the assumptions made by Weaver et al. (1977) and the dynamic age of the shell can be over-estimated by a factor of up to 2-3.

4.1.2 Super Novae

The evolution of shells formed as a result of SNes has been studied by numerous groups. McCray & Kafatos (1987) discuss the formation of an expanding shell formed from multiple SNes. The additional energy deposited via SNe into the wind-formed shell is approximately equivalent to that deposited through stellar wind action, although there is a delay in the re-acceleration of the shocked front owing to the travel time of the blast through the shell interior. Each SNe contributes approximately 70% of the initial blast energy into kinetic shell re-expansion, the remainder being emitted as radiative cooling. Cox (1972) and Chevalier (1974) have constructed a model that describes the luminosity of the shell resulting from an instantaneous deposition of energy into the ISM through a supernova event. The relation describing the total energy is given by:

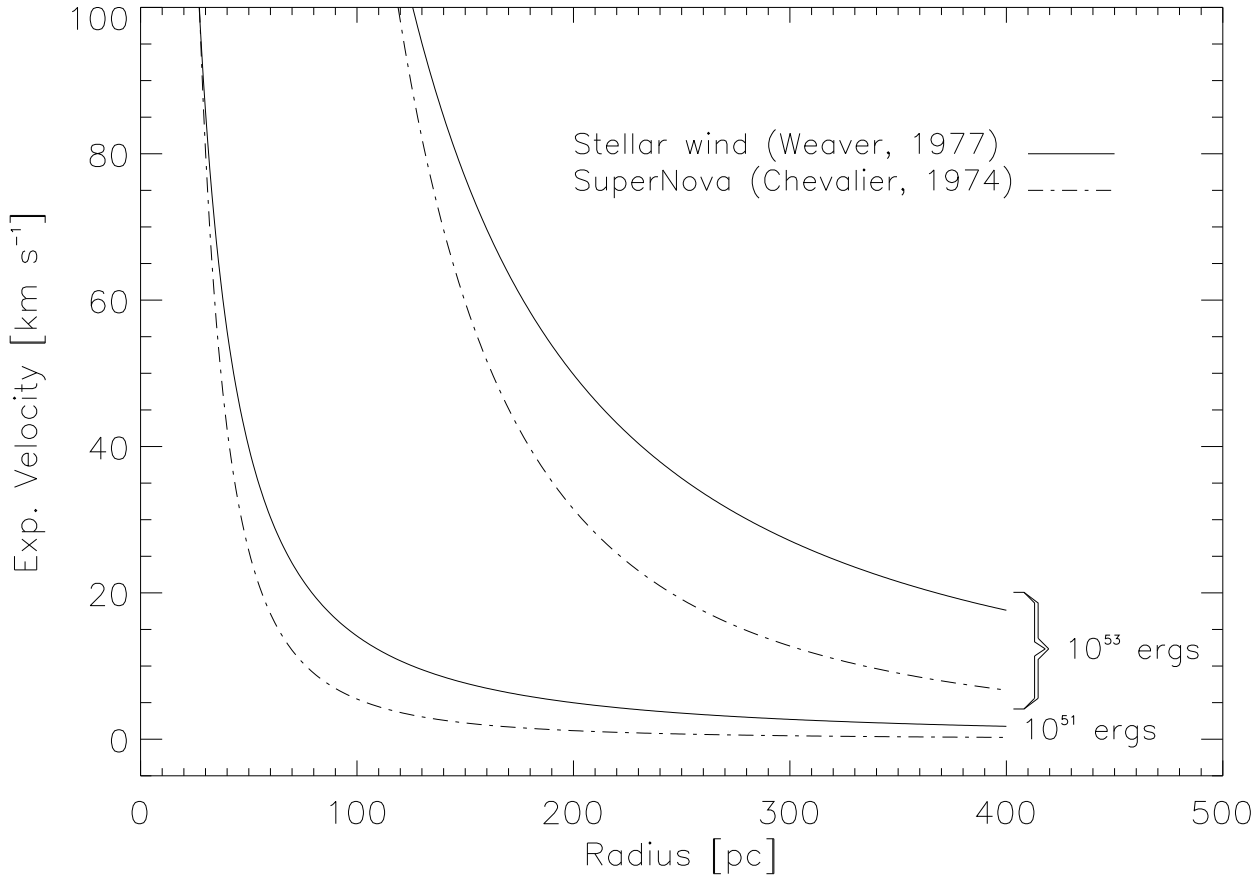

Figure 4.2: A comparison of constant energy curves of the radius and expansion velocity for bubbles formed generated by SNe (Chevalier, 1974) and by Stellar wind (Weaver et al. 1977). For the two energies shown (10^{51} and 10^{53} ergs, the SNe model predicts a smaller radius and slower expansion velocity than does the Stellar wind model.

$L_W = 5.3 \times 10^{43} n_o^{1.12} V_{sh}^{1.40} R^{3.12} erg$ (Chevalier, 1974)

These formulae are also derived under the assumption that the ISM density is homogenous. The fundamental differences between the stellar wind and the SNe model are that the SNe requires a series of instantaneous energy deposition events, whereas the stellar wind model assumes a continuous and a more gradual energy deposition rate. In general, the supernova model will predict a smaller shell radius and expansion velocity for a given shell energy than will the stellar wind model (See Figure. 4.2).

4.1.3 Gamma Ray Bursts

The cause of Gamma Ray Bursts (GRBs) are generally not well understood, although common model scenarios include the collisions of Neutron stars (e.g. Blinnikov et al. 1984) or the collapse of super-massive objects (Paczyński, 1998). It has been estimated that these events can deposit $\sim 10^{52}$ ergs into the ISM (Wijers et al. 1998), $\sim$10 per cent of which is imparted as kinetic energy into the local medium. Measurements of the extra Galactic gamma ray flux by Wijers et al. (1998), have led to an estimate for the probability of a GRB event of once per 40 million years per galaxy. These estimates assume that the GRB events release energy isotropically and without beaming. Modelling has shown that beamed GRB events can produce spherical structures after $\sim$5 Myr (Ayal & Piran 2001).

4.1.4 HVC collisions

The kinetic energy imparted by an cloud infalling into a homogenous medium has been shown to be capable of generating a spherical expanding volume (Tenorio Tagle et al. 1986). Simulations of infalling clouds by Tenorio Tagle et al. (1986) included a range of scenarios: where the density, velocity and radius of the infalling projectile are varied, as well as the density of the target medium and the thermodynamic process (radiative or adiabatic). The size and shape of the generated hole were shown to be dependant on these parameters and the more energetic impact scenarios using small radii and high density projectiles were found to form tunnels in the ISM rather than spheres.

4.1.5 Ram pressure

Bureau & Carignan (2002) have suggested that the stripping action of the intergalactic medium on infalling cluster members could also generate holes and tunnels. Such a process has been postulated as a mechanism for enlarging already existing holes or dimples only. Complete expanding spherical features are not formed by this mechanism. The feasibility of this hypothesis has been studied through simulations only tentatively, although with promising results.

4.2 Magellanic Bridge Expanding Shell survey

The ATCA+Parkes Magellanic Bridge HI dataset (see Chapter 3) has been visually examined for apparently expanding volumes. All projections (RA-declination, velocity-declination and RA-velocity) of the data cube were examined using the KARMA applications KSLICE-3D and KPVSLICE. The criteria for this survey are based on those defined by Brinks & Bajaja (1986) and Puche et al. (1992) in shell surveys of M31 and Holmburg II galaxies. A ring feature was catalogued as an expanding HI shell if the following criteria were satisfied:

i - An expanding shell must be observed as a complete ring, or a rough ring shape, within the velocity range occupied by the shell (Criterion *iv*, Puche et al. 1992).

ii - Expansion must be observable in both position-velocity projections across at least three velocity channels and with a stationary centre throughout the channel range occupied by the shell. This criterion was modified from Criterion *ii*, Puche et al. (1992), where the ring integrity is examined only in the RA-Dec projection

iii - The rim of the ring has good contrast (i.e. relatively high column density) with respect to the ambient column density of the channel maps (Criterion *iii*, Puche et al. 1992).

Note that the criteria here target rim-brightened, expanding HI shells and attempt to exclude HI holes that do not appear to show expansion in both velocity projections. This differs from the HI holes studied in IC10 by Wilcots & Miller (1998) for example, where although all HI holes were examined for a double peaked velocity profile, none were found. The velocities of the receding and approaching sides for each shell, as well as the shell radius (in arcmin), were measured. The Heliocentric velocity of the shell was calculated as the average of the velocities of the approaching and receding sides of the shell, while the expansion velocity is half the absolute difference in these velocities. It should be pointed out here that in an effort to reduce an element of subjectivity, typically inherent in surveys for HI expanding shells, it was required that the three above criteria be strictly satisfied. The effects of such strictness are apparent in a statistical examination of the resulting dataset and these are discussed in Section 4.4.

Figures 3.8a and 3.9 show that the Magellanic Bridge connects smoothly with the SMC, both spatially and in velocity. These figures also show that the orientation of the Bridge is almost exactly parallel to the lines of constant Declination. By assuming a distance of 60 kpc to the centre of the Small Magellanic Cloud at RA=$1.0^{\rm h}$ and a distance of 50 kpc to the centre of the LMC at RA=$5.33^{\rm h}$, we can estimate the distance to individual shells within the Magellanic Bridge with a simple linear interpolation between the two Clouds from an empirical relation: $D(kpc) = 57.7 - (RA - 2^h) \times 2.3$.

To facilitate a useful comparison of expanding shell surveys for the SMC and other HI systems, the stellar-wind scenario by Weaver et al. (1977) (equations 4.1 and 4.2) is assumed. Equation 4.1 is further multiplied by the dynamic age (in seconds) to arrive at an estimate of the total shell energy. We use n=0.06 $\rm cm^{-3}$ as estimated in Chapter 3.

4.2.1 HI shell survey results and analysis

We have detected and catalogued 163 complete candidate shells according to the selection criteria detailed above.

Figure 4.3 shows an integrated intensity map of the Magellanic Bridge overlaid with the positions and sizes of HI shells, as well as the positions of OB associations from a catalogue compiled by Bica & Schmitt (1995). The limiting magnitude of this OB association survey is V=20.0. In an attempt to eliminate bright foreground stars, only associations where (B-V)>0.0 were included. A superficial visual examination of Figure 4.3 shows a general correlation between HI column density, the number density of expanding shells and with the number density of OB associations. This is discussed further in Section 4.3.

The RA, Dec, heliocentric velocity, expansion velocity, radius (in arcmin and in parsecs), kinematic age and energy for each shell are listed in Table 4.1. Figure 4.4 shows the RA-Dec, RA-Vel and Vel-Dec projections for an example shell #51. Although this is not a large shell, the expanding volume is clear in the figure.

Parameters of the Magellanic Bridge shell population are collated and plotted against Right Ascension in Figures 4.5a-4.5d. The shell parameters are shown as log histograms in Figures 4.8a-4.8d. A comparison of Magellanic Bridge and SMC shell histogram parameters is shown in Table 4.2 and plotted against Right ascension in Figures 4.7a-4.7c.

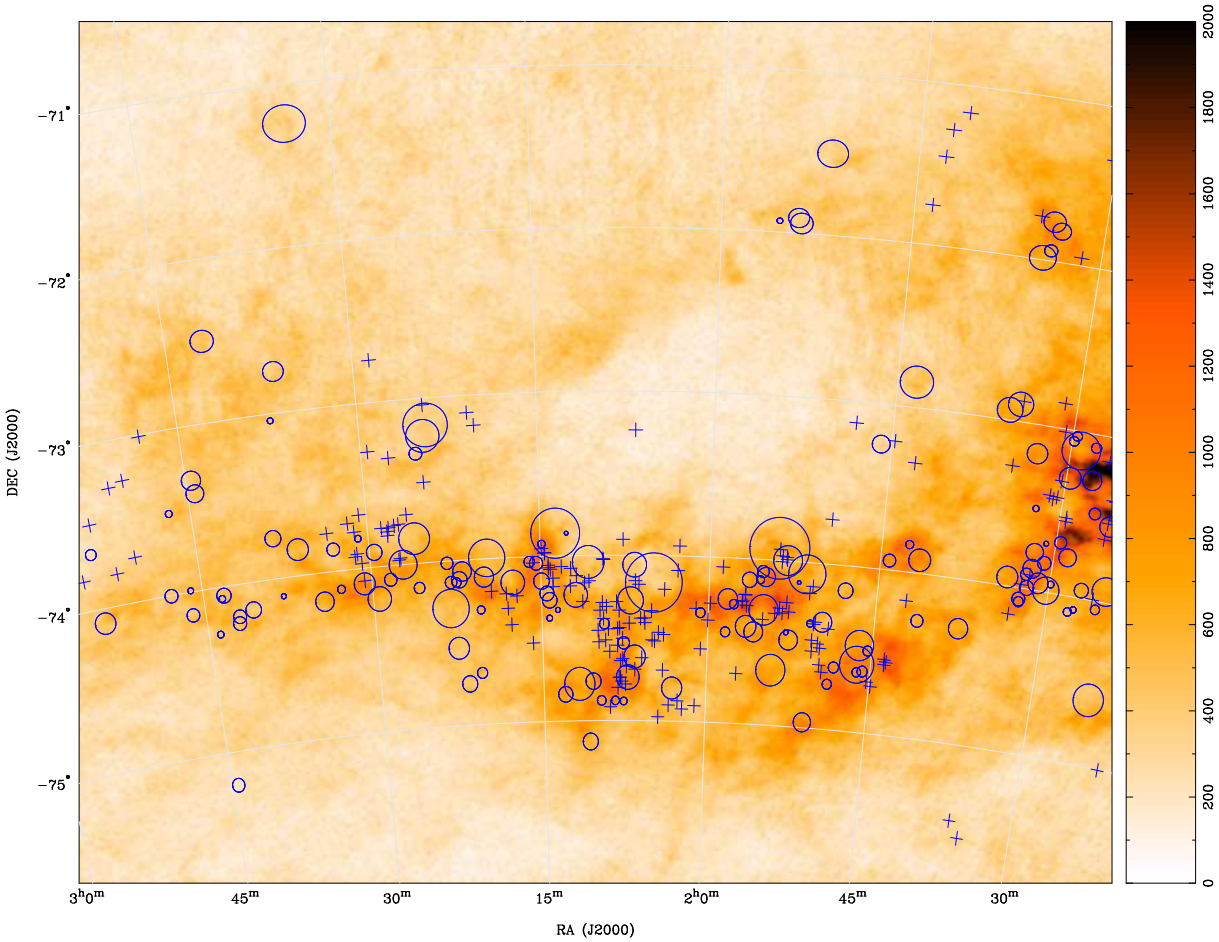

Figure 4.3: HI shells and OB associations within the Western Magellanic Bridge from this survey are overlaid on an integrated intensity HI image. The positions of shells are represented as circles, where the circle radii correspond to shell radii. The shells appear to be mainly confined to regions of higher HI column density. Positions of Young OB associations (crosses) have been taken from a catalogue by Bica & Schmitt (1995). The transfer function is linear with units in K·km s^{-1}.

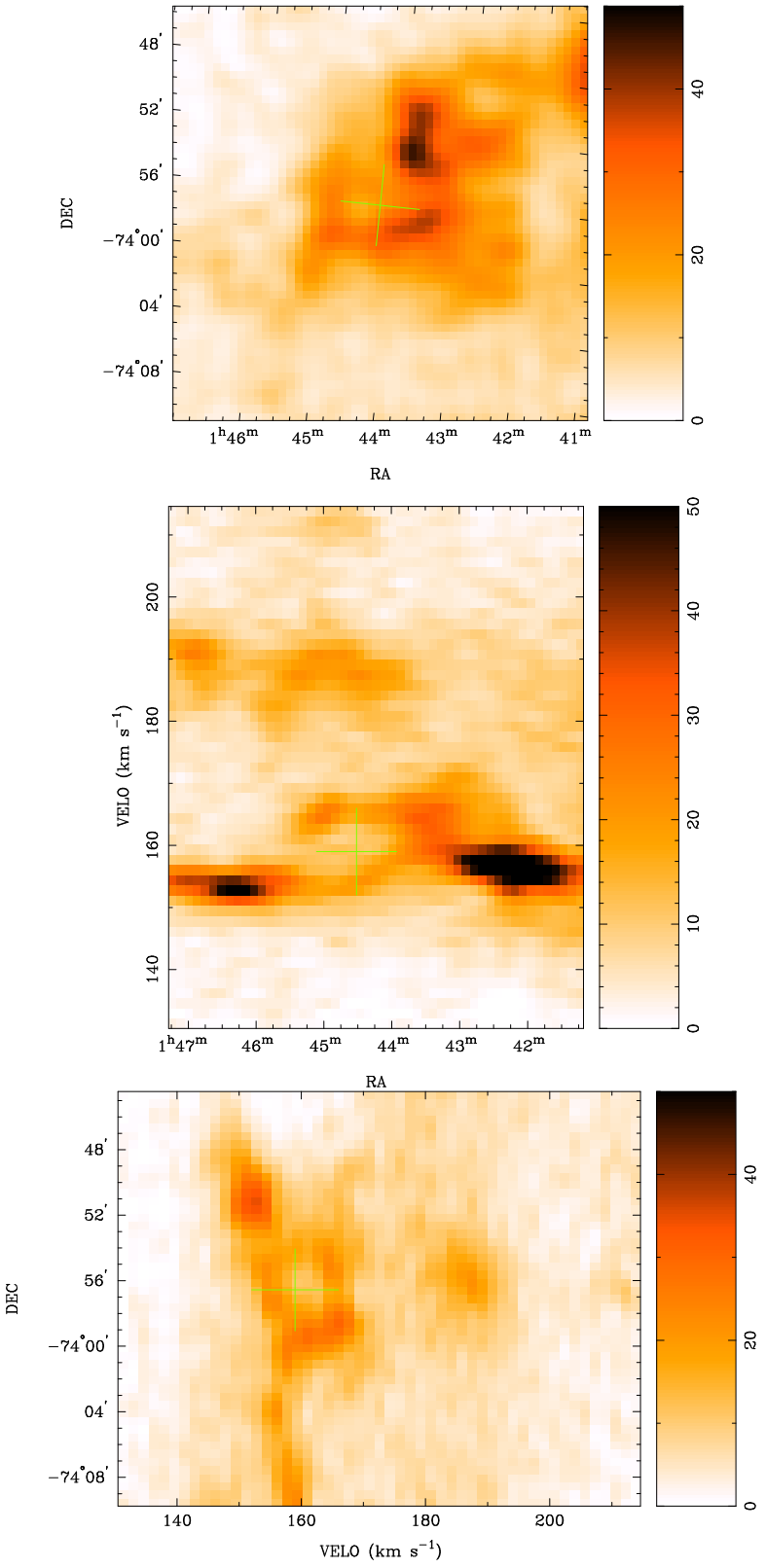

Figure 4.4: Three cuts through the combined datacube centred on shell #51. *a) Top.* RA-Declination projection, *b) Middle.* RA-Velocity projection, *c) Bottom.* Velocity-Declination projection. The cross overlay shows the position size and velocity of the shell as listed in the catalogue of table 4.1. The colourscale is shown in the Wedge, units are in K.

Table 4.1: Table of Magellanic Bridge Shell Parameters

Shell Number	Right Ascension (J2000)	Declination (J2000)	Heliocentric Vel. (km s^{-1})	Exp. Vel. (km s^{-1})	Radius (′)	Radius (pc)	Dynamic Age (Myr)	Energy (log erg)
1	01:21:36.1	-73:29:03.0	150.3	4.1	3.0	54.3	7.9	47.9
2	01:22:39.7	-73:05:30.2	172.6	12.1	5.0	90.7	4.5	49.5
3	01:22:59.0	-73:25:30.9	168.2	11.0	3.5	63.1	3.4	49.0
4	01:23:01.1	-74:06:23.3	158.5	7.6	3.0	54.7	4.3	48.5
5	01:23:06.2	-73:30:24.0	189.5	2.1	2.9	53.3	15.0	47.3
6	01:24:24.5	-73:23:24.9	151.8	8.0	3.2	58.3	4.4	48.6
7	01:24:48.5	-74:35:50.9	192.9	3.8	5.9	107.4	17.1	48.7
8	01:24:58.6	-73:11:38.8	147.2	6.0	1.7	30.8	3.1	47.5
9	01:24:59.9	-73:55:55.4	164.0	10.8	5.2	94.3	5.3	49.5
10	01:25:30.5	-72:58:50.8	147.8	8.2	3.2	57.3	4.2	48.6
11	01:25:40.1	-73:32:23.6	173.4	12.4	3.7	66.8	3.2	49.1
12	01:25:40.1	-74:03:03.9	167.3	4.9	1.8	31.8	3.9	47.4
13	01:27:06.6	-73:28:41.7	147.0	5.8	2.1	38.5	4.0	47.8
14	01:27:08.7	-73:57:06.7	147.0	5.8	2.7	48.3	5.0	48.1
15	01:27:34.3	-74:04:34.1	147.8	5.0	1.2	21.1	2.6	46.8
16	01:27:49.0	-73:17:03.5	175.9	5.0	3.5	62.6	7.6	48.3
17	01:27:54.6	-73:04:56.4	185.1	3.7	1.8	33.4	5.5	47.2
18	01:28:03.0	-74:05:41.3	139.6	3.3	1.6	28.2	5.1	46.9
19	01:28:08.0	-71:19:46.1	204.7	2.5	0.6	11.2	2.7	45.4
20	01:28:48.4	-73:46:15.5	153.5	5.9	3.2	58.9	6.0	48.3
21	01:29:08.3	-73:0 6:55.5	161.8	15.7	6.9	125.3	4.8	50.2
22	01:29:36.7	-73:41:17.0	165.1	6.8	2.2	40.8	3.6	48.0
23	01:29:38.2	-73:01:54.7	184.9	5.8	1.7	31.6	3.3	47.5
24	01:29:41.0	-73:17:30.0	175.0	2.5	3.9	71.6	17.4	47.8
25	01:29:50.5	-73:03:54.9	186.7	5.0	1.7	31.7	3.8	47.4
26	01:29:53.3	-73:56:56.2	169.3	6.6	1.2	22.4	2.0	47.2
27	01:30:14.3	-73:59:26.6	159.5	18.3	5.0	90.1	3.0	49.9
28	01:30:44.4	-73:49:42.0	160.2	2.5	2.5	45.2	11.0	47.2
29	01:30:50.3	-73:42:32.8	171.5	7.6	0.9	16.7	1.3	46.9
30	01:31:00.8	-73:57:16.1	150.3	5.8	3.8	68.2	7.1	48.5
31	01:31:42.3	-73:46:20.6	157.2	7.7	3.2	58.7	4.6	48.6
32	01:31:43.3	-73:52:25.4	173.4	5.8	3.4	62.5	6.5	48.4
33	01:31:56.5	-73:59:39.0	177.3	4.7	2.7	49.3	6.3	47.9
34	01:32:07.4	-73:54:43.4	175.4	7.8	2.2	40.5	3.1	48.1
35	01:32:09.9	-73:30:28.4	186.1	4.0	1.2	20.9	3.1	46.6
36	01:32:28.8	-74:05:03.7	156.9	5.8	1.9	33.8	3.5	47.6
37	01:32:31.0	-74:04:04.6	173.0	8.7	2.5	44.6	3.1	48.3
38	01:32:44.0	-73:10:36.6	178.4	10.7	3.7	67.0	3.8	49.0
39	01:33:22.8	-71:48:40.0	219.2	5.0	3.1	56.3	6.8	48.1
40	01:33:45.4	-73:56:49.3	151.7	5.0	3.9	71.5	8.6	48.5
41	01:34:00.8	-71:56:16.8	221.2	4.1	2.2	40.3	5.9	47.5

Table 4.1: Table of Magellanic Bridge Shell Parameters

Shell Number	Right Ascension (J2000)	Declination (J2000)	Heliocentric Vel. (km s^{-1})	Exp. Vel. (km s^{-1})	Radius ($'$)	Radius (pc)	Dynamic Age (Myr)	Energy (log erg)
42	01:34:01.6	-71:45:36.7	217.4	9.4	3.7	67.8	4.3	48.9
43	01:34:35.3	-71:59:16.7	206.5	16.9	4.5	82.1	2.9	49.7
44	01:34:40.5	-72:53:42.3	208.8	4.9	4.5	81.0	9.8	48.6
45	01:35:30.8	-72:56:17.7	194.0	8.2	4.5	82.4	6.0	49.1
46	01:37:28.5	-74:18:04.7	151.9	10.7	3.7	67.2	3.8	49.0
47	01:41:13.7	-74:17:12.3	149.5	6.6	2.3	42.1	3.8	48.0
48	01:41:34.9	-73:55:11.1	166.0	9.9	4.1	74.4	4.5	49.1
49	01:42:35.9	-73:49:56.2	162.7	3.3	1.5	27.1	4.9	46.8
50	01:43:26.2	-72:50:40.3	141.2	14.8	5.9	106.5	4.3	49.9
51	01:44:13.0	-73:56:33.6	159.4	6.6	2.4	42.6	3.9	48.0
52	01:45:22.9	-74:30:06.7	146.3	6.7	1.8	32.8	2.9	47.7
53	01:45:42.2	-74:37:44.4	148.6	4.1	2.0	36.0	5.2	47.4
54	01:45:53.5	-73:14:36.7	177.5	4.9	3.2	58.7	7.1	48.2
55	01:46:10.2	-74:28:26.5	181.6	5.8	5.5	99.7	10.4	49.0
56	01:46:13.9	-74:38:14.5	148.6	4.1	1.7	30.9	4.5	47.2
57	01:46:15.5	-74:35:28.3	172.6	21.4	6.7	121.6	3.4	50.4
58	01:47:50.3	-74:09:04.4	153.0	4.8	2.8	51.1	6.4	48.0
59	01:48:21.7	-74:37:16.0	193.2	2.5	2.0	36.2	8.8	47.0
60	01:48:50.7	-74:43:32.9	156.9	2.5	1.8	33.0	8.0	46.8
61	01:49:41.1	-74:21:14.6	157.7	11.5	3.6	65.7	3.4	49.1
62	01:50:47.3	-74:22:06.0	140.4	2.5	1.3	23.4	5.7	46.4
63	01:50:53.0	-74:58:02.2	194.0	5.0	3.5	62.8	7.6	48.3
64	01:51:20.8	-74:04:17.7	160.2	10.7	7.1	128.1	7.2	49.9
65	01:51:37.8	-71:29:54.2	218.7	3.3	5.0	91.4	16.6	48.4
66	01:52:01.3	-74:07:30.4	193.2	2.5	0.7	12.5	3.0	45.6
67	01:52:39.9	-74:28:39.3	166.7	9.2	3.6	65.4	4.3	48.9
68	01:52:55.7	-74:25:55.6	155.2	2.5	0.9	16.7	4.0	45.9
69	01:53:07.1	-73:59:49.6	177.5	16.5	5.4	98.4	3.6	49.9
70	01:53:42.2	-71:56:22.3	221.2	7.4	3.8	68.9	5.6	48.7
71	01:53:54.5	-73:55:32.6	174.5	16.4	11.2	203.9	7.5	50.8
72	01:53:56.6	-71:54:25.2	227.8	4.1	3.5	63.9	9.3	48.1
73	01:54:07.5	-74:39:59.6	173.2	14.7	5.7	104.0	4.2	49.9
74	01:54:58.2	-74:06:18.6	176.7	7.4	3.5	63.2	5.1	48.6
75	01:55:03.3	-74:18:18.2	151.1	3.3	5.6	100.7	18.3	48.5
76	01:55:14.3	-74:04:22.8	197.3	3.3	2.2	40.1	7.3	47.3
77	01:55:26.0	-71:55:51.5	231.1	2.5	1.0	18.1	4.4	46.0
78	01:55:26.6	-74:07:25.4	181.6	2.5	1.4	26.2	6.4	46.5
79	01:55:52.4	-74:26:29.3	165.1	14.0	3.6	66.1	2.8	49.2
80	01:56:25.1	-74:07:38.5	154.4	8.2	2.8	50.5	3.7	48.4
81	01:56:35.2	-74:24:37.4	157.8	6.1	4.0	72.2	7.1	48.6
82	01:57:44.1	-74:16:46.9	153.1	4.6	1.7	30.9	4.0	47.3

Table 4.1: Table of Magellanic Bridge Shell Parameters

Shell Number	Right Ascension (J2000)	Declination (J2000)	Heliocentric Vel. (km s^{-1})	Exp. Vel. (km s^{-1})	Radius ($'$)	Radius (pc)	Dynamic Age (Myr)	Energy (log erg)
83	01:58:17.8	-74:15:00.1	173.4	15.7	3.7	67.7	2.6	49.4
84	01:58:25.4	-74:26:58.8	150.3	7.4	1.8	32.9	2.7	47.8
85	02:00:42.8	-74:20:22.1	161.8	4.2	1.8	32.8	4.7	47.3
86	02:03:10.0	-74:47:60.0	154.3	9.7	4.0	72.4	4.5	49.0
87	02:04:56.9	-74:09:49.5	169.3	16.5	10.8	195.8	7.1	50.8
88	02:06:37.1	-74:36:46.6	175.0	12.4	4.2	76.0	3.7	49.3
89	02:06:40.2	-74:03:24.4	159.2	5.7	4.5	81.6	8.7	48.7
90	02:07:01.1	-74:16:22.8	166.8	7.4	4.9	89.4	7.2	49.1
91	02:07:14.4	-74:44:13.9	190.6	5.4	4.5	81.1	9.1	48.7
92	02:07:36.9	-74:52:55.5	178.3	2.5	1.4	25.2	6.1	46.5
93	02:07:37.6	-74:31:49.5	192.3	3.3	2.2	40.8	7.4	47.4
94	02:08:22.9	-74:52:42.2	191.5	4.1	1.6	28.3	4.1	47.1
95	02:09:22.0	-74:24:50.4	159.4	3.3	1.9	34.9	6.3	47.2
96	02:09:39.6	-74:52:41.1	195.6	8.2	1.7	31.5	2.3	47.8
97	02:10:24.6	-74:45:41.8	168.4	4.1	3.0	54.1	7.9	47.9
98	02:10:43.4	-75:07:32.4	179.3	5.8	3.1	55.5	5.8	48.2
99	02:10:47.1	-74:02:21.4	169.3	6.6	6.0	108.7	9.9	49.2
100	02:11:55.9	-74:14:15.8	161.0	5.0	4.5	81.6	9.9	48.6
101	02:11:40.8	-74:46:36.4	178.2	9.5	6.0	108.7	6.8	49.6
102	02:12:41.1	-73:51:45.8	166.8	2.5	0.7	12.9	3.1	45.6
103	02:12:59.9	-74:50:18.2	202.2	9.9	2.8	51.6	3.1	48.6
104	02:13:33.4	-74:19:36.4	180.0	5.8	0.9	16.9	1.8	46.7
105	02:13:38.6	-73:51:40.4	174.2	9.9	9.1	165.6	10.1	50.1
106	02:14:16.4	-74:16:01.9	171.8	3.7	2.8	51.2	8.2	47.8
107	02:14:19.0	-74:22:30.8	162.5	3.6	1.1	20.2	3.4	46.5
108	02:14:30.1	-74:13:30.9	179.2	6.5	2.7	49.0	4.5	48.2
109	02:14:52.2	-73:55:31.4	157.7	4.9	1.4	25.7	3.1	47.1
110	02:14:57.8	-74:08:59.0	174.8	10.5	3.0	54.2	3.1	48.7
111	02:15:24.1	-74:02:26.0	176.0	7.9	2.5	45.3	3.4	48.3
112	02:16:00.2	-74:01:50.9	174.2	7.1	2.0	36.1	3.1	47.9
113	02:17:31.6	-74:09:05.1	179.9	11.6	4.5	81.5	4.2	49.4
114	02:19:44.4	-73:59:40.6	180.0	7.4	6.8	123.8	10.0	49.5
115	02:20:04.0	-74:06:35.8	191.8	6.0	3.7	66.2	6.6	48.5
116	02:20:27.5	-74:18:28.7	153.0	4.0	1.5	27.3	4.1	47.0
117	02:20:37.8	-74:41:20.6	163.6	7.4	2.0	36.3	3.0	47.9
118	02:21:49.5	-74:45:03.8	168.4	2.5	3.0	54.0	13.1	47.5
119	02:21:58.9	-74:04:08.2	179.0	6.8	3.5	64.1	5.7	48.6
120	02:22:16.1	-74:07:03.6	187.9	2.8	3.0	54.1	11.6	47.6
121	02:22:31.3	-74:07:58.7	161.8	4.1	1.8	31.8	4.6	47.2
122	02:22:38.2	-74:31:54.4	174.2	4.9	4.0	72.2	8.7	48.5
123	02:23:00.7	-74:07:51.3	171.7	4.1	2.2	40.0	5.8	47.5

Table 4.1: Table of Magellanic Bridge Shell Parameters

Shell Number	Right Ascension (J2000)	Declination (J2000)	Heliocentric Vel. (km s^{-1})	Exp. Vel. (km s^{-1})	Radius (′)	Radius (pc)	Dynamic Age (Myr)	Energy (log erg)
124	02:23:09.2	-74:17:17.3	186.5	10.8	7.0	126.4	7.0	49.9
125	02:23:15.9	-74:00:46.8	186.5	4.2	2.2	40.7	5.8	47.6
126	02:24:22.0	-73:09:51.4	210.4	12.8	8.0	144.6	6.8	50.2
127	02:24:39.6	-73:13:46.7	210.9	15.6	6.0	108.7	4.2	50.0
128	02:25:21.0	-73:20:04.4	195.6	4.9	2.3	42.2	5.1	47.8
129	02:25:50.4	-74:08:59.0	176.2	3.6	2.0	37.1	6.2	47.3
130	02:25:59.9	-73:50:55.5	184.1	6.6	5.8	104.4	9.5	49.2
131	02:27:08.1	-74:00:02.3	189.1	5.6	5.3	95.4	10.2	48.9
132	02:28:20.2	-74:05:06.7	177.5	3.3	2.4	42.7	7.8	47.4
133	02:29:27.4	-74:11:41.0	172.6	3.3	4.5	81.0	14.7	48.2
134	02:29:35.0	-73:54:36.6	175.9	3.3	2.9	53.2	9.7	47.7
135	02:30:39.9	-74:05:40.3	192.9	8.2	4.0	72.5	5.3	48.9
136	02:30:53.6	-73:49:02.4	180.0	2.5	1.2	22.1	5.4	46.3
137	02:32:46.2	-74:06:44.8	193.2	3.3	1.5	27.0	4.9	46.8
138	02:33:08.1	-73:52:02.2	178.3	2.5	2.4	43.3	10.5	47.2
139	02:33:28.3	-71:14:38.1	218.7	4.9	6.9	125.4	15.3	49.2
140	02:34:20.9	-74:10:31.3	175.0	2.5	3.5	63.9	15.5	47.7
141	02:36:12.9	-73:50:28.3	184.1	3.3	4.0	71.8	13.1	48.1
142	02:36:31.7	-72:44:43.6	217.1	8.2	3.6	66.0	4.8	48.8
143	02:37:14.5	-73:02:31.0	195.6	3.3	1.1	19.7	3.6	46.4
144	02:37:55.5	-74:06:38.4	175.0	2.5	1.0	17.4	4.2	46.0
145	02:38:14.9	-73:45:19.3	184.0	6.4	3.0	53.8	5.1	48.3
146	02:40:44.6	-74:10:01.6	182.4	3.3	3.0	53.7	9.8	47.7
147	02:41:57.7	-72:30:05.2	204.7	5.8	4.0	73.3	7.6	48.6
148	02:42:01.7	-74:11:43.9	185.7	6.6	2.5	45.0	4.1	48.1
149	02:42:06.9	-74:14:11.7	187.3	5.6	2.5	45.4	4.9	48.0
150	02:43:10.9	-74:03:15.0	194.0	6.6	2.7	49.5	4.5	48.2
151	02:43:22.1	-74:04:18.7	180.4	2.2	1.2	22.6	6.1	46.2
152	02:43:58.2	-74:17:02.4	185.7	3.3	1.2	22.5	4.1	46.6
153	02:44:21.8	-73:24:49.1	191.5	4.1	3.3	59.0	8.6	48.0
154	02:44:25.6	-75:12:03.8	201.9	3.9	2.5	45.3	6.9	47.6
155	02:44:31.8	-73:19:53.9	193.2	4.1	3.5	63.4	9.2	48.1
156	02:46:01.2	-73:59:27.8	191.5	4.1	1.1	20.0	2.9	46.6
157	02:46:07.5	-74:08:29.2	187.4	4.9	2.4	44.0	5.3	47.8
158	02:46:50.2	-73:30:29.9	193.2	4.1	1.3	23.3	3.4	46.8
159	02:47:46.1	-74:00:12.2	198.1	5.8	2.5	44.6	4.6	48.0
160	02:48:22.5	-75:49:42.1	201.4	4.1	2.4	44.1	6.4	47.7
161	02:50:26.4	-75:52:17.8	200.6	3.3	4.2	75.9	13.8	48.2
162	02:53:55.7	-74:05:22.7	184.1	3.3	3.9	70.9	12.9	48.1
163	02:54:03.4	-73:39:47.1	210.2	2.7	2.0	36.3	8.2	47.0

	Magellanic Bridge	Small Magellanic Cloud
Mean Shell Radius,(R_s)	58.6pc	91.9 pc
σ(R_s)	33.2 pc	65.5 pc
Mean Expansion Velocity, (V_s)	6.5 km s^{-1}	10.3 km s^{-1}
σ(V_s)	3.8 km s^{-1}	6.3 km s^{-1}
Mean Dynamic Age, (T_s)	6.2 Myr	5.7 Myr
σ(T_s)	3.4 Myr	2.8 Myr
Mean Energy, (L_s)	48.1 log(erg)	51.8 log(erg)

Table 4.2: Comparison of properties of Magellanic Bridge Shells (this study) and Small Magellanic Cloud Shells (Staveley-Smith et al. 1997). The mean and standard deviation of each property are given.

4.2.1.1 Statistical comparison

Table 4.2 shows that the mean shell radius and expansion velocity of the Magellanic Bridge shell population are smaller than for the SMC population, while the mean kinematic age is slightly larger. The dispersions of shell radius and expansion velocity of the Bridge population are also slightly lower than the SMC population, while the dispersion for kinematic age, which is dependent on both the shell radius and expansion velocity, is slightly larger for the Bridge population. We also see that the mean energy of the shell population is considerably lower in the Magellanic Bridge than for the SMC. To a large extent, the disagreement between the mean energy and mean radii here is probably an effect of a different shell selection criteria used for this survey (see also Figure 4.7). This is discussed in more detail in Section 4.4.

4.2.1.2 Right Ascension plots

Figures 4.5a -4.5d show the Dynamic age, expansion velocity, shell radius and heliocentric velocity for each of the shells plotted against Right Ascension. A number of observations can be made immediately from these Right Ascension plots:

- There does not appear to be *gradual* systematic variation of shell age with RA, as shown in Figure 4.5a. Although there is a subtle tendency of older shells to be found at higher RA. This is discussed further in Section 4.4.
- Figure 4.5b shows that the mean expansion velocity appears to decrease towards the LMC (see also Figure 4.6). This figure shows also that the dispersion of expansion

velocity is reduced after $2^h\,20^m$, where the values become less scattered.

- There is no general trend of shell radius with RA, as seen in Figure 4.5c.
- The RA-Vel plot (Figure 4.5d) highlights the smoothly increasing Heliocentric velocity of the HI shells of the Magellanic Bridge towards the LMC and shows a few shells arranged in apparent loops and filaments. The HI shells appear to be more densely clustered on the lower velocity side of the Bridge and we see that the low velocity edge is well defined in shell centres. The higher velocity region appears to harbour relatively fewer shells and is is more difficult to locate the trailing edge of the HI volume.

Figure 4.6 shows the variation of the mean dynamic age, mean expansion velocity and mean shell radius against RA along the sampled region in the Magellanic Bridge. These plots include parameters of shells found during this survey only and are averaged in five intervals across the observed region. This plot highlights some of the trends mentioned above. More specifically however, we see that there are suggestions of important changes in the shell parameters at later RAs: the mean shell radius begins to decreases more quickly at RA $>\sim 2^h\,24^m$ and the mean dynamic age peaks at the same co-ordinate. Clearly, the average properties of the shell parameters undergo some transition at $2^h\,02^m <$RA$< 2^h\,24^m$. This is discussed in more detail in Section 4.4.5.

Figure 4.7a-4.7c compares the dynamic age , the radii and the expansion velocities of the Magellanic Shells with those of SMC shells (Staveley-Smith et al. 1997). We see from these Figures that there is no obvious discontinuity in the mean of the shell kinematic age between the SMC and the Magellanic Bridge. This suggests that there is a continued flow of matter between the two systems. However, the Figures showing the shell radii and expansion velocities (Figures 4.7a,c) along the Bridge and SMC reveal a sharp discontinuity corresponding to the position of overlap between the two surveys. These figures highlight differences between the SMC and Bridge shell selection criteria. This is discussed further in Section 4.4.

4.2.1.3 Histogram Analysis

Histograms of various properties of the Magellanic Bridge shells are shown in Figure 4.8. Shell parameters follow a power law distribution (e.g. Oey & Clarke, 1997) and the

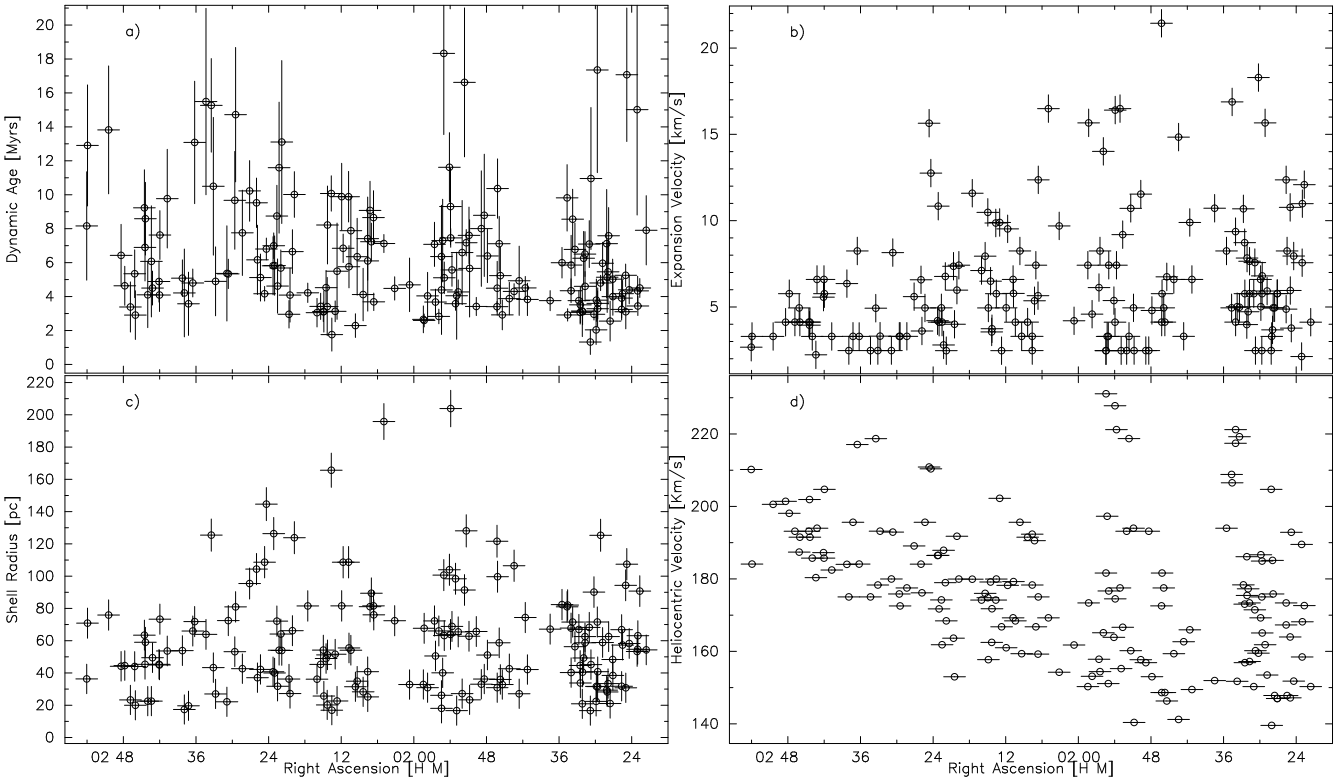

Figure 4.5: Parameters of Magellanic Bridge shells, plotted against RA. *a) Dynamic Age*, *b) Expansion Velocity*, *c) Shell radius*, *d) Heliocentric Velocity.*

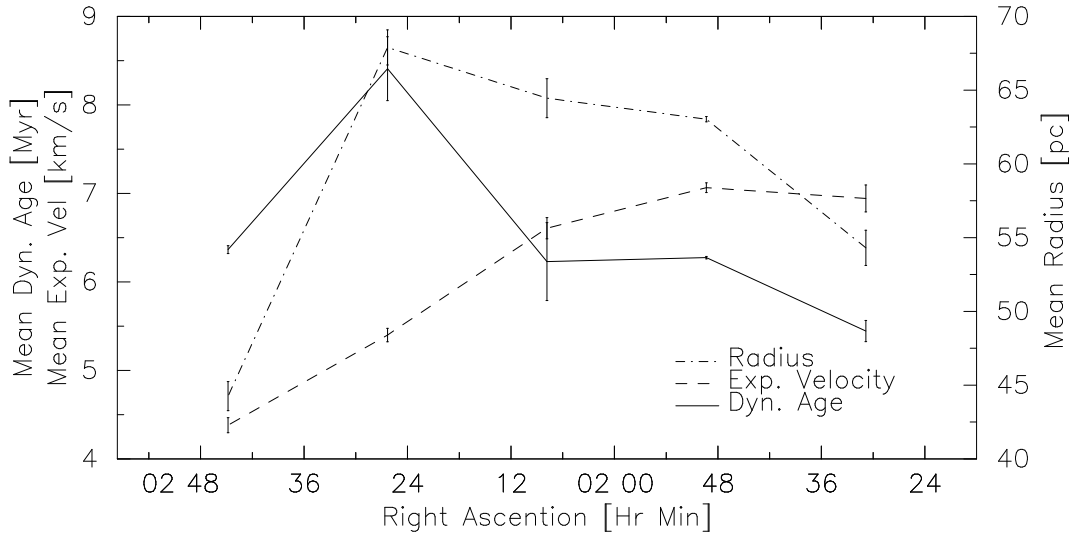

Figure 4.6: Mean Shell dynamic Age *(solid line, axis on the left side)*, Expansion velocity *(dash line, left axis)* and Shell radius *(dot-dash line, right axis).* Error bars mark the standard error of the mean.

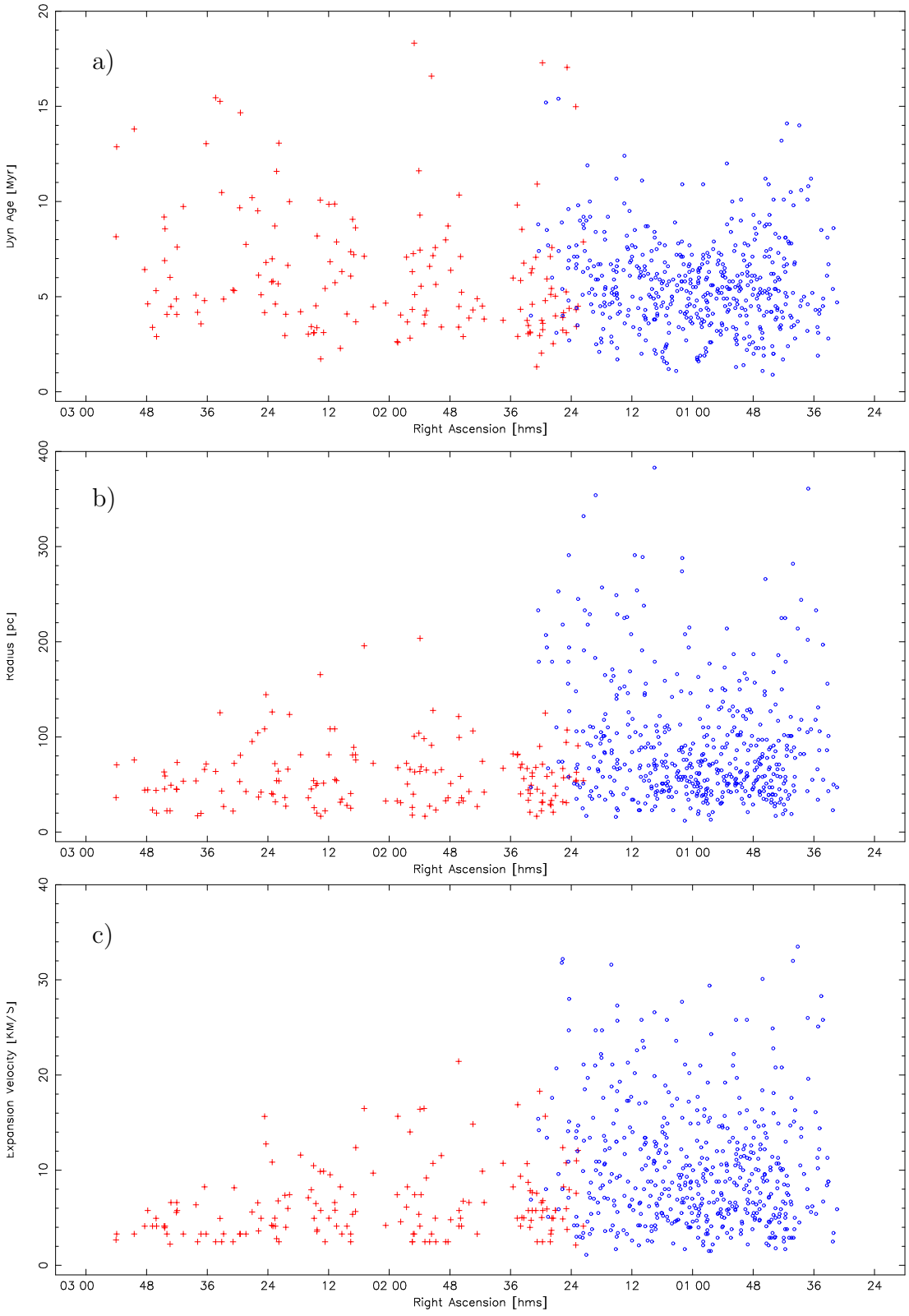

Figure 4.7: Shell properties of the SMC and Magellanic Bridge as a function of Right Ascension. Top to bottom: a) *Dynamic age*, b) *Shell radius* c) *Expansion Velocity*. The red crosses represent shells in the Magellanic Bridge (this survey), while the blue circles represent data from the SMC shell survey (Staveley-Smith et al. 1997).

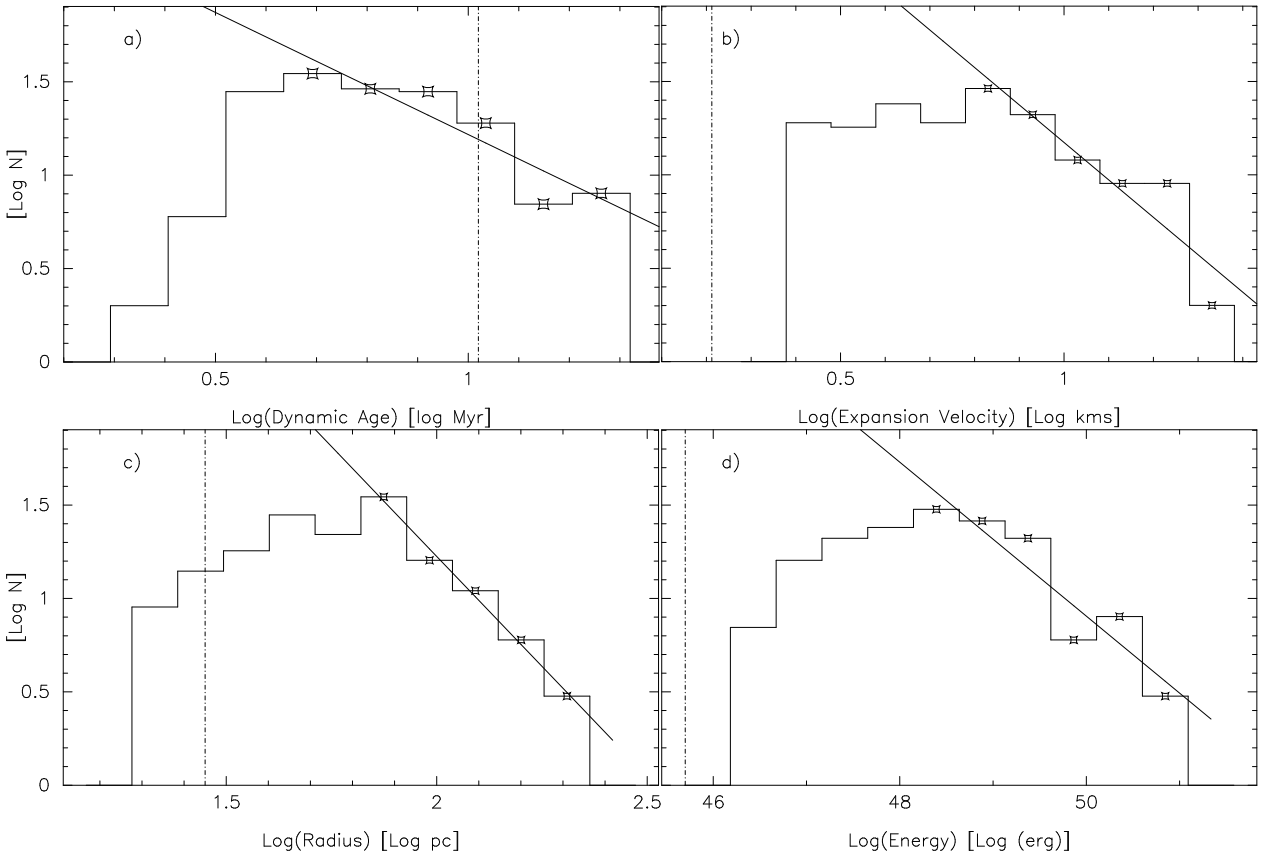

Figure 4.8: Number frequency of Magellanic Bridge Shell parameters: *a)Dynamic age, b) Expansion Velocity, c) Radius* and *d) Energy.* The vertical *dot-dash* line marks the limits imposed by angular resolution (98″) and velocity resolution (1.61 km s^{-1}). As the distributions of Shell parameters follow a power law, we are able to determine a characteristic slope in log (N) - log (parameter) space.

frequency histograms in log space can be fit with a linear model. Power law slopes are fitted histograms of each of the parameters: dynamic age, expansion velocity and radius and are compared with those from the SMC and HoII in Table 4.3.

These measured values for each of the slopes vary slightly, depending on the bin size used for each histogram. The tabulated figures represent the average α (where α is the slope in linear space and is related to the slope in log space γ with $\alpha = 1 - \gamma$), while the errors represent the range of α while varying the number of bins from 10 to 20.

It can be seen that the power-law fit of the expansion velocity for shells populating the Magellanic Bridge appears to be reasonably consistent with that of the Holmberg II and SMC shell population population. Although the slope of the fit to shell radius distribution is considerably steeper, this is most probably due to a deficiency of larger diameter shells

	Holmberg II	SMC	Bridge
Number of shells	51	509	163
Expansion Velocity, α_v	2.9±0.6	2.8±0.4	2.6 ±0.6
Shell Radius, α_r	2.0±0.2	2.2±0.3	3.6±0.4

Table 4.3: Power law of shell radius and expansion velocity (α_r and α_v) for Holmberg II (Puche, 1992), the SMC (Stanimirović, 1999) and the Magellanic Bridge. The Slope in linear space (α) is related to the slope in log space (γ) by $\alpha = 1 - \gamma$

(and is discussed in Section 4.4). We are therefore finding a similar distribution pattern of shell ages throughout these systems. When comparing these three systems, we should bear in mind that the kinematic conditions of the HoII galaxy are not necessarily reproduced in the SMC and the Magellanic Bridge. Specifically, HoII is a disk galaxy and is not obviously tidally perturbed.

4.3 Distribution of Blue Associations

4.3.1 Spatial correlation with HI expanding shells

It was mentioned previously that the OB associations population of the Bridge appeared to superficially correlate with that of the HI expanding shell population. A more careful study of these two populations reveals that the detailed alignment of the associations with shell centres is in fact rather poor: young blue clusters can be seen grouped about higher HI density regions rather than interior to HI circular voids as we might expect for stellar wind or SNe generated shells. In particular, grouping is found about the rims of some larger shells and filaments. Quantitatively, we find that ∼40 per cent of Magellanic Bridge shells have one or more associations within a distance from its centre equal to or less than its radius.

We would not expect to find any OB associations responsible for forming a wind-blown shell outside the shell radius. Any motion of the OB association relative to the shell would result in the shell having a significantly deformed and non-spherical shape (Weaver et al. 1977) and would therefore have been excluded from the survey. The poor spatial correlation statistic of OB associations and HI expanding shells is contrary to the popular theory of the formation by stellar wind and SNe (Weaver et al. 1977; Chevalier, 1974).

We should bear in mind that the mean Magellanic Bridge shell age is approximately equivalent to that of an O type star and any related stellar association may be too faint to have been included in the OB catalogue. A study of the spatial correlation of the SNe and HI shell population of the HoII galaxy has been conducted by Rhode et al. (1999). This study was designed to test the hypothesis of stellar wind and SN explosions acting as the engine for the expansion of a HI shells. The conclusions from this analysis were that under the assumption of a normal initial mass function, the OB cluster brightness was such that the HI shell distribution was strongly inconsistent with the theory of formation by SNe. We have observed a similarly poor correlation here.

4.3.2 Properties of nearby HI

To quantitatively test the spatial correlation of OB associations and HI column density in the Magellanic Bridge, the mean column density of a 90″ (3 pixel) box centred on each of the catalogued OB association positions is presented as a histogram in Figure 4.9 (black columns). Overlaid on this is a second histogram, representing the entire map itself (white columns). The histogram shows that ∼50 per cent of the catalogued OB association positions correlate with a mean column density of $\gtrsim 1.2\times10^{21}$ cm^{-2}, only 8 per cent correspond to column densities equal to or less than half that density and ∼10 per cent are associated with regions of column density greater than 2.4×10^{21} cm^{-2}. These are similar results to those of Grondin & Demers (1993), who found that stellar positions correlate with column densities $\sim10^{21}$ cm^{-2} and that very few associations correlate with low HI column densities. The data representing the black bars in Figure 4.9 represents less than 2 per cent of the entire map area.

Figure 4.10 shows the mean column density variation as a function of distance from the centres of each catalogued OB association. The decrease of the HI with radius is generally linear, with a slope of $\sim$-0.5×10^{18} cm^{-2}pc^{-1}, however, there is an apparent excess of HI at short radii ($\lesssim$80 pc). This contrary results of Grondin & Demers (1993) where a local deficiency of HI was found nearby to Magellanic Bridge OB associations.

Data used by Grondin & Demers (1993) was that obtained from the Parkes telescope by Mathewson & Ford (1984) and has a resolution of ∼14′(∼244 pc) whereas the minimum resolution of the dataset used here is ∼98″ (∼28.5 pc). Figure 4.10 also shows the mean integrated HI as a function of radius, offset $5^{\rm m}$ (∼90 pc) south for each OB association.

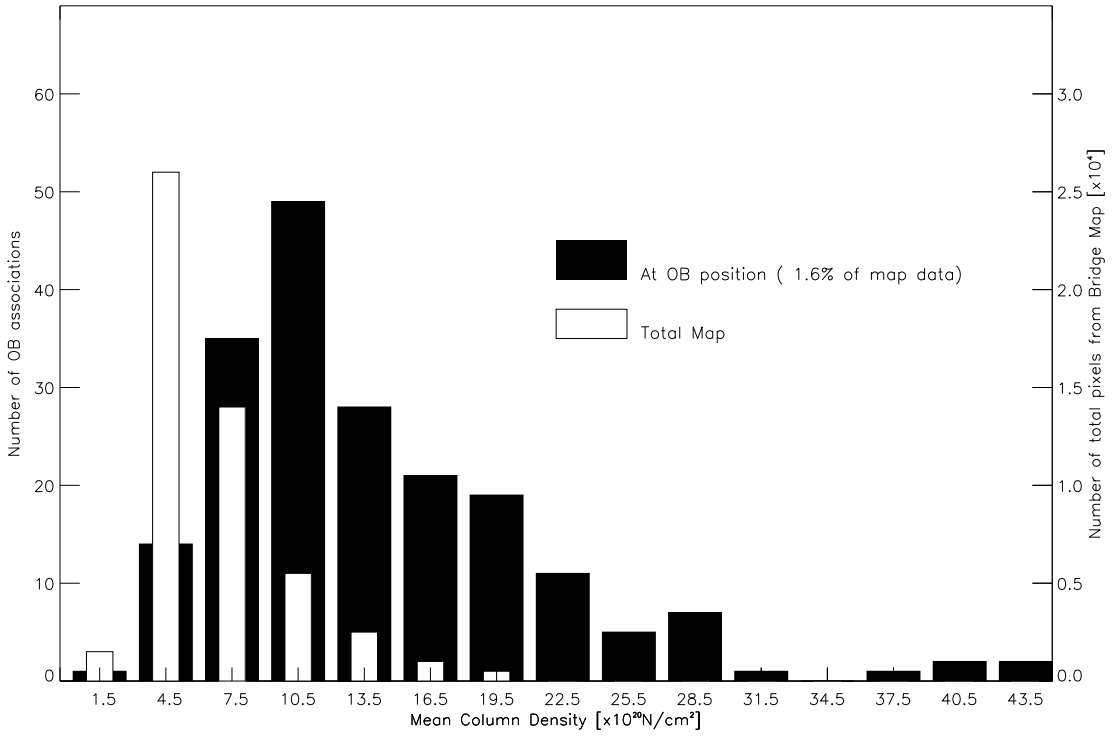

Figure 4.9: *Black and left hand axis:* Histogram of mean column density within a $90'' \times 90''$ square centred around each OB association (from catalogue by Bica & Schmitt 1995). *White and right hand axis:* Histogram of mean column density of entire map. Map is binned into $90'' \times 90''$ resolution.

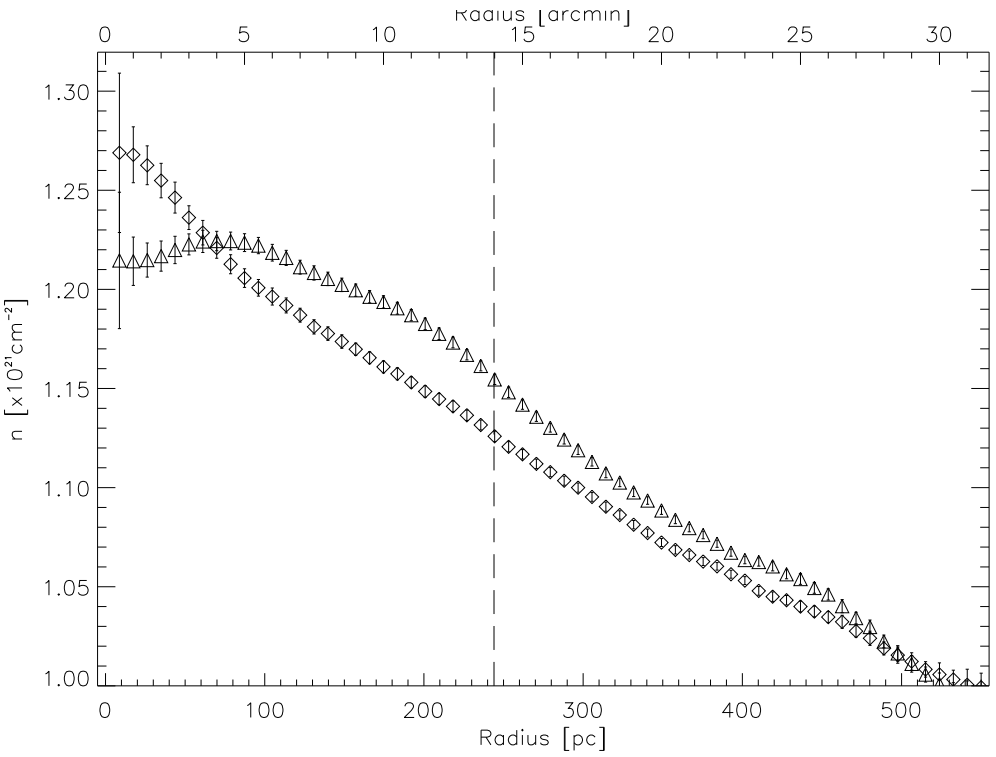

Figure 4.10: Diamonds show the mean HI as a function of distance from the centred of the OB positions, while triangles show mean HI as a function or radius, offset from OB centres by $\sim 5'$ southward. A positive departure is apparent for radii <80 pc ($\sim 5'$). The offset highlights the fact that the OB associations are generally associated with a local peak in integrated HI. Vertical dashed line shows limit of spatial resolution from Mathewson & Ford (1984) dataset. Error bars mark one standard error.

This line shows a peak in HI excess at a distance equivalent to the offset, showing that the excess is real and is centred on the OB associations.

4.4 Factors affecting the Survey

This survey has selected a sample of shells that, compared with the HI shell population of the SMC, appears to be relatively deficient in large-radii shells (See Table 4.3 and Figure 4.7b). This is almost certainly due to a different and tighter selection function. This survey demands a regular and identifiable ring shape in all three projections before such a structure can be accepted as an expanding HI shell. Incomplete, or significantly distorted shells cannot be accurately parameterized and it is not always clear that such structures are genuine expanding HI shells. Other HI shell surveys have used a more relaxed criteria and have permitted partially incomplete ring shapes to be classified as an expanding shell.

Given that this survey is sensitive to the same range of scales as the SMC surveys made by Staveley-Smith et al. (1997) and Stanimirović et al. (1999), this then leads us to question the apparent tendency for large shells to be more susceptible to fragmentation and distortion. McCray & Kafatos (1987), Ehlerova et al. (1997) have determined that for thin walled expanding shells, instabilities will cause the shell to fragment after some time. These authors calculate that shells will tend to self-destruct from intrinsic instabilities at radii $\sim$1 kpc, which is much larger than the maximum radii of the Magellanic Bridge shell population. There must therefore be additional processes catalysing the fragmentation, or otherwise affecting the integrity of the large-scale HI shells within this population. We will examine some of these in the next few sections.

4.4.1 Deformation by secondary starformation

Star formation occurring within the compressed gas comprising the shell wall may be responsible for deformation of the shell shape. Mass and energy loss from a star forming within the compressed gas of an existing shell may blow open a new shell in the primary shell wall, leading to deformation of the primary shell and ultimately to a departure from the signature shell shape. A shell expanding into a low density region will not accumulate a high density rim as quickly as one embedded in a higher density and as star formation usually occurs only after a threshold column density is reached, we might not expect shells that are expanding into a low ambient density medium to be as readily disturbed by secondary star formation. Secondary star formation within the shell wall has been observed in the SMC (Stanimirović, 1999) and also the LMC (Kim et al. 1997).

4.4.2 Deformation from density stratification

Although not listed in this study, Shell-like features, such as blow-outs, or chimneys were found occasionally throughout the cube. A blow-out or a tunnel can develop by a shell expanding close to a region of lower relative density. The expanding gas can blow through the boundary separating the two densities, such as through the wall of a gas cloud and into the low density region. Such structures can also form through the merging of two expanding shells and have been observed in the Galaxy (e.g. McClure-Griffiths et al. 2000), as well as other galaxies (e.g. Ott et al. 2001). Under these conditions, the calculation of the dynamic age, which is based on an assumption of constant and

homogeneous ambient gas density, is incorrect. The HI in the Bridge is seen to be quite turbulent and the surface density of the catalogued shells indicates that shell merging or blowouts, may occur quite frequently in the Bridge. A study of these shell-like structures will be included in a future project.

4.4.3 Size limitations

Any constraints on shell radii imposed by the extent of the gas in the Magellanic Bridge are not considered to be significant to this study. The height of the high HI density region in the Bridge, in Declination, is almost four times the diameter of the largest shell found from this survey, although this height is of the same order of the diameter of the largest supershell in in the SMC (Stanimirović et al. 1999a). The largest shell radius found during this survey was 11.7′, equivalent to ∼204 pc and the radius of the largest supershell found in the SMC was ∼910 pc.

4.4.4 Tidal stretching

Given the tidal forces responsible for the formation of the Bridge, tidal stretching is an obvious possible mechanism for the deformation of coherent spherical shells. However, of the shells surveyed, there does not appear to be any significant tendency for elongation or stretching along the SMC-LMC direction. Considering the relatively small fraction of the Bridge lifetime that the shell population will have been exposed to tidal forces, we can conclude that tidal shearing of the shells is not a significant cause of distortion.

4.4.5 Change of environment in the Magellanic Bridge

Vishniac (1983) has suggested that local inhomogeneities in the ambient HI gas may cause the shell to distort from perfect spherical symmetry and we note that Figure 3.8 shows the HI has a complex and turbulent structure down to 98″ (∼29pc). The chaotic nature of the gas comprising the Magellanic Bridge may be responsible for premature fragmentation of the HI shells. Shells fragmented in this way do not satisfy criteria *i* (from Section 4.2) and are not included in this catalogue.

We have mentioned that this survey has uncovered a region within the Magellanic Bridge

containing a slight excess of older shells (Figure 4.6). These shells have significantly slower expansion velocity and although they also have a slightly smaller radius, the net result is a mean dynamical age which is a factor of two or so greater than the rest of the Magellanic Bridge shell population. From Figures 4.5a-d, the transition of these two regions appears is most clear at around RA $2^{\rm h}\,15'$. The region containing the older shells lies to the east of this.

The average integrated HI and HI velocity dispersion for the central region containing the higher HI column density are plotted in Figures 4.11a and 4.11b. It can be seen that the fluctuation of the mean column density is relatively low at RA higher than $2^{\rm h}\,15^{\rm m}$. Similarly, the velocity dispersion becomes somewhat lower above this RA, although there are still some larger scale variations present, as well as a decreasing gradient with RA. In general however, the velocity dispersion and HI column density are smaller and with less variation above $2^{\rm h}\,15^{\rm m}$, suggesting that this region is less dynamic than the western part. A reference to Figure 3.8b shows that the velocity bimodality appears to terminate at this RA. We suggest that the younger HI expanding shells west of $2^{\rm h}\,15^{\rm m}$ are more quickly ruptured from the relatively higher turbulence and possibly from secondary star formation, while those populating the eastern side remain intact for a longer time, possibly because of the more quiescent nature of the ambient gas.

4.5 Discussion of the Stellar wind model.

4.5.1 Energy deposition

The associations catalogued by Battinelli & Demers (1992), which were later included in the catalogue by Bica & Schmitt (1995), constitute many poorly populated (mean N $\sim$8) associations and clusters. (Bica, priv. comm. 2002) mentions that the associations and clusters become more populated towards the SMC and that a few of the associations may be composed of later type stars, although the majority are of O-B type. We can see that the shells listed in Table 4.1 are generally of very low energy. Given that the mean shell energy is rather small when compared with the standard approximation of the energy for a single O5 type star ($\sim 10^{51}$ erg, e.g. Lozinskaya, 1992), poorly populated associations, comprising low-mass, later type stars, might be capable of producing these low energy structures found in the Bridge. It is curious however, that we do not observe

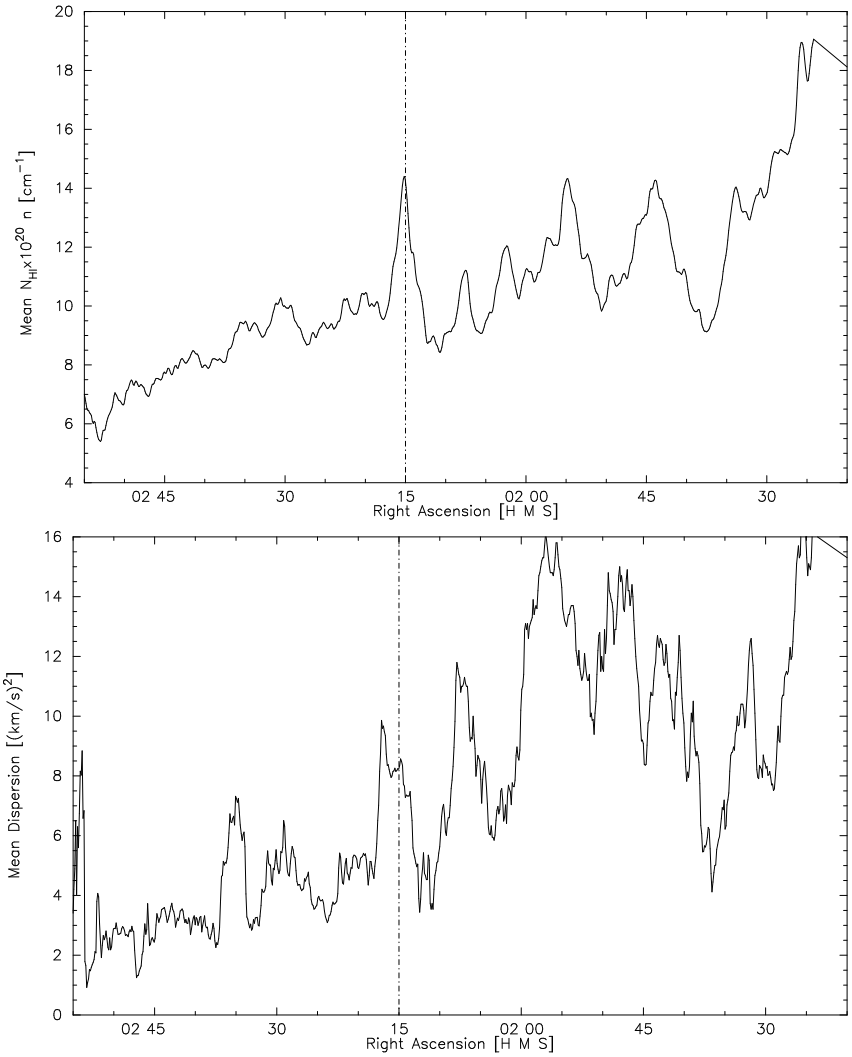

Figure 4.11: The variation of HI integrated intensity *(top)* and HI velocity dispersion *(bottom)* with Right Ascension. The data is averaged over the high HI column density region across a selected area of Figure 3.8 (approx $-73^\circ\,40'$ to $-74^\circ\,40'$). These plots suggest a transition of the gross morphologies of the HI in the Bridge after approximately $\sim 2^{\rm h}\,15^{\rm m}$.

a larger fraction of expanding shells centred about many of these observable associations and clusters and that the regions surrounding the associations are not depleted in HI. The lack of spatial correlation of HI shells and an obvious energetic source has been noted before however (e.g. Rhode et al. 1999). Alternative scenarios to the stellar wind engine are discussed in the context of the Bridge shell population in Section 4.6.

A total of 198 associations and clusters are found within the observed Bridge region where 163 shells are found. The SMC survey comprises ∼500 shells and includes 987 associations and clusters from the same catalogue (Bica & Schmitt, 1995). We find that we have almost one shell per association or cluster in the Bridge, and almost double this for the SMC. This could reflect different shell formation and destruction mechanisms in the two regions, although the relatively higher shell population in both cases ultimately calls into question the idea of stellar wind-driven expanding shells

We find that the mean energy of Bridge HI shells is a relatively small value of $\sim 1.9\times10^{49}$ ergs and a total energy of $\sim 3.2\times10^{51}$ erg. Table 4.1 shows that only six of the 163 shells have an energy greater than 10^{50} ergs and none are greater than 10^{51} ergs (for an ambient density of ~ 0.06 cm^{-2}). The total HI mass of the observed Magellanic Bridge region was calculated in Chapter 2 to be 1.5×10^{8} M$_{\odot}$ giving a shell power per HI mass of 2.1×10^{43} ergs/M$_{\odot}$. Using a mass of 3.8×10^{8} M$_{\odot}$ for the SMC and a total shell energy of $\sim 6.7\times10^{54}$ ergs (Staveley-Smith et al. 1997 and Stanimirović et al. 1999a), we calculate a power per HI mass of 1.8×10^{46} ergs/M$_{\odot}$ for the SMC. We see that the shells populating the Bridge are significantly less powerful per mass than those of the SMC. We see also that the median SMC shell energy is $\sim 10^{50.2}$ ergs and that the median Magellanic Bridge shell energy is some orders lower at $\sim 10^{48}$ ergs. However, given the strict shell selection criteria, these relative values should be considered as lower limit only.

4.5.2 The Ages of Bridge shells and Bridge OB associations

Figure 4.5 shows that, despite the apparent lack of large radius shells in the Magellanic Bridge shell sample, the kinematic age distribution is consistent with that of the SMC population. It can be seen that the average dynamic age of ∼6.2 Myr (Table 4.2) of the Magellanic Bridge shell population is far younger than the date of the most recent Magellanic Cloud interaction, shown by simulations to be approximately 200 Myr ago (e.g. Gardiner, Sawa & Fujimoto, 1994). There is also a lack of agreement with ages of

OB associations, determined through spectroscopy (Hambly et al. 1994) and isochrone fitting (Grondin, Demers & Kunkel, 1990; Battinelli & Demers, 1998), to be in the range 7-25 Myr. These values can differ with the average shell dynamic ages calculated here by up to a factor of almost four. Allowing for re-acceleration by WR stars as noted by Shull & Saken (1995) still does not bring the dynamic age to one that is comparable with the association ages estimated by Grondin, Demers & Kunkel (1992) and Demers & Battinelli (1998). It is difficult, therefore, to become convinced that the majority of the spherical expanding HI structures found here in the Magellanic Bridge are powered by stellar winds.

During the survey for HI shells in the SMC, Staveley-Smith et al. (1997) found a large number of shells with a tightly confined distribution of ages that were too young to be conveniently related to an episode of star formation triggered by the Magellanic Cloud encounter and under the assumption that HI shells are commonly driven by stellar winds, they suggest that as the Magellanic System is close to perigalacticon, it may be experiencing sufficient tidal disruption to stimulate a more recent period of star formation. If this were the case, there is no reason that the Bridge would not experience similar disruption, although we note a slightly larger spread of ages (Table 4.3).

It is worth noting that the assumptions made in calculating the kinematic age are not necessarily satisfied in every study. The equations used in this paper, as derived by Weaver et al. (1977), assume a homogeneous medium and relate only to the expansion phase of the shell. The Magellanic Bridge can be seen to have structure and dynamics down to the smallest observed scales and it is difficult to assess the extent to which the inhomogeneities affect the estimations of kinematic age and shell luminosity. The kinematic ages estimated in this paper are used more as means to compare between systems where data have been subjected to the same assumptions, rather than an measure of the absolute age of the shell. Alternative models exist and give rise to different estimates of the shell parameters. From the SNe model derived by Chevalier (1974), the mean Magellanic Bridge shell energy is estimated to be $\sim 5 \times 10^{49}$ ergs, which is an order of magnitude larger than the estimates made using the stellar wind model (Weaver et al. 1977). As the Weaver model has been used in studies of the SMC and HoII we have also used it also in this study to preserve some continuity.

4.6 Alternatives to the stellar wind model

The lack of spatial correlation of the stellar population and the Shell population imply that other mechanisms may be operating to produce the observed spherical, expanding HI structures. As discussed earlier, these include energy depositions through Gamma Ray Bursts (GRBs), High Velocity Cloud impacts (HVCs) and ram pressure effects. We will examine the alternatives in the context of the Bridge HI shell survey results.

4.6.1 Gamma Ray Bursts

Measurements of the gamma ray flux by Wijers et al. (1998), have led to an upper-limit estimate of the probability of a GRB event of once per 40 million years, per galaxy. If we apply this probability estimate to the Magellanic Bridge and assume the age of the Bridge is $\sim$200 Myr, as found by computer simulations (e.g. Gardiner, Sawa & Fujimoto 1994), we can estimate $\sim$5 Gamma ray Burst events since its creation. The number of shells found in the Bridge is clearly in excess of this and there is no plausible way to justify the source of the majority of HI expanding features as GRB relics. However, caution should be taken when assuming the Magellanic Bridge will have the same kind of GRB frequency as a galaxy and considering that the estimate by Wijers et al. (1998) is a maximum rate. The Bridge has a relatively small total mass and it is likely to have a significantly lower star formation rate. However, taking these into account can only decrease the estimated GRB frequency. Additionally, the shell energies, as derived using both Weaver and Chevalier models, are three and two orders of magnitude respectively lower than the expected energy from a GRB. We conclude that the low GRB frequency and the insufficient shell energy suggest that GRB events are not a dominant mechanism for shell formation and expansion within the Magellanic Bridge.

4.6.2 HVCs

The results of cloud impacts by Tenorio Tagle et al. (1986) show that shells produced this way have radii which are consistent with those measured from the Magellanic Bridge shell population. A superficial argument against the formation of shells in the Bridge by HVC impacts is that of the non-uniform distribution of the shell centres. There should be no reason that HVC impacts should be detected only at higher column densities, other than

a lack of sensitivity, i.e. the HVC impact sites might exist, though the survey is incapable of detecting them. It should be noted that the simulations used a medium of density 1 cm^{-3}. The estimates of the density of the HI in the Magellanic Bridge from Chapter 3, are two orders of magnitude lower than this. We might therefore expect that an HVC cloud impact, such as the ones simulated by Tenorio-Tagle et al. (1986) would have a more destructive effect than the simulations show. Such destructive impacts may not generate a complete, spherically expanding shell which would consequently be excluded from this survey. As such, although we can see from Fig.4.3 that the distribution of the surveyed HI expanding shells appears to be chiefly confined to regions of higher HI, we cannot confidently rule out this mechanism of shell formation for the entire Bridge shell population on the basis of this non-uniform distribution.

4.6.3 Ram Pressure

Throughout the shell survey, great care was taken to ensure that the catalogued expanding shells were largely complete. The process of enlarging existing HI holes in a gaseous region proposed by Bureau & Carignan (2002) does not form a complete expanding sphere. This process therefore cannot be discussed in the context of the current survey. A future work will focus on shell-like features in the Bridge where an analysis of shell formation through ram pressure is much more relevant.

4.7 Summary

A survey of HI spherical expanding shells of the Magellanic Bridge has uncovered 163 examples of such structures. Generally, shells found within the Magellanic Bridge are less energetic, expand more slowly and are smaller than those found within the SMC, although this survey has shown that the mean kinematic age of shells in the Magellanic Bridge of $\sim$6.2 Myr is approximately equivalent to that of the SMC of $\sim$5.7 Myr. Although the HI column density and OB distribution seem to spatially correlate very well, as well as the distribution of HI expanding shell features and HI column density, we have found very poor correlation between the HI shells and OB association distributions in the Magellanic Bridge. In addition, there appears to be a local *excess* of HI within $\sim$80 pc of the OB associations. These findings generally do not support the popular idea of stellar wind

being the driving engine of an HI shell. Formation by GRBs also do not satisfactorily describe the energies and distribution of the observed shell population. HVCs may be an important process to bear in mind in the case of the Magellanic Bridge, although without accurate knowledge of the HVC population and what effect they have when impacting into tenuous ISM, a definitive assessment of the importance of the mechanism cannot be made.

A comparison with other HI shell surveys of the Magellanic-type galaxies, the SMC and HoII has shown that the survey appears to be insensitive to shells with large radii. An examination of other HI surveys indicate that this survey used here was particularly rigorous in the definition of an expanding shell. As a result of the strictness of the selection criteria, we have found that a region of the Bridge, in which an excess of older shells exists, corresponds with a region of lower HI velocity dispersion. On the basis of this, we have suggested that shells are prone to fragmentation in a dynamic environment, where the tendency to fragmentation is somehow dependent on shell age and size.

Chapter 5

Statistical analysis

"I've got a bad feeling about this...."- Han Solo, 1980's

We have seen in Chapters 3 and 4 that the structure of the HI in the Magellanic Bridge is quite complex. Structure is found across the entire observed spatial range, from $\sim 98''$ up to $\sim 7^\circ$. This Chapter presents an analysis of techniques which aim to parameterize the structure hierarchy of the HI in the Bridge and expose any underlying trends.

One of the more successful and prevalent tools used to measure the structure hierarchy involves the calculation of the *Spatial Power Spectrum*. Knowledge of the Spatial Power Spectrum gives insight into the range of spatial scales and their relative importance. This is an important parameter, since the organisation of spatial scale has a direct influence on the efficiency of energy transport throughout the system and also vice versa: the transport of energy shapes the arrangement and distribution of spatial scale. Knowledge of the spatial power spectrum can help to identify any processes that cause a dominance or a deficiency of structure at a particular scale.

A somewhat newer approach to understanding the underlying spatial structure trends involve the use of the *Spectral Correlation Function* (SCF). The SCF could be described as a spatial structure function: calculating the SCF leads to an estimate of the 'similarity' of two spectra as a function of projected separation.

Section 5.1 of this Chapter details the methodology, results and some discussion of the Magellanic Bridge HI power spectrum. Section 5.2 presents the methodology, results and discussion of an analysis of the Bridge using the SCF. Finally, Section 5.3 contains a more dedicated interpretation of the results of the power spectrum and SCF analyses.

Caution must be exercised when applying statistical methods involving large-scale averaging in that the subject of the analysis is appropriately homogenous. The rapid spatial and velocity variability of the HI of the Magellanic Bridge noted in Chapters 3 and 4 indicates a turbulent and chaotic morphology over the entire range of observed spatial and velocity scales. As such, we have opted for an piece-wise approach for the study both of the Spatial Power Spectrum and the SCF. The details for treatment of the data prior to the actual measurements are discussed in the relevant sections.

5.1 Spatial Power spectrum

The Spatial Power Spectrum provides a measure of the power as a function of spatial scale. For a fluid region in thermodynamic equilibrium and containing structure over a complete range of spatial scales, the power transmitted as a function of scale can be characterized by a power-law:

$$P(k) \propto k^{\gamma}$$

where k is the wave number of the spatial frequency.

The slope of the power spectrum, γ is an important parameter and is dependent on the type of processes active within the region of interest. Analyses of the HI in the SMC have revealed a power spectrum which is featureless and very well approximated with single component (Staveley-Smith et al. 1998; Stanimirović et al. 1999a; Stanimirović et al. 1999b; Stanimirović & Lazarian, 2001). The remarkable linearity of the power spectrum indicates a lack of any scale dominant processes and the authors of these analyses suggest that this may be evidence for a large radial extent of the SMC.

A composite power law is observed when the dynamics of a system are shaped by a process (or processes) which generate excess power over a specific range of scales.

$$P(k) \propto C_1 k^{\gamma_1} + C_2 k^{\gamma_2}.$$

For example, supernovae are capable of injecting power across scales of tens of parsecs. The constants C_1 and C_2 are dependent on the relative importance of the two terms (see also Elmegreen & Scalo, 2004; Scalo & Elmegreen, 2004, for a detailed review of turbulent processes). A power spectrum containing multiple exponents has been observed in the

LMC in an analysis by Elmegreen, Kim & Staveley-Smith (2001). In this case, a break in the power law was found at around 100 pc. This was considered to be evidence for the finite thickness of the LMC disk.

The application of the Power Spectrum analysis was developed further by Lazarian & Pogosyan (2000). It was shown that the spectral index for a given velocity interval is modified from the static density distribution by small-scale velocity fluctuations, as long as the range of the fluctuations are larger than the size of velocity interval of the dataset. The degree to which the velocity structure modifies the overall spectral index can be estimated by measuring the variation of the index for a range of velocity integrated widths.

Lazarian & Pogosyan (2000) refer to a series of velocity regimes, called the 'thick' and the 'thin' regimes. The regime for which the range of the velocity fluctuations is much larger than that of the velocity thickness is the 'thin' regime, where the static density power spectrum can be modified by velocity fluctuations in the HI. Velocity intervals much greater than the velocity fluctuations fall into the 'thick' regime, where the velocity fluctuations have become averaged out and the observed power index is a measure of the static density distribution. Lazarian & Pogosyan (2000) have shown that the power index of a turbulent dataset will tend to steepen for thicker velocity intervals, until the velocity interval becomes greater than the range of the velocity fluctuations and successively thicker velocity ranges will not result in further modifications to the power index. From this, it is possible to obtain an estimate of the 3 dimensional density index and of the modification to the power index due to the velocity fluctuations. Table 5.1 shows the expected modification of the static density power spectrum index due to a turbulent component and depending on the static 3-D density index (Lazarian & Pogosyan, 2000; Stanimirović & Lazarian, 2001).

An analysis of the power spectrum has been made of a number of HI datasets, including that of the SMC (Staveley-Smith et al. 1998; Stanimirović et al. 1999a; Stanimirović et al. 1999b; Stanimirović & Lazarian, 2001), the LMC (Elmegreen, Kim & Staveley-Smith, 2001), the Magellanic Stream (Stanimirović, Dickey & Brooks, 2002) and the Galaxy (Green, 1993; Crovisier & Dickey, 1983; Dickey et al. 2001). The effect of velocity averaging on the spectral index as explained by Lazarian & Pogosyan (2000) has been corroborated using the SMC HI dataset (Stanimirović 1999) by Stanimirović & Lazarian

	Shallow 3-D density	Steep 3-D density
2-D Intensity spectrum, Thin slice	$\propto k^{n+m/2}$	$\propto k^{-3+m/2}$
2-D Intensity spectrum, Thick slice	$\propto k^{n}$	$\propto k^{-3-m/2}$
2-D Intensity spectrum, Very Thick slice	$\propto k^{n}$	$\propto k^{n}$

Table 5.1: The effect on Power Index arising from small-scale random turbulence as estimated from theoretical considerations by Lazarian & Pogosyan (2000). The SMC dataset was found to conform to the outcomes predicted by Lazarian & Pogosyan (2000) in a later analysis by Stanimirović & Lazarian (2001). The 3-D density refers to the static spatial power index, where modifications by velocity fluctuations are negligible.

(2001). This study showed that integrating over successively thicker velocity intervals steepened the power index from ~ -2.8 to ~ -3.3. Similar studies on the Galaxy by Dickey et al. (2001) showed that velocity integrating caused a shift of the power index from ~ -3 to ~ -4. An analysis of the SMC power spectrum (Stanimirović & Lazarian, 2001) did not detect a flattening of the index with velocity integrated thickness (i.e. the power index was a continually changing function of velocity integrated thickness). This indicates that the velocity fluctuations in the SMC exist over the complete range of velocity intervals available.

5.1.1 Calculating the spatial power index

The algorithm used to calculate power as a function of wave number from a spectral line dataset is straightforward. This study presented here generally follows the processes and methodologies used by Stanimirović et al. (1999a), Stanimirović & Lazarian, (2001), Elmegreen, Kim & Staveley-Smith (2001) and Dickey et al. (2001):

1. *Apodizing*: Under a fast Fourier transform (FFT) operation, the finite size of the dataset and the spatial 'top hat' sampling function generates $\sin(x)/x$ ringing in the transformed dataset. The ringing can be almost eliminated by applying an effective tapering mask to the dataset prior to calculating the Fourier transform. The mask is the called the 'apodizing' mask here and is simply a tailored blank image of the same pixel dimensions as the dataset. The entire mask is set to a value of 1, although the edges of the mask Gaussian taper to zero over a pre-defined band

thickness. Unfortunately quite a lot of the dataset can be lost to the tapering mask. For this study, we use an edge band 50 pixels wide and a Gaussian function with a FWHM of 30 pixels. Figure 5.1 *(top)* shows a cross section through the centre of a dummy blank image of 512 × 512 pixels, before and after applying the apodizing procedure. The original profile is shown as the 'top hat' type function, while the profile of the blank image after applying the apodizing mask is shown as the profile which Gaussian tapers to the edges of the plot. The bottom plot in Figure 5.1 shows a cut through the centres of the Fourier transform of both the original (top hat) sampling function and apodized image. We can see from these plots that neglecting to apply the apodizing filter can generate some very large unwanted signals which manifest as infinite ringing in the transformed data. The transform of the apodized image, on the other hand, shows very little ringing and the image is dominated by the low frequency power. This is the preferable condition, although we eliminate ringing at the cost of data. For a dataset 512 × 512 pixels, approximately 35% of the data is lost to the apodizing mask, for a 256 × 256 pixel dataset, this fraction is ∼62%. It is obvious that there are severe limitations on the size of the set that may be sampled using processes which involve calculating the Fourier transform.

2. *Calculating the Transform*: The Fourier transform for the apodized image is calculated (in this case, the IDL procedure FFT was used). The power is measured in the UV plane from the sum of the squares of the real and imaginary components of the transform (e.g. Stanimirović, 1999). An example of the output of this step is shown in Figure 5.2. The finite sampling of the UV space by the ATCA manifests as the brighter concentric sampling rings seen in this image. In fitting power laws to data with such a sampling function, care must be taken to avoid using unsampled regions in the UV plane.

3. *Azimuthal averaging*: The resulting UV power dataset is azimuthally averaged, in rings of logarithmically increasing widths across constant baseline intervals. This leads to an average measurement of power as a function of wave number $< P(k) >_{\Delta k}$. The resulting data are fit with a single component function across continuous ranges on the UV plane (i.e. for baselines where 10<D<600 λ), taking care to avoid any regions which have no data (The fit and error is calculated from the noise-weighted data set with the IDL task POLYFIT).

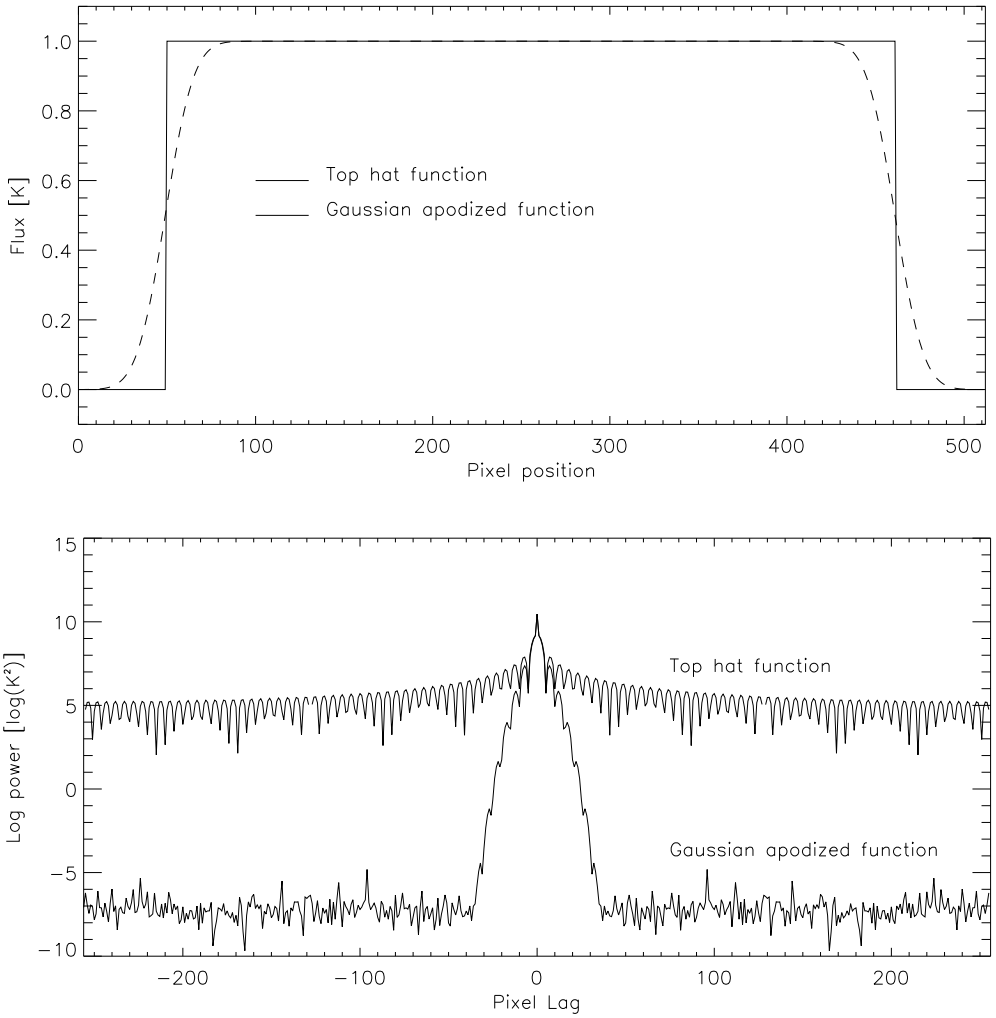

Figure 5.1: This Figure highlights the need for the apodizing process before calculating the 2-D Fourier transform for an image dataset. The top plot shows a cross section through a blank 512^2 pixel image before apodizing (*solid line*) and after apodizing (*dotted line*). The bottom plot shows the Fourier transform for the un-apodized blank image (*solid line*) and for the Gaussian apodized blank image (*dotted plot*). The scaling for the y axes of these plots are rather arbitrary, but the bottom plot shows the log of the total power of the transformed images.

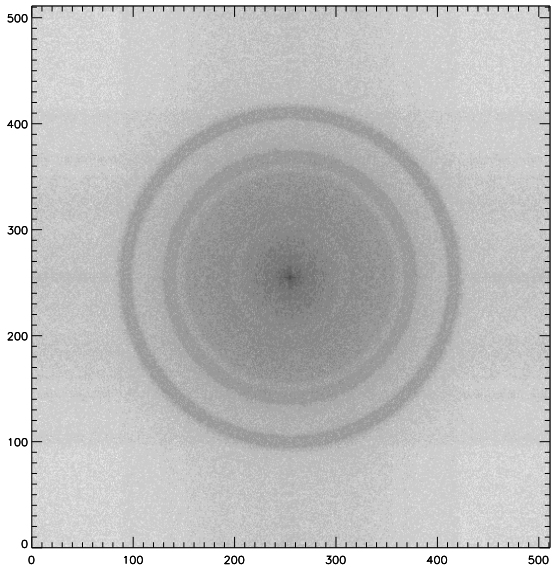

Figure 5.2: Example image of the Fourier inversion for the integrated HI intensity map of the Magellanic Bridge (See Fig 3.8a). The sampling rings shown result from the finite sampling of the UV plane by the ATCA. The UV region observed by the Parkes Telescope has been scaled to merge with the ATCA dataset and comprises the very centre (i.e. small baselines) of the FFT image. The scale here is normalised so that the centre $\sim$1.0 and the data on the periphery $\sim$0

For this dataset, the non-circularity of the UV sampling function is negligible (see also Figure 5.2) and no compensation is made for any ellipticity of the tracks. The maximum HI column density for this dataset is very low (3×10^{19} cm^{-2}) and any corrections for self-absorption are unnecessary (See discussion by Minter, 2002). In this analysis the fits are made across baselines which have been continuously observed in the UV plane. For the ATCA + Parkes dataset used here, these are D$<600\lambda$. ATCA beam effects start to become important for $\sim$D$>700\lambda$. Green (1993) has made some efforts to compensate Galactic power spectra for effects of noise and beam affects. However, we find that typically the power contributed by the noise is a tiny fraction of that received at low spatial frequencies and becomes significant only for very large frequencies ($>700\lambda$). As these high frequencies are usually compromised by the ATCA beam, they are already excluded from the fitting process. Generally, there is no compensation necessary for noise in this analysis.

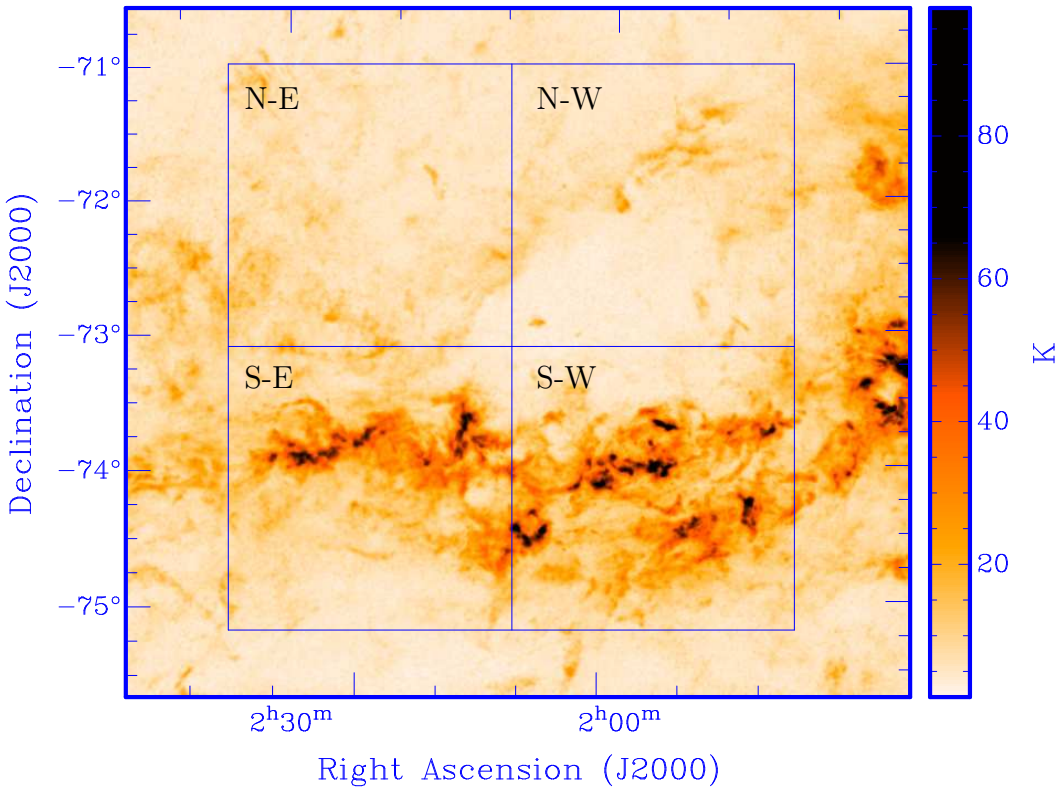

Figure 5.3: Peak intensity map of the entire Magellanic Bridge HI dataset. The overlaid square indicates the four 256 × 256 pixel (∼5 kpc×5 kpc) subsections over which the power spectra analysis is performed.

5.1.2 The power spectrum data set

Figure 5.3 shows the peak intensity map of the HI of the Magellanic Bridge. The Figure shows a diverse range of morphologies: some regions are bright and filamentary, others are more tenuous and smooth. In this section, we will probe the power spectra for four regions in the Bridge, corresponding to four different kinematical and morphological regions. The four regions are defined by the grid overlaid on Figure 5.3. Each of these regions has an area of 256×256 pixels (corresponding to ∼5 kpc×5 kpc area).

The regions will be referred to as (*clockwise starting from the bottom left on Figure 5.3*) the South East (SE), North East (NE), North West (NW) and the South West (SW) regions.

We see that the south west region is dominated by bright, filamentary HI across the entire surface. The HI in the south east region is similarly filamentary, although the spatial coverage of the HI is less complete. The North east region defines an area of less

diverse structure and the HI appears relatively tenuous and smooth. The North west region is dominated by a part of a large HI loop filament. We know from Figure 3.8a and Figure 3.9 in Chapter 3 that the HI in the northern part of the Bridge is offset to higher velocity. The northern two regions correspond to this part of the Bridge.

5.1.3 The Power index as a function of Velocity

5.1.3.1 Results

The power spectrum is calculated for each velocity channel for each of the four regions of Figure 5.3. An example spatial power spectrum, typical for the Magellanic Bridge dataset, is shown in Figure 5.4. The spectra has been calculated for the South East subregion and a velocity channel at $\sim$169 km s^{-1}. We see that as for the SMC (Stanimirović 1999) and the Galaxy (Green, 1993), the Magellanic Bridge power spectrum is very well fit with a single power index. Shown also on this plot is the power spectrum for a sample noise dataset and the power spectrum for a gaussian of 98″ (i.e. the resolution of these observations). This last spectrum shows the effects of the ATCA beam at higher spatial frequencies ($\gtrsim$600λ). We also see that typically, the power from noise represents an entirely negligible contribution at low spatial frequencies and becomes much more important only at the higher frequencies.

The variation of γ as a function of heliocentric velocity in each of the four regions (as defined in Figure 5.3) is plotted in Figure 5.5. The purple line with error bars (left axis) indicates the power index, while the curved dotted red line (right axis) shows the mean integrated HI brightness as a function of velocity. The index and mean flux for the highest and lowest velocity ranges where the index $\approx$0 (and the mean flux is very low) are not plotted. The straight dot-dash line shows the RMS level of the dataset (right axis).

5.1.3.2 Discussion

The plots of Figure 5.5 suggest a relationship between the mean brightness temperature and the index of the power-law, in that a low T$_B$ is associated with a shallow (i.e. flatter) power spectrum. This is more striking particularly for velocity channels where the mean T_B <2 K or so. This effect is primarily a manifestation of the increasing relative importance of the noise component. For channels where where T$_B$ is low, the spectrum

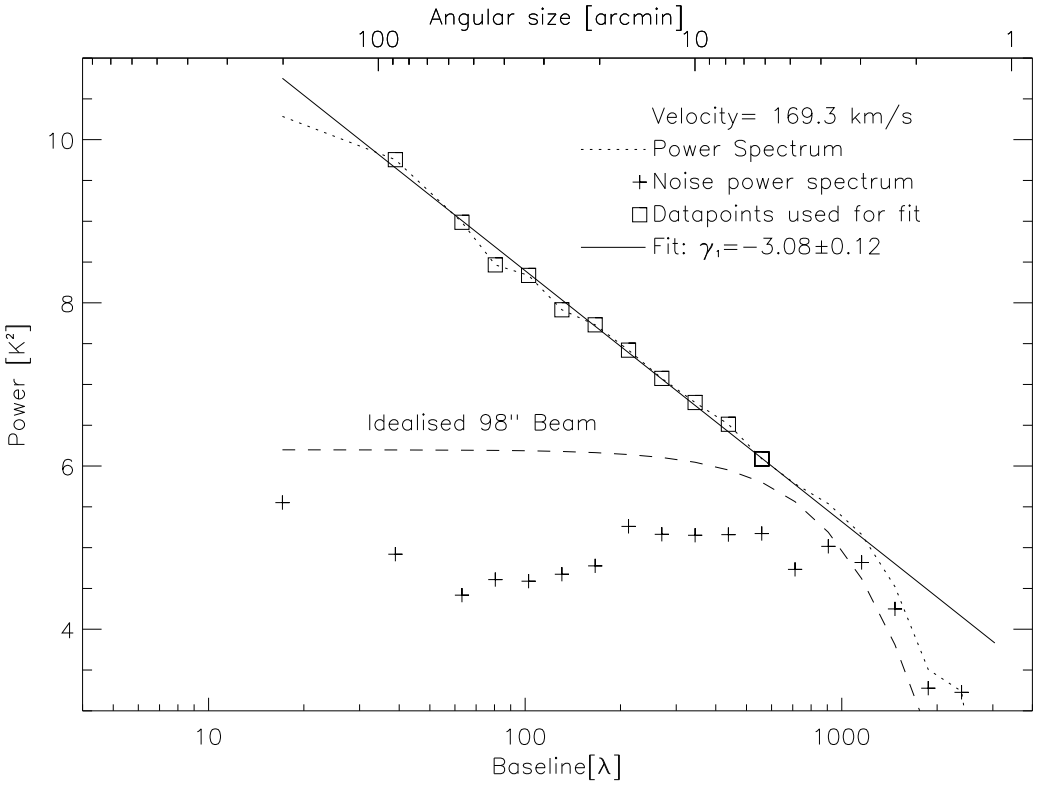

Figure 5.4: Example power spectrum from the South East sub-region, at velocity ∼169 km s^{-1} (heliocentric). The spectrum is typical for channels which contain bright HI. The line shown is fitted to the points marked with a square. Importantly, we see that the power spectra of the Bridge are able to be fit well with a single component. Also shown on this plot is the power spectrum for a channel containing only noise (crosses) and the 98″ beam.

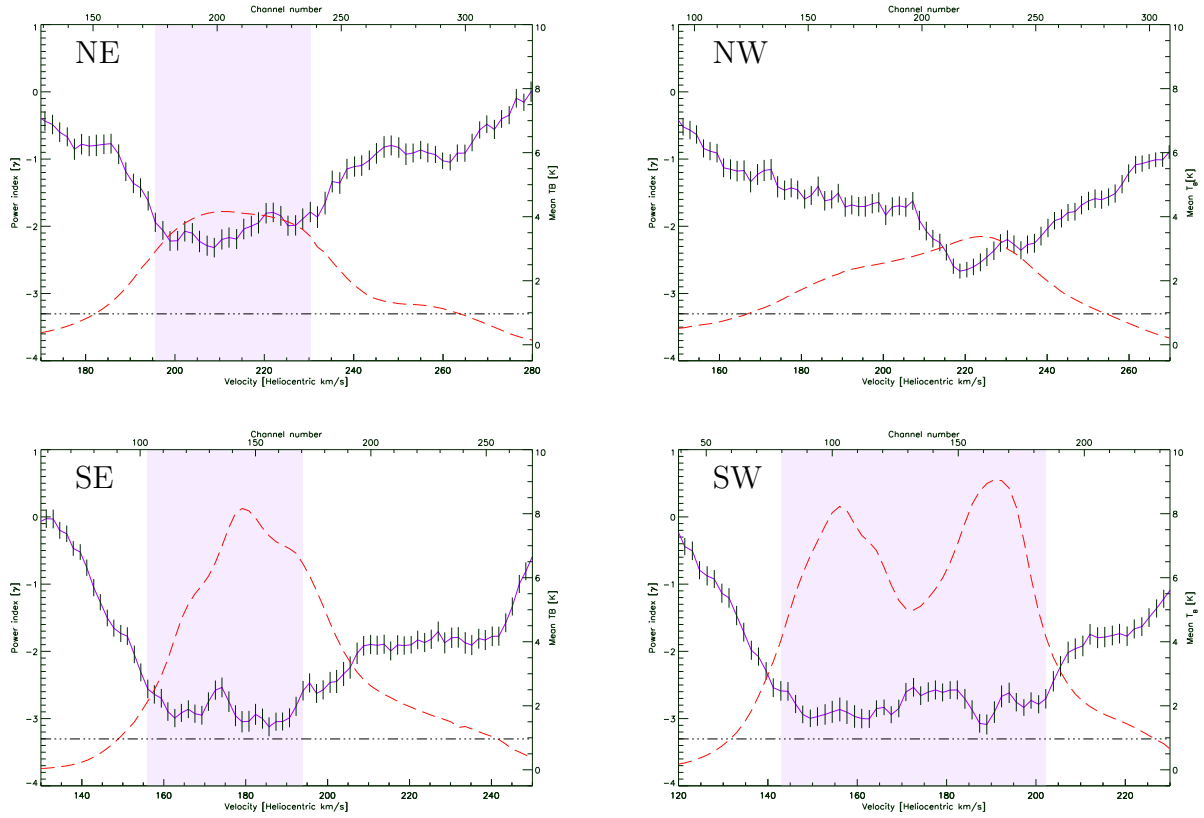

Figure 5.5: Variation of the index γ ($P(k) \propto k^{\gamma}$) as a function of velocity for all four regions is plotted here as the purple line with error bars (*left axis*). The total integrated HI brightness is overplotted as the red dotted line (*right axis*). The position of the plots here correspond to those shown in Figure 5.3 (e.g. the plot for the South East region is shown in the bottom left). The shaded regions are those over which the power index is relatively constant and $T_B \gtrsim$3-4 K, and are the subjects for the study of the variation of index with integrated velocity thickness in the next section. The velocity intervals shown here are those for which $\gamma \lesssim 0$. The dot-dash line indicates the RMS of the data, as measured in a line-free channel of the region.

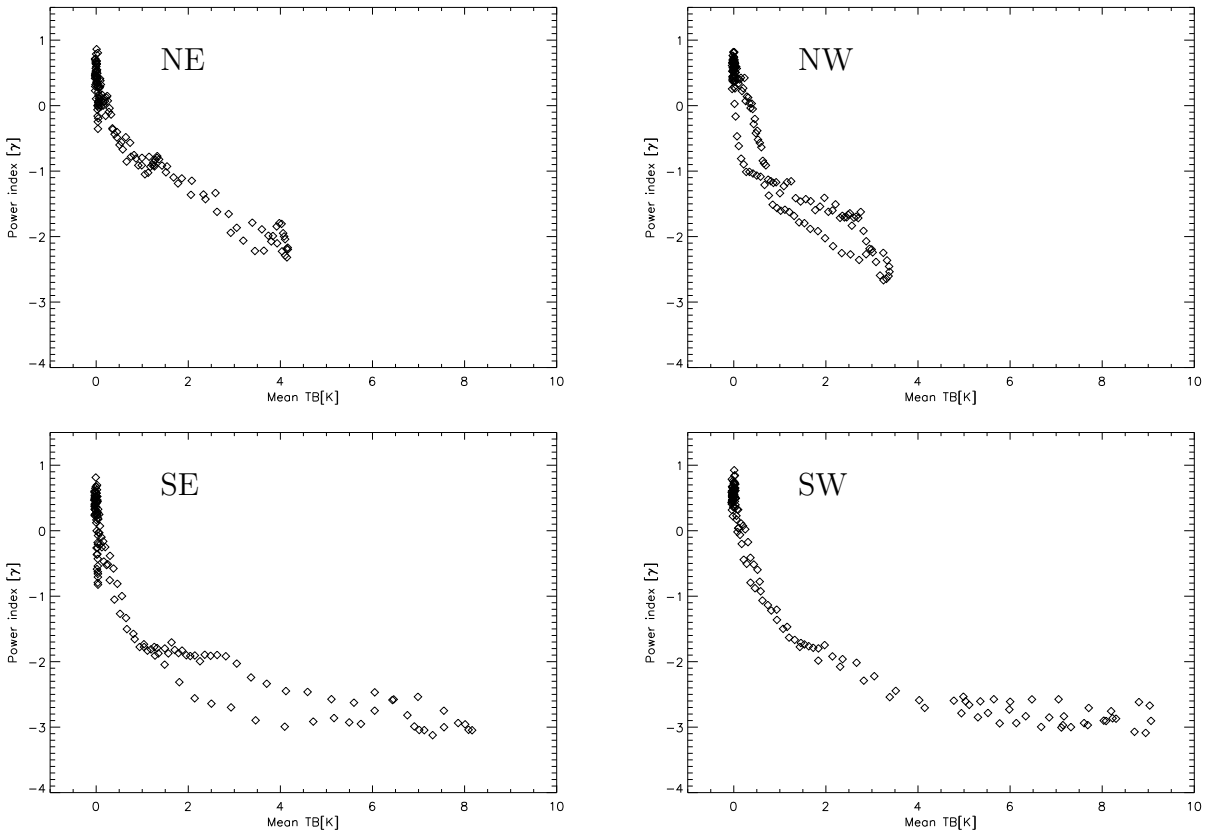

Figure 5.6: Variation of the index γ ($P(k) \propto k^{\gamma}$) as a function of mean brightness per channel T_B for all four regions. The relationship between the index and T_B is clear, demonstrating the importance of noise on the slope of the index for low values of T_B (i.e. those $<\sim$4 K). The apparent loop-like structure however also indicates that the relationship between γ and T_B is not perfect. The plots for the southern two regions show that the value of γ achieves a minimum value for $T_B >\sim$4 K.

becomes 'whiter'.

In the case of the SW region where the variation of T_B is very large, We see that the variations of T_B are not necessarily reflected by similar variations of γ, which appears to have a limiting slope of approximately -3. The same is true also for the NE region, although the lowest index is ~ -2 in this case. It is more difficult to see a similar limiting effect in the NW region, although γ achieves a minimum value of ~ -2.

An index of $-11/3$ is expected for fluids showing a Kolmogorov-type turbulent structure. The fact that this is approximately the index for the brightest channels of the southern regions suggests that the HI here conforms to this kind of structure arrangement. A similar power index was derived for the HI of the SMC: Stanimirović (1999) and Stanimirović & Lazarian (2000) have shown that the structure in the SMC may conform to a fractal structure and has a spatial power index which is approximately -3 across the entire velocity range. We can infer that similar physical processes appear to be active in both the SMC and this part of the Magellanic Bridge.

From simulated datasets where the turbulent HI is arranged in long filaments, Minter (2002) showed that the slope of the power spectrum for short baselines is approximately $\sim -8/3$. We find that the indices for the northern regions conform more easily to this value, although in this case the slope is consistent across all baselines. The northern higher velocity component of the Magellanic Bridge is clearly subject to very different processes to those found in the southern lower velocity component. It is of great interest that two so kinematically different masses are found so closely spaced position and in velocity. The origins of the two components are discussed further in Chapter 6.

The plots in Figure 5.5 for the two southern regions show a rapid episode of flattening of the spatial power index of approximately $\Delta\gamma = +0.5$ at $\sim$175 km s^{-1}-190 km s^{-1} . These velocities correspond to the interval *between* the velocity bifurcation seen in Figure 3.8b. The flattening of the index here suggests a change in the morphology of the HI : a relative deficiency of power from large scales would lead to a flattening of the power spectrum. We can confirm from the appropriate maps of Figure 3.10 that this region appears devoid of a large scale component, with only a bright and filamentary component remaining. This bimodal structure is a dominant feature of the Magellanic Bridge and its origin is also discussed further in Chapter 6.

5.1.4 The Power index as a function of Velocity thickness

One of the critical results seen from the previous section is the large variation of the fitted power index, as a function of velocity and as a function of spatial position. This has important ramifications for this part of the analysis, where we attempt to remove the effects of velocity fluctuations as outlined by Lazarian & Pogosyan (2000) by computing the Fourier transform for data subsets which have been averaged over a range of velocity intervals. This technique assumes that the morphology of the original dataset is quite homogenous over the velocity range of interest.

Due to the rapid variation of γ with velocity in this HI dataset, we cannot test the variation of γ as a function of velocity integrated thickness across the entire velocity interval. Instead we are obliged to select velocity windows, within which the variation of the power indices appear to vary little. Unfortunately, this limits our velocity thickness range considerably. In this case, we choose regions with roughly constant $\gamma(v, \Delta v = 1.6 \text{ km s}^{-1})$. In addition, To avoid sampling velocity channels which appear to be dominated by noise, we further limit the selection criteria to channels for which the mean T_B is at least 4σ (i.e. $\approx$4 K) above the RMS noise (shown as a a horizontal dot-dash line in Figure 5.5). The relationship of γ with T_B for this dataset is shown in Figure 5.6. We see here also that γ is affected by noise for values of $T_B <\sim 4$ K.

The selected velocity intervals are marked with a coloured vertical band in Figure 5.5. For the north west subregion however, there is no velocity range over which the power index is particularly consistent. For this reason, we will not attempt to study the quality of the velocity fluctuations of this subregion.

The following velocity ranges are selected from the indicated sub-regions:

North West: None
North East: 196 - 230 km s^{-1}
South West: 143 - 203 km s^{-1}
South East: 156 - 194 km s^{-1}

For this test, we process the data in the following way:

1. The dataset is cut into windows in the velocity dimension, so that the velocity range of each slice is equal to an interval over which we wish to study the modification by velocity fluctuations. The mean intensity for each component is calculated. The data now is simply a lower velocity resolution set.

2. Each channel in this new cube is subject to the normal apodizing and Fourier transform treatment of the previous analysis. As before, this constitutes multiplication with a Gaussian edge mask, followed by the calculation of the Fourier transform. The datacube at this stage now consists of a collection of Fourier transformed images. The mean transform of the entire set is then calculated. This dataset is now a single two dimensional image and represents the mean transform across the fragment velocity thickness.

   It is clear now why we must select a dataset which is quite homogenous in velocity. Any radically different structure present in the sampled region will skew the results of this averaging step.

3. As for the previous section, the mean power as a function of baseline is calculated by azimuthally averaging around in logarithmically increasing baseline intervals. A single component log-log fit to the spectra is estimated.

4. The entire process is repeated for each velocity thickness of interest. The end result is an estimation for the mean power index as a function of velocity integrated thickness.

5.1.4.1 Results

The modification of the power index as a function of velocity integrated thickness for all three regions is shown in Figure 5.7.

The result of primary interest here is the apparent steepening of the spatial power index with increasing velocity thickness, seen to occur for all three studied regions. This is entirely consistent with predictions made by Lazarian & Pogosyan (2000) and also with results obtained from both the SMC dataset (Stanimirović et al. 1999a; Stanimirović & Lazarian, 2001) and suggests that there is some component of velocity fluctuations present throughout the Magellanic Bridge dataset. We can estimate the factor by which the velocity fluctuations modify the power index n and thereby the three dimensional

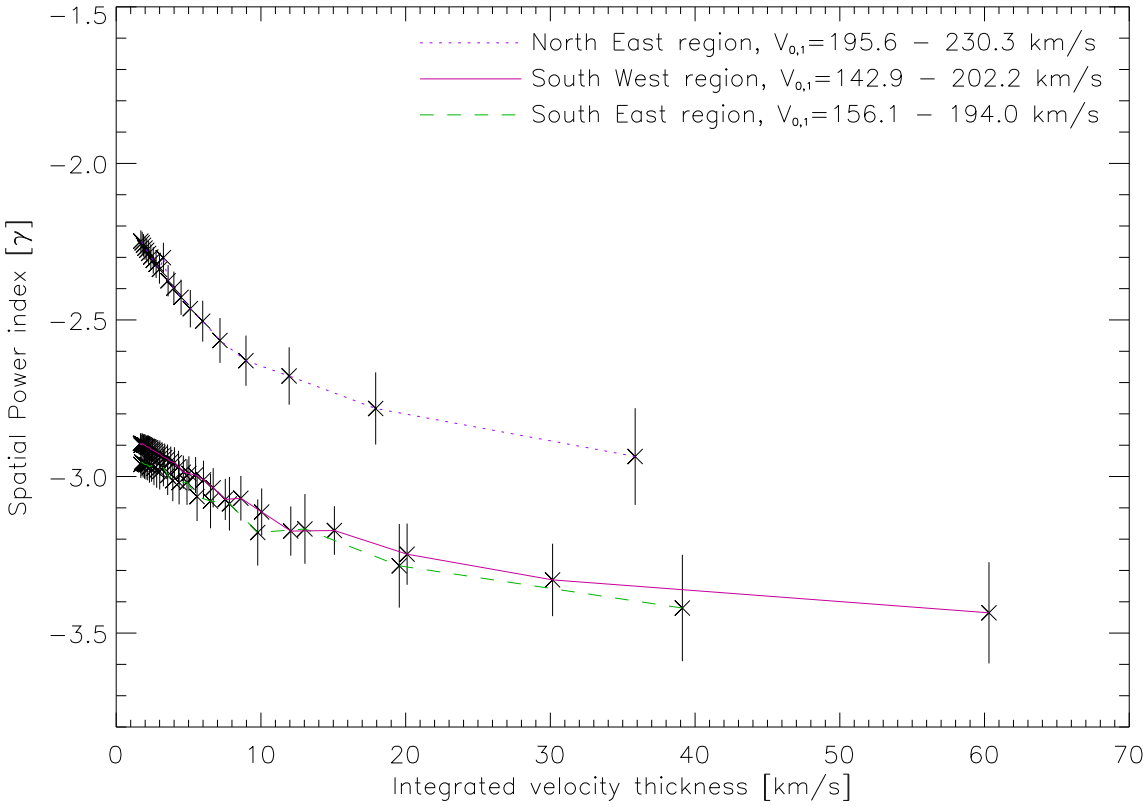

Figure 5.7: Modification to the power index as a result of successively thicker velocity averaging for three of the four subregions shown in Figure 5.3. The power index of the North East region is quite distinct from the southern regions and shows flattening of the power index at higher velocity intervals. The two Southern regions do not convincingly show flattening of the power index across the studied velocity range.

	γ_{Thin}	γ_{Thick}	γ 3-D Velocity
South East	-3.05 ± 0.06	-3.4 ± 0.2	-3.6 ± 0.3
South West	-2.94 ± 0.04	-3.4 ± 0.2	-3.9 ± 0.2
North East	-2.24 ± 0.03	-2.9 ± 0.2	-4.5 ± 0.4

Table 5.2: Spatial power indices for thickest and thinnest velocity slices for the three sampled regions in the Magellanic Bridge (SE,SW and NE regions of Figure 5.3). The degree by which two dimensional velocity fluctuations affect the power index are shown, along with the estimated 3-D velocity index (see Lazarian & Pogosyan, 2000 and also Table 5.1).

velocity index from these results, according to the conditions detailed by Lazarian & Pogosyan (2000) (reproduced in Table 5.1). These values are shown in Table 5.2.

5.1.4.2 Discussion

Figure 5.7 clearly shows a fluctuating velocity component present in all three of the tested regions. The degree to which the velocity fluctuations modify the index appears to be quite similar for the Southern two regions and is markedly different for the Northern region.

The derived power index is as not substantially modified for the southern two regions and we see that the derived three dimensional velocity index for both of these two regions is in agreement within the errors. The power indices show no sign of flattening at the largest velocity intervals and therefore show no indication of a transition between the 'thin' and 'thick' velocity regimes. The velocity fluctuations here are clearly larger than the maximum velocity range used in this study. This is also consistent with results obtained from a similar study on the SMC (Stanimirović & Lazarian 2000).

Table 5.2 shows that the variations for the NW region indicate a three dimensional velocity index of ~-4.5. The derived velocity index is extremely steep and indicates an overwhelming deficiency of high-velocity fluctuations. We see from Figure 5.7 that the power index for this region turns over at $\sim$10 km s^{-1}, which is approximately one third or quarter of the entire velocity interval tested for this region. In this case, we can observe

here the transition between the 'thin' and thick' velocity regimes mentioned by Lazarian & Pogosyan (2000) where the intrinsic velocity dispersion becomes smaller than the width of the velocity integrated window. Once again we see evidence for substantial differences in the structure of the northern and southern parts of the Bridge. The possible three dimensional configuration of these components is discussed with reference to numerical simulations in more detail in Section 6.2.

5.1.5 Probing for structure in the UV plane

Any structure in a dataset which shows a directional preference will manifest as an oblique, elongated artifact in the Fourier transformed image. The elongation will be perpendicular to the direction of the inherent structure in the un-transformed image. It is possible to test for any directional bias of the HI in the Bridge by examining the power as a function of azimuthal angle in more quantitative detail.

Figure 5.8 shows the variation of logarithm of power for the integrated intensity map for each of the four sub regions (see Figure 5.3) as a function of azimuthal angle and across the baseline interval 100-600 λ. This selected baseline range is the same as that used in the analyses of the spatial power index above and corresponds to a spatial scale range of 600-200 pc.

These Figures also show three over-plotted concentric rings. The middle ring indicates the mean log power for the baseline range 100-600 λ, while the inner and outer ring show factors of ten above and below the mean power. For all cases, the power is consistently close to the overall mean value for all azimuthal angles. Therefore these results do not convincingly suggest any azimuthal anisotropy in the Fourier inverted dataset. This contradicts what we might expect from a visual inspection of the dataset, where we see bright filamentary and large-scale HI structure which appear to be aligned in the East-West direction.

It is likely that the dynamic range of any structure in the HI images is insufficient to manifest as features in the Fourier transform: for such a feature to be distinct it is necessary to have a power at least 2–3 orders of magnitude larger than the surrounding structure. This is equivalent to an integrated temperature difference of 10-30 K·km s^{-1}. The apparent East-West structure of Fig. 5.3 shows an integrated brightness range significantly smaller

than this, typically only ∼2–5K·km s^{-1} less than the ambient and less structured HI. In addition, these structures are not particularly well defined, which will dilute the overall effect.

We now turn to a technique which is capable of performing a comparitative analysis using a much smaller spatial sample and with a limited dynamic range.

5.2 Spectral Correlation Function

The SCF is a relatively new technique which attempts to measure the 'similarity' between two spectra in a datacube. The SCF algorithm is such that a perfect match between the two spectra will yield an value of unity and value of zero for no similarity or for an anti-correlation.

The SCF attempts to preserve the information in the third dimension of a datacube. This is desirable, as conventional techniques tend to discard much of the three-dimensional information by compressing the data into a two dimensional display (e.g. moment maps) and as such, only a small fraction of the data can be studied at any one time. An additional advantage of the SCF approach is that it operates directly in the image domain and a Fourier transform is not necessary. This reduces problems arising from the finite sampling and the associated edge effects. However, the noise sensitivity of the SCF as used here forces a compromise to be made in regards to sample area.

The early forms of the technique were used derive an estimate of spectra similarity over a lag range which was defined by the velocity dispersion of the spectra of interest. It was therefore limited to datacubes that were described by a simple, single velocity component. Later modifications to the SCF made by Padoan, Rosolowsky & Goodman (2001), included a parameter which weights the function by the ratio of the RMS of the signal and noise. These modifications improved its ability to handle noise and expanded its use to more complex and multi-component spectra and across any range of spatial lags. Generally, the similarity of the spectra will decrease as a logarithmic function of spatial lag. For a system where a characteristic scale is present, this new application of the SCF will begin to measure a decorrelation at spatial lags greater than that scale.

The new version of the SCF was applied the LMC HI dataset in a study by Padoan

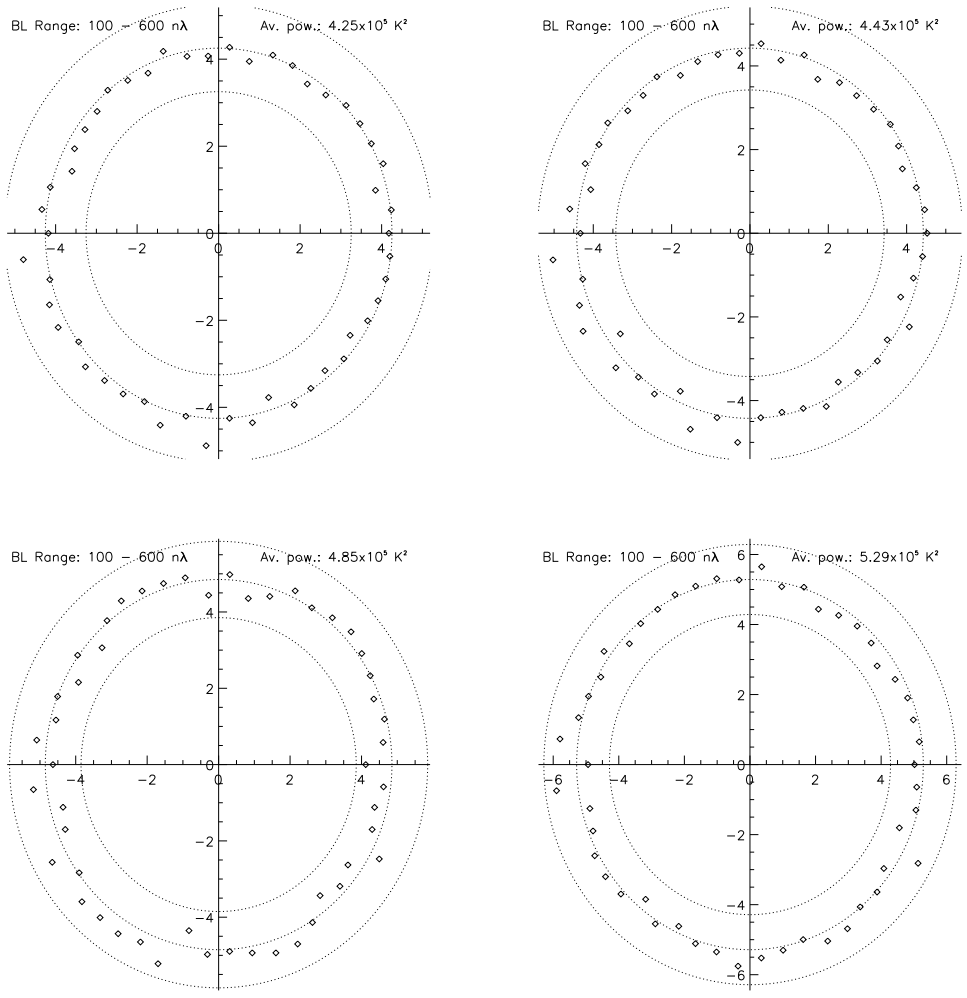

Figure 5.8: The variation of power in the Fourier transform of an integrated intensity map for each of the four regions. The log of Power is shown as a function of azimuthal angle (a log display helps to highlight the larger scale variation and hides the smaller noise fluctuations). The inner and outer dotted circles show factors of ten greater and less than the mean power for this baseline interval (shown as middle dotted circle). We see that there is no convincing indication of coherent structure in the Fourier transformed data for any of the four regions.

et al. (2001). In this study, the SCF showed a decorrelation at approximately 180 pc. Although this value was not in particularly good agreement with earlier Power Spectra analysis on the same data set which suggested a thickness from the disk of approximately 100 pc (Elmegreen, Kim & Staveley-Smith, 2001), the results for the SCF were nonetheless regarded as further evidence for a characteristic thickness of the LMC disk.

A more recent study of the SCF (Padoan, Goodman & Juvela, 2002) has shown that the slope of the SCF is dependent on the velocity dispersion of the spectra under analysis. They suggest that unphysical synthetic stochastic models will show distinct behavior as a function of line width and conclude that the SCF can be used as a test of authenticity of simulated datasets.

We aim here to test the Magellanic Bridge HI dataset using the SCF. The results of this study will be compared to those from the SCF study of the LMC HI dataset and with the results obtained from the study of the Spatial Power spectrum of the previous section.

5.2.1 Calculating the SCF

The algorithm used to calculate the SCF will be the same as that employed in the study of the LMC dataset (Padoan et al. 2001). The SCF algorithm is defined in the following way (Rosolowsky et al.1999; Padoan et al, 2001):

$$S_o(\mathbf{r}, \mathbf{\Delta r}) = \left(\frac{\mathcal{S}_o(\mathbf{r}, \mathbf{\Delta r})}{\mathcal{S}_{o,N}(\mathbf{r})} \right) \tag{5.1}$$

with the numerator being being defined (using a script $\mathcal{S}$) by:

$$\mathcal{S}_o(\mathbf{r}, \mathbf{\Delta r}) = \left(1 - \sqrt{\frac{\sum_v [T(\mathbf{r}, v) - T(\mathbf{r} + \mathbf{\Delta r}, v)]^2}{\sum_v T(\mathbf{r}, v)^2 + \sum_v T(\mathbf{r} + \mathbf{\Delta r}, v)^2}} \right) \tag{5.2}$$

The noise term in the denominator is defined (using a script $\mathcal{S}$) by:

$$\mathcal{S}_{o,N}(\mathbf{r}) = \mathbf{1} - \frac{\mathbf{1}}{\mathbf{Q(r)}} \tag{5.3}$$

where Q($\mathbf{r}$) is the noise 'quality' and is given by:

$$Q(\mathbf{r}) = \frac{1}{R} \sqrt{\sum_v T^2(\mathbf{r}, v)} \tag{5.4}$$

where W=the width of the velocity channels and R is the RMS in signal free parts of the cube.

Rosolowsky et al. (1999) also proposed an adaptation of the SCF which attempts to scale the two spectra which are the subject of the algorithm with a factor s applied to one or other of the spectra: T($\mathbf{r}, v$) or T($\mathbf{r}$+$\Delta\mathbf{r}$,v). The motivation for the adaptation was to create a tool which is sensitive to differences between the overall *shape* of the spectra, rather than between the entire spectra (i.e. irrespective of differences in overall brightness). Although this is of interest, it is not attempted here, since we aim to search for net variations in entire spectra and variations in brightness are an important factor.

We aim to generate 'maps' of the SCF for a number of regions in the HI Magellanic Bridge dataset: $S_o(\mathbf{r},\Delta\mathbf{r})$. We follow the algorithm outlined below:

1. *Dataset Selection.* A region of interest is defined within the datacube. The region has a square cross-section, with a side of N pixels. The SCF is calculated iteratively using every spectrum in this region as the subject spectrum in turn.

2. *Calculate $S_o(\mathbf{r},\Delta\mathbf{r})$ map.* A new larger region of an area of $(2N-1)^2$ is defined with the subject spectrum at the centre. The $S_o(\mathbf{r},\Delta\mathbf{r})$ for each spectrum in this region is calculated relative to the centre subject pixel. This process forms a two dimensional map, where the pixel brightness is proportional to the similarity of each spectrum to that of the centre spectrum. The value for the centre pixel in this SCF map is approximately unity and all other pixel values are <1. This map is stored for later averaging.

3. *Repetition and averaging.* The second step from above is repeated for each pixel in the initial (N^2) region of interest. Ultimately, a total of N^2 $S(\mathbf{r},\Delta\mathbf{r})$ maps are obtained, each having an area of $(2N-1)^2$. The final result is determined by finding the mean for all of the calculated SCF maps: $S(\Delta\mathbf{r})= \langle S_o(\mathbf{r},\Delta\mathbf{r})\rangle$

This approach requires a 'buffer' of spectra, at least N pixels wide around the region of interest. Without the buffer, there is not a uniform sampling population for each pixel of the SCF map and edge effects start to become important.

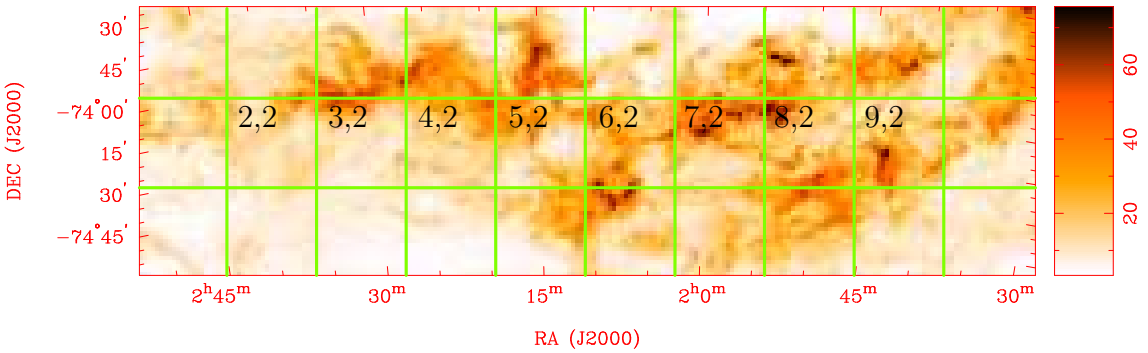

Figure 5.9: Peak pixel map of a subregion of the Magellanic Bridge HI dataset. The overlaid grid shows the 3×3 regions for which the S(Δ**r**) maps are calculated. The centre of each region is marked with the relevant grid reference. Regions on the outer edge constitute the buffer.

5.2.2 SCF data set

In Chapter 3 we mentioned that the beam width of the dataset was approximately 98″. This is equivalent to approximately three pixels and in order to remove any systematic errors arising from sampling spectra which are dependent, only every third pixel in the x and y directions of the original HI dataset is selected.

It would of course be ideal to compare the outcomes of the both the SCF and power spectrum analyses from identical datasets. However, the SCF does not cope well for sets dominated by noise, since this tends to yield spurious values of S(Δ**r**). For this study then, we select a region in the Bridge containing the brightest HI. This region is shown in Figure 5.9 and overlaps with the two southern regions used in the analysis of the power spectrum in the previous section (See Figure 5.3).

The 10×3 grid overlaid on Figure 5.9shows the set for which eight calculations of an S(Δ**r**) map are made. Each small square defines a 21^2 pixel area. The numbering on the Figures shows the grid reference of the centre square region defining the subject spectra (see step one from above). The S_o(**r**,Δ**r**) is calculated for all spectra within each box relative to all spectra within 40 pixels (see step two from above). Overall, we obtain 8 different maps of S_o(Δ**r**) from this dataset.

Position	Total signal $\pm 0.3\times10^5$[K·km s^{-1}]	$S_o(\Delta r)_{N-S}$ $\times10^{-2}$[pc^{-1}]	$S_o(\Delta r)_{E-W}$ $\times10^{-2}$[pc^{-1}]
2,2	8.2	-14.3±0.2	-12.1±0.2
3,2	8.8	-19.6±0.5	-11.2±0.3
4,2	9.9	-15.4±0,7	-14.7±0.7
5,2	11.0	-31 ±1	-19.4±0.3
6,2	12.1	-26.3±0.4	-21.4±0.6
7,2	13.0	-28.4±0.7	-18.5±0.2
8,2	13.6	-28.9±0.7	-21.8±0.7
9,2	12.9	-21.5±0.6	-18.2±0.6

Table 5.3: List of total integrated brightness and S_o slopes in the East-West and North-South directions for each of the eight regions analysed with the SCF.

5.2.3 SCF results

The results for the SCF analysis are shown Figure 5.10. The left column shows the eight integrated intensity maps for the corresponding SCF maps as shown in the centre column.

One of the most striking features in many of the $S(\Delta\mathbf{r})$ maps is the lack of radial symmetry. The easternmost three regions (the first three rows of maps and plots in Figure 5.10) are perhaps the least asymmetrical, though in most cases even here some structure is present.

The study of the SCF for the LMC HI dataset involved azimuthal averaging of the SCF for values at constant spatial lag and composing a line of best fit for $S_o(\Delta\mathbf{r})$. We clearly cannot take the same approach here since we will obscure the apparent directional variation for $S_o(\Delta\mathbf{r})$.

Instead, we isolate the middle 5 rows and middle 5 columns, corresponding to the $S_o(\Delta\mathbf{r})$ in the E-W and N-S directions ($S_o(\Delta\mathbf{r})_{E-W}$ and$S_o(\Delta\mathbf{r})_{N-S}$) . Plots of the mean $S_o(\Delta\mathbf{r})_{E-W}$ and $S_o(\Delta\mathbf{r})_{N-S}$, folded about $\Delta\mathbf{r}$=0 are shown in the rightmost column of Figure 5.10. In every case, we see that the rate of change of the $S(\Delta\mathbf{r})$ is steeper in the N-S direction than that for the E-W direction.

Table 5.3 lists the total integrated HI brightness, the slopes for the $S_o(\Delta\mathbf{r})_{N-S}$ and $S_o(\Delta\mathbf{r})_{E-W}$ fits and the S_o departure scale where appropriate.

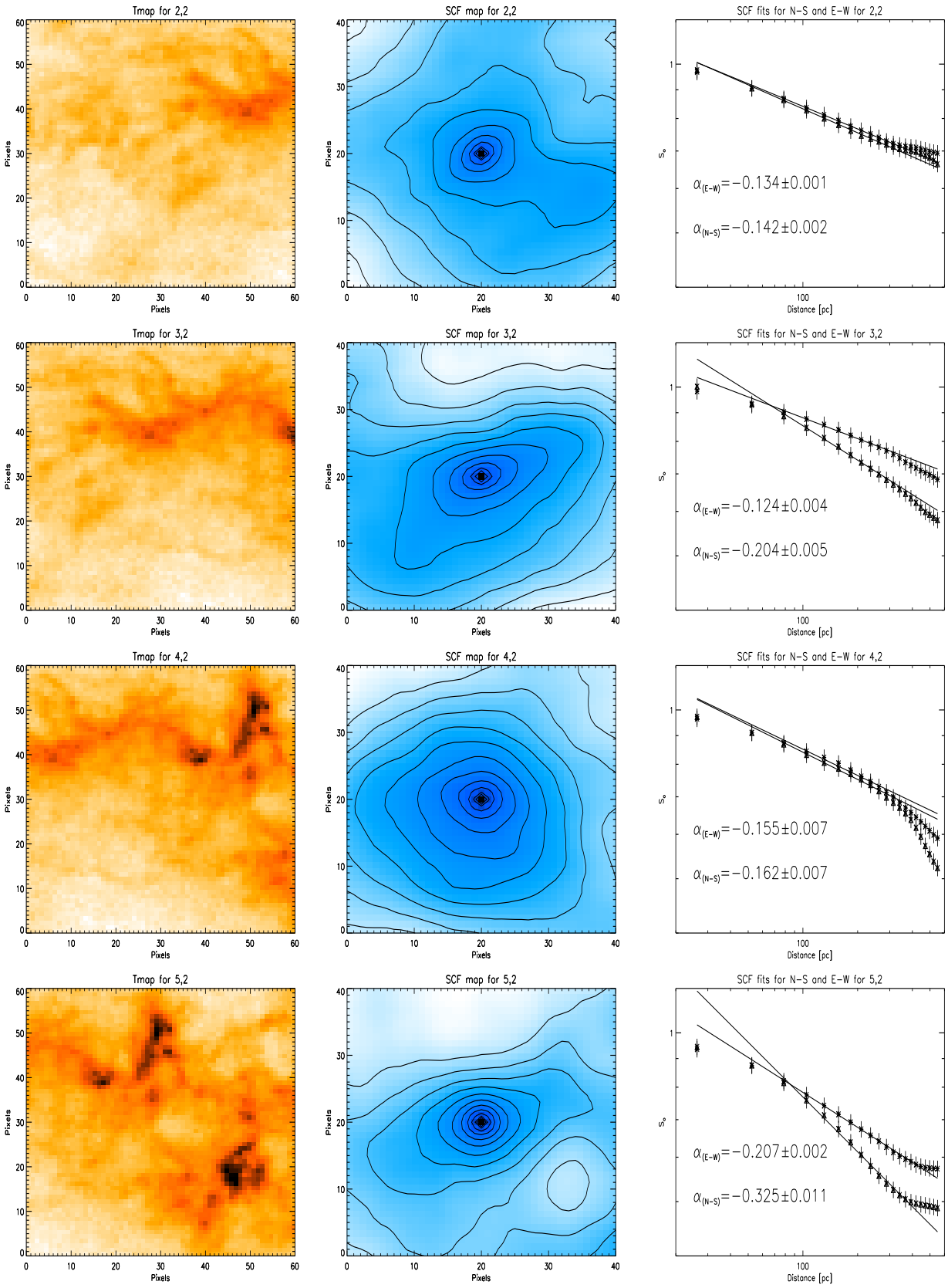

Figure 5.10: Peak temperature maps, and associated $S(\Delta \mathbf{r})_{E-W,N-S}$ maps for Regions 1-4 from Figure 5.9. Greyscale of temperature maps are a linear transfer function from 45 to 700 K. The contours of the SCF begin at S_o=0.4 and are at intervals of 0.05.

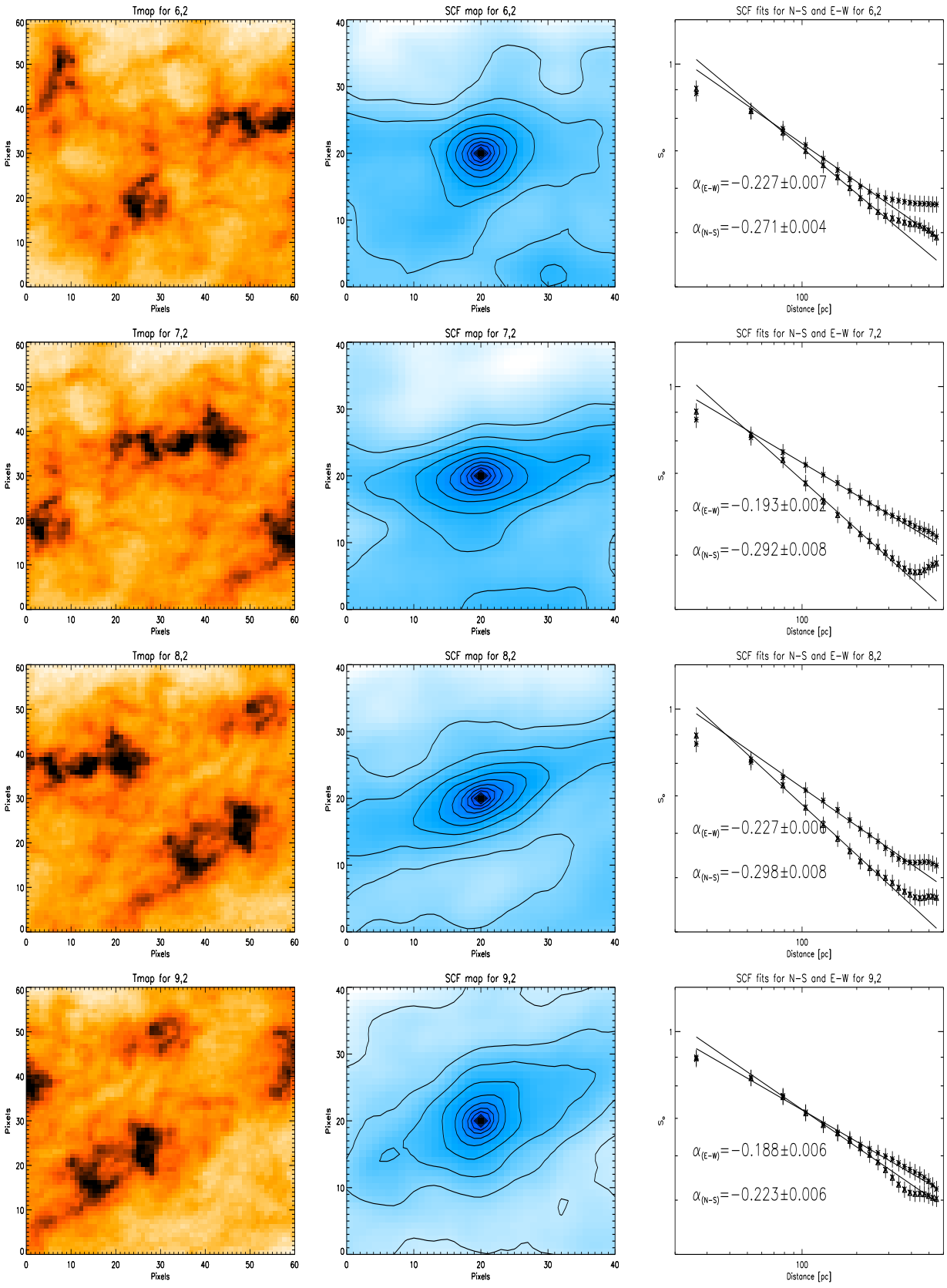

Figure 5.10: *cont.* Peak temperature maps and associated $S(\Delta \mathbf{r})_{E-W,N-S}$ maps for Regions 5-8 from Figure 5.9. Greyscale of temperature maps are a linear transfer function from 45 to 700 K. The contours of the SCF begin at S_o=0.4 and are at intervals of 0.05.

5.2.4 SCF discussion

The lack of radial symmetry in the maps of $S_o(\Delta\mathbf{r})$ is itself an interesting result. The obvious extension in roughly the East-West direction indicates a more persistent similarity of spectra along that line. The SCF is unique in that it probes the entire spectrum in the third (velocity) dimension. What we see here is that the rate of change of the entire *spectra* (rather than a single velocity channel, or integrated brightness) across the entire sampled velocity range is more gradual in the East-West direction than in the North-south direction.

We interpret the East-West $S_o(\Delta\mathrm{r})$ structure as a result of the tidal stretching imposed by the LMC-SMC interaction although in this case the morphology of the HI is already visually suggestive of this process. We should also bear in mind that the brightest parts of the dataset may be dominating the SCF results, and biasing the structure of the SCF maps.

Most of these plots in the rightmost column of Figure 5.10 for $S_o(\Delta\mathbf{r})_{E-W}$ and $S_o(\Delta\mathbf{r})_{N-S}$ show a departure from a the fit at approximately 200-400 pc. The scale at which the departure occurs is not particularly consistent for each sample. We also see that the departure occurs at scales which are the limit of the tested areas (i.e. $\sim$500 pc). As such, the observed departure at this scales should therefore be regarded with caution.

5.3 Summary of the Power Spectrum and SCF

We have attempted two comparable analyses of the HI filamentary component of the Magellanic Bridge.

By studying the power spectrum of the HI in the Magellanic Bridge, we have found that the morphology and kinematical structure of HI in the Magellanic Bridge is extremely diverse and appears to be separated into a bright, turbulent region and a tenuous, more quiescent region. The more turbulent region is found at a lower velocity range and at a lower declination. The minimum derived indices of the power spectra from the brightest regions of the Bridge is ~ -3. The power spectra here are featureless and can be fit with a single powerlaw. This is a result similar to that from power spectrum analyses of the adjacent SMC (Staveley-Smith et al. 1998; Stanimirović et al. 1999a; Stanimirović et al.

1999b; Stanimirović & Lazarian, 2001). The similarity of the Bridge power spectra with that of the SMC lends further support for the SMC origin of this part of the Bridge.

The more tenuous and higher velocity parts do not show power index similar to the lower velocity regions or the SMC. Power spectra from this part of the Bridge show evidence for a very steep three dimensional velocity index and a lack of rapid velocity fluctuations. This is consistent with the smooth visual appearance of this region and is indicative of relatively quiescent gas.

A study of the azimuthal isotropy of the Fourier transform of the HI dataset does not show any such East-West structure due to the insufficient dynamic range afforded by that technique. It appears then that the SCF is more successful in detecting structure trends over a smaller dynamic range.

The analysis using the SCF has shown more quantitatively the effects of tidal stretching on this dataset. Limitations of the application of the SCF confined the region sampled to the brightest parts of the Magellanic Bridge, although it has confirmed that the observed HI spectra in this region vary more slowly along the approximate direction of the tidal stretching.

The SCF also shows a suggestion for a characteristic scale length, which is not observed in the power spectra for the same region. The departure is at the limits of the sampled scale range and any interpretation should be made carefully.

Chapter 6

Large-scale features

"Maybe blowing this part of the universe all to hell will make me feel better.."-
Bender, 2001

In Chapter 4 a detailed analysis was made of the apparent HI expanding shell population. In Chapter 5 a statistical analysis of the spatial and velocity structure of the HI of the Bridge was presented. These statistical methods use large population samples in an attempt to extract any underlying trends. However such studies also obscure any features which deviate from the characteristics of the general population. As is the case for the small scale structure, the large scale structure of the HI in the Magellanic Bridge is unique, complex and involved. A dedicated study of some large scale aspects of the HI in the Bridge is presented here.

In Chapter 3, a brief mention was made of various large scale features in the Bridge which offer evidence for episodes of extremely large energy deposition events:

1) At more northern declinations ($\lesssim -73$), part of the HI mass in the Bridge appears to be offset to higher velocities relative the brighter parts of the Bridge.

2) The brightest part of the HI appears to be bifurcated in velocity. This bifurcated region extends into the SMC and along much of the length of the Bridge.

3) A large, rim-brightened and roughly elliptical filament loop is found off the north eastern edge of the SMC. The loop encompasses a region of relatively low HI column density and is found only in the higher velocity parts of the dataset.

In this Chapter we will attempt to parameterize and understand the formation mechanisms for these three large-scale features of the Bridge: Section 6.1 discusses the methodology and outcomes of a Gaussian decomposition of HI spectra in the Bridge. Section 6.2 will present a discussion of the structure of the velocity discontinuity. A comparison of the morphology of the HI in the Bridge with existing N-Body numerical simulations of the Magellanic System will also be presented in this Section. The origin of the velocity bifurcation will be discussed in Section 6.3 and various evolution mechanisms which may be responsible for creating the large HI loop will be discussed in Section 6.4. A summary of observations and conclusions is made in Section 6.5

6.1 Gaussian Decomposition for HI spectra

HI line profiles in the Magellanic Clouds have been found to be typically rather simple. The LMC HI profiles can be described using only one Gaussian component (Luks & Rohlfs, 1992), while the SMC morphology is more readily described using two components (Stanimirović, 1999).

Apart from the initial surveys of HI in the Magellanic Bridge by Kerr, Hindman & Robinson (1954) and by Hindman, Kerr & McGee (1963), the most comprehensive HI profile analysis across the entire length of the Bridge was completed by McGee & Newton (1986). The study by McGee & Newton (1986) analysed HI spectra collected from 217 pointings with the Parkes 64 m Telescope. A Gaussian decomposition was attempted for each spectrum and it was found that most HI spectra in the Bridge could be described using five or more Gaussian components and a few could be decomposed into as few as three components. By considering profiles on the basis of position within the Bridge, this study found that the components could be assembled into ten different velocity groups. However, the authors showed that after adjusting for the gradient in heliocentric velocity, the profiles could be grouped more properly into eight distinct velocity regimes. Although the study by McGee & Newton (1986) did not make any conclusions about the general morphology of the Magellanic Bridge in relation to those of the Magellanic Clouds, this study shows that general properties of the large scale flow can be interpreted from an analysis of a Gaussian decomposition.

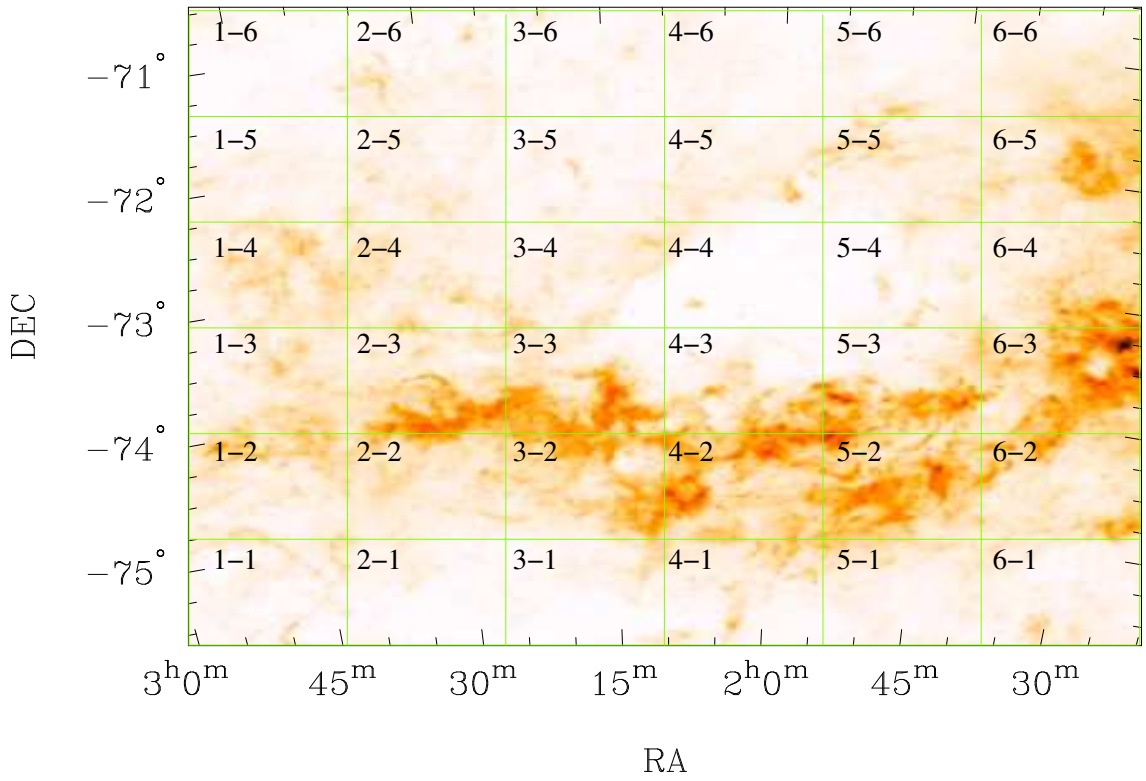

Figure 6.1: Peak pixel map of HI region observed according to Chapter 3. The grid shows the regions for which average spectra were calculated. Sub-regions are indexed so that the south-east (*bottom left*) is 1-1, increasing to the west and to the north as shown. The mean spectra for each region are shown in Figure 6.2

6.1.1 Preparation of the dataset

Without reproducing the analysis by McGee & Newton (1986), this Chapter will attempt a similar Gaussian decomposition approach using the current HI dataset (see Chapter 3). This set encompasses a much smaller field of view than that used in the study by McGee & Newton (1986) and for the sake of simplicity, the spectral datacube has been binned up into a 6×6 grid. Figure 6.1 shows the peak pixel map of the observed HI of the Magellanic Bridge with a grid overlaid. The grid shows the regions over which the spectra have been block averaged to yield a set of 36 spectra. In the following, each block will be referred to as *sub-region n-m* where n is the position along the East-West direction, *n=1* being the eastern-most column and *m=1* being the southernmost row. Thus, 1-1 refers to the bottom-left square shown in Figure 6.1.

Gaussian fits are attempted for each of the block-averaged spectra from Figure 6.1. The ORIGIN 7 software package is used for the Gaussian fitting. As any spectra can be composed of an infinite number of Gaussian fitting schemes, the appropriate scheme was

selected so that the number of Gaussian components is minimised while keeping the χ^2 is as close to 1 as possible. From Chapter 5 we know that there is a tendency for the spectra to preserve a similarity in the E-W direction. As such, further discrimination between viable alternative fitting schemes was based on the decomposition alternatives for spectra in the east or west direction.

6.1.2 Gaussian fitting results

Figure 6.2 show each of the spectra, overlaid with the associated Gaussian fits. Tables 6.4-6.9 at the end of this Chapter list the central velocities, widths and amplitudes for the fitted Gaussian schemes for each sub-region 1-1 to 6-6.

The simplest fitting scheme for any of the Magellanic Bridge spectra here use only three components (e.g. subregion 1-5). The most complex can be reproduced from six components (e.g. sub-region 4-3). This is similar to the findings by McGee & Newton (1986), who have found increasing complexity for spectra associated with high column density and have derived fitting schemes from up to seven components. We make no comparison of the relative number of complex components here with the study by McGee & Newton (1986), since this is entirely dependent on the number and spatial distribution of the profiles examined.

Figure 6.3 shows plots of the centroids of the fitted components as a function of Right Ascension in both the heliocentric and Galactic standard of rest velocity frames. Each East-West row (See Figure 6.1) occupies a new plot. In an attempt to understand some continuity of the velocity components from East to West, plotted also on these Figures are lines joining the centroids of the components. The lines are coloured in an attempt to highlight the evolution of the components in declination (low velocity = blue, high velocity = red). The most plausible continuity between velocity centroids were selected after considering the velocities, widths and areas of the Gaussian components for each sub-region. Lines which converge onto a single point indicate merging (or splitting) of components between sub-regions.

A few interesting features are worth noting from the Gaussian fitting results:

- We can see that row 3 contains the most complex spectra, which were fit with 4 to 6 components. This row corresponds to the region of highest HI column density in

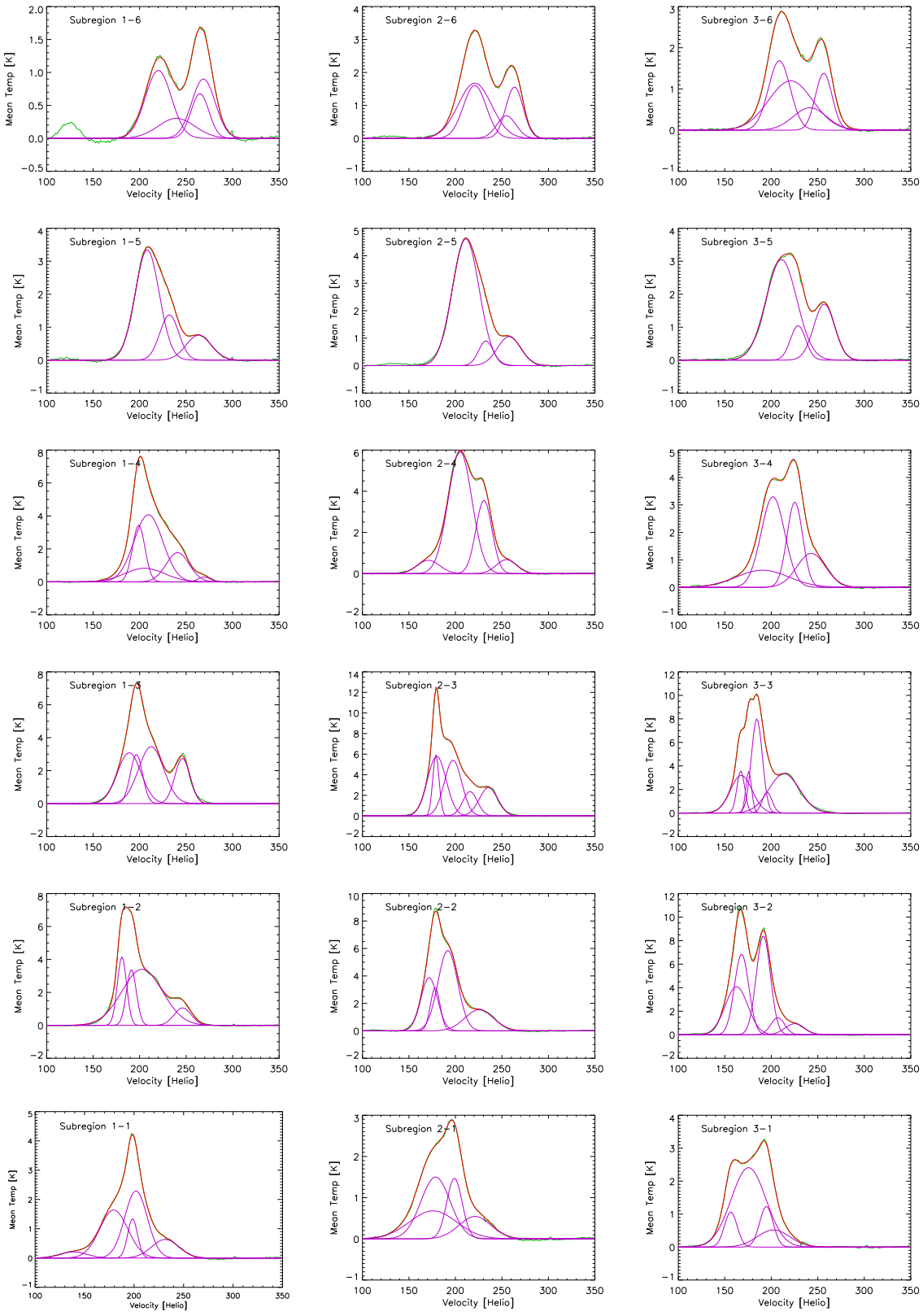

Figure 6.2: Mean spectra for sub-regions 1-1 to 3-6 (from Fig 6.1) (*green*). Each plot also shows fitted Gaussian components (*purple*). The plot of the sum of the fitted components is overplotted (*red*) (this typically obscures the green line). The fitting is determined with ORIGIN 7 software.

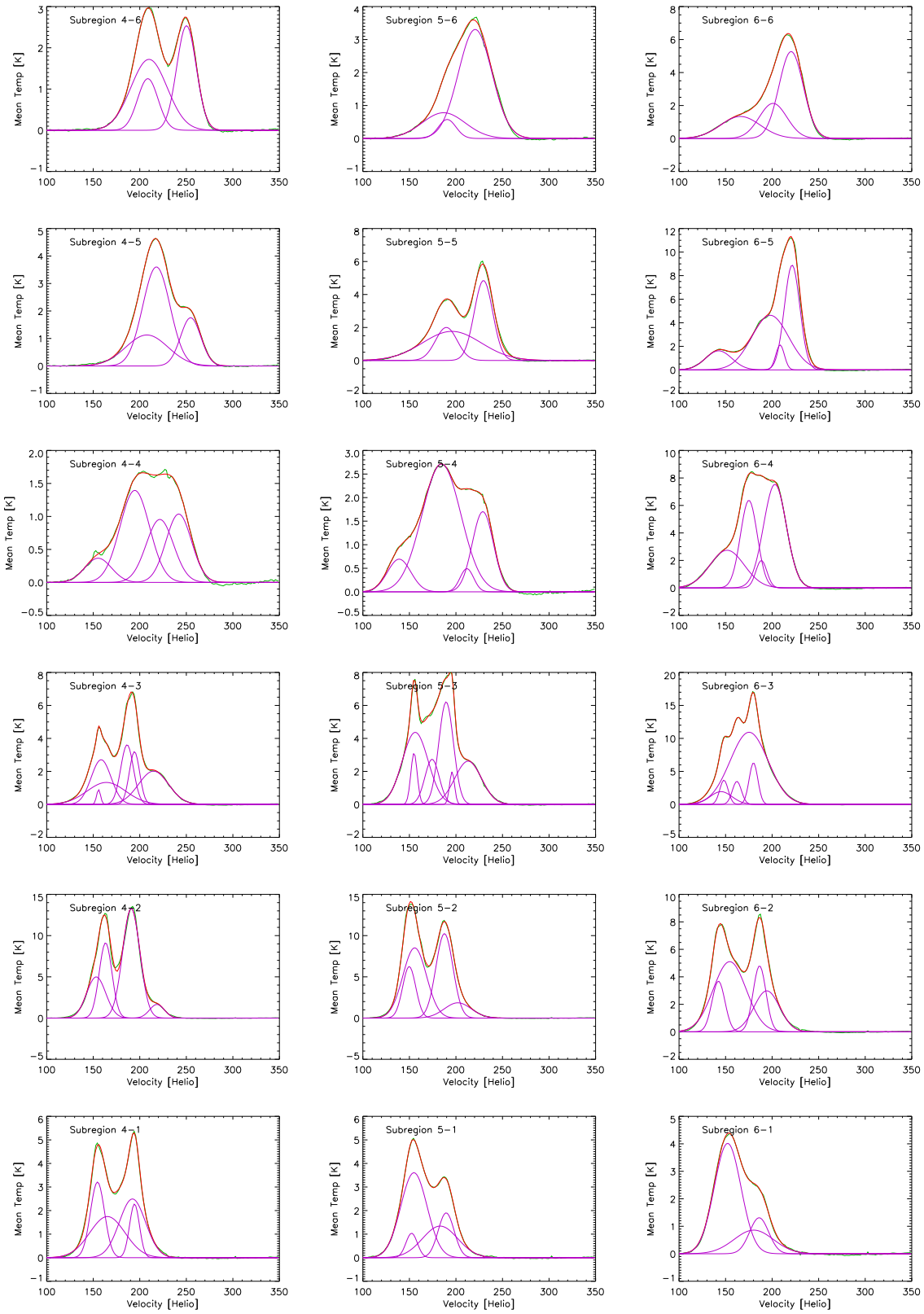

Figure 6.2: *Cont.* Mean spectra for sub-regions 4-1 to 6-6 (from Fig 6.1) (*green*). Each plot also shows fitted Gaussian components (*purple*). The plot of the sum of the fitted components is overplotted (*red*) (this typically obscures the green line). The fitting is determined with ORIGIN 7 software. Regions 3-1 to 7-3 show the velocity bifurcated area. we see the shift in velocity of the dominant component for the norther three regions.

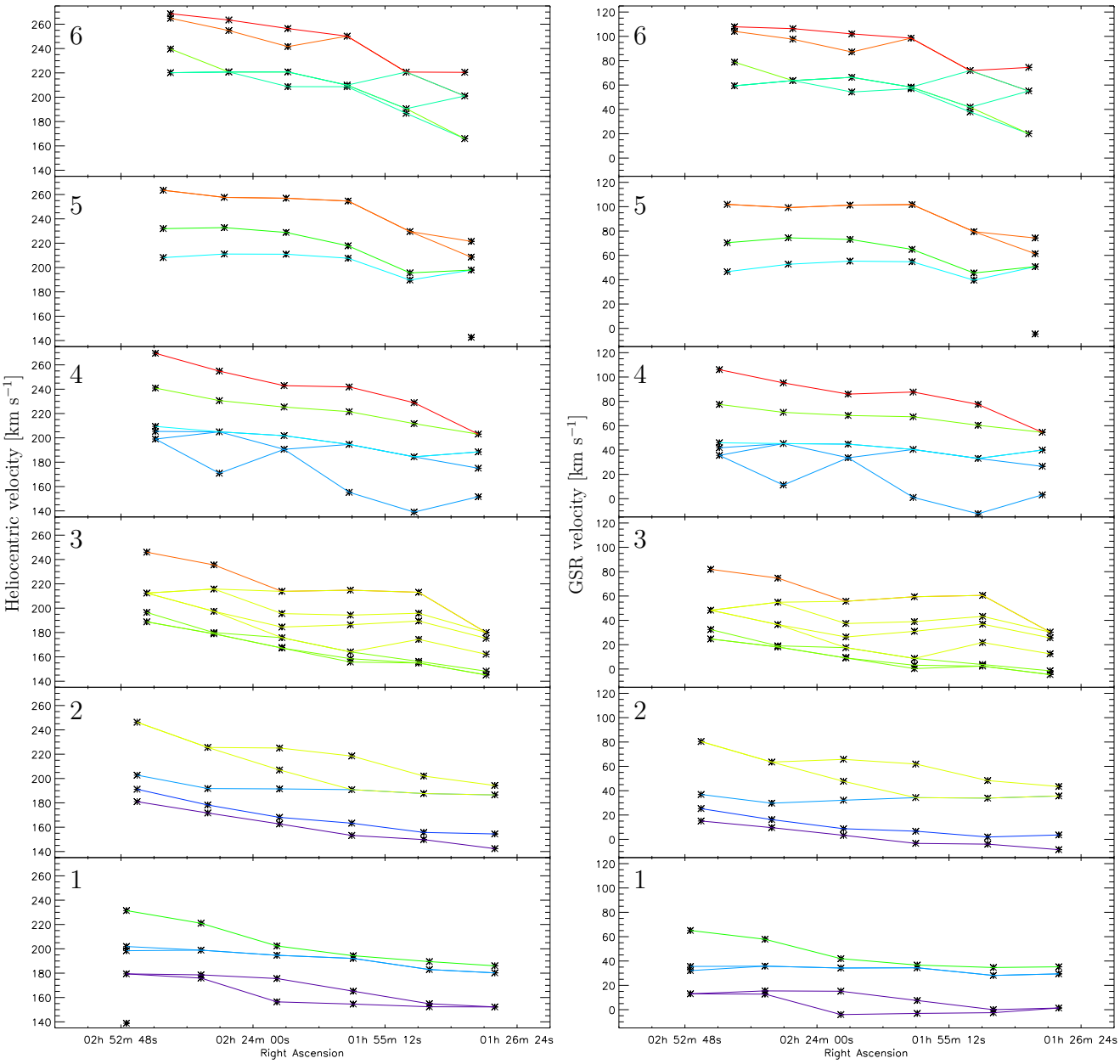

Figure 6.3: Velocity of centroids of Gaussian components for each sub-region in rows (*rows 1-6 are bottom to top*), plotted as a function of Right Ascension and both Heliocentric velocity (*left*) and Galactic Standard of Rest (*right*). The overplotted lines show a suggested evolution of the components in the RA direction. The velocity bifurcation is clear in the plots for rows 1 and 2. The HI shell and velocity shifted component can be seen as higher velocity components, shown in plots for rows 5 and 6. The colour scheme is arbitrary and highlights the shift of the components to higher velocities in the northern rows.

the Bridge. We might expect a higher number of components in the more turbulent HI region within this row.

- As noted previously, the HI profiles for the southwest of the Bridge (subregions $m>3$, $n<3$) show evidence for a bimodality. This is a dominant feature of the Bridge and will be discussed further in section 6.3.

- The velocity centroids make a sudden and significant shift to higher velocities for rows 5 and 6. The velocity shift is discussed in section 6.2.

- Despite the adjustment for GSR, some residual velocity gradient of increasing GSR with RA remains. The relative excess radial velocity amounts to approximately $4\times10^{-}3$ km s^{-1} per parsec and is likely to be a result of the ellipticity of orbit the Magellanic System around the Galaxy (See Gardiner, Sawa & Fujimoto, 1994; Gardiner & Noguchi, 1996). The elipticity causes a difference in the projected radial velocities as seen here.

In general, although it appears that the more westerly profiles of the Bridge require a more complex arrangement of Gaussian components, for the most part the HI spectra appear to be basically bimodal. The profiles of the body of the SMC are similarly bimodal (e.g. Mcgee & Newton, 1986; Stanimirović 1999). This similarity of structure seen in the Bridge and the SMC supports a scenario where this part of the Bridge is tidally extracted from the SMC.

The remainder of this chapter will focus on an investigation of the velocity features highlighted by the Gaussian analysis.

6.2 Velocity discontinuity

As already mentioned in Chapter 3 and 5, HI in the northern part of the Bridge is offset in velocity from the rest of the Bridge by $\sim$40 km s^{-1} (see Figure 3.9b). A shift in the centroids of the fitted Gaussian components is also apparent in the northern spectra shown in Figure 6.2. In this section, we attempt to identify where this clearly discontinuous region fits into the overall morphology of the Bridge. Figure 3.9b is reproduced here in Figure 6.4 for convenient reference.

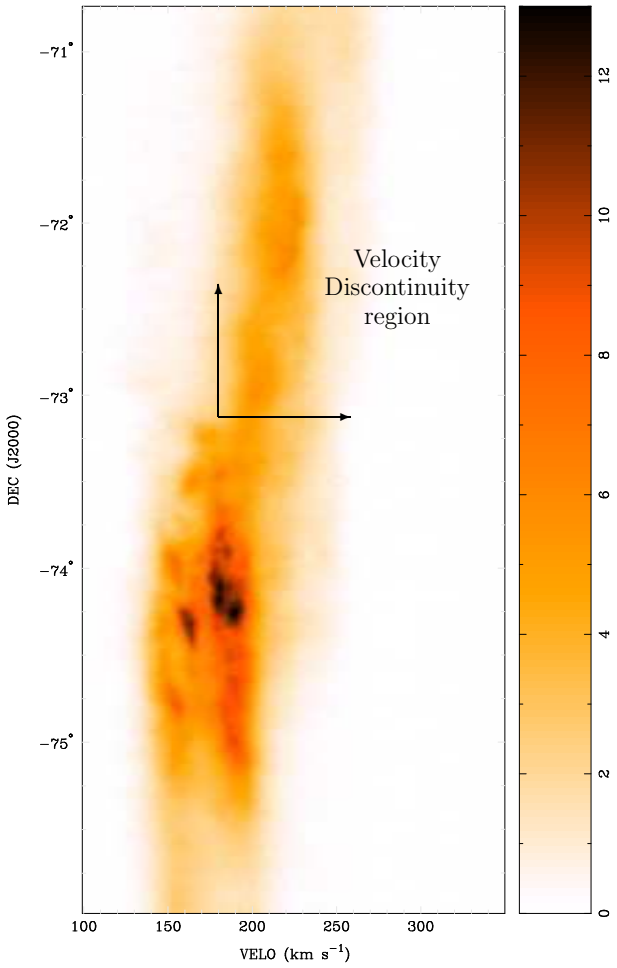

Figure 6.4: Duplicate of the integrated intensity map of Figure 3.9b, the units are K·km s^{-1}. This Figure shows the integrated HI intensity for the Velocity-Declination projection of the HI dataset presented in Chapter 3. Note that the declination scaling is correct only at the centre RA of the dataset, at $2^{\rm h}\,08^{\rm m}\,7.6^{\rm s}$. The discontinuity in the mean velocity of the HI mass is shown here at declinations $< -73^\circ\,13'$.

From Figure 6.4 we see that the velocity discontinuity begins between 190-200 km s^{-1}. The northern HI is unimodal in velocity and has a FWHM of approximately 40 km s^{-1}. The HI in this region appears much more tenuous and homogenous than that in the southern part: there is no obvious bright HI filamentary or clumpy morphology present. The velocity offset for the high velocity component, relative to the centre velocity of the rest of this part of the Bridge is approximately $\sim$40 km s^{-1}.

The origin of the high velocity component is unclear from Figure 6.4 alone. It is helpful in this case to use larger scale and lower spatial resolution maps to understand how this high velocity component fits into the overall structure of the Bridge. Figure 6.5 shows position-position maps for a range of velocity intervals from an HI dataset of the Magellanic region collected during the Parkes Multibeam survey conducted by Brüns (2003).

The dataset shown in Figure 6.5 has been re-averaged into 23 km s^{-1} wide intervals. The first four velocity channels (120-189 km s^{-1}) shown in this Figure are dominated by the highest density parts of the western Bridge and the eastern part of the SMC. Above 189 km s^{-1} we see the first indications of the higher velocity, tenuous HI link between the SMC and the LMC. The link is contiguous at 212 km s^{-1}. At 235 km s^{-1} we see no remnants from the brightest parts of the Bridge which were so dominant at lower velocities. We see also in this Figure that the higher velocity tenuous part is shifted slightly to more northern declinations than the brighter, turbulent part.

The top panel of Figure 6.6 shows a peak intensity map of the RA-velocity projection of the same Multibeam HI datacube shown in Figure 6.5. Prior to the creation of this map, the dataset was re-gridded to force the lines of constant Right Ascension to be parallel. In this Figure, we can see the SMC and the LMC as the bright HI regions in the left and right of the Figure. We again see that much of the HI in the Magellanic Bridge is quite faint and tenuous. The brightest parts appear as an extension of the SMC. Also in this Figure we see a second 'spur' in HI which extends from the SMC at higher velocities.

The observed HI structure of the Bridge, as described above, has good similarities with the results of N-Body numerical simulations of the Magellanic system by Gardiner, Sawa & Fujimoto (1994). We reproduce their Figure 12 here in the bottom panel of Figure 6.6. In this Figure, the SMC (assumed position at RA $00^{h}\,52^{m}\,49^{s}$, Dec. $-72^{\circ}\,49'40''$, J2000) is at θ_B=0°, while the LMC (assumed position at RA $5^{h}\,23^{m}\,34^{s}$, Dec. $-69^{\circ}\,45'5''$, J2000) is at 23°. For these simulations, self-gravitation of the particles is negligible and cloud-

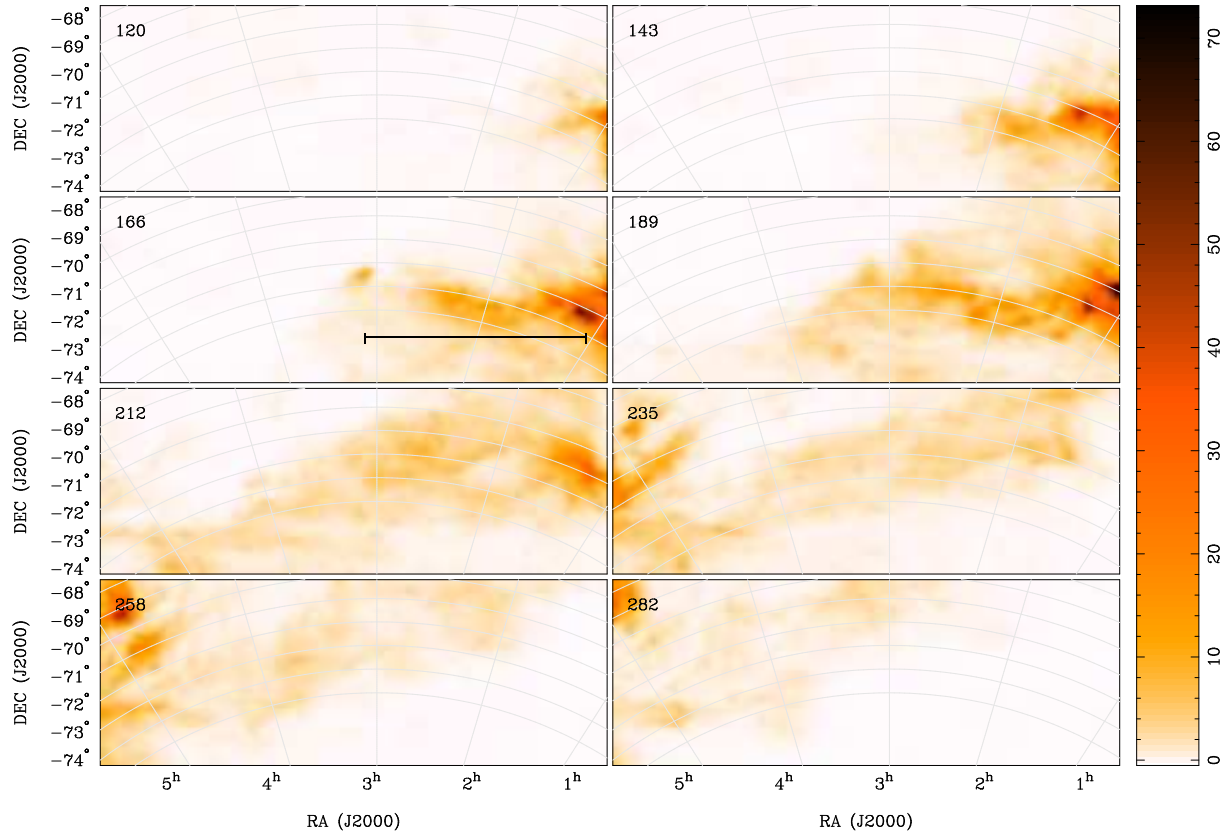

Figure 6.5: Velocity averaged channel maps for the Intercloud region observed with the Parkes telescope and Multibeam system (Brüns 2003). These maps have been averaged over 28 channels ($\sim$23.0 km s^{-1}). The heliocentric velocity of the centre of the averaged range is shown in the top left of each panel. The units are scaled with a square root transfer function, with units in K. The black line overplotted in the 166 km s^{-1} velocity range indicates the cut made to produce Figure 6.9.

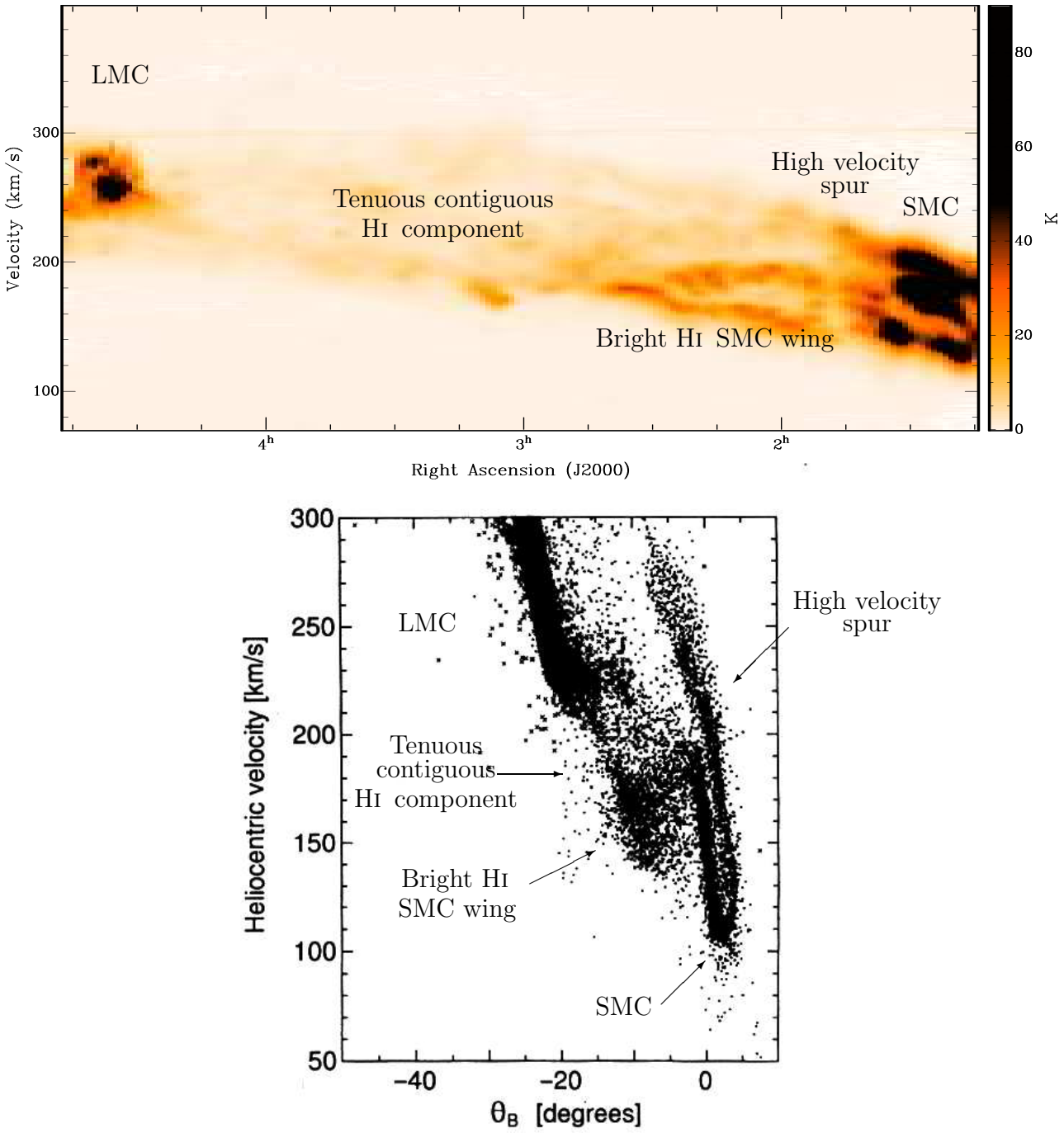

Figure 6.6: *Top:* Re-gridded peak pixel map of entire Bridge, taken with the Multibeam receiver (Brüns 2003). The line at ∼300 km s^{-1} is interference. The SMC and LMC are visible as marked and we see that the Bridge is dominated by relatively tenuous HI. The brighter part of HI in the Bridge at low velocities appears contiguous with the SMC. *Bottom:*Results of an N-Body numerical simulation of the Magellanic System by Gardiner, Sawa & Noguchi (1994). The x-axis is RA and although severely compressed relative to the top plot, we see a general correlation of the positions and velocities of the simulated particles to the observed HI distribution. Note also that the top and bottom panels do not span the same Right Ascension range.

collisions are not considered. The SMC has a spiral morphology and the SMC/LMC mass ratio is 1/10. The Galaxy halo is assumed to extend past the Magellanic Clouds to 100 kpc. We see that in particular, the bright part of the Bridge, the tenuous inter-cloud region and the high velocity spur are all well reproduced in the simulations.

Figure 6.7 is a reproduction of Figure 11 from Gardiner, Sawa & Noguchi (1994). This Figure shows the position vs radial distance for the N-Body simulation results conducted by these authors. In this Figure, we see that the nearer arm of the SMC appears to be much more important in the intercloud region than is the more distant arm. Figures 6.6 and 6.7 together indicate that the nearer arm of the SMC forms the higher velocity, more turbulent part of the Bridge, while the more distant arm forms the more tenuous high velocity spur and velocity offset region seen in Figure 6.4.

We are now in a position to follow up findings made from analyses in past Chapters. We have found from Chapter 4 that the higher velocity component of the Bridge appears to be relatively deficient in an expanding HI shell population. We also know from Chapter 5 that the high velocity part is relatively quiescent and homogenous with slow velocity fluctuations and a steep spatial power index. Assuming the simulations accurately reflect the actual distribution of the HI in the SMC, we might now ask why one arm is apparently so morphologically different to the other. A viable explanation may be that the nearer arm is much more involved in the tidal perturbations generated by the SMC and LMC interaction. This interaction would be responsible for injecting energy across a wide range of scales and triggering new episodes of star formation. The distant arm however, is much more isolated from the tidal event and as a result, it is much less turbulent.

In the absence of both distance and position information, the Bridge has typically been treated as a single, contiguous feature. The simulations by Gardiner, Sawa & Fujimoto (1994), confirmed here by real observations, show that this is no longer an appropriate interpretation.

6.3 Bifurcation

A Bimodal distribution of the velocity profiles of the Magellanic Bridge has already been noted in Chapter 3 and in the Gaussian component analysis at the beginning of this Chapter. Figures 3.8b and 6.3 show that the bimodality appears to extend in RA from

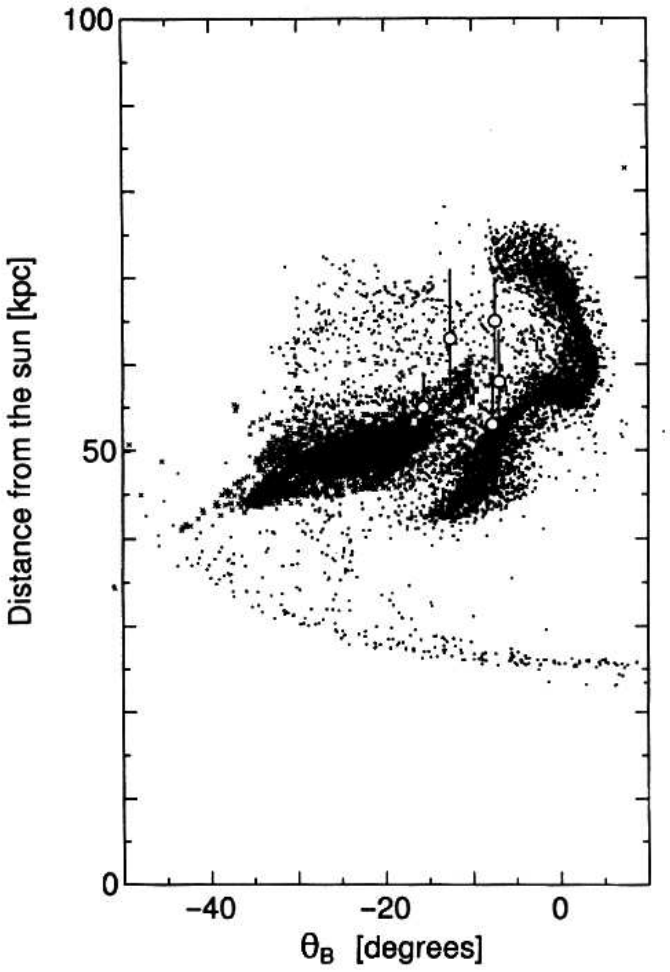

Figure 6.7: Reproduction of Figure 11 from Gardiner, Sawa & Fujimoto (1994). This Figure shows the position vs distance projection of the N-Body simulations of the Magellanic System. We see that the near arm of the SMC forms the actual SMC-LMC link, while the distant arm is much less involved. The open circles shown in the Figure indicate the distances of OB associations as measured by Grondin et al. (1992).

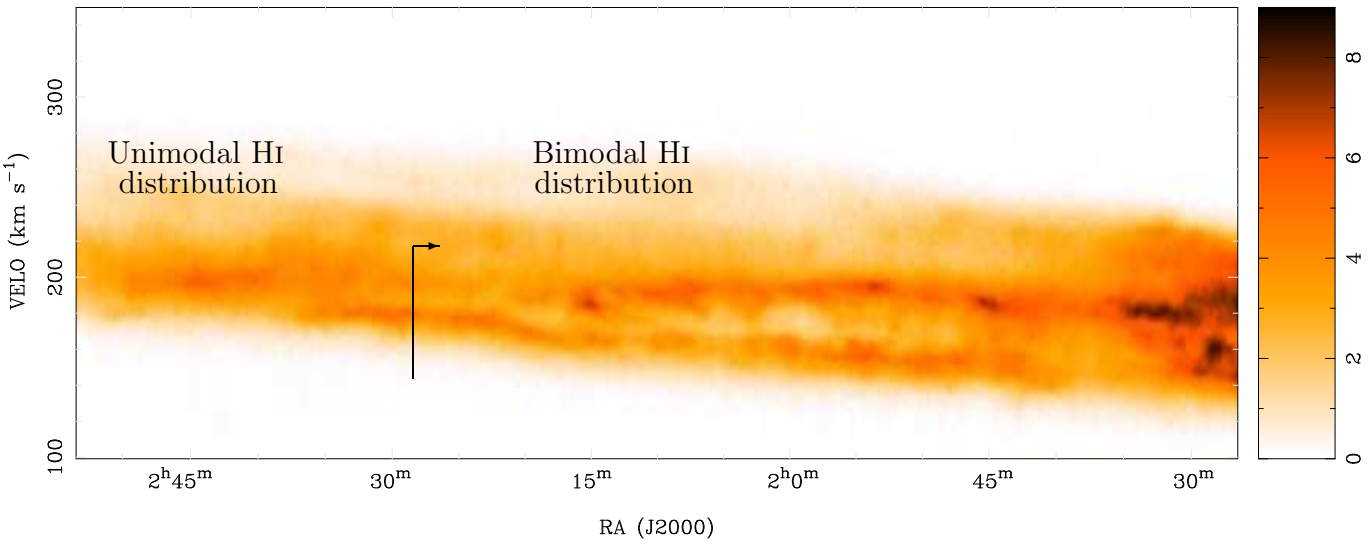

Figure 6.8: Duplicate of integrated intensity map of Figure 3.8b, the units are in K·km s^{-1}. This Figure shows the integrated HI intensity for the RA-Velocity projection of the ATCA and Parkes surveyed area (see Chapter 3).

the SMC to approximately $2^h\,20^m$, where it suddenly converges to a unimodal profile, Figure 3.8b is reproduced here in Figure 6.8 for more convenient reference. From the Velocity-Declination projection shown in Figure 6.4, we can see that the bimodality continues in the southward direction through low HI column densities. A reference to the plots of numerical simulation results by Gardiner, Sawa & Fujimoto (1994) shown in Figure 6.6 do not show evidence for a velocity bifurcation as seen here. This suggests that this feature is not formed by gravitational forces.

The two components of the bimodality occupy similar extent in declination and right ascension and appear as parallel sheets or filaments in the position-position-velocity dataset. If we choose a region for which the filaments appear to be easily separable in velocity: RA $2^h\,21^m\,4''$- $1^h\,37^m\,0^s$, Dec. $-73°\,28'17''$- $-75°\,32'33''$ (J2000), we can calculate a mass for the low and high velocity components of 4.3×10^7 and 3.8×10^7 solar masses respectively. These sheets are moving apart from each other at $\sim$30 km s^{-1} (see Chapter 3) and we can estimate a total energy necessary to generate the bifurcation for the selected part of the Bridge with $\frac{1}{2}\sum MV^2$ as 9×10^{52} erg, yielding approximately $\sim2\times10^{52}$ erg/degree^2. This equivalent to the energy output from $\sim$100 supernovae events per 1×10^6 pc^2. In fact, given the density of O and B type stars in the Bridge, this is not an unreasonable density distribution. However, to form the observed structure, all supernovae events along the

$\sim$2.6 kpc of the bifurcated area would have to be roughly correlated in time and velocity. Given the large areas over which the correlation must occur, this is clearly an unreasonable demand. We must look for alternative scenarios to explain the formation for the observed HI velocity bifurcation.

Again, we refer to the wide-view, lower resolution dataset (Brüns, 2003) to study the scenario in a larger scale context. Figure 6.9 shows a cut in declination of this Multibeam HI dataset. The direction and position of the cut is shown as a black line in Figure 6.5. We can see from the Figure that the bimodality is continuous into the SMC, indicating that the bimodality in fact originates from there. Shown also on Figure 6.9 are profiles at the Right Ascensions indicated by the vertical lines. We see that within the SMC at $1^{\rm h}\,05'15''$, the velocity separation of the two peaks is 49 km s^{-1}. At $1^{\rm h}\,17'40''$, the interface of the Bridge and SMC, the separation is approximately 42 km s^{-1}. At $1^{\rm h}\,43'29''$, the peak separation is 33 km s^{-1}. Just before the termination of the bimodality at $1^{\rm h}\,8'21''$, the velocity separation of the two peaks is 26 km s^{-1}. Clearly the separation of the peaks is not constant along the length of the Bridge, although it varies slowly until its sudden termination at $\sim 2^{\rm h}\,15^{\rm m}$. Overall, these observations suggest that the progenitor of this feature existed in the SMC *before* the tidal extraction process began and was drawn into the Bridge during its formation. Numerical simulations indicate that the Bridge began forming approximately 200 Myr ago (e.g. Gardiner & Noguchi, 1996). The energy estimate made above probably greatly underestimates the total energy deposited in this shell-like feature, since the extension into the SMC was not incorporated into the calculations of the total mass.

The feature in the SMC from which the bimodal arrangement arises was interpreted by Hindman (1967) as a single HI shell (SMC 1) and was later interpreted by Staveley-Smith et al. (1997) as a conglomeration of smaller expanding shells: SMC HI-498,SMC HI-495 and SMC HI-499. Table 6.1 shows the expansion velocity and predicted ages for these shells. We see that the ages for all of these shells are $\lesssim$15 Myr. There is obviously considerable discrepancy between the estimated ages of the shells from the survey by Staveley-Smith et al. (1997) and the supposed formation age of the Bridge. This is a difficult contradiction to reconcile. A tidal perturbation however, may distort the local medium in such a way that fundamental assumptions involved in the shell-expansion model by Weaver et al. (1977) become invalid. For example, a tidal perturbation would permit a shell to expand more easily in the direction of the influence, which would lead

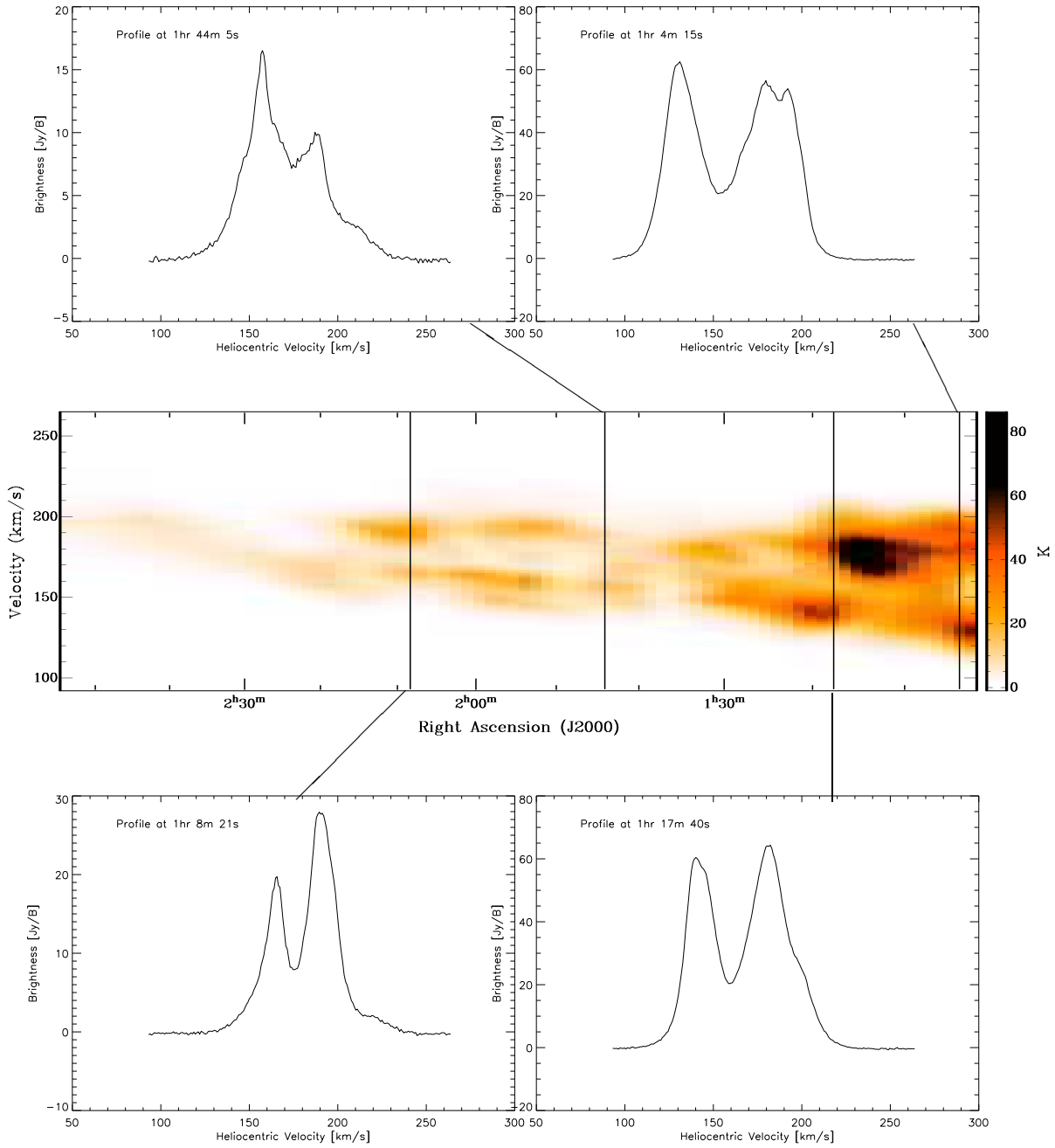

Figure 6.9: Slice through the ATCA/Parkes HI dataset. The position of this cut through the entire cube is indicated in the 166 km s^{-1} velocity range only of Fig 6.5. The overlaid lines show the positions and directions (bottom-top) of the three profiles shown around the map. The bimodal arrangement of the HI in the Bridge is clear and appears to be an extension of the morphology of the SMC.

Shell	RA (J2000)	Dec (J2000)	Expansion Velocity [km s^{-1}]	Heliocentric Velocity[km s^{-1}]	Age [Myr]	Radius [pc]
SMC HI-495	01:27:47	−73:02:16	17.6	158.0	6.0	179
SMC HI-498	01:29:01	−73:15:04	8.0	273.1	15.2	207
SMC HI-499	01:30:25	−73:27:44	14.2	160.7	7.4	179

Table 6.1: Properties of SMC shells from Staveley-Smith et al. (1997). These authors suggest that the larger shell, SMC 1 as parameterized by Hindman (1967), is in fact composed of a conglomeration of smaller shells shown here. The largest and oldest shell responsible in generating this feature (SMC-HI 498) has a kinematical age of ∼15 Myr. These estimates are made using the Weaver et al. (1977) stellar-wind model

to an under-estimation of the shell age.

From the data shown here, it is apparent that the bimodal structure of this part of the Bridge is simply an extension of an existing feature found in the SMC. It is not clear exactly how the original SMC bifurcation may have formed. In order for a stellar winds or supernovae scenario to be accepted, serious discrepancies in the sequence of events need to be clarified.

6.4 Magellanic Bridge HI loop

The large elliptical HI loop which forms the subject of this section is seen near the western edge of the ATCA+Parkes dataset and is located on the Northeast edge of the SMC. This loop has a diameter of ∼2 kpc and we have seen from Figure. 3.8a and Figure. 3.10 that the loop exists within the tenuous higher velocity component discussed in Section 6.2. We have seen in Section 6.2 that numerical simulations by Gardiner, Sawa & Noguchi (1994) suggest that this higher velocity component is associated with a distant arm of the SMC and does not effectively link the SMC and the LMC.

Figure 6.10 shows the RA-Dec, Vel-Dec and RA-Vel projections of a sub-cube containing only the HI loop and across the velocity range 190.7-231.9 km s^{-1}. This subset is selected because most of the morphology of the loop is clear in this range and can be cleanly removed from the lower velocity and brighter HI component. These maps show an HI structure which is suggestive of an expanding shell (i.e. an approaching and receding side). The overlaid ellipse shows the approximate size, shape and expansion velocity of the loop.

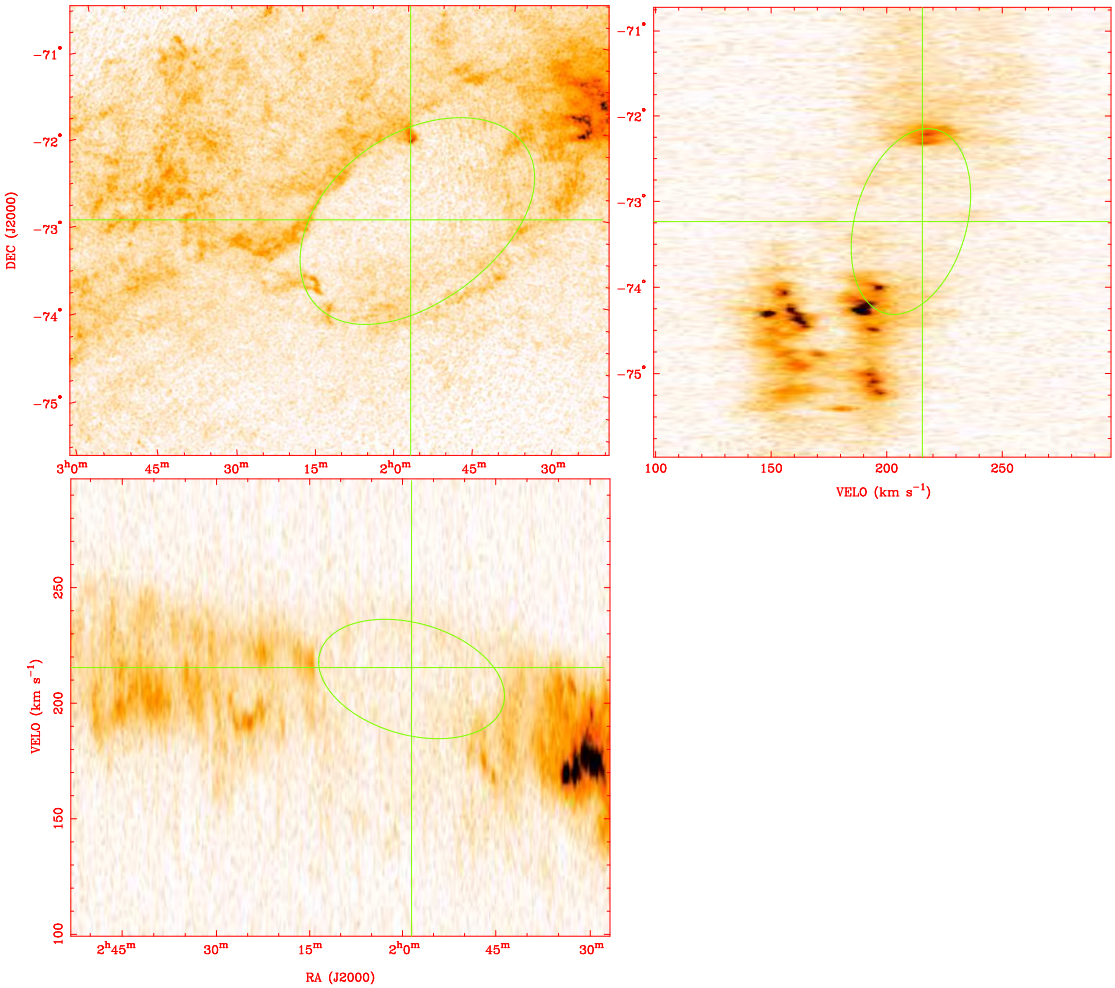

Figure 6.10: Cuts thought the ATCA+Parkes HI datacube centred on the large Magellanic Bridge Loop. The lines on each projection mark the positions of the remaining two cuts. $RA{=}1^{\rm h}\ 58^{\rm m}\ 31^{\rm s}\ Dec{=}\ -73^{\circ}\ 14'\ 4''\ Vel{=}215.4\ km\ s^{-1}$. The ellipse shows the approximate size and shape of the loop in all three dimensions. These are parameterized in Table 6.2

RA	(J2000)	$1^h\,58^m$	
Dec	(J2000)	-73° 14′	
Velocity	(Helio)	217.1 km s^{-1}	
Loop interior RMS		56K·km s^{-1}	
Axis diameter	Major	∼1.60 kpc	
	Minor	∼1.02 kpc	
Position angle		50°	
(North → East)			
Mass		2.7×10^7 M$_\odot$ [1]	3rd axis diameter 2.1 kpc
		4.4×10^6 M$_\odot$ [2]	3rd axis diameter 3.5 kpc

[1]Derived from total HI in loop and rim
[2]Derived from nearby HI column density

Table 6.2: Physical parameters of large shell-like loop feature in the Magellanic Bridge. The two alternative methods for calculating the swept-up mass yield values which are similar. The first method is perhaps less precise, since the area over which the total column density is measured is somewhat arbitrary. The values in the last column of the last two rows show estimates of the dimension of the loop in the radial direction for each derived mass and using a column density of 0.06 cm^{-3}.

The top panel of Fig 6.11 shows the integrated intensity over 190.7-231.9 km s^{-1} from the HI dataset (Chapter 3). The two traces shown in the bottom two panels are intensity profiles, as marked by the lines overplotted on the HI map. The traces highlight the degree of rim-brightening and the relative lack of material in the centre of the loop. The brightness of the rim is up to a factor of ∼3.5 brighter than the RMS of the loop interior. The large peak at offset 2.2° in the long trace (left trace of Fig 6.11) is probably not related to the HI loop rim.

Table 6.2 shows some of the physical parameters of the loop, including some estimates of the ratio of signal intensities for the filament against that from the loop interior.

6.4.1 Evolution of Magellanic Bridge loop

Such a large feature clearly indicates a very large and localised energy injection. The obvious candidate mechanisms include the standard HI expanding shell formation scenarios. e.g. stellar wind and supernovae and HVC impacts. In addition, there have been suggestions that the loop is co-incident with the L1 Lagrange point for the SMC-LMC

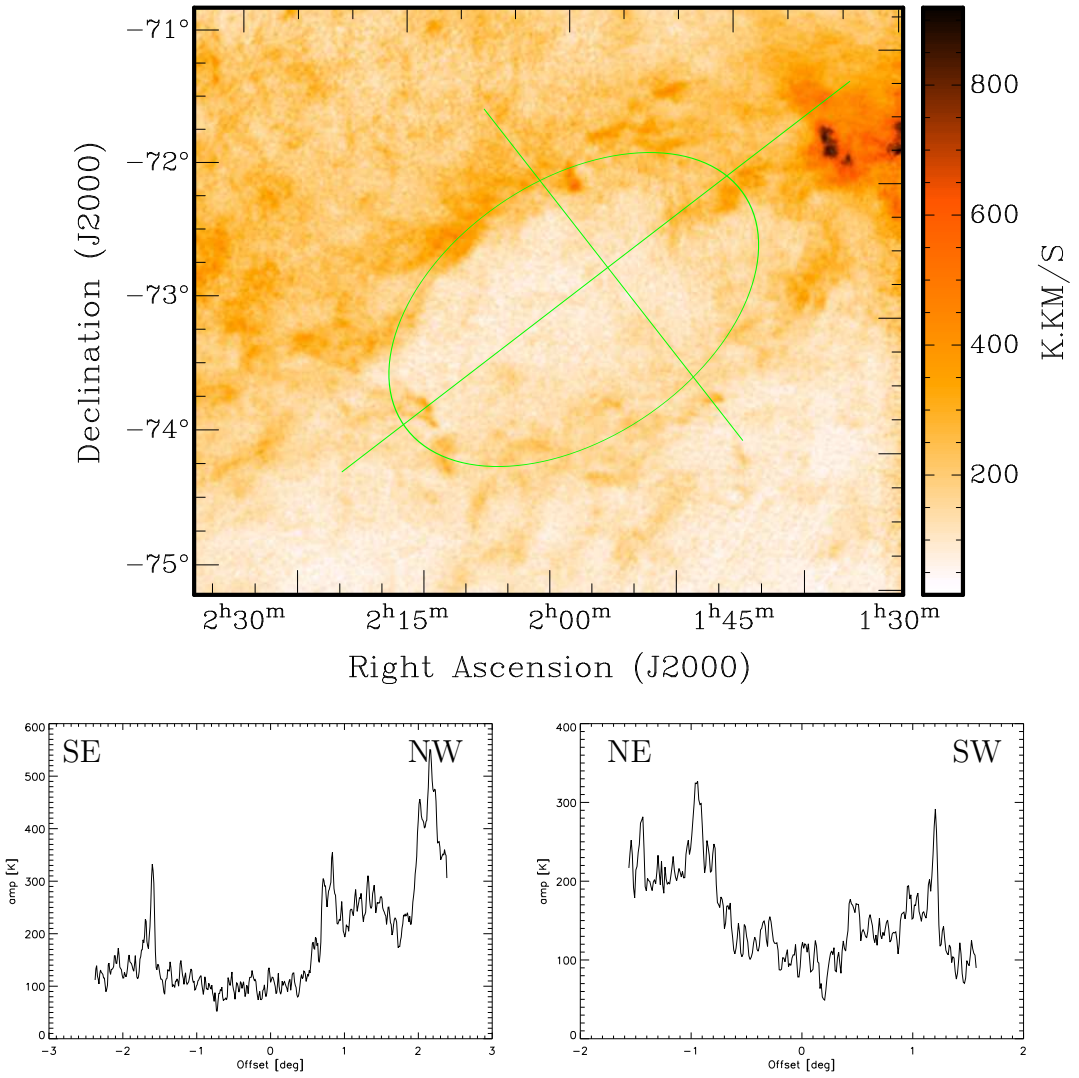

Figure 6.11: *Top:* Integrated intensity of large Magellanic Bridge HI loop region, across interval 190.7 km s^{-1}−231.9 km s^{-1}. The oval marks the estimated perimeter of the loop and the two lines show the positions and directions of the two intensity traces shown below. *Bottom:* Integrated intensity traces, as shown on the Integrated intensity map. *Left:* intensity trace along the long axis (*South east* to *North west*). *Right:* intensity trace along the short axis (*North east* to *South west*). This Figure highlights the relative deficiency of material inside the loop and the degree of rim-brightening of the loop filament.

system (Wayte 1990). The following sections will present a discussion on each of the alternatives.

6.4.1.1 Stellar wind / SNR

The structure of this large loop suggests a morphology similar to that of an expanding HI shell. Faint and incomplete velocity features can be seen from the velocity projection on Figure 6.10 at approximately $\sim$191 km s^{-1} – $\sim$232 km s^{-1}, indicating an expansion velocity of 20-30 km s^{-1}. Table 6.3 shows the expansion velocity and the related shell energy, under the two scenarios derived by Weaver et al. (1977) (the stellar wind model) and Chevalier (1974) (the SNe model). the table also shows estimates for the kinetic energy of the loop calculated using classical 1/2MV^2 relation.

Given the large radius of this void, it is appropriate under a stellar-wind expansion scenario to consider the case where the diameter of the shell is greater than the scale height of the ISM region which consequently ruptures through the surface of the gas volume. In this case, the hot gas inside the forming shell will freely expand out through the rupture and further evolution of the shell is driven by the existing momentum of the shell wall. This scenario is therefore referred to as the *momentum conservation phase* (See Spitzer, 1968; Woltjer, 1972; Dyson & Williams, 1980), where the momentum of the wall at the time of the shell 'breakout' is conserved throughout the remaining development of the shell. Following Spitzer (1968), we can apply conservation of momentum considerations to estimate the velocity of expansion at the time of phase transition, assuming a scale height of the ISM of $\sim$2 kpc and further, to estimate the time elapsed since breakout (following $t = t_{BO}(R/R_{BO})^{1/4}$). The resulting modification to the canonical dynamical age determined using Weavers formalism is a factor of approximately 2 and is shown in Table 6.3. Different formalisms yield varying predictions of the extent of the age modification. These are also shown in Table 6.3. The general consensus appears to be that the shell itself is a significant fraction (25%-35%) of the estimated age of the Bridge itself (the difference in ages estimated using the different formalisms are due to different assumptions of the energy input mechanisms and the estimates of the expansion rates). It is curious then, that the shell appears to have suffered no tidal distortion. We have seen in section 6.2 that the systemic velocity of this feature corresponds to the relatively un-perturbed, radially extending arm. The effects of the extreme projected angle may

be quite significant in regards to the measured size of this feature, although any angle of the arm relative to the plane of the sky would in fact exacerbate apparent projection distortions unless the feature were a spherical void, rather than a 'chimney' or tunnel.

We see from the table that the energy required to generate a feature of this size is entirely inconsistent with any other estimates for expanding shells found within the Magellanic Bridge and also the SMC (See Chapter 3). Using a typical estimate of the power from an O-type star, we find that an association of around 10-100 stars is required to generate a feature of this size. At 20-30 Myr, the supposed shell is much older than a typical age for a massive star and as such, we do not expect to find any residual members for this association. A reference to the OB association catalogue by Bica & Schmitt (1994) does not reveal any associations within the interior of the shell.

In any other larger system, an association of a few hundred stars would be unremarkable. However, OB associations numbering more than $\sim$10 are uncommon in the Magellanic Bridge (Bica, priv. comm. 2001) and is not clear how such a relatively well populated association comes to be at this location. The implication from the relatively young age of the shell compared to that of the Bridge is that the progenitor association formed on site, rather than being tidally pulled from the SMC. This in itself is an anomaly, since it would necessitate very active and very localised star formation within what appears to be a very tenuous medium, with a column density far below that which is typical for starformation (e.g. Grondin & Demers, 1993). Considering the large energy deposition necessary to form this feature and the unlikely occurrence of such a well populated stellar association in the Bridge, the stellar wind and supernova scenario does not appear suitable to explain the formation of this feature.

6.4.1.2 HVC impact

The idea of an clump of material infalling and colliding with a larger gaseous region was presented in Chapter 3 during a discussion of possible shell formation mechanisms. We revisit it here in the context of the large Magellanic HI loop.

Tenorio-Tagle (1986) has shown through a variety of two dimensional numerical simulations how an HI cloud infalling into a gas layer can generate an expanding shell-like structure. In each simulated case, the size, impact velocity and the density of infalling mass were varied, as well as variations between radiative and adiabatic processes. It is

Scenario	Energy	Age
Internal Kinetic	53.1 log ergs[1]	62 Myr[2]
Weaver Method	53.5 log ergs[3]	38 Myr[4]
Modified Weaver age.		
(incl. Shell 'Breakout' at 2 kpc)		
Pure Momentum conservation		71 Myr[5]
Woltjer		58 Myr[6]
Dyson & Williams		51 Myr[7]
Chevalier Method	53.9 log ergs[8]	

R=$\frac{R_{maj}+R_{min}}{2}$ V_{exp}=20.5 km s^{-1} M_{sh}=1.8×10^{7}M$_\odot$

[1]$E_{kin} = \frac{1}{2}\sum MV^2_{exp}$ [2]$T_{kin} = \frac{R_{sh}}{v_{exp}}$

[3]$E_{Weav} = 1.5 \times 10^5 (\frac{r}{100pc})^5 (\frac{T}{10^6 yr})^{-3} (\frac{n_o}{1cm^{-3}}) L_\odot T_{kin}$

[4]$T_{Weav} = \frac{3}{5}(\frac{R_{sh}}{pc})(\frac{v_{exp}}{kms^{-1}})^{-1}$

[5]$T_{mom} = T_{bo}(1 + (R/R_{bo})^{1/4})$ $T_{bo} = \frac{3}{5}(\frac{R_{bo}}{pc})(\frac{M_{sh}V_{exp}}{M_{bo}})^{-1}$ $M_{bo} = 1.1 \times 10^7 M_\odot$

[6]$T_{Wolt} = T_{bo} + (5T_{bo}/8)(3/5 + [R/R_{bo}]^{1/4})$

[7]$T_{D\&W} = T_{bo} + (R/4V_{bo})([R/R_{bo}]^{1/4} - 1)$

[8]$E_{Chev} = 5.3 \times 10^{43} n_0^{1.12} R_{sh}^{3.12} v_{exp}^{1.4}$

Table 6.3: Comparison of Energy and age Estimates from canonical stellar wind (Weaver et al. 1977) and SN (Chevalier, 1974) HI shell formation scenarios. The value derived for the Kinetic energy of the shell uses a mass estimate based on a measurement of the surrounding HI column density (see the second method in Table 6.2) and assumes no external forces or radiative losses. This estimate is unrealistic, it is included here for a comparison only. The Weaver model assumes a time-constant energy input via stellar wind. Modified age estimates assume momentum-driven expansion after shell breakout of the ISM at R=1 kpc (see Spitzer, 1968; Woltjer, 1972; Dyson & Williams, 1980). T_{bo} is estimated using Weaver dynamical age calculations and M_{bo} is estimated from conservation of momentum considerations. Energy estimates using Chevalier formalism assumes a single-event energy input through Super-nova explosions

difficult to reliably apply the outcomes of the simulations by Tenorio-Tagle (1986) to the context of the Magellanic Bridge HI loop, since the conditions tested by the simulations are not particularly representative of those found in Bridge. In particular, the densities of the simulated galactic gas are one to two orders of magnitude higher than those estimated for the Bridge. In addition, estimations for the scale height of the Bridge are significantly larger than those tested by Tenorio-Tagle (1986).

Instead, we apply some of the concepts of Tenorio-Tagle (1986) in an effort to obtain some idea of the size, velocity and density of any object capable of initiating the formation of this loop feature. From Tenorio-Tagle (1986), we can estimate the density of the infalling mass with:

$$n[cm^{-3}] = 9.78 \times 10^{-43} \frac{E_{kin}}{R_c^3 V_c^2} \tag{6.1}$$

By limiting the values for the density, n, and the radius, R_c (pc), of the infalling cloud, we will be able to determine the impact velocity, V_c (km s^{-1}), necessary to create this feature. We will use the stellar wind scenario (Weaver et al. 1977) to estimate the energy, E_{kin} (erg), required to generate this loop: E$_{kin}$=3.98$\times$10^{52} erg.

Distances to HVCs are, in general unknown, or at very least, difficult to measure. HVC's for which the distance is known are typically relatively close to our Galaxy and are within a few hundred parsecs (e.g. Wakker, 2001). Apart from the clouds which are kinematically related to the Magellanic System (Putman et al. 2003; Brüns, 2003) The population of HVC's at Magellanic Distances is almost entirely uncertain. We will therefore turn to nearer HVCs for a first estimate of the HVC densities and radii.

Absorption measurements by van Woerden et al. (1999) have placed tighter constraints on the radial distance for the HVC 'Chain A', one of the earliest HVC HI cloud complexes studied. These studies found a total mass of between 10^5 and 2×10^6 M$_\odot$. Although this particular cloud was actually found to be relatively much closer to the Galaxy than is the Magellanic System, we can use this cloud as a template to probe further the plausibility of HVC impacts as the energy source for the Magellanic Bridge HI loop.

Wakker, Oosterloo & Putman, (2002) have presented high-resolution studies of HVCs with radii as low as 7.5 pc and with densities as high as 20 cm^{-3}. The minimum velocity for projectile such as this to create the observed loop would be approximately 2200 km s^{-1}, which equates to $\sim$2400 km s^{-1} in the Heliocentric rest frame and $\sim$2176 km s^{-1} in the

LSR frame. This might be considered to be an upper limit, although a cloud moving at such a high LSR velocity is extremely unusual (Wakker, 2001; van Woerden et al. 1999).

We can use a study of HVCs in and around the Magellanic System as an additional check. Brüns (2003) made a detailed study of the Leading Arm complex, which exists at LSR velocities between 200 and 350 km s^{-1}. The densities reported by Brüns (2003) are highly dependant on temperature and have a range between 5 cm^{-3} for cool clouds and 0.2 cm^{-3} for warmer clouds. There are extreme difficulties in determining the densities and radii for these clouds, since the distance parameter is so poorly known.

Figure 6.12 the variation of the density and radius for a HVC with the kinetic energy required to generate the Magellanic Bridge HI loop for four ranges of Velocity (LSR = 200/214, 185/230, 140/275 and 65/350 km s^{-1}) using masses and densities based on findings by van Woerden et al. (1999) and Wakker, Oosterloo & Putman (2002). The plot shows that in general, only very dense or large-radii HVCs only are capable of generating this kind of feature. Even for the highest velocity HVC, with a LSR velocity of $\sim$350 km s^{-1}(equivalent to an impact velocity of $\sim$142 km s^{-1}), the densities are unrealistically high for the small radii clouds. Wakker, Oosterloo & Putman, (2002) were careful to stress that the small radius, high density cloud they were able to parameterize was something of an exception. However, even this cloud would not be able to generate the necessary kinetic energy unless it was moving exceptionally quickly.

Aside from the kinematical requirements for the generation of such a feature as that observed in the Magellanic Bridge, we might also expect to find some debris or other morphology in the loop which would be indicative of an impact. The interior of the loop is remarkably uniform and featureless; there appears to be no other debris detectable within the line of sight. Specifically, the morphology of the loop does not show any excess material which we would expect to be swept up in the direction of the infalling matter, although the direction of any impactor is entirely unknown. The symmetry of the loop is quite a strong argument against the infalling matter scenario.

Formation of the Magellanic Bridge loop by an in falling cloud cannot be ruled out, since we cannot definitively say that a projectile of such high density and velocity does not exist. Current research however, does not support a high probability.

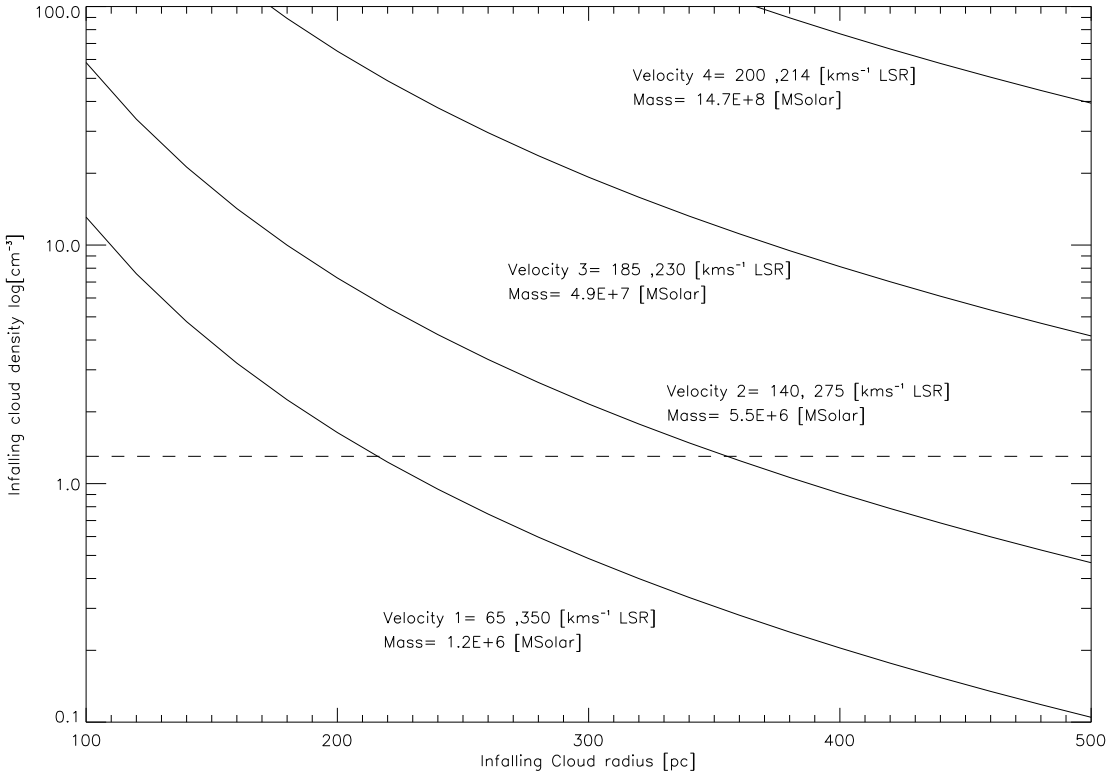

Figure 6.12: Plot showing the variation of HVC radius and HVC density for four velocity ranges for an HVC with the necessary energy to generate the Magellanic Bridge HI loop. The two values indicate the cloud can be falling from the low or high velocity (i.e. the impact velocity $=V_{Bridge} \pm V_{cloud}$). The horizontal dotted line indicates the high density of the HVC detected by Wakker, Oosterloo & Putman, (2002). The radius of this high-density HVC was which is too small to be conveniently marked on the above plot. Overall, we see that unrealistically large radii are necessary to produce an HVC with densities compatible with recent density measurements.

6.4.1.3 Lagrange point

The possibility that the Magellanic Bridge loop had formed around the first Lagrange (L1) point was suggested by Wayte (1990). Unfortunately, this author did not go into any detail or rigor regarding this proposal.

The L1 point is a gravitationally unstable region in space between two masses. Material in the L1 point will not be stationary and will tend to fall towards one of the two masses. The change in the potential field will be more rapid towards the closest (and least massive) object. For comparable masses, the variation in the potential is more gradual.

For a two-body system, comprising point masses, the distance of the L1 point along the line joining the two masses (R_{L1}) will be found from:

$$R_{L1} = R\Big[1 - \Big(\frac{M_1}{3(M_2 + M_1)}\Big)^{1/3}\Big] \tag{6.2}$$

where R is the separation of the masses, M_1 and M_2. Wayte (1990) suggests mass ratio of the two clouds: M_{LMC}/M_{SMC} of 4.0 which would put the Lagrange point at R$\sim$15 kpc, much closer to the LMC than the observed position of the loop. Gardiner, Sawa & Noguchi (1994) and Gardiner & Noguchi (1996) use a mass ratios of of 6.6 - 10. From equation 6.2, we that in these cases the L1 point occurs at 0.65 R-0.69 R along the line joining the SMC and LMC. These positions also do not coincide with the observed location of the HI loop.

Furthermore, numerical simulations (Gardiner, Sawa & Fujimoto, 1984; Gardiner, & Noguchi, 1996; Gardiner, Sawa & Fujimoto, 1994; Murai & Fujimoto, 1980) generally fail to clearly reproduce this significant loop.

We have already shown a good agreement of N-Body simulations of the Magellanic System with real observations (Gardiner, Sawa & Noguchi, 1994). The simulations showed that the Bridge as observed, is a superposition of two arms of the SMC. The entire loop is located within the higher velocity component of the Bridge as discussed in Section 6.2. If we can associate this higher velocity region with the distant arm, as suggested by the simulation results, shown in Figures 6.6 and 6.7, then the loop is no longer on the line joining the two clouds, an impossible position for the Lagrange point.

Numerical simulations do not appear to reproduce the existence of the large HI loop as

observed in the Magellanic Bridge. Simulations in fact suggest that the loop is located in a part of the SMC which is not on the line joining the centres of the SMC and LMC. The Lagrange point scenario for the formation of this loop is entirely incompatible with numerical simulations.

6.4.2 Other large HI holes and loops

Numerous large-scale loops and holes have been discovered in HI surveys of various objects. It is useful to discuss some of these here in the context of the Magellanic Bridge HI loop.

6.4.2.1 M101

The expanding hole found and parameterized by Kamphuis, Sancisi & ven der Hulst, (1991) is slightly larger and more energetic than the hole found in the Magellanic Bridge. It has a diameter of 1.5 kpc, a larger expansion velocity of 50 km s^{-1} and an estimated mass of 3×10^7 $M_\odot$. The estimated age of the M101 shell is 150 Myr. The location of this hole, in one of the stronger HI regions inside a spiral arm, is strongly indicative of a stellar wind or supernova formation mechanism. In this case, shell formation by stellar wind or SNe is not an unlikely process, since well populated associations are not infrequent in well-developed and large systems such as M101. The same situation is not so readily applied to the Magellanic Bridge.

6.4.2.2 NGC6822

A high-resolution study of the HI of the nearby Dwarf galaxy, NGC6822 made by De Blok & Walter (2000) revealed one of the largest HI holes known. The NGC6822 hole has a size of 2.0×1.4 kpc. No approaching or receding features for this shell were detected, so the expansion velocity was assumed to be equivalent to that of the velocity dispersion of the disk; $\sim$7 km s^{-1}. Under the assumption of a stellar wind or Supernova central driving engine, these authors used an ambient density of $n_o \approx 0.1$ cm^{-3} to estimate the formation timescale for this feature of $\sim$100 Myr and an energy input of $\sim10^{53}$ ergs. Although the size of the hole found in NGC6822 is far larger than the hole in the Bridge, it appears that a far smaller mass of neutral hydrogen is involved in its formation. De

Blok & Walter, (2000) use measurements of the scale height of NGC6822 to estimate the amount of removed HI material as 1.6×10^6 $M_\odot$.

The proposed scenario for the formation of the NGC6822 shell involves a starburst, perhaps triggered by the nearby passage of a companion. This was a general and rather unqualifiable conclusion and the authors were careful to point out that the formation mechanism for the loop feature of NGC6822 is largely unknown.

6.4.2.3 Shapley III - LMC

The Shapley constellation III in the LMC contains a number of HII regions arranged in a ring, which has been shown to be coincident with an expanding HI shell (Dopita, Mathewson & Ford, 1985). This shell is comparable in size and expansion velocity to the feature in the Magellanic Bridge and shows evidence for an approaching and receding faces. With a diameter of $\sim$1.8 kpc, the expansion velocity of $\sim$36 km s^{-1}, together with an estimate of the mass of the swept-up material of $7.7\times10^6 M_\odot$ gives a total kinetic energy of $\sim10^{53}$ ergs. In all respects, this feature in the LMC appears to be very similar to that found in the Magellanic Bridge. However, the driving mechanism for the LMC feature is again much less speculative, since the interior is well populated with rich stellar clusters, at least one of which, with N $\sim$1000, is capable of supplying the necessary energy input on its own.

6.4.2.4 NGC1313

A large and well formed $\sim$1.6 kpc expanding shell was found in the spiral NGC1313 in an optical and HI study by Ryder et al. (1995). The energy input necessary to form this feature was calculated assuming a series of SNes (McCray & Snow, 1979) and was found to be approximately 9.8×10^{53} ergs. The authors of this research remarked on the symmetry of the formed shell and concluded that such a feature could be formed only through an internal energy deposition mechanism, rather than by collision or tidal disruption.

The shell of NGS1313 is similar in size and total luminosity to the shell found in the Bridge. Kinematically however, these shells are quite different: the shell of NGC1313 is expanding almost twice as quickly and is therefore much younger. The shell of NGC1313 shows well-defined approaching and receding faces, whereas those of the Bridge shell are

much more ambiguous. Once again, the NGC1313 system has a much more densely distributed stellar population than does the Bridge and formation by stellar wind and SNe is a more probable scenario for this shell.

Largely, comparable holes in comparable galaxies are typically justified under a stellar wind scenario. We have demonstrated that it is unlikely that the loop found in the Bridge is formed by stellar wind, supernovae or HVC impact, and we have rejected the theory of its formation by the unstable Lagrange point. The large radii loop observed in the Magellanic Bridge remains a unique and puzzling feature.

6.5 Summary

Some of the more striking and larger scale features of the Magellanic Bridge were analysed and discussed in this Chapter with a view to understanding processes which have shaped such structures.

The velocity distribution of the HI in the Bridge appears to be quite compatible with results from numerical N-Body simulations. The simulations imply that the denser and more turbulent part comprises a closer arm and the turbulent and filamentary structure seen in this part of the Bridge may be generated through its tidal involvement with the LMC. The higher velocity component appears to form the much more distant arm. This arm is much more independent from the Bridge and as a result, the HI is more smoothly distributed and is much less perturbed.

It appears that the HI of the brightest part of the Magellanic Bridge is organised into two sheets in velocity space. The bifurcation shows every indication of having originated in the SMC and has since been tidally extracted into the Bridge during the SMC/LMC tidal interaction $\sim$200 Myr ago. The original SMC feature may be a superposition of a number of stellar-wind blown shells, however the estimated ages of these shells is not consistent with the estimated age of the Bridge.

A large loop filament is located on the N-E corner of the SMC and appears to be embedded in the high velocity HI mass. The energy required to create such a loop is equivalent to a few hundred Supernova explosions. The HI may be distributed in a way which is reminiscent of an expanding HI region, suggestive of a stellar wind or SN energy injection

Region	Centre Position [HMS] [DMS] (J2000)	Component #	Central Velocity [km s^{-1}Helio]	Width [km s^{-1}Helio]	Amplitude [K]
1-1	02:51:37 -75:15:22	1	138.8	27.0	0.21
		2	179.4	28.4	1.64
		3	198.5	10.0	1.34
		4	201.9	22.9	2.29
		5	231.5	27.4	0.63
2-1	02:35:20 -75:25:18	1	176.0	50.4	0.68
		2	178.6	31.5	1.50
		3	198.9	16.5	1.47
		4	221.0	34.4	0.54
3-1	02:18:47 -75:30:38	1	202.4	34.8	0.52
		2	194.7	14.5	1.23
		3	175.6	37.3	2.41
		4	156.4	13.7	1.06
4-1	02:02:08 -75:31:18	1	154.6	15.2	3.21
		2	165.2	38.0	1.75
		3	192.1	28.2	2.49
		4	194.3	10.6	2.28
5-1	01:45:32 -75:27:16	1	154.9	28.2	3.61
		2	152.4	12.2	1.04
		3	183.0	37.9	1.34
		4	189.5	17.1	1.90
6-1	01:31:16 -74:27:41	1	152.2	28.6	4.02
		2	180.3	42.2	0.86
		3	186.1	20.4	1.31

Table 6.4: Parameters for Gaussian decomposition for row 1 (see Figure 6.1)

mechanism. The size of stellar association required to create this feature through the action of stellar winds or SNe is extraordinary for the Magellanic Bridge. Similarly, estimates show that the energy requirements for infalling an HVC are not quite compatible with recent measurements for HVC masses, velocities and densities. A suggestion that the loop has formed as a result of the Lagrange point is not consistent with numerical simulations. Its high velocity locates it in a more distant arm of the SMC, and not in a position compatible with the L1 point.

Region	Centre Position [HMS] [DMS] (J2000)	Component #	Central Velocity [km s^{-1}Helio]	Width [km s^{-1}Helio]	Amplitude [K]
1-2	02:49:17 -74:24:36	1	181.0	10.0	4.16
		2	191.2	10.7	3.38
		3	202.8	43.8	3.40
		4	246.3	18.6	1.06
2-2	02:33:52 -74:34:02	1	225.5	30.7	1.55
		2	191.8	21.2	5.86
		3	171.7	17.8	3.88
		4	178.2	10.3	3.16
3-2	02:18:12 -74:39:06	1	168.1	15.4	6.86
		2	162.7	24.3	4.09
		3	191.5	15.2	8.41
		4	207.0	14.9	1.45
		5	225.0	20.6	0.94
4-2	02:02:27 -74:39:43	1	153.2	20.5	5.00
		2	163.3	13.7	9.12
		3	190.9	18.5	13.3
		4	218.5	15.8	1.66
5-2	01:46:46 -74:35:54	1	149.8	14.1	6.25
		2	155.7	25.3	8.52
		3	87.6	18.3	10.2
		4	202.0	29.0	1.85
6-2	01:31:16 -74:27:41	1	142.4	13.9	3.68
		2	154.5	35.4	5.11
		3	186.5	13.8	4.80
		4	194.3	27.5	2.98

Table 6.5: Parameters for Gaussian decomposition for row 2 (see Figure 6.1)

Region	Centre Position [HMS] [DMS] (J2000)	Component #	Central Velocity [km s^{-1}Helio]	Width [km s^{-1}Helio]	Amplitude [K]
1-3	2:47:10 -73:33:32	1	196.5	13.1	2.99
		2	188.8	25.5	3.09
		3	212.4	27.2	3.46
		4	246.0	16.4	2.74
2-3	02:32:32 -73:42:31	1	179.9	20.1	5.79
		2	179.0	6.75	5.95
		3	197.4	18.7	5.41
		4	215.8	15.7	2.37
		5	235.6	19.7	2.76
3-3	02:17:41 -73:47:21	1	167.7	23.5	3.20
		2	167.2	8.38	3.57
		3	175.7	6.19	3.54
		4	184.5	11.8	8.01
		5	195.5	10.5	1.76
		6	213.8	32.7	3.36
4-3	02:02:45 -73:47:56	1	164.1	41.4	1.33
		2	155.8	4.27	0.89
		3	158.5	21.3	2.71
		4	186.4	13.7	3.61
		5	194.3	11.2	3.19
		6	214.8	32.1	2.02
5-3	01:47:52 -73:44:18	1	156.3	27.7	4.37
		2	155.0	6.83	3.12
		3	174.3	15.4	2.73
		4	189.4	15.7	6.21
		5	195.8	5.33	1.98
		6	213.1	28.5	2.62
6-3	01:33:09 -73:36:28	01	145.1	23.7	1.93
		2	148.2	9.02	3.67
		3	162.2	9.70	3.49
		4	180.0	9.33	6.30
		5	175.3	40.6	10.9

Table 6.6: Parameters for Gaussian decomposition for row 3 (see Figure 6.1)

Region	Centre Position [HMS] [DMS] (J2000)	Component #	Central Velocity [km s^{-1}Helio]	Width [km s^{-1}Helio]	Amplitude [K]
1-4	02:45:17 -72:42:09	1	269.5	12.8	0.30
		2	240.9	24.7	1.77
		3	209.4	30.9	4.08
		4	199.0	13.4	3.44
		5	205.3	42.8	0.83
2-4	02:31:20 -72:50:45	1	170.9	24.1	0.65
		2	254.8	21.8	0.68
		3	230.6	17.3	3.56
		4	204.9	25.6	5.93
3-4	02:17:13 -72:55:21	1	190.6	56.2	0.62
		2	201.8	25.3	3.30
		3	225.3	16.8	3.11
		4	242.9	30.8	1.24
4-4	02:03:01 -72:55:55	1	241.9	27.4	1.04
		2	221.6	29.3	0.96
		3	194.6	31.8	1.40
		4	155.3	28.5	0.37
5-4	01:48:52 -72:52:27	1	139.0	25.2	0.69
		2	184.4	41.8	2.71
		3	211.7	14.6	0.49
		4	228.9	22.7	1.70
6-4	01:34:51 -72:44:58	1	151.6	37.0	2.74
		2	175.0	18.1	6.37
		3	188.5	11.9	1.99
		4	203.0	24.4	7.54

Table 6.7: Parameters for Gaussian decomposition for row 4 (see Figure 6.1)

Region	Centre Position [HMS] [DMS] (J2000)	Component #	Central Velocity [km s^{-1}Helio]	Width [km s^{-1}Helio]	Amplitude [K]
1-5	02:43:34 -71:50:28	1	208.2	26.0	3.35
		2	232.0	20.3	1.37
		3	263.5	26.9	0.76
2-5	02:30:15 -71:58:43	1	211.1	28.8	4.62
		2	232.8	15.8	0.90
		3	257.7	25.1	1.06
3-5	02:16:47 -72:03:07	1	210.9	33.0	3.05
		2	228.8	16.4	1.05
		3	257.0	22.5	1.70
4-5	02:03:15 -72:03:40	1	207.7	45.5	1.13
		2	217.9	29.4	3.60
		3	254.6	21.8	1.76
5-5	01:49:46 -72:00:20	1	195.6	63.0	1.76
		2	189.7	23.2	2.00
		3	229.6	19.8	4.85
6-5	01:36:24 -71:53:10	1	142.6	28.3	1.62
		2	197.9	39.6	4.64
		3	208.6	9.19	2.12
		4	221.5	16.6	8.89

Table 6.8: Parameters for Gaussian decomposition for row 5 (see Figure 6.1)

Region	Centre Position [HMS] [DMS] (J2000)	Component #	Central Velocity [km s^{-1}Helio]	Width [km s^{-1}Helio]	Amplitude [K]
1-6 cline3-6	02:42:00 -70:58:29	1	220.1	28.0	1.03
		2	239.6	39.5	0.31
		3	264.9	19.3	0.68
		4	268.6	25.3	0.90
2-6	02:29:16 -71:06:24	1	220.9	34.0	1.68
		2	220.8	24.6	1.61
		3	254.8	20.7	0.68
		4	263.5	18.6	1.56
3-6	02:16:24 -71:10:38	1	208.7	23.5	1.69
		2	220.8	47.2	1.20
		3	241.6	35.9	0.54
		4	256.4	17.9	1.38
4-6	02:03:29 -71:11:09	1	209.9	38.9	1.72
		2	208.6	22.0	1.25
		3	250.2	21.0	2.54
5-6	01:50:35 -71:07:57	1	186.8	46.4	0.78
		2	190.6	18.8	0.58
		3	220.7	35.9	3.30
6-6	01:37:48 -71:01:04	1	165.9	42.8	1.34
		2	201.0	29.8	2.13
		3	220.4	26.1	5.27

Table 6.9: Parameters for Gaussian decomposition for row 6 (see Figure 6.1)

Chapter 7

Hα emission regions in the Magellanic Bridge

"Is the FAUST *catalogue the list of the damned?"*- Grahame Muller, 2003

Throughout the past, few dedicated studies of Hα from the Magellanic bridge have ever been made. An initial study by Johnson, Meaburn & Osman (1982) detected 'faint nebulosity' in a wide-field image of the Magellanic System . This detection was followed up with observations at discrete locations with a Perot-Fabry interferometer by Marcelin, Boulesteix & Georgelin (1985).

A comprehensive study of Hα emission regions in the SMC and LMC by Davies, Elliot & Meaburn (1976) resulted in the commonly referenced DEM Catalogue. This lists and describes the brighter Hα emission features apparent in the LMC and SMC. This study did not penetrate into the Bridge and listed only a few objects east of the molecular region N88 at RA $01^{\rm h}\,24^{\rm m}\,08''$, Dec. $-73^\circ\,08'56^{\rm s}$ (J2000).

Later additions to the DEM catalogue were made by Meaburn (1986) after a re-analysis of the Bridge Hα plates for structures in the Magellanic Bridge. Objects DEM168 - DEM172 were added to the SMC-LMC Hα catalogue, although the focus of this work was the large Hα shell: DEM171.

DEM171 was again analysed by Parker (1998) and Graham et al. (2001) finally made a spectroscopic study of this Hα object. This study made measurements of the shell size and expansion velocity from one dimensional spectrographic data. The Hα region was found to be at Magellanic velocities and estimates of its age and luminosity were made.

Since the studies by Meaburn (1986), higher sensitivity Hα observations of the Magellanic system have been made. The subject of this chapter is to present a preliminary catalogue and discussion of new Hα features within the Bridge using this higher-sensitivity dataset.

Section 7.1 explains the origin and processing of the Hα dataset. The methods involved in undertaking the Hα survey are also explained in this section. Section 7.2 presents a discussion of the known Hα features in the Magellanic Bridge, with reference to possible ionisation mechanisms. Where this is not known, or conjectured, comparisons are made with the HI dataset for additional information. The catalogue and a similar discussion of new Hα features is covered in Section 7.3.

7.1 The Hα Dataset

The Hα dataset used in this Chapter was obtained using the UK-Schmidt telescope (UKST). This facility is located at the Siding Spring Observatory in Coonabarabran, Australia (*Lat. -31.27 Long. +149.07*). UKST has a 1.2m diameter aperture and a 6° field of view. The detector is a 'Tech-pan' film (Parker & Malin, 1999) and the Hα bandwidth is selected with a 'HA659' interference filter . This filter has a bandpass of 70 Å at a central wavelength of 6590 Å.

These data used are part of a Magellanic System-wide Hα survey (under the project number 'T1117'). The relevant field for this study is labelled 'MC09'. This field overlaps well with the regions already surveyed in HI with the ATCA and Parkes telescopes (see Chapter 3). The Hα field is observed for 180 minutes.

Following observations, the plate is optically scanned using a specialised scanning facility called SuperCosmos, and stored as raw digital information. This Facility is located at the Royal Observatory Edinburgh (ROE). As the UK-Schmidt dataset as received from SuperCosmos is un-calibrated, all data shown here is the raw, digital dataset. The pixel spacing of the SuperCosmos dataset is $\sim 0.6''$.

7.1.1 Data preparation

Data received from SuperCosmos do not have a co-ordinate system attached. Due to distortions caused by the telescope, it is extremely difficult to apply a co-ordinate system

manually. Fortunately the SuperCosmos facility provides software which can extract a region of interest and correctly apply a co-ordinate system (ftp://ftp.roe.ac.uk/pub/nch/code and references from that site).

The major drawback of Hα data obtained with the UKST facility is the difficulty involved in extracting interference artifacts arising from the Hα filter itself. The artifacts are so significant that it is often extremely difficult to obtain well-calibrated data. Calibrated data is available online for some regions however, although the Magellanic System fields have not been calibrated at the time of writing. As such, where it is necessary to report intensity levels, these are calculated as a factor of the nearby noise. As the film has a non-linear response, it is even difficult to obtain an estimate of the relative brightness of an object. It is the intention that this catalogue therefore be used as a preliminary reference for follow-up spectroscopic observations.

7.1.2 Searching for Hα in the Magellanic Bridge

As discussed in Section 2.1.3, Hα emission follows a recombination process, requiring some energetic mechanism to pump the hydrogen into an excited state, such as radiative heating or collisional excitation. One such source of a UV flux capable of ionising the ISM is a young hot O or B type stars or stellar associations. This is a thermal process, although the ISM can also be ionised through the exchange of kinetic energy, for example, by an impacting object. These collisional processes are non-thermal.

It is possible to distinguish the active process to some extent by searching for continuum emission in the regions of the observed Hα flux. Stellar associations for example, will be apparent in continuum observations whereas sites of cloud collisions will be invisible.

For this Hα survey, continuum information is not yet available. As such, this Hα survey is useful only to isolate interesting Hα features. An attempt is made to suggest *possible* ionisation mechanisms, although further quantitative analysis with calibrated observations and consultation with continuum information are vital in order to properly ascertain the correct mechanism.

This search for Hα emission regions from this dataset was accomplished using two methods sequentially:

- Visually inspecting Hα data and isolating obvious Hα regions. Objects found this way are usually extended and relatively bright.
- Appealing to established catalogues of objects which are commonly associated with Hα regions (e.g. OB association catalogues, FAUST UV source catalogues), then inspecting the Hα dataset around each of these catalogued positions. In these cases, the Hα emission is usually unimpressive and concentrated in a collection of point-like objects.

In many cases, the ionisation mechanism responsible for the processes leading to Hα emission are not always clear. A focus of this Chapter will be to present a discussion of possible mechanisms of ionisation for each object. For both approaches outlined above, object catalogues are extensively referenced in an effort to locate possible sources for ionising flux. Hα regions where the ionisation mechanism is interesting or unclear will be discussed in more detail.

A search for Hα emission within the Magellanic Bridge using criteria outlined above has resulted in the identification of eleven new Hα regions and four regions for which an identification already exists (DEM168-DEM172). The positions and some comments of the Magellanic Bridge Hα features are presented in Table 7.1. The numbering of the regions and the listing of the Hα features increases towards the west (MBHa1-MBHa11). Due to the size of the Hα dataset and the variations in the brightness of the Hα emission regions, it is impractical to display the Hα dataset in its entirety. Four Sub-regions of the dataset where noteworthy Hα emission has been located are shown in Figures 7.2 -7.3. A peak brightness HI map shown in Figure 7.1 locates the four Hα subregions with overplotted squares.

7.2 Re-visiting known Bridge Hα objects

The analysis of some Hα features in the Bridge by Meaburn (1986) was an extension of a previous Hα survey of both the Magellanic Clouds by Davies, Elliot and Meaburn (1976). Meaburn (1986) located an additional four objects near the easternmost point of the SMC wing. At the time this analysis was made, these were the only known coherent Hα structures in the Bridge. They are the brightest, but not the largest of the Hα features that may be found within the Bridge. The objects parameterized by Meaburn (1986) are

Catalogue Name	Position [HMS,DMS] (J2000)	Description
DEM168[1]	02:12:24 -74:11:00	Diffuse irregular patch $\sim 7 \times 4$ arcmin^2 diameter
DEM169[1]	02:11:07 -74:09:57	Faint elongated filament $\sim 11'$ long
DEM170[1]	02:05:42 -74:24:25	Semicircular arc $\sim 0.9''$ diameter
DEM171[1]	02:07:49 -74:44:14	Filamentary shell $7.9'$ diamter
DEM172[1]	02:08:59 -74:55:00	Diffuse patch $\sim 4'$ across
MBHa11	01:57:02 -74:15:38	Diffuse patch $\sim 88'' \times 81''$ (RA and Dec)
MBHa10	01:56:44 -74:13:10	Diffuse Patch, some point-like components $55'' \times 46''$ (RA and Dec)
MBHa9	01:56:36 -74:17:00	Diffuse patch $55'' \times 59''$ (RA and Dec)
MBHa8	01:56:30 -74:15:02	Diffuse patch $72'' \times 61''$ (RA and Dec)
MBHa7	01:56:43 -74:31:16	E-w filament. $214''$ long, $39''$ wide
MBHa6	01:50:30 -74:08:15	Complex Centre $16.8' \times 18.3'$ (RA and Dec)
MBHa5	01:50:20 -74:21:22	Mostly point-like components Some diffuse emission $58'' \times 70.4''$ (RA and Dec)
MBHa4	01:50:05 -74:37:26	Circular filament $4.5' \times 4.2'$ (RA and Dec)
MBHa3	01:49:28 -74:39:12	Diffuse patch $65'' \times 79''$ (RA and Dec)
MBHa2a	01:43:50 -74:34:05	Diffuse patch $148'' \times 148''$ (RA and Dec)
MBHa2b	01:43:21 -74:31:32	Diffuse patch $101'' \times 103''$ (RA and Dec)
MBHa1a	01:40:47 -73:50:44	Arc filament $13.6'$ long
MBHa1b	01:41:05 -73:55:43	Arc filament $6.3'$ long

[1]Meaburn, 1986

Table 7.1: List of known and new Hα features found in the western part of the Magellanic Bridge.

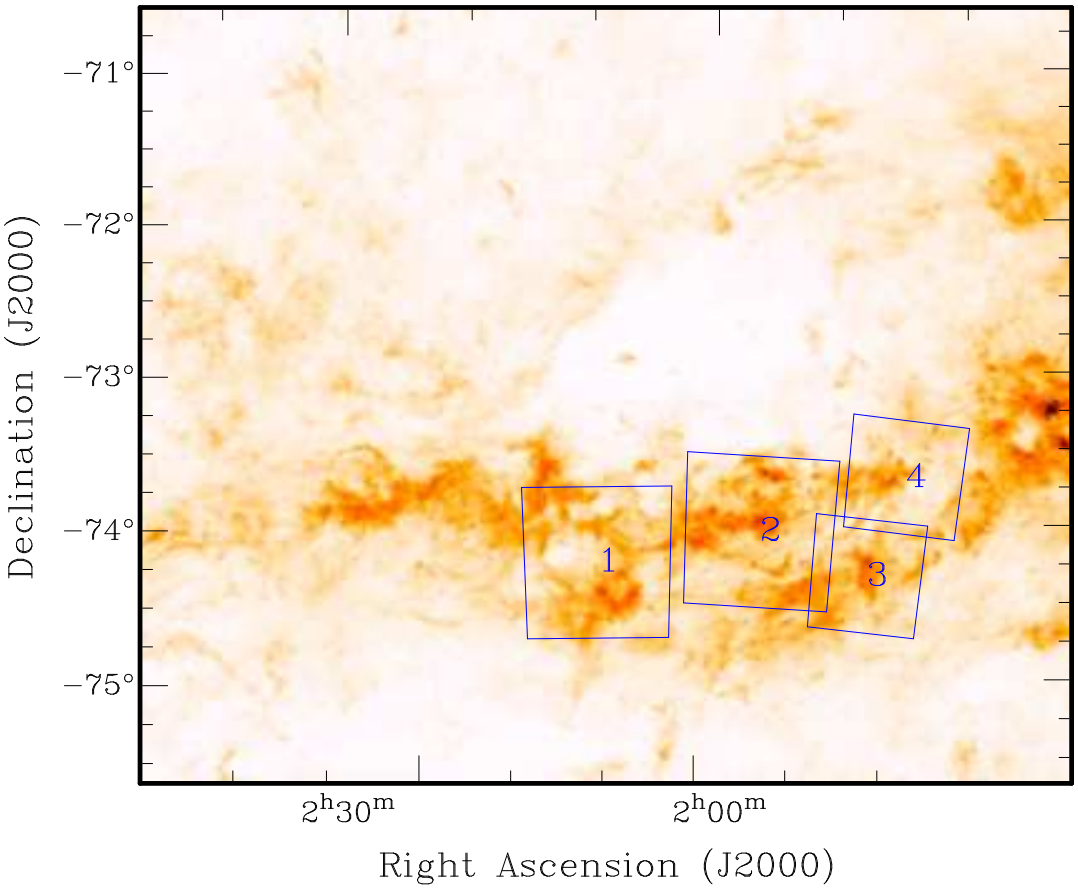

Figure 7.1: Peak temperature image of the HI dataset of Chapter 3. The overlaid squares locate four sub-regions in which Hα emission has been identified. Figures 7.2-7.3 show the Hα corresponding to each of the sub-regions.

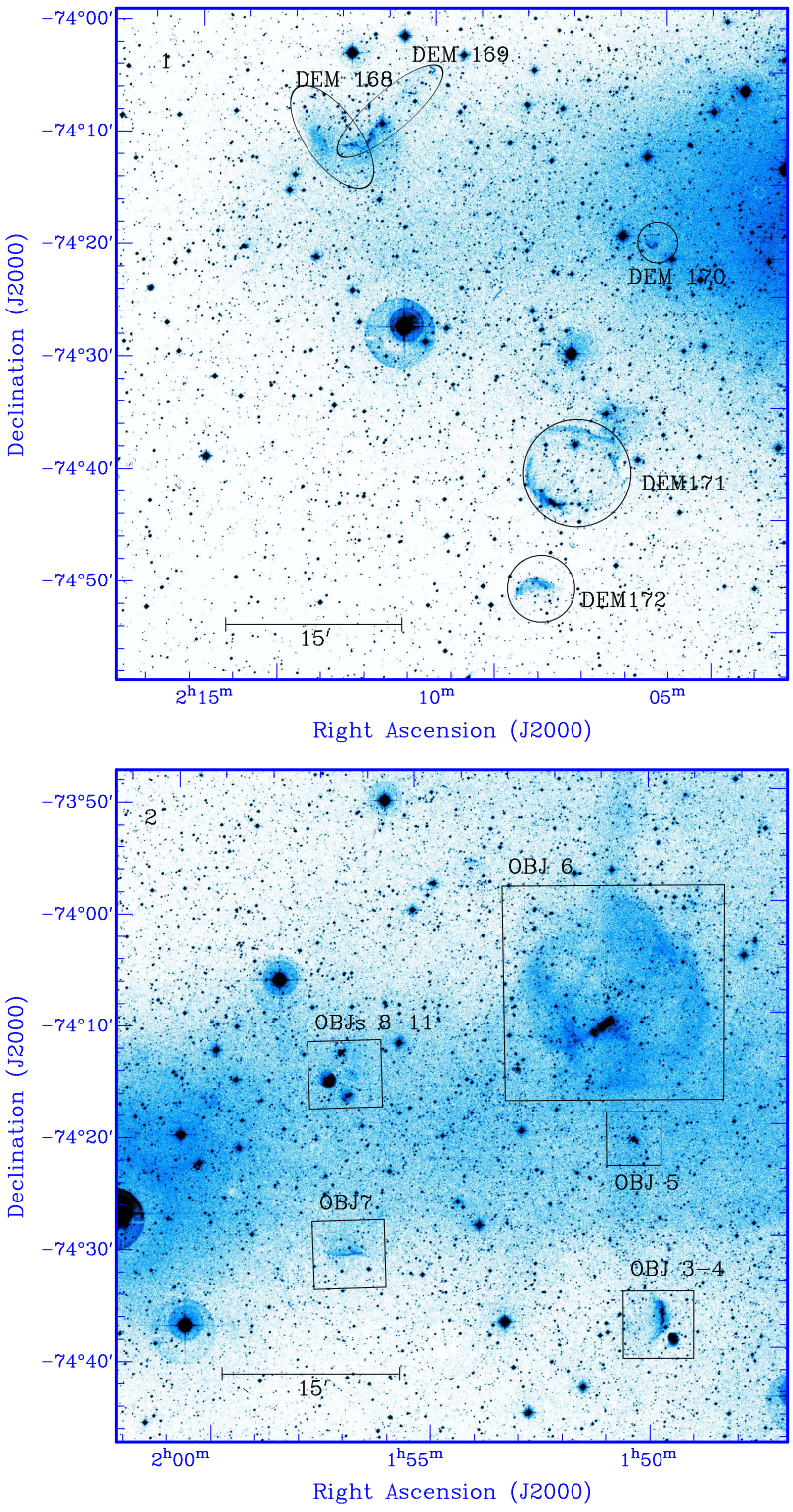

Figure 7.2: Hα Regions 1 (*top*) and 2 (*bottom*). As the dataset cannot be calibrated due to Hα filter artifacts, the colour table is arbitrary and is optimised for each panel. The Hα emission of region 1 contains all previously known Hα emission features in the Magellanic Bridge: DEM168 - DEM172 (Meaburn, 1986; see also Marcelin, Boulesteix & Gorgelin, 1985). This figure shows significant artifacts from the Hα filter as apparent emission on the north-western side of the field. Region 2 contains new Hα objects MBHa3-MBHa11. The filter artifacts is also apparent in this panel as an 'east-west 'bar' of Hα emission. Spatial scaling is shown with a bar of 15 arcminutes marked in each panel.

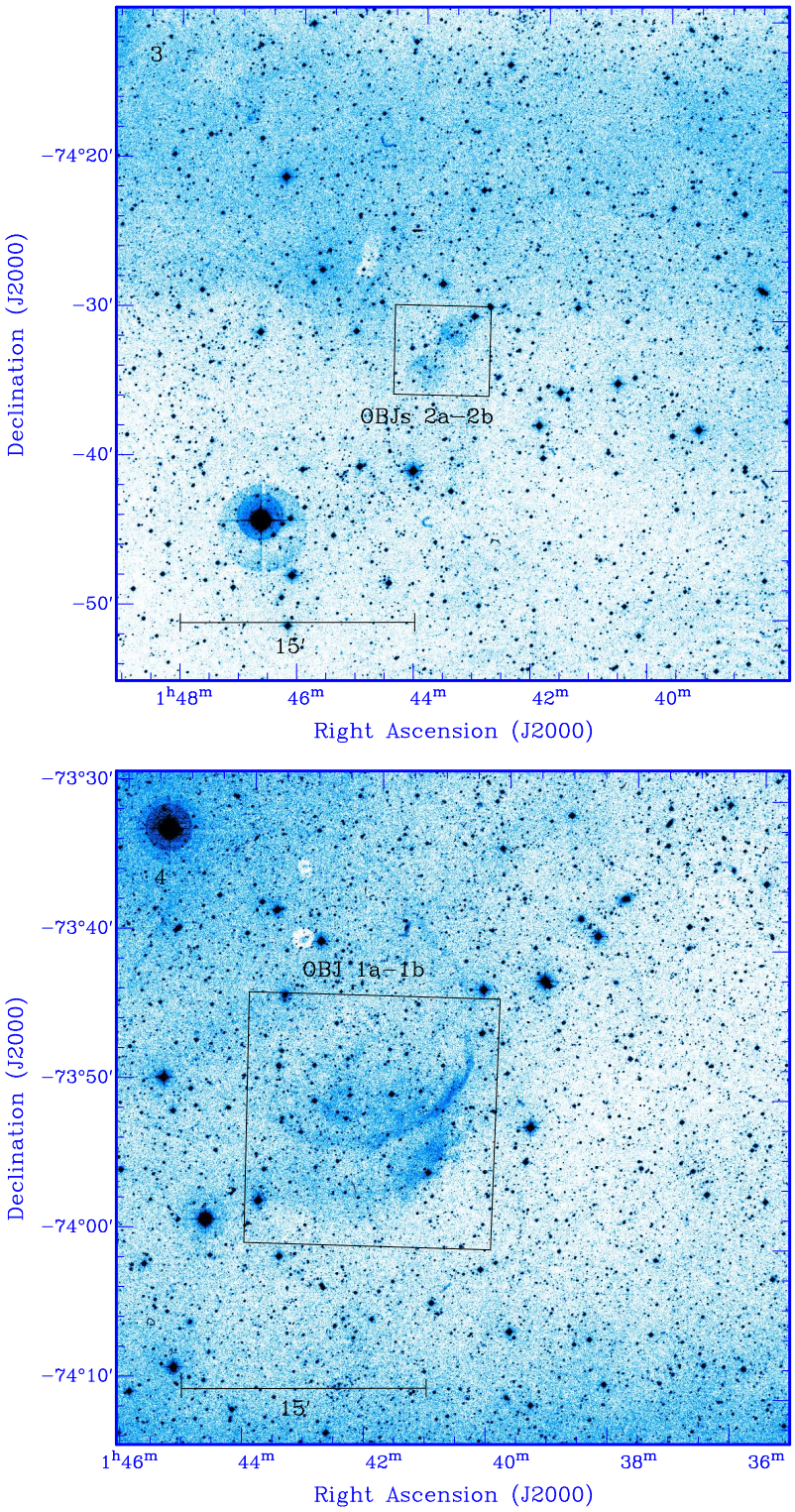

Figure 7.3: Hα dataset for the regions 3 (*top*) and 4 (*bottom*). As the dataset cannot be calibrated due to Hα filter artifacts, the colour table is arbitrary and is optimised for each panel. Region 3 includes new Hα features MBHa2a-MBHa2b, Region 4 contains new Hα objects MBHa1a-1b. The spatial scaling is shown in each panel with a 15 arcminute bar. The filter artifacts is apparent in these figures as an east-west 'bar' of Hα emission along the top panel and on the the southern edge of the bottom panel.

	Meaburn (Hα)	Parker (Hα)	Graham (Hα)	Shell 91 (HI)
RA(J2000)	$02^h\,07^m\,50^s$	$02^h\,07^m\,56^s$	$02^h\,07^m\,14^s$	$02^h\,07^m\,14^s$
Dec. (J2000)	$-74^\circ\,44'14''$	$-74^\circ\,44'06''$	$-74^\circ\,44'14''$	$-74^\circ\,44'14''$
Radius	3.93'	4.3'	∼4'	4.5±0.5'
Age	5 Myr (wind) 8 -210 Myr (SN)	–	0.53 Myr	9±2 Myr
Vel (heliocentric)	–	–	192.5 km s^{-1}	190±2 km s^{-1}
Exp. velocity			37.0 km s^{-1}	5±2 km s^{-1}
Candidate Source	O star stellar wind, SN	PN, SNR, WR shell	WR	–

Table 7.2: Comparison of parameters of the HI /Hα Shell DEM171 (HI shell#91) as observed in HI and Hα (Meaburn 1986, Parker 1998, Graham et al. 2001)

listed as the top five entries in Table 7.1. Each of these features will be re-visited here. The focus of the discussion for these features will be in the context of HI observations, ionisation mechanisms (where this has not previously been discussed in the literature) and the more sensitive Hα dataset used here.

7.2.1 Object DEM171

The large Hα shell within the Bridge at RA $02^h\,07^m\,14^s$, Dec. $-74^\circ\,44'14''$ (J2000) was detected in Hα and examined first by Meaburn (1986). A later analysis of the shell was made by Parker (1998) and then finally in more detail by Graham et al. (2001).

This Hα shell is found to be closely aligned to an identifiable expanding HI shell and is parameterized and listed as #91 in the HI expanding shell catalogue of Chapter 4. The HI shell is located at ∼RA $02^h\,08^m\,8^s$, Dec. $-74^\circ\,42'46''$ (J2000) and is found to be a typical example of the Magellanic Bridge HI expanding shell population. Hα parameters as estimated by Meaburn (1986), Parker (1998) and by Graham et al. (2001) and the parameters of HI shell #91 are compared in Table 7.2. A map of the HI peak brightness temperature of the region around the shell is shown in the top left panel of Figure 7.4. The positions of the Hα shell as measured by Meaburn and the HI shell #91 are overlaid. The corresponding Hα dataset is shown on the top right of the figure. A line overplotted in both panels indicates the position and direction of the position-velocity map shown in the bottom of the Figure. The position-velocity map clearly shows the expanding HI shell #91 as an ellipse in HI brightness.

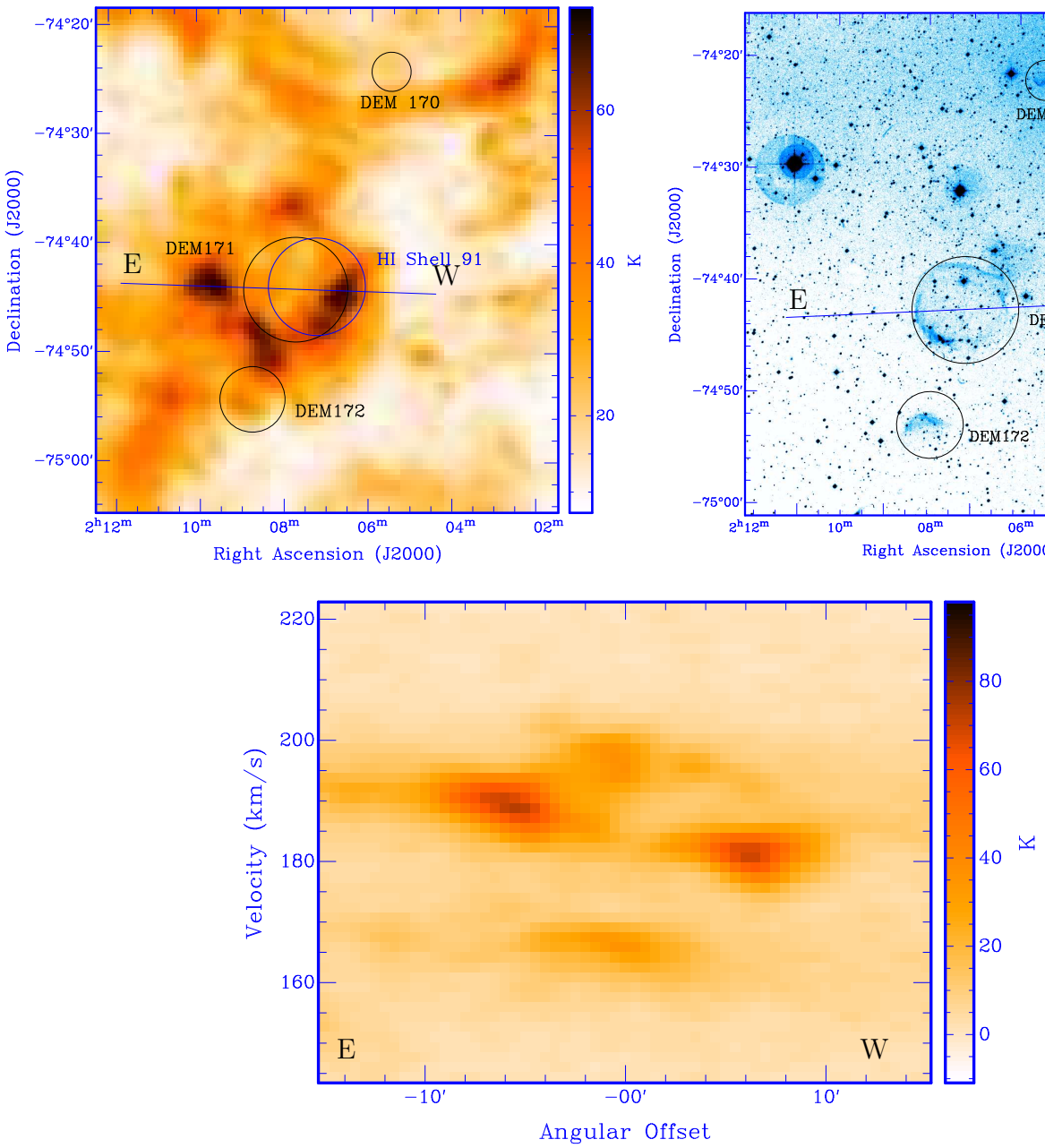

Figure 7.4: (*Top left*) HI map of region around shell #91 overlaid with the positions of the numbered Hα 'nebulous' regions (from Meaburn 1986). The HI shell is shown to be closely aligned with the Hα shell DEM171 (*top right*). Also shown are DEM172 and DEM170, two of the other Hα 'nebulous regions'. In the case of DEM172, this corresponds to a small local HI intensity maximum (for this peak temperature map), although there is no clear HI shell associated with this object. The Figure has a linear transfer as shown in the colourbar. The blue line at approximately -74° 44′14″ shows the position and direction of the section shown at the bottom of the figure. This cut shows the receding and approaching sides of an expanding shell at ∼185 km s^{-1} and ∼196 km s^{-1} (heliocentric).

The ionising mechanism of this HI +Hα shell is still not confidently known. Meaburn (1986) suggests a single O star is responsible for the illumination of the Hα shell. Parker has commented that UV source FAUST 392 corresponds closely to the centre of the shell, is probably a low surface brightness Planetary nebula (PN) or even a supernova remnant, although the low energy derived in the this study does not suggest a typical supernova as the expansion mechanism for this shell. Graham et al. (2001) have located a candidate Wolf-Rayet (WR) within the shell rim and suggest that this object may be the source of ionisation and the resulting Hα emission feature. The general concensus is that the ionisation of the ISM is by radiative heating from a central source. The circular morphology of the Hα feature is certainly consistent with this interpretation.

Table 7.2 shows that the age and radius determined here for shell #91 as derived from the HI data is in general agreement with these parameters determined from Hα data by Meaburn (1986), although there is considerable discrepancy of the expansion velocity and hence the kinematic age with findings of Graham et al. (2001). Figure 7.4 shows a slice through the HI datacube at -74° 44′14″. We see bright regions in the bottom panel of Figure 7.4, at Heliocentric velocities of ∼185 km s^{-1} ∼196 km s^{-1} which can are interpreted as the approaching and receding sides of the shell. We do not find any HI emission at the higher velocity of ∼225 km s^{-1} corresponding to that measured in Hα as measured by Graham et al. (2001).

7.2.2 Object DEM172

DEM172, (Meaburn, 1986) is shown in Figure 7.4 as a slight crescent-shaped feature. This feature was not considered in any detail by Meaburn and some analysis is attempted here.

As shown in Figure 7.4 this feature does not appear to be associated with any HI expanding shell, although it does show a coincidence with an HI clump, the geometry of which is otherwise unremarkable. Table 7.3 lists distances for all catalogued objects within 3′ of DEM172. The objects listed here are seen to be exclusively OB associations from Demers & Irwin (1991), along with a FAUST detection. All or any of these objects are theoretically able to ionise such a feature on their own, however, DI91 529 is clearly the object closest to the centre of the feature and is in fact located inside the crescent-like shape, on the southern side. This association is also very bright visually and in the blue

Object	Position [HMS DMS] (J2000)	Angular Sep. [′]	Projected Sep. [pc]	Visual Mag. [M_v]	B-V Colour ind.
[DI91] 529 [1]	**02:08:54.1** -74:55:06.0	**0.47**	**8.2**	**15.58**	**-0.5**
[DI91] 500[1]	02:08:38.7 -74:54:30.0	1.07	18.7	17.21	-0.31
[DI91] 495[1]	02:08:35.5 -74:55:08.0	1.36	23.8	16.16	-0.54
[DI91] 508[1]	02:08:40.7 -74:55:43.0	1.43	24.9	17.55	-0.33
FAUST 394[2]	02:08:38.0 -74:56:36.0	2.26	39.4		

[1]Demers & Irwin (1991)
[2]Bowyer et al. (1995)

Table 7.3: Table of distances for catalogued objects within 3 arcmin of Hα feature DEM172. Bold entries indicate the objects nearest the Hα feature.

band. Apart from this, there is no reason that all of these objects do not contribute to the ionisation of the local HI and indeed, the beamsize of FAUST ($\sim 2'$, Bowyer et al. 1995) is such that this detection may be due to any or all of the objects listed in Table 7.3. Without Hα flux measurements, there is no way to estimate the strength of the Hα emission and then to estimate the exact source of ionising radiation.

7.2.3 Object DEM170

The feature catalogued as DEM170 is one of the smallest and most curiously shaped objects from the extended DEM catalogue. It can be seen in the right panel of Figure 7.4 as a small inverted crescent. The left panel of Figure 7.4 shows no correlation of this Hα feature with any HI structure, however, the resolution of these observations may be too large to discern a related HI feature. Table 7.4 lists OB associations and potential ionisation sources within a few arcminutes of this feature. In this case, we see that the OB association DI91 173 is closest to the Hα feature and also is located almost within the crescent. Again, Hα spectroscopic measurements will help understand the exact ionisation mechanism.

Object	Position [HMS DMS] (J2000)	Angular Sep. [′]	Projected Sep. [pc]	Visual Mag [M_v]	B-V Colour ind.
[DI91] 173[1]	02:05:39.1 -74:23:40.0	**0.70**	**12**	18.4	-0.29
[DI91] 199[1]	02:06:0.6 -74:24:36.0	1.40	24.5	17.68	-0.32
[DI91] 158[1]	02:05:23.0 -74:25:30.0	1.61	28.1	17.35	-0.42
[BS95] 226[2]	02:05:46.0 -74:22:42.0	1.71	29.9		

[1]Demers & Irwin (1991)
[2]Bica & Schmitt (1995)

Table 7.4: Table of distances for catalogued objects within 2 arcmin of Hα feature DEM 170. Bold entries indicate the objects nearest the Hα feature.

7.2.4 Objects DEM168, DEM169

Figure 7.5 shows the peak temperature HI (*upper left*) and Hα (*upper right*) maps for the area around DEM168 and DEM 169. DEM 168 and DEM 169. We will assume that DEM 168 is associated with the diffuse part and DEM 169 is the relatively bright filament, with little diffuse component.

A section through the HI cube is indicated by the blue line in the upper maps of Figure 7.5 and shown in the position-velocity map in the lower part of the Figure. We see that DEM168 correlates well with an apparently expanding HI region. This location is co-indicent with the position of shell #100 from the HI expanding shell Catalogue in Chapter 4. This shell has an estimated kinetic age of 9.9 Myr and a luminosity of $10^{48.6}$ ergs. The luminosity of this shell is quite low. Under the assumption that the shell expansion has been driven by stellar winds, a single low mass B or A type star would be capable of depositing this amount of energy into the ISM.

Figure 7.5 shows a non-circular shape to the Hα emission region DEM168, which appears to delineate the southern, but not the northern boundary of an HI clump. This is actually quite tenuous HI which has a relatively large optical depth for any ionising radiation.

Table 7.5 lists distances of catalogued objects found within 5 arcmin of the combined Hα feature DEM168-DEM169. The closest objects to DEM 168 and DEM 169 are DI91 748 and WG71 II 45 respectively. These are both young OB associations and DI91 748

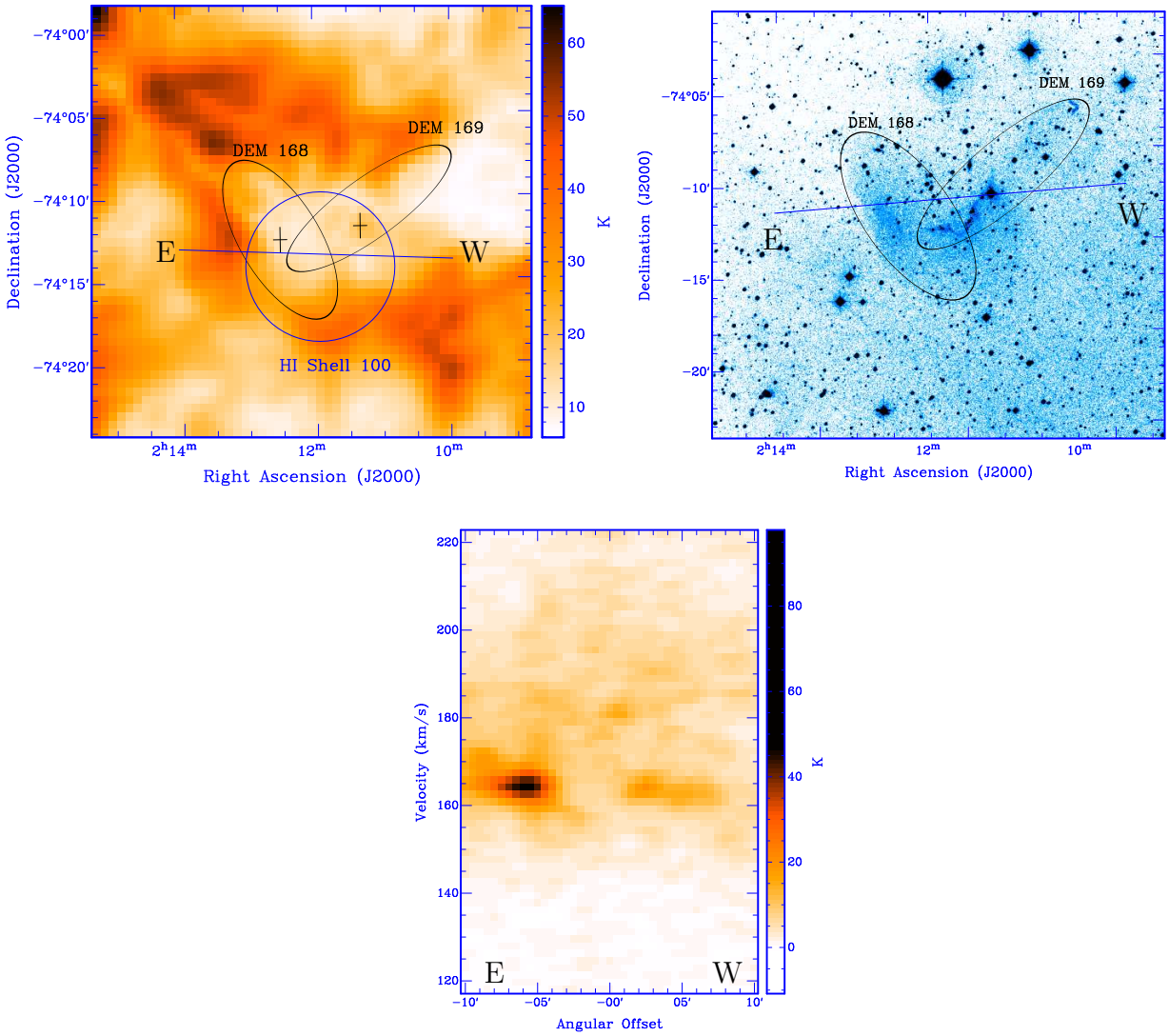

Figure 7.5: (*Top left*) HI (shell #100) and numbered Hα 'nebulous' regions (from Meaburn 1986), overlaid on magnified HI RA-Dec peak temperature map. This is another example of an HI shell shown to be closely aligned with an Hα feature. In this case, shell #100 from the catalogue in Chapter 4 is shown to be closely associated with the Hα feature DEM169 (*top right*). The crossed indicate the positions of centres of the objects. The HI map has a linear transfer as shown in the colourbar. The blue line at approximately -74° 11′47″ shows the position and direction of the cut through the HI datacube shown in the bottom of the figure. This shows the receding and approaching velocities of this shell as 170 km s^{-1} and 156 km s^{-1} (heliocentric) respectively. The cut was made close to the centre of the HI shell.

is particularly bright. Magnitude information is not available for the WG association catalogue. In this case there may be a combination of phenomena giving rise to the observed Hα emission. The expanding shell indicates a centrally located energy deposition source, possibly driving a shock front and the diffuse, extended nature of the Hα emission suggests additional heating via radiation from some hot source.

7.3 New Hα Features of the Magellanic Bridge

This part of the Chapter will present new and un-catalogued Hα regions in the Bridge. The new objects found here will be presented in order from east to west.

7.3.1 Objects MBHa8-11

Figure 7.6 shows an expanded view from Figure 7.2 centred on the Hα emission associated with with the Hα objects MBHa8-11. These objects are spatially close and to some extent, appear geometrically similar. As such, they will be discussed concurrently in this section.

Overlaid on Figure 7.6 are the positions of catalogued objects within a 5′ radius from the centre of the object cluster (shown by the circle in the figure). Shown in Table 7.6 are the positions of the catalogued objects with their angular and projected spatial separations from each of the four Hα features MBHa8-11. These features will now be discussed in some detail:

7.3.1.1 Object MBHa11

Object MBHa11 is the the brightest of the four Hα objects MBHa8-11. It shows a very diffuse morphology, with little discrete component. Figure 7.6 and Table 7.6 show that the object 1 is spatially co-incident with OB associations BS95 217, BS95 216 (Bica & Schmitt, 1985) and also with the object IRAS 0162-7430. From the Bica & Schmitt catalogue, we find that there is some confusion between BS95 217 and BS95 216 in that it BS95 216 may in fact be a more centrally condensed part of the much larger OB association BS95 217. In any case, these OB associations are likely candidates for radiatively ionising the local ISM and giving rise to the observed Hα emission from this object.

We can see also that IRAS object 01562-7430 is also spatially co-incident with this object.

Object	Position	DEM168		DEM169		Magnitude	B-V
	[HMS DMS] (J2000)	Sep.[′]	Sep.[pc]	Sep. [′]	Sep. [pc]	[U V B]	Colour ind.
[DI91] 719[1]	02:11:55.7 -74:12:37.0	2.42	42.2	2.55	4.46	15.24 [V]	-0.41
[DI91] 701[1]	02:11:40.8 -74:12:40.0	3.43	59.9	1.64	28.7	15.71 [V]	-0.2
[DI91] 708[1]	02:11:45.8 -74:11:19.0	3.35	58.4	1.83	32.0	17.56 [V]	-0.36
FAUST 409[2]	02:11:52.0 -74:11:12.0	3.01	52.6	2.27	39.6		
[WG71] II- 45[3]	02:11:30.0 -74:11:60.0	4.21	73.4	**0.70**	**12.2**	10.77 [v]	
[DI91] 737[1]	02:12:16.3 -74:12:31.0	1.02	17.8	3.89	67.9	18.18 [V]	-0.25
[DI91] 717[1]	02:11:55.0 -74:10:48.0	3.05	53.3	2.60	45.4	16.25 [V]	-0.38
[DI91] 676[1]	02:11:13.7 -74:13:47.0	5.40	94.3	2.00	34.8	16.43 [V]	-0.43
[DI91] 742[1]	02:12:24.2 -74:11:16.0	1.42	24.7	4.41	76.9	18.47 [V]	-0.28
[WG71] II- 79[3]	02:12:24.0 -74:11:00.0	1.67	29.2	4.44	77.5	14.1 [V]	
[DI91] 748[1]	02:12:31.1 -74:11:39.0	**0.95**	**16.6**	4.84	84.6	17.39 [V]	-0.28
[DI91] 731[1]	02:12:09.7 -74:09:54.0	3.07	53.6	3.90	68.1	18.3 [V]	-0.21
[DI91] 746[1]	02:12:29.3 -74:10:44.0	1.87	332.7	4.85	84.6	16.62 [V]	-0.51
[DI91] 739[1]	02:12:18.7 -74:09:51.0	2.88	50.2	4.47	77.9	14.05 [V]	-0.38
[WG71] II- 82[3]	02:12:24.0 -74:09:60.0	2.65	46.2	4.73	82.6	14.1 [V]	
[DI91] 738[1]	02:12:16.9 -74:09:36.0	3.15	55.1	4.48	78.1	17.8 [V]	-0.32

[1]Demers & Irwin (1991)
[3]Bowyer et al. (1995)
[3]Westerlund & Glaspey (1971)

Table 7.5: Table of distances for catalogued objects within 5 arcmin of Hα features DEM 168 and DEM 169. Bold entries indicate the objects nearest the Hα feature.

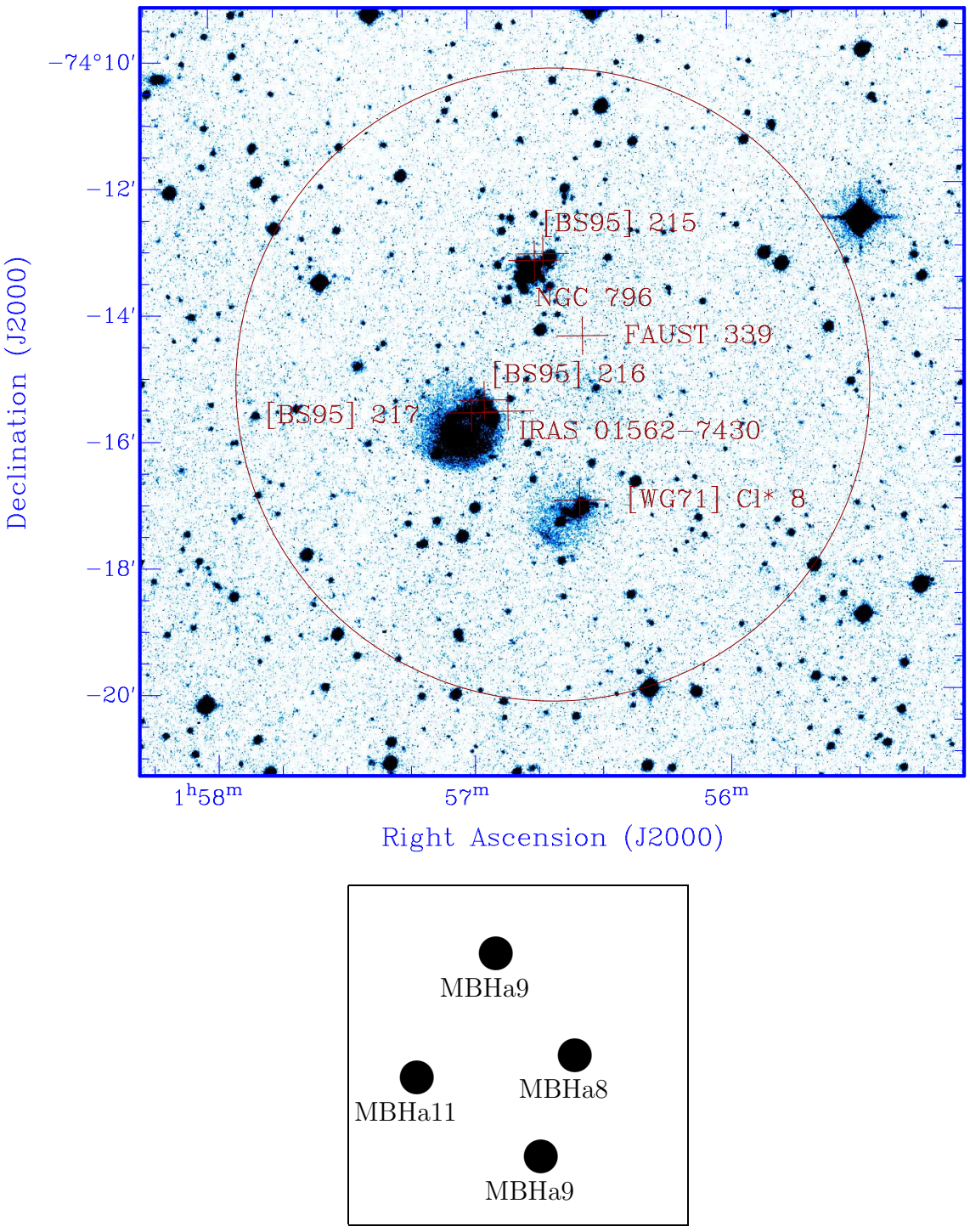

Figure 7.6: *Top:*) Magnification of the Hα objects MBHa8-11 (see Figure 7.2, bottom) (Locator map is shown on *bottom*). Over plotted here are the positions of the four objects and also those of catalogued sources within a 5 arcmin radius around the objects (shown by the circle). The colour scale is arbitrary and is selected to maximise the contrast.

Object	Position	MBHa11		MBHa10		MBHA9		MBHa8		Additional
	[HMS DMS] J2000	dθ [′]	dr [pc]	dθ [′]	dr [pc]	dθ [′]	dr [pc]	dθ [′]	dr [pc]	Information
IRAS 01562-7430[1]	01:56:51.5 -74:15:35.0	0.71	13	2.47	43.1	1.76	30.8	1.56	27.2	
FAUST 339[2]	01:56:34.0 -74:14:24.0	2.27	39.5	1.41	24.6	2.60	45.4	**0.69**	**12**	
[BS95] 216[3]	01:56:57.0 -74:15:24.0	0.41	7.2	2.40	41.9	2.14	37.4	1.87	32.6	OB Cluster
[BS95] 217[3]	01:57:0.0 -74:15:36.0	**0.14**	**2.4**	2.66	46.5	2.15	37.6	2.11	36.9	OB Cluster
[WG71] Cl 8[4]	01:56:35.0 -74:16:60.0	2.28	39.9	3.88	67.8	**0.07**	**1**	2.00	34.8	OB Cluster
NGC 796[5]	01:56:45.0 -74:13:12.0	2.69	47.0	**0.08**	**1.3**	3.85	67.2	2.10	36.6	Star Cluster
(Also WG71 CL) 9[4]										OB Cluster
[BS95] 215[3]	01:56:43.0 -74:13:06.0	2.84	49.6	0.10	1.7	3.93	68.6	2.13	37.1	OB Cluster

Table 7.6: Positions and angular and spatial separations of of Hα features MBHa8 - 11 and catalogued objects within a 5 ′radius. The bold entries indicate the catalogued objects closest to each of the Hα features.

[1] Kleinmann et al. (1986)
[2] Bowyer et al. (1995)
[3] Bica & Schmitt (1995)
[4] Westerlund & Glaspey (1971)
[5] Dreyer (1888)

This represents a detection of warm dust, heated by the absorption of higher energy radiation from nearby stars. The co-incidence of these objects point to the existence of a star-forming region. To confirm the star formation scenario, this location should be explored further at molecular transition wavelengths.

7.3.1.2 Object MBHa10

This feature is shown to be much less diffuse than object 11 and appears as a collection of bright, discrete clumps of Hα emission. This feature is very closely aligned with the Stellar cluster NGC 796 (Also WG71 9, Westerlund & Glaspey, 1971) and also with BS95 215 from the Bica & Schmitt (1995) catalogue. The Bica & Schmitt catalogue refer to NGC 796 as being 'inside' BS95 215. We assume then that these refer to the same object. Overall, this feature is clearly radiatively heated and may be a slightly more evolved stellar cluster, which has blown much of its ambient gas and dust away.

7.3.1.3 Object MBHa9

MBHa9 shows a discrete clumpy component as well as a slightly diffuse and extended component. It is closely aligned with the Westerlund & Glaspey (1971) object WG71 Cl 8. These authors make no special comment about this object. In the absence of any other likely mechanism, WG71 8 is again a possible young stellar association involved in ionising the ISM. The association may be at a later evolutionary stage than for MBHa2 and more of the ambient ISM remains nearby.

7.3.1.4 Object MBHa8

This feature is the faintest of the apparent sub-group of objects MBHa8-11 and there are no catalogued objects that are clearly associated with it. Although the FAUST 339 object is the closest, it is not centrally located in the Hα object. The ionisation mechanisms for this object are entirely unclear, possibly this object is in the very beginning stages of star formation and young proto-stars inside the cloud have begun to ionise the nearby hydrogen gas.

Figure 7.7 shows an HI integrated intensity map of region corresponding to that from Figure 7.6 and we see here that all Hα regions are confined to relatively high HI column

Object	Position [HMS DMS] (J2000)	Angular Sep. [′]	Projected Sep. [pc]
FAUST 333[1]	01:54:54.0 -74:30:00.0	**7.39**	**128.9**
FAUST 348[1]	01:58:48.0 -74:31:06.0	8.34	145.6
FAUST 343[1]	01:57:26.0 -74:40:06.0	9.28	162.0
FAUST 331[1]	01:54:38.0 -74:36:42.0	9.93	173.4

[1] Bowyer et al. (1995)

Table 7.7: List of distances for catalogued objects within 10 arcsec of Hα object MBHa7. The bold entries indicate the catalogued objects closest to the Hα features.

densities. Interestingly, they also appear to be on the periphery of a shell or crescent-like feature. Although we see no expanding HI shell associated with this location (Table 4.1), this may comprise the rim of an old expanding region that has since ruptured or deformed beyond recognition.

7.3.2 Object MBHa7

Hα Object MBHa7 as shown in Figure 7.8 appears to have a very linear morphology. The circle marked in the figure indicates the spatial radius which defines the limits of a search for catalogued objects. The circle is considerably larger than the Hα region in an effort to locate any objects which may be related to the Hα region. Table 7.7 lists the positions of each of the catalogued objects and their distances from the centre of this Hα feature. The Figure and the table suggest that no observable OB associations or UV sources are conveniently associated with this Hα region.

It is also difficult to correlate any HI features to this object. Figure 7.9 shows the RA-Dec and Vel-Dec projections of an HI subcube around the Hα object MBHa7. The Figures show that there are no real HI features in position or velocity that correlate particularly well with the spatial extent of the Hα region.

Some image manipulation to remove the brightest sources from the Hα dataset and some subsequent smoothing reveals some faint and very small arc-like extensions to this Hα region. Figure 7.10 (*top*) shows a highly contrasted and smoothed Hα image of object MBHa7. The loop appears to extend to the north and is contiguous with the main body of Hα emission. The loop is slightly flattened in Declination and has a radius of $\sim 1'15''$ and

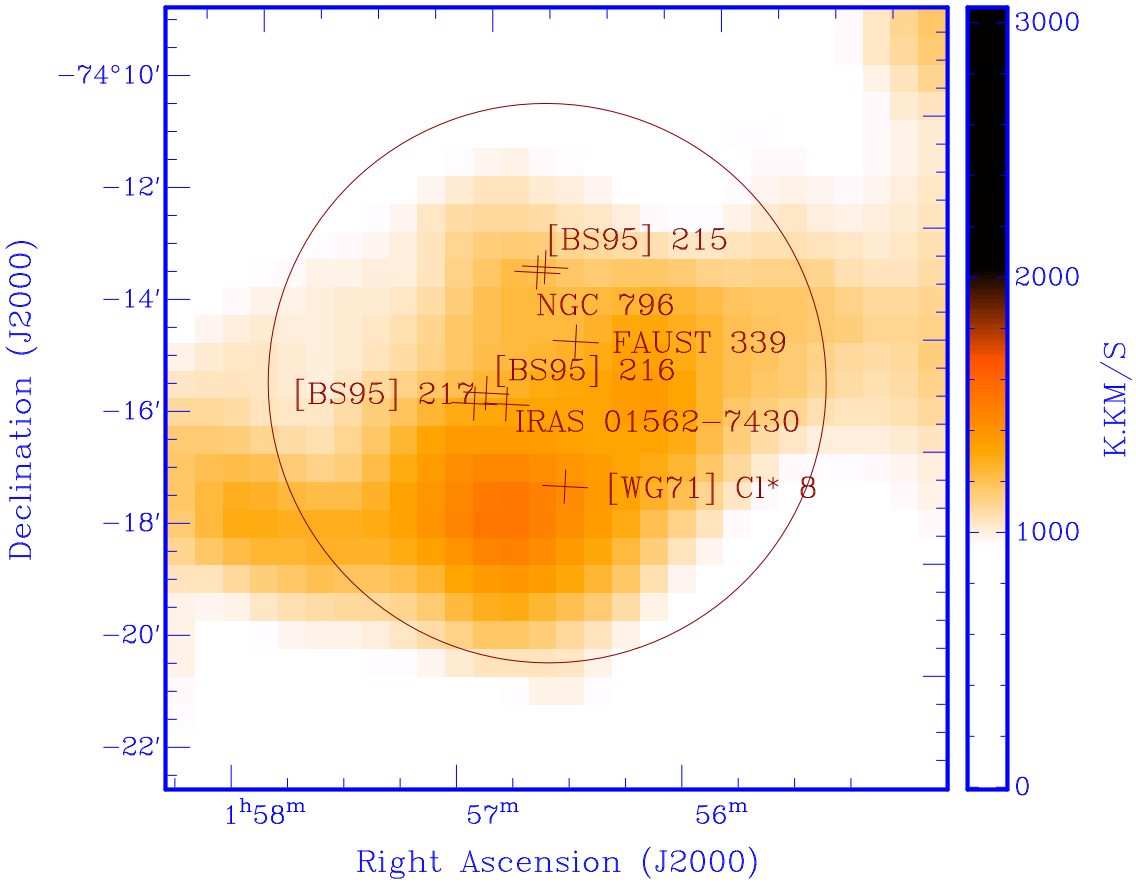

Figure 7.7: HI region corresponding to that from Figure 7.6 and encompassing the locations of MBHa8-11. All catalogued (and Hα) objects appear to be located on the edge of a high HI column density crescent.

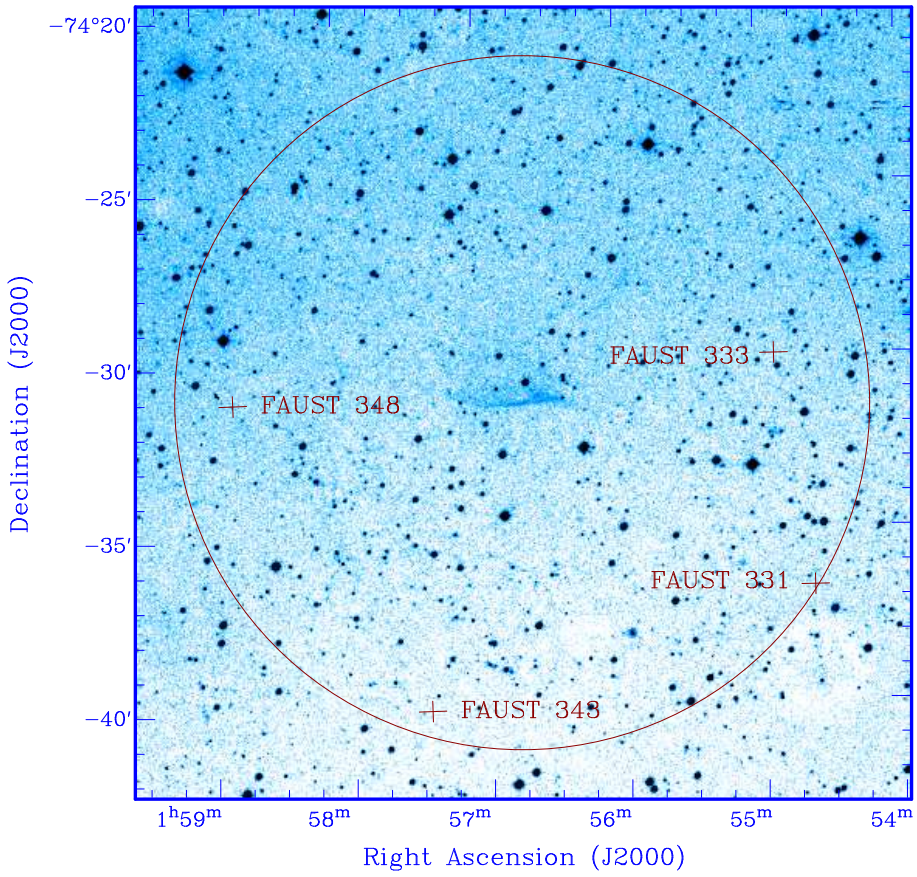

Figure 7.8: Magnification of the Hα object MBHa7 (see Figure 7.2, bottom). Over plotted here is the catalogued position of the objecct and also those of catalogued sources within a 10 arcmin radius around the objects (shown by the circle). The colour scale is arbitrary and is selected to maximise the contrast.

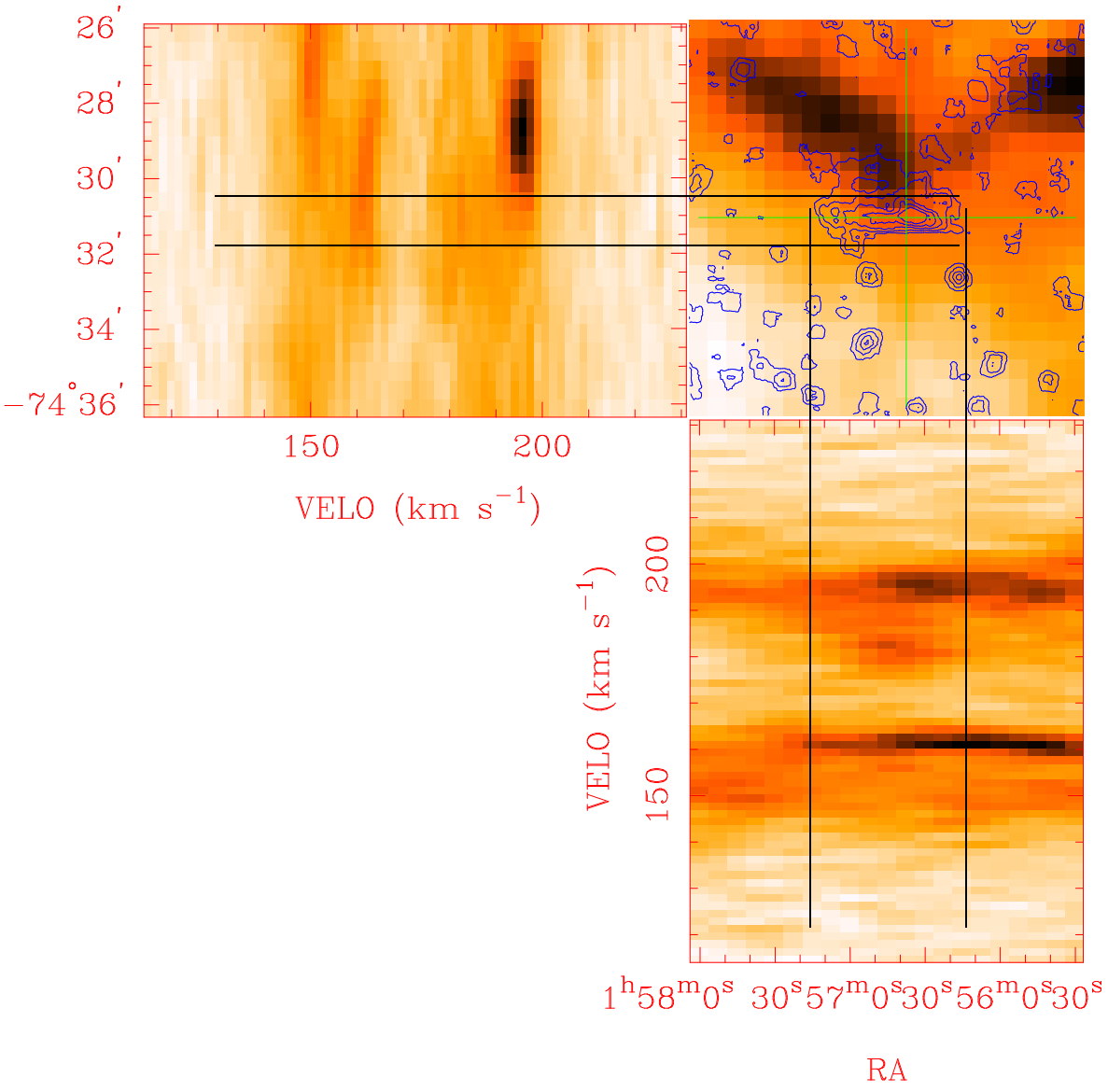

Figure 7.9: HI subcube around Hα region MBHa7. The RA-Dec (*Top-right*) shows the integrated HI intensity, overlaid with the Hα contours (intervals in 10% of maximum Hα intensity). The colour scale is a linear transfer funciton, the RA-Dec. projection has a maximum-minimum intensity of ∼237-74K·km s^{-1}. The velocity projections have a maximum-minium intensity of 32-0 K. The dotted green lines show the positions of the RA-Vel (*Top-left*) and Vel-Dec (*Bottom*) slices. The black lines indicate the spatial extent of the Hα region in the RA and Dec. directions. There is some suggestion of an HI feature in the RA-Vel projection at around 180 km s^{-1} (helicentric), although there is no corresponding features in the Vel-Dec projection.

$\sim 1'40''$ in the NS and EW directions respectively. Such a loop in Hα is usually indicative of an expanding region, powered by a centrally-positioned energy source, such as a bright star, or other energetic object. This kind of small-scale is below the resolution of the HI dataset presented in Chapter 2 so we cannot examine the morphology of the HI for a similar construction. It should be noted that this faint emission is only approximately 2.3 times that of the noise.

The Hα map of Figure 7.10 also shows a series of vertical lines overlaid. These show the position and direction of the traces in the lower panels of Figure 7.10. It can be seen that this Hα region has a sudden increase in brightness on the southern edge, while the brightness of the northern side appears to taper somewhat. This morphology is suggestive of a shock interface, where in impacting cloud shocks the ISM, thereby exciting the ISM. Futhermore, this Hα feature appears to be isolated with no other bright Hα regions or catalogued OB associations nearby. Despite a lack of any HI features which we can relate to this object, from these considerations we can suggest that this Hα feature has been generated through a cloud-cloud collision.

7.3.3 Object MBHa6

This Hα feature appears to have a fairly large and complex structure. From Figure 7.11 (*top*), we can see that the general appearance is of three loops arranged around a brighter somewhat central feature. There are numerous catalogued objects that may be associated with this Hα feature. Figure 7.11 also shows the positions of catalogued objects found within 10 arcmin of the centre of the feature. The positions of the catalogued objects and their distances from the centre of MBHa6 are listed in Table 7.8.

No catalogued objects coincide exactly with the brightest central part of MBHa6. There is a clustering of objects around RA $1^{\rm h}\,50^{\rm m}$, Dec. $-74^\circ\,8'$(J2000), in particular, the detection FAUST 318 is located close to this position. Given the relatively central location of the FAUST object within MBHa6, it is a reasonable guess that this object may be a significant source of ionisation flux for this Hα region.

The corresponding integrated intensity HI map, also in Figure 7.11 (*bottom*), shows there is a small degree of correlation between the extent and morphology of the Hα region and that of the HI. In particular, the brightest Hα region corresponds well with a moderately

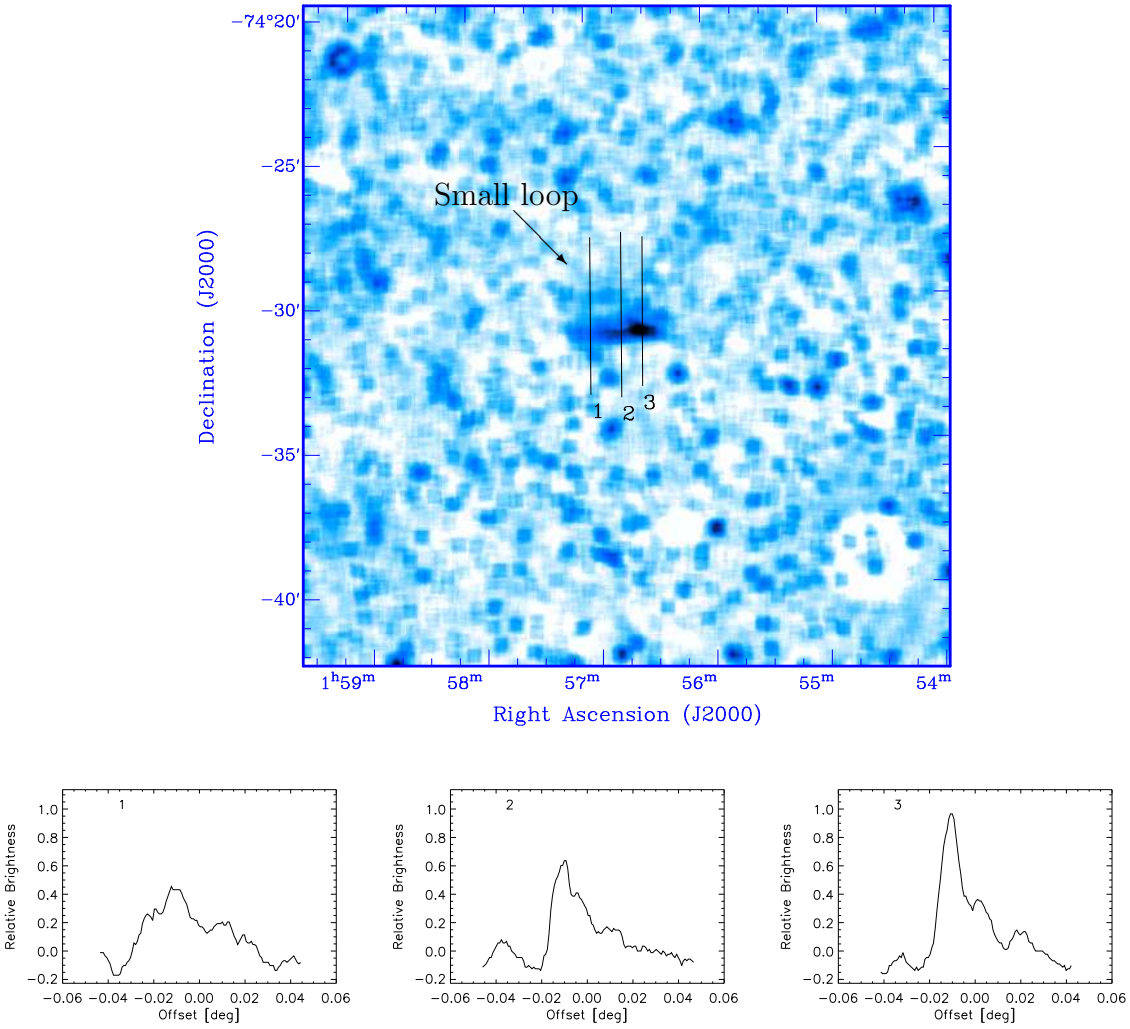

Figure 7.10: Clipped and smoothed map of Hα emission around object MBHa7 (*Top*) and intensity traces (*Bottom*). The overlaid lines show the positions of the traces shown under the figure. The direction is from south to north in each case. The steep southern increase in brightness is most obvious in the middle and rightmost traces (2 and 3). Trace 3 passes directly through the position of maximum Hα emission.

bright HI region and also we see that the general shape of the Hα region appears to correlate well with the lower density regions of the HI map. As for DEM169, this may be due to the relatively low volume density allowing a large optical depth and a deeper penetration by ionising radiation.

We notice from Table 7.8 that three objects (including a FAUST object) are closest to the centre of the feature. Object 3 (SkKM 357) is listed in the catalogue of late-type super giant stars, compiled by Sanduleak (1989). Such a late-type star can hardly have the necessary flux output in the UV range to be notable by FAUST. It is likely then, that object 1 (OM 19), from the catalogue of high-velocity stars (Carozzi, 1971) is responsible for this FAUST detection. We notice that this object is a bright B type star and as such, this object may also be responsible, at least in part, for ionising flux which has led to the Hα emission. The study by Carozzi (1971) for this object made measurements only of the velocity relative to the observatory of 115 km s^{-1} and as no date for the observations is given, we cannot convert this into a heliocentric velocity to ascertain its relationship to the Magellanic System.

We can see also from the Figure that the region around a number of the other catalogued objects (AMM77 88, BS95 205, UBV 1878 and WG71 5) appear also to be slightly ionised. These objects are all either OB associations, or individual bright stars and they may all be contributing to a pervasive, high energy flux which leads to the large Hα feature seen here.

7.3.4 Object MBHa5

The Hα object MBHa5 is slightly southwest of MBHa6 and as seen in Figure 7.12, it appears as a collection of bright points and does not show any extended or nebulous structure.

There are again numerous objects which may be nearby to this Hα feature. Those within 5 arcmin of this Hα feature are listed in Table 7.9, along with their distance from the centre of MBHa5. We see from the Figure that the object FAUST 317 is well spatially correlated with this Hα feature. Given the $\sim 2'$ beamsize of FAUST (Bowyer et al. 1995), it is likely that FAUST 317 is associated with this Hα object. There is also excellent agreement of MBHa5 with the ESO catalogue (Holmberg et al. 1974) which list this object as a

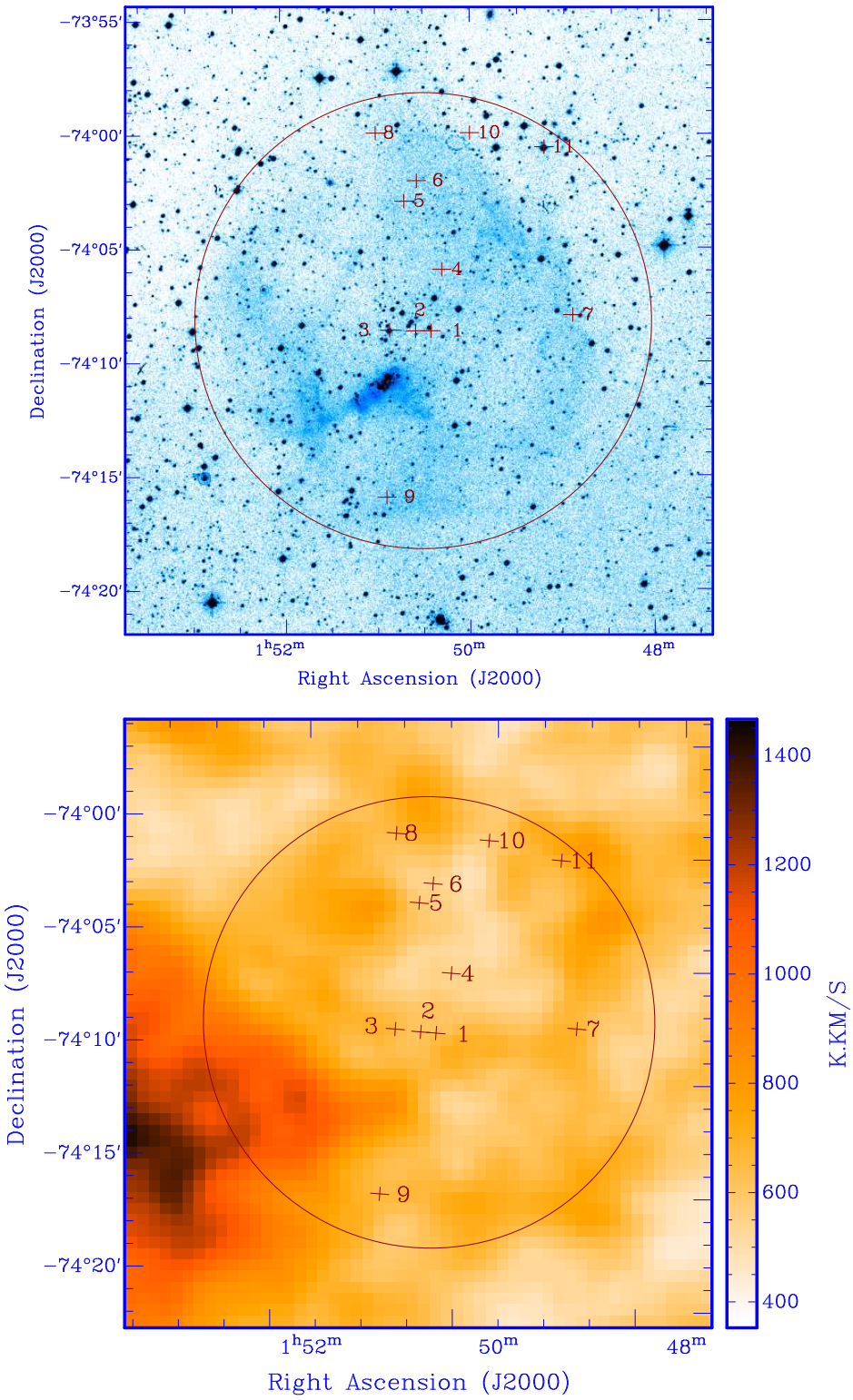

Figure 7.11: (*Top*) Magnification of Hα object MBHa6 (see Figure 7.2, bottom). The crosses indicate positions of catalogued objects. The circle indicates the limit of the catalogued search at 10 arcmin. The corresponding HI integrated intensity distribution (*bottom*) shows some correlation with the morphology of the Hα region, particularly with the brightest Hα region and we also see that the rim of the Hα region appears to trace the edge of the HI void. The key for the object numbering is on Table 7.8

Figure Reference	Object	Position [HMS DMS] (J2000)	Angular Sep. [′]	Projected Sep. [pc]	Magnitude [U V B]	Spectral Type	Additional Information
1	OM 19[1]	01:50:25.0 -74:08:42.0	**0.56**	**9.9**	12.4 [B]		High Velocity Star
2	FAUST 318[2]	01:50:35.0 -74:08:42.0	0.56	9.9			
3	SkKM 357[3]	01:50:51.6 -74:08:40.0	1.53	26.8			Late-type giant
4	UBV 1916[4]	01:50:42.0 -74:03:0.0	5.31	92.7	12.83 [B], 12.68 [V]	A2	
5	[BS95] 205[5]	01:50:34.0 -74:02:06.0	6.16	107			
6	UBV 1878[4]	01:48:54.0 -74:08:00.0	6.57	115	12.08 [B], 12.07 [V]	B6	
7	[WG71] Cl 5[6]	01:51:0.0 -74:00:00.0	8.50	148			OB Cluster
8	SMC ASS 70[7]	01:50:54.0 -74:16:00.0	7.92	138			Stellar Association
9	[AM77] 88[8]	01:49:12.6 -74:00:37.0	9.30	162	12.04 [B],12.11[V]	B8Ia3	High Velocity Star

[1]Obs. de Marseille Carozzi (1971)
[2]Bowyer et al. (1995)
[3]Sanduleak (1989)
[4]Blanco et al. (1968)
[5]Bica & Schmitt (1995)
[6]Westerlund & Glaspey (1971)
[7]Hodge (1985)
[9]Ardeberg & Maurice (1977)

Table 7.8: List of distances for catalogued objects within 10 arcsec of the geometric centre of the Hα complex, object MBHa6. The bold entries indicate the centre of the region, at $1^{\rm h}\,50^{\rm m}\,30^{\rm s}$ -74° 08′15″.

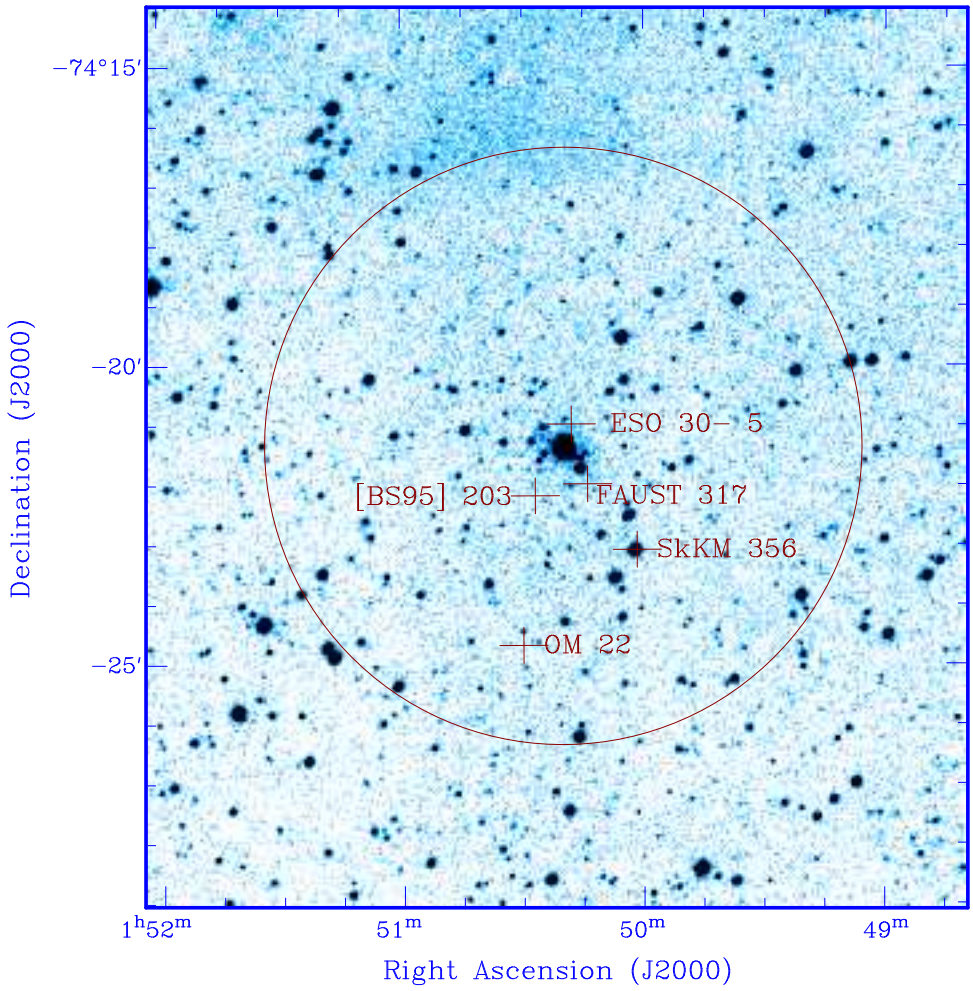

Figure 7.12: Magnification of Hα object MBHa5 (see Figure 7.2, bottom). The crosses denote positions of SIMBAD objects. The circle indicates the limit of the catalogued search at 5 arcmin around this object.

'Star Cluster'. In addition, we see that BS95 203 is also close, but not coincident with the centre of the Hα feature. Both BS95 203 and ESO 30-5 are close enough to confused with the beam of FAUST. FAUST 317 is probably an amalgam of detections from these two objects. This feature is clearly a stellar association/cluster. The observed Hα flux is probably pumped by the energetic radiation emitted from this cluster.

7.3.5 Objects MBHa3-4

The two Hα features MBHa3 and MBHa4 are shown in the Hα map of Figure 7.13 (*top*). MB Ha4 is the crescent-shaped feature, while MBHa3 is the smaller, more compact and almost round feature to the south-west of the crescent. The corresponding integrated

Object	Position [HMS DMS]	Angular Sep. [″]	Projected Sep. [pc]	Magnitude [U V B]	Spectral Type	Additional Information
ESO 30- 5[1] (Also Lindsay 114[2])	01: 50: 18.0 -74: 21: 00.0	**0.39**	**6.8**			Stellar Cluster
FAUST 317[3]	01:50:14.0 -74:22:00.0	0.75	13			
[BS95] 203[4]	01:50:27.0 -74:22:12.0	0.96	18			OB cluster
SkKM 356[5]	01:50:01.7 -74:23:06.0	02.13	37.1	13.5 [V]		Late-Type Giant
OM 22[6]	01:50:30.0 -74:24:42.0	03.40	59.4		B	High Velocity Star

[1]Holmberg et al. (1974) and papers of that series
[2]Lindsay, 1958
[3]Bowyer et al. (1995)
[4]Bica & Schmitt (1995)
[5]Sanduleak (1989)
[6]Obs. de Marseille Carozzi (1971)

Table 7.9: List of distances for catalogued objects within 5 arcsec of Hα object MBHa5. The bold entries indicate the catalogued objects closest to the Hα features.

intensity HI map for this region is shown as the bottom panel of Figure 7.13. We see that this figure is dominated by bright HI column density feature. The shape of MBHa4 is consistent with the edge of the HI feature and the peak of the HI column density is coincident with MBHa3. Although these features may not be spatially connected via Hα emission they are discussed concurrently in this section.

Over plotted on the Hα and HI maps of Figure 7.13 are the positions of all catalogued objects within 7 arcmin of the two features. Table 7.10 also lists these objects, as well as their distances from the two features.

7.3.5.1 MBHa4

From Figure 7.13 we see that three catalogued objects are appear to be spatially associated with MBHa4. These are WG71 3, a stellar cluster (Westerlund & Glaspey, 1971), FAUST #313 and IRAS 01489-7452. The fact that this region is observed by both FAUST and IRAS indicates some interesting kinematical and environmental conditions.

Figure 7.13 shows some faint evidence for some symmetry in the crescent-like shape of MBHa4 on the eastern side. Figure 7.14 shows the Hα map of Figure 7.13 subjected to a brightness cut-off and a 20 pixel square smooth mask. The true circular shape of MBHa4 is striking in this Figure, suggesting that this region is either being illuminated from a centrally located source and is thus heated radiatively, or is an expanding spherical shock and the ionisation arises from the transition of a supersonic shock front through the ISM. There is no entry in the expanding shell catalogue in Chapter 4 for an HI expanding shell at this location, nor are there any catalogued positions for an object inside the shell. The line, overlaid on Figure 7.14 indicates the direction and position of the position velocity cut through the HI cube shown in the bottom panel of Figure 7.14. The morphology of the HI position-velocity map does not show evidence for an HI expanding shell. The velocity resolution for the HI dataset as $\sim$1.6 km s^{-1} and we can estimate that if this feature *were* expanding, the maximum expansion velocity for this shell will be $\sim$4.9 km s^{-1}. This is not a high enough shock velocity to ionise the ISM into an Hα emission region. Therefore, this Hα region must be heated radiatively.

The WG71 object embedded in the brightest parts of the Hα emission is almost certainly responsible for additional ionisation. This region may in fact represent a site of star formation, perhaps catalysed by a past era of sudden compression of the ISM by the

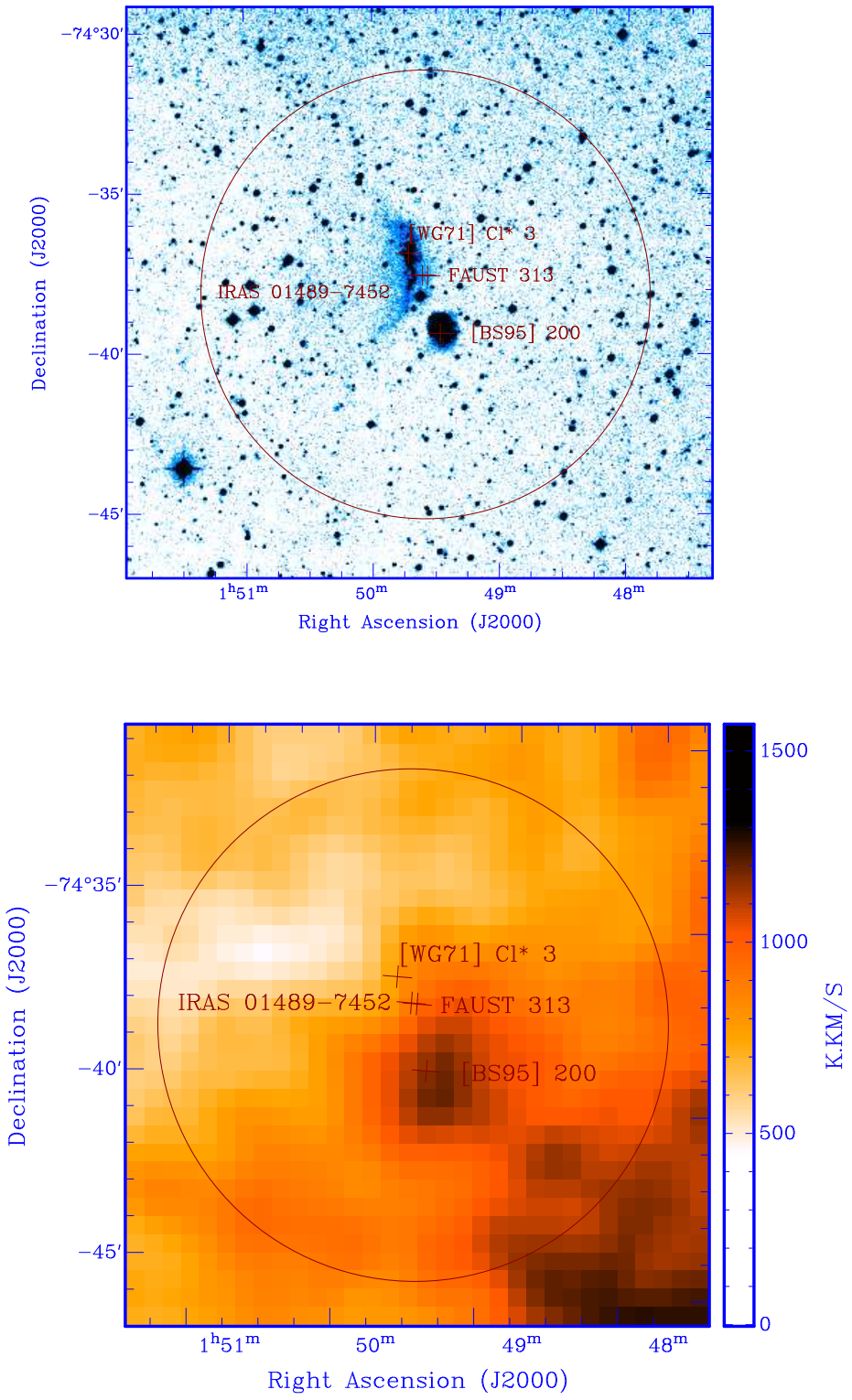

Figure 7.13: (*Top:*)Magnification of Hα objects MBHa3 and MBHa4 (see Figure 7.2, bottom). MBHa3 is the roughly circular diffuse region, while MBHa9 is the crescent shaped emission region (*Bottom*). An integrated intensity HI map, corresponding to the region shown above. Integrated intensities are shown in the colour bar. The crosses denote positions of catalogued objects. The circle indicates the limit of the catalogued search at 7 arcmin around these objects.

Object	Position	Hα Object MBHa4.		Hα Object MBHa4.		Additional
	[HMS DMS] (J2000)	Sep. [′]	Sep. [pc]	Sep. [″]	Sep. [pc]	Information
[WG71] Cl* 3[1]	01:49:43.0 -74:36:54.0	**1.55**	**27.1**	2.51	3.73	OB cluster
IRAS 01489-7452[2]	01:49:36.4 -74:37:35.0	1.90	33.2	1.71	29.8	
FAUST 313[3]	01:49:34.0 -74:37:36.0	2.06	36.0	1.65	28.8	
[BS95] 200[4]	01:49:28.0 -74:39:24.0	3.14	54.8	**0.20**	**3.5**	OB Cluster

[1]Westerlund & Glaspey (1971)
[2]Olnon et al. (1986)
[3]Bowyer et al. (1995)
[4]Bica & Schmitt (1991)

Table 7.10: List of distances for catalogued objects within 7arcsec of Hα object MBHa3 and MBHa4. The highlighted entries indicate the catalogued objects closest to the Hα features.

expanding shell. The FAUST detection is evidence of a high UV flux, while the IRAS detection is evidence for a high volume density. This region on the edge of the shell is an ideal candidate location for secondary star formation and is also a suitable environment in which to search for molecular transition lines.

7.3.5.2 MBHa3

There is only one catalogued object which is found to spatially correspond with this Hα object. Bica & Schmitt list BS2000 as 'nebulous'. As such, we know that this diffuse region is visible also in the Blue plates which formed the dataset for this survey.

The morphology of this object and the coincidence with the BS91 object suggests that this object is also likely to be a young star forming region and is also a pertinent position to observe for molecular tracers which are associated with such processes. This feature is undoubtedly ionised by the BI91 object, although continuum information must be studied for confirmation.

7.3.6 Objects MBHa2a and MBHa2b

Figure 7.15 (*top*) shows the structure of the distribution of Hα of MBHa2a-2b. MBHa2a is the south-eastern round region, while MBHa2b is the north-western region. It is unclear what relation parts a and b have with each other, however, visually, they appear contiguous in Hα and will be considered part of the same feature.

In general, the Hα emission for these objects is weak and tenuous. Figure 7.15 shows the distribution of the Hα , as well as the positions of relevant catalogued objects. Table 7.11 lists the positions for each of the catalogued objects, as well as the distances from the positions marked with a black circle + cross in the top panel of Figure 7.15.

The bottom part of Figure 7.15 shows the HI integrated intensity for a region slightly larger than that shown for the Hα emission. We see here that the Hα emission features are spatially coincident with a ring-like feature although we do not find any HI expanding shell centered on this loop-like feature in the HI expanding shell survey in Chapter 4. The morphology of the Hα does not trace the loop formed by the HI and as such, it is unlikely that the ionisation is caused by an energetic source centrally located in the torus.

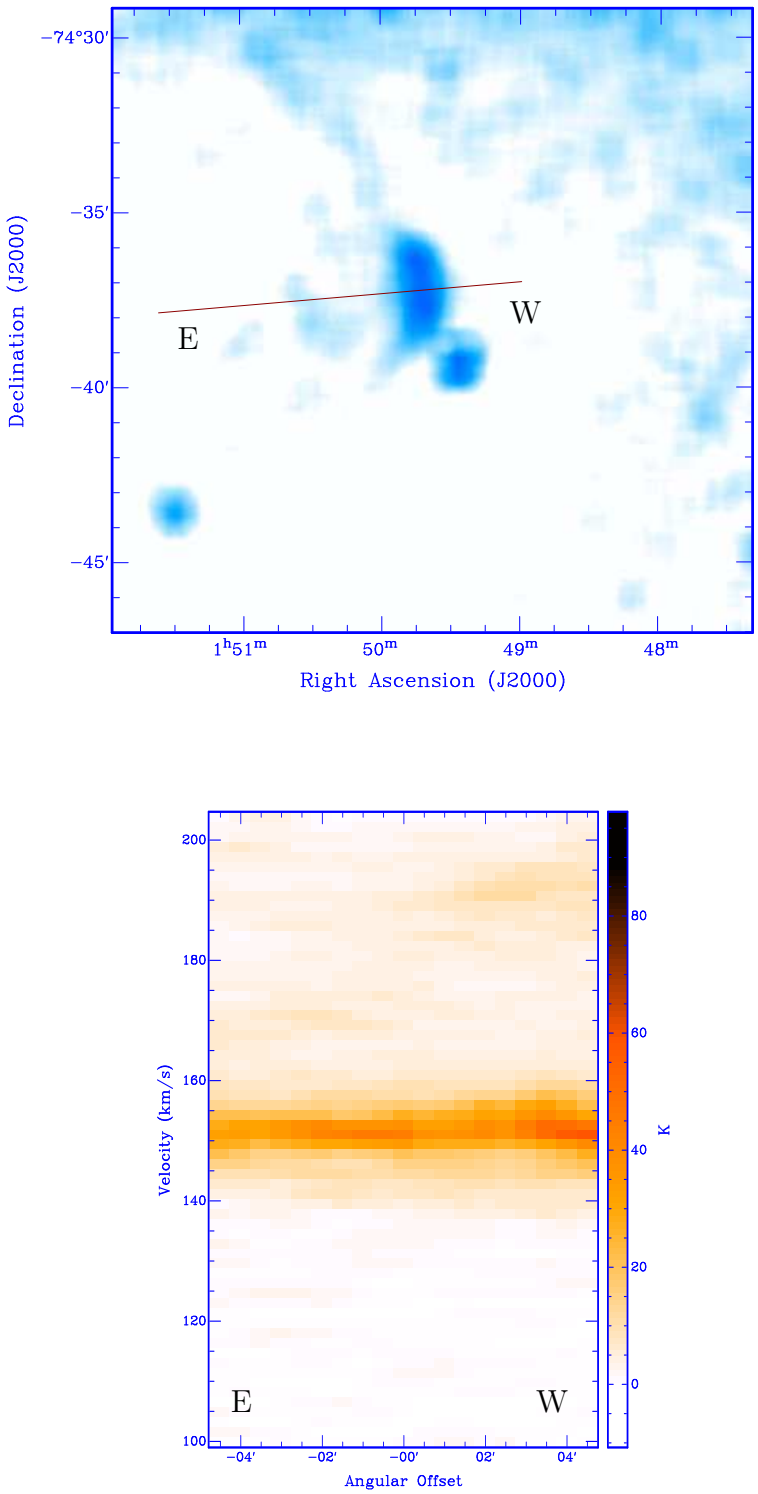

Figure 7.14: (*Top:*) Hα features MBHa3-MBHa4 with an 20 pixel (∼4 pc) smoothing. This figure emphasises the circular shape of this Hα figure. The Hα feature has a radius of ∼37.5 pc. The black line shows the direction and position of the cut made through the HI dataset. The position-velocity map along this line is shown (*bottom:*). This circular Hα cannot be associated with an expanding HI feature with a measurable expansion velocity associated with it (i.e. V_{exp} <4.89 km s^{-1}).

From the figure, we see there are no obviously bright Hα structures, although the positions of the catalogued objects correlate very well with the general distribution of the Hα emission. The most reasonable ionisation mechanism responsible for the Hα emission for these features therefore is via direct radiative heating from the nearby OB associations.

7.3.7 Object MBHa1a and MBHa1b

These objects shown in Figure 7.16 (*top*), appear as a prominent arcs, around which we see some fainter Hα emission. MBHa1a is the northern and longer Hα feature, and MBHa2 is the southern feature. The bottom panel of Figure 7.16 shows the integrated intensity HI map for the same region. We see that there are HI structures that roughly correlate with the Hα structures, although the correlation is not outstanding.

The morphology of Hα features themselves resemble that of a series of two or three bow shocks. We see from the expanding shell catalogue from Chapter 4 that there are no complete expanding shells that may be confidently associated with this Hα feature.

Over plotted on Figure 7.16 are the positions and locations of various catalogued objects within a 10 arcmin radius around the centre of this Hα object and we notice yet again that a FAUST object is nearby, as is the object AM77 85. AM77 85 is a B1 type, super-giant star, which is quite capable of ejecting enough energy into the ISM to cause ionisation. This object may also be responsible for the FAUST detection.

Other catalogued objects nearby this feature, such as the KDI reference, is a member of a catalogue for Carbon stars. This source is unlikely to have the UV flux necessary to ionise the ISM significantly.

7.3.8 Summary of new Hα features of the Bridge

Eleven new Hα features have been located within the Magellanic Bridge. Although the data has not been calibrated, this survey will serve as a useful reference from which more detailed analysis may be launched. Generally, many Hα objects are found in close proximity to a known sources of UV flux. These objects are all capable of causing the ionisation which leads to Hα emission. In some cases however, no candiate ionisation sources were identified.

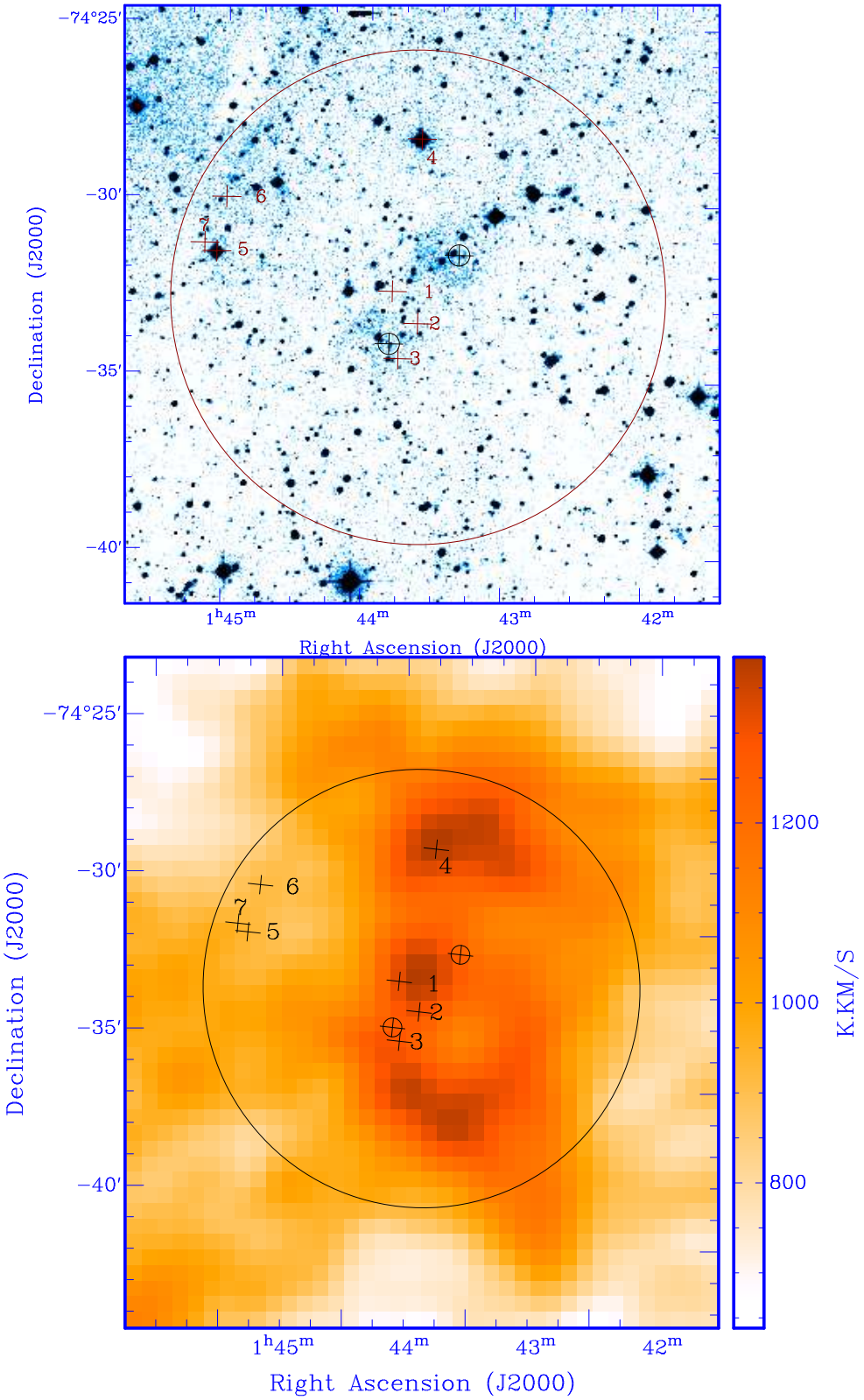

Figure 7.15: Magnification of Hα objects MBHa2a and MBHa2b (see Figure 7.3, top). The crosses denote positions of SIMBAD objects. The circle indicates the limit of the catalogued search at 7 arcmin around these objects. (*Bottom:*) HI integrated intensity for a slightly larger region than that shown in *top*. This Hα region appears to be located on the rim of a toroidal feature.

Figure Ref.	[HMS DMS] (J2000)	Position Sep. [′]	Hα Object 2a. Sep. [pc]	Hα Object 2a. Sep. [′]	Hα Object 2b. Sep. [pc]	Hα Object 2b. [U B V]	Magnitude Type	Spectral Information	Additional
1	[BS95] 193[1]	01:43:49.0 -74:32:36.0	1.48	25.9	**2.15**	**37.5**			OB Cluster
2	[BS95] 191[1]	01:43:38.0 -74:33:30.0	0.99	17.3	2.27	39.6			OB Cluster
3	[BS95] 192[1]	01:43:46.0 -74:34:30.0	**0.49**	**8.6**	3.40	59.4			OB Cluster
4	PPM 367367[2]	01:43:37.8 -74:28:16.1	5.87	102	3.45	60.3			PPM Catalogue
5	CPD-75 119[2] (also OM 15[3])	01:45:03.8 -74:31:32.5	5.54	96.6	6.86	120	11.74 [B],11.74 [V]	B9Ia	High Vel. Star.
6	LB 3226[4]	01:45:00.0 -74:30:00.0	6.20	108	6.78	118	13.03 [V]		Blue object
7	FAUST 294[5]	01:45:09.0 -74:31:18.0	5.95	103	7.21	126			

[1]Bica & Schmitt (1991)
[2]Roeser & Bastian (1988)
[3]Obs. de Marseille Carozzi (1971)
[4]Lee & Burkhead (1971)
[5]Bowyer et al. (1995)

Table 7.11: Positions and angular and spatial separations of Hα features MBHa2a-2b and catalogued objects within a 7 ′radius. The bold entries indicate the catalogued objects closest to each of the Hα features.

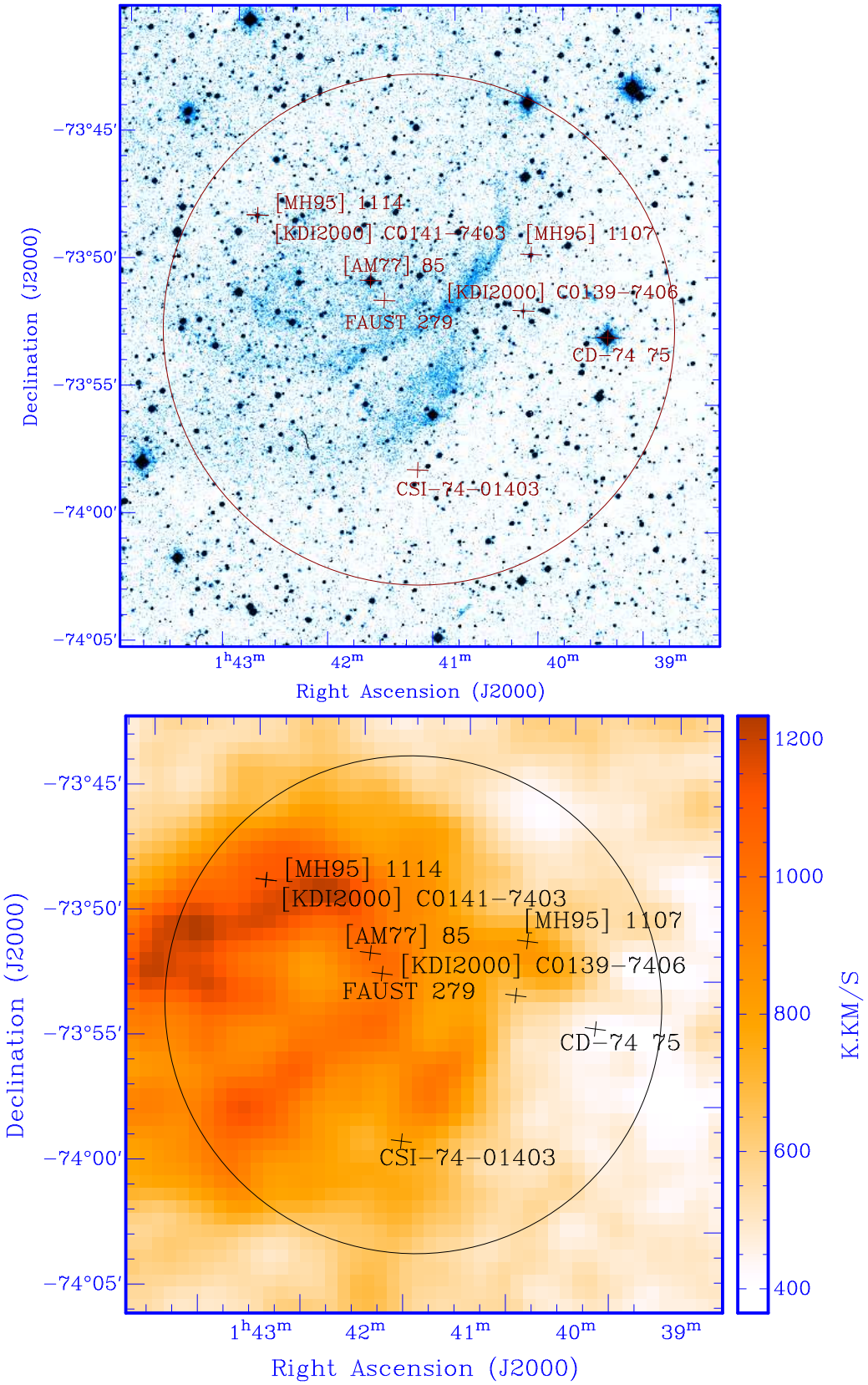

Figure 7.16: (*Top:*) Magnification of Hα objects MBHa1a and MBHA1b (see Figure 7.3, bottom). The crosses denote positions of SIMBAD objects. The circle indicates the limit of the catalogued search at 10 arcmin around the Hα objects. The corresponding HI region is shown *bottom*

Object	Position [HMS DMS] (J2000)	Angular Sep. [′]	Projected Sep. [pc]	Magnitude [U B V]	Spectral Type	Additional Information
FAUST 279[1]	01:41:34.0 -73:51:24.0	**1.77**	**30.9**			
[AM77] 85[2]	01:41:42.1 -73:50:38.0	2.70	47.1	11.86 [B],11.84[V]	B1.5Ia	
[KDI2000] C0139-7406[3]	01:40:15.5 -73:51:37.0	4.16	72.6			Carbon Star
[MH95] 1107[4]	01:40:12.4 -73:49:24.0	5.29	92.3			Carbon Star
UBV 1778[5]	01:41:12.0 -73:58:00.0	5.50	96.0	11.81 [B],11.88[V]	B0	
CPC 86794[6]	01:39:27.4 -73:52:32.0	7.40	129	10.78[B],10.21[V]	G0	
[MH95] 1114[4]	01:42:46.6 -73:48:12.0	7.75	135			Carbon Star
[KDI2000] C0141-7403[3]	01:42:46.7 -73:48:12.0	7.75	135			Carbon Star

[1]Bowyer et al. (1995)
[2] Ardeberg & Maurice (1977)
[3] Kunkel, Demers & Irwin (2000)
[4] Morgan & Hatzidimitriou (1995)
[5] Blanco et al. (1968)
[6] Jackon & Stoy (1954)

Table 7.12: List of distances for catalogued objects within 10 arcsec of Hα object MBHa1a. The bold entries indicate the catalogued objects closest to the Hα feature.

Table 7.13 summarises the Hα features and their proposed ionisation mechanisms as discussed here.

It should be once again stressed that this Chapter is only a reference to the positions of the Hα objects in the Bridge. Without continuum information, the processes of ionisation leading to the observed Hα emission are only speculative.

Hα Object	Proposed ionisation mechanism	Candidate energy source
MBHa11	Nearby radiative heating	WG71 79, BS95 216
MBHa10	Nearby radiative heating	BS85 215/NGC 789
MBHa9	Nearby radiative heating	WG71 8
MBHa8	Nearby radiative heating	FAUST 339?
	Kinetic heating?	
MBHa7	Collisional heating	??
MBHa6	Nearby radiative heating	OM 19, UBV 1916, BS95 205
		UBV 1878, WG71 5 SMC Ass70
MBHa5	Nearby radiative heating	ESO 30-5, BS85 203 (FAUST 317?)
MBHa4	Nearby radiative heating	WG71 3 (FAUST 313)
	Central radiative heating	??
	Collisional heating?	
MBHa3	Nearby radiative heating	BS95 200
MBHa2a	Nearby radiative heating	BS95 191, BS95 192, BS95 193?
	Kinetic heating?	
MBHa2b	Nearby radiative heating	??
	Kinetic heating?	
MBHa1	Nearby radiative heating?	AM77 65 (FAUST 279)
		MG95 110,UBV 1778

Table 7.13: Summary of new Hα regions detected in the Magellanic Bridge, showing possible ionisation mechanisms which may be responsible for producing the observed Hα emission.

Chapter 8

Search for CO regions in the Magellanic Bridge

"So, basically, you have detected an alien civilization who just drive around in a lot of really polluting cars?"
- Justin Ulland (aka 'Dipper'), 2001

The blue stellar population which have been found to be kinematically associated with the Magellanic Bridge are typically young, with ages ranging between 5 Myr to ∼100 Myr (Hambly et al. 1993; Grondin et al. 1990;Demers & Battinelli, 1998). Numerical simulations have indicated that the age of the Bridge is approximately 200 Myr (e.g. Gardiner & Fujimoto, 1996). The existing young stellar population found within the Bridge therefore was not tidally extracted from the SMC and instead have formed much more recently *in situ*. We expect then, that the Bridge will be host to sites of active star formation.

Sites of Carbon Monoxide (CO) emission have typically been regarded as indicators for sites of new star formation (e.g. Rubio et al. 1991) and yet despite the apparent young age of the stellar population in the Bridge, no CO emission regions have been found. This Chapter presents the outcomes of a preliminary search for CO in the Magellanic Bridge and will pave the way for future CO surveys in the Bridge and other low-metallicity regions.

Section 8.1 will elaborate on past CO and metallicity studies in and around the Magellanic Bridge and SMC. Section 8.2 details the candidate CO emission site selection procedure and Section 8.3 presents the observation tools and methods. Section 8.4 presents the

results and some preliminary analysis and Section 8.5 goes into more detail of the results of the survey in the context of the SMC and of the Magellanic Bridge. The outcomes of the CO survey are summarised in Section 8.6

8.1 CO and metallicity studies of the SMC and Bridge

The Magellanic Clouds, as well as the Magellanic Bridge, have been the focus for a variety of searches of molecular transition lines. From these searches, a number of different carbon isotopes, as well as other molecular species have been identified. It appears that the Clouds are rather metal deficient, the SMC particularly so (Israel et al. 1993 and papers of that series). Rubio et al. (1991) and Israel et al. (1993) have found that the low CO luminosity of the SMC, being weak and cold in comparison to Galactic Molecular Clouds, may be due to a smaller molecular cloud size which may be in turn due to a higher UV radiation field causing more thorough photo-disassociation . These authors also suggest that the higher UV field of the SMC is the product of a more active star formation per unit mass than the Galaxy and lower absorptive dust fraction. Rubio, Lequeux & Boulanger (1993) note that the luminosity and metallicity of CO regions within the SMC are similarly less than those of the Galaxy, although they do not speculate on a reliable and direct correlation between these two parameters. Spectral studies of young, early-type stars throughout the SMC (Rolleston et al. 1993) have shown that the heavy-metal abundance within this SMC is not homogeneous and is lower than Galactic values.

A few stars within the Bridge and the region just east of the SMC have been found to be more metal deficient than star-forming regions in the SMC by $\sim$0.5 dex (Rolleston et al. 1999). More recent spectral studies towards the centre of the Bridge by Lehner et al. (2001) confirm the mismatch of abundances between the SMC and the Magellanic Bridge and these authors suggest that the Bridge comprises a mix of gas from SMC gas and from its relatively un-enriched halo.

Israel et al. (1993) made extensive searches for CO emission regions within the SMC towards locations selected from IRAS maps and from known HII emission regions. They found that strong sources of CO emission were generally associated with regions where the ratio of 60 μm and 100 μm flux densities (S_{60}/S_{100}) were $S_{60}/S_{100} \lesssim 1.0$ and that sites of CO emission where $S_{60}/S_{100} \gtrsim 1.0$ were relatively weak. In general, SMC CO line

emissions were found to be weaker and narrower than those of Galactic CO emission.

At this stage, CO emission of any kind has not previously been reported in the Magellanic Bridge further east than the molecular cloud N88, which occupies the north eastern corner of the SMC. N88 has also been observed in a number of other molecular lines (Testor et al. 1999). Smoker et al. (2000) have conducted a search using the Swedish ESO Sub-millimetre Telescope (SEST) for ^{12}CO (1-0) near the centre of the Magellanic Bridge, towards a region of cold atomic hydrogen (Kobulnicky & Dickey 1999). This target was considered a likely candidate based on studies by Garwood & Dickey (1989), who had found that CO emission regions were occasionally associated with cold atomic gas. These SEST observations by Smoker et al. however, showed no ^{12}CO (1-0) emission down to an RMS of 60 mK.

Maps of CO emission from the tidally affected M81 galaxy have shown that some CO regions can be associated with tidally extruded HI (Taylor, Walter & Yun, 2001), although the correlation is not particularly outstanding and the CO appears to only trace loosely the HI mass.

CO emission in Tidal Dwarf Galaxies (TDGs) has been found to correlate generally with regions of high HI column density by Braine et al. (2001), although only single pointings were made during this study. TDGs are thought to condense from the remnant material exported from a host galaxy during a tidal stripping event (e.g. Braine et al. 2001). They may represent a class of objects where star-formation has preceded significant tidal perturbation. This is the reverse of the sequence of processes thought to be active in the Magellanic Bridge and is a relevant benchmark to bear in mind.

8.2 Source Selection

CO requires a surface on which to form and in instances where UV flux may be high enough to cause disassociation, a buffer of absorbing material is necessary to surround the CO region. As such, candidate CO regions were selected for this survey based on findings by Israel et al. (1993), Taylor, Walter & Yun (2001) and Braine et al. (2000, 2001) and through comparisons of maps of far-IR emission and of HI column density. In general, 60 μm emission across the Bridge is negligible except for a few sparsely distributed bright peaks, with a maximum brightness of $\sim$1.5 MJy sr^{-1}. As discussed in Chapters 3 and

4, the HI distribution contrasts in being rather clumpy with a filamentary component throughout much of the Bridge.

Candidate regions were those where the 60 μm to 100 μm flux density ratio S_{60}/S_{100} <0.2 were co-incident with a local HI integrated intensity maximum. Throughout the Bridge, six candidate regions satisfying this criteria have been identified. Due to the difficulties in observing such faint extra-Galactic CO emission however, only one of these regions has been investigated for ^{12}CO (1-0) emission at this time. The other five, un-observed CO candidate sites have lower S_{60}/S_{100} ratios, lower 60 μm emission and with one exception, all have OB associations and IRAS sources within a few tens of parsecs (projected). A concerted study of the remaining sites will be the subject of a future paper.

8.3 Observations

Two separate observing sessions have resulted in the detection of ^{12}CO in the Magellanic Bridge. The preliminary detection was made with the ATNF Mopra telescope at Coonabarabran, Australia. Follow-up confirmation observations were made at the same co-ordinates, as well as some adjacent locations with the SEST telescope, in La Silla, Chile.

8.3.1 Mopra

The 22m Mopra telescope[1] located at Coonabarabran, Australia, was used to examine one pointing (RA $01^{\rm h}\,56^{\rm m}\,47^{\rm s}$, Dec. $-74^\circ\,17'41''$, J2000) only. These observations were made during the evening and night of 11^{th} of October 2000 and during the night of 13^{th} December 2000.

The two SIS receivers of Mopra were tuned to 115.19GHz. The correlator was configured to give 64 MHz bandpasses with 1024 channels for both receivers, resulting in a velocity range of $\sim$167 km s^{-1}, a velocity channel spacing of $\sim$0.163 km s^{-1}and a beamwidth of $\sim 20'$.

During observing runs, the telescope was calibrated every $\sim$45 minutes with observations

[1]The Mopra telescope is part of the Australia Telescope which is funded by the Commonwealth of Australia for operation as a National Facility managed by CSIRO.

of an ambient temperature source. Reference observations were made of an area located two minutes south of the source. Total on-source time was ∼682 minutes.

Observations of the molecular region N88 were made for calibration purposes. The ^{12}CO (1-0) signal strength of ∼200mK for N88 is 40% of the brightness measured by Rubio et al. (1996) and is in general agreement with the estimated efficiency of the Mopra Telescope (Kesteven M., Priv. Comm.).

The pointing corrections for the telescope were made before each ∼6 hour observing session using SiO maser sources. Corrections were repeated until accuracy was consistently $\lesssim 5''$.

All data was reduced following standard procedures, using the ATNF SPC reduction package: The quotient of on-source and off-source spectra were first calculated, giving background subtracted raw data. A third order polynomial was then fit to the dataset to remove a slowly varying baseline.

8.3.2 SEST

Confirmation of the Mopra detection and further observations were conducted with the SEST during the evenings and nights of December 15^{th}-17^{th} 2001.

The SESIS 100 receiver was tuned to 115.19 GHz and the correlator was configured to the High Resolution Spectrometer settings, giving a $45''$ beamwidth and a 83.6MHz bandpass of 2000 channels. This yields a velocity range of ∼218 km s^{-1} and a velocity channel spacing of ∼0.109 km s^{-1}.

The Double Beam Switching (DSW) mode was used for these observations. This employs a focal plane chopper wheel that rotates at 6Hz to observe the off-source position, located $+2^{\rm m}\,27^{\rm s}$ in azimuth away from the source.

During observing runs, pointing and focus corrections were made every two hours, using the SiO maser R Doradu (∼8Jy) where possible, otherwise R Aquarius was used (∼5Jy). Calibration checks were made approximately every 5 minutes.

Four pointings were made at beam-width sized offsets from the primary position. Positions, HI column densities and S_{60}/S_{100} values for these pointings are included in Table 8.1. The pointings are numbered in the order in which they were observed.

Pointing	Offset		HI Col. dens.	S_{60}/S_{100}	Obs.time	RMS (after	S/N
	RA	Dec.	[cm^{-2}]		[min]	reduction)[mK]	
1	0.0	0.0	2.7×10^{21}	0.18	157	21	6.5
2	0.0	$+45''$	2.7×10^{21}	0.24	48	34	6.1
3	$+45''$	$+45''$	2.6×10^{21}	0.23	48	39	-
4	0.0	$+90''$	2.5×10^{21}	0.26	48	39	3.1

Table 8.1: Positions, HI column densities and S_{60}/S_{100} values for the detected CO cloud and adjacent positions (See Figure 8.1). The reference position is at RA $01^{\rm h}\,56^{\rm m}\,47^{\rm s}$, Dec. $-74^\circ\,17'41''$(J2000). Observation times and RMS values are reported for the SEST observations

Figure 8.1 shows the position of the candidate emission region on an HI integrated intensity map. The sub-image shows the observed positions, nearby OB associations extracted from an OB catalogue (Bica & Schmitt. 1995) and contours of 60 μm brightness.

Pointing 1 was observed for a total of 157.1 minutes, on-source time. The other three positions were observed for 48 minutes each, on-source time. System temperatures ranged between $\sim$500-590 K.

Data were reduced using the XS data reduction package. The raw spectra had velocity resolution of $\sim$0.11 km s^{-1} and this was increased to a final value of $\sim$0.33 km s^{-1} during reduction to increase the signal-to-noise. Data were scaled to compensate for the main-beam efficiency using T_A=T_{MB}/0.7. All data were baseline subtracted with a single linear baseline, although in most cases this was hardly necessary and a higher order fit did not improve S/N significantly. The resulting RMS values, (after rebinning across three velocity channels) and the on-source times are shown in Table 8.1.

8.4 Spectra and analysis

The initial detection made with the Mopra telescope is shown in Figure 8.2. This detection has a S/N of $\sim$3.5. Spectra obtained with the SEST are shown in Figure 8.3 for each of the pointings 1-4. Table 8.2 summarises the parameters for gaussian fits made to SEST spectra from pointings 1,2 & 4, as well as integrated intensity determined from the fit parameters. The analysis package XS was to make the gaussian fitting.

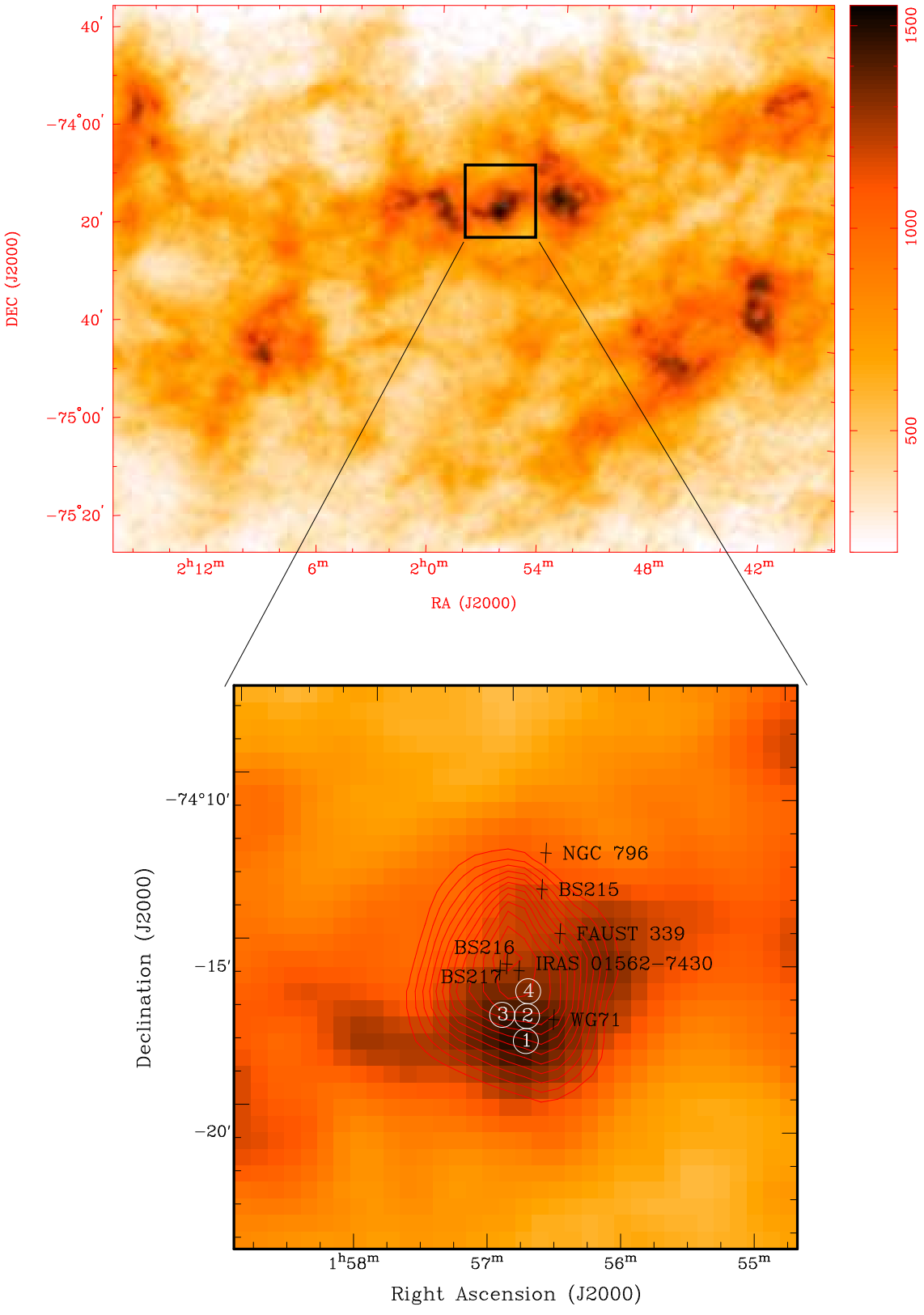

Figure 8.1: Integrated HI intensity map of the Magellanic Bridge and a blowup of the candidate CO emission area. Pointings are shown as circles labelled as pointings 1-4. Contours correspond to the 60 μm brightness of 0.1 to 1.20 MJy sr^{-1}. Crosses define the positions of OB associations, FAUST objects and IRAS sources nearby (from catalogues by Bica & Schmitt, 1995 and Westerlund & Glaspey, 1971).

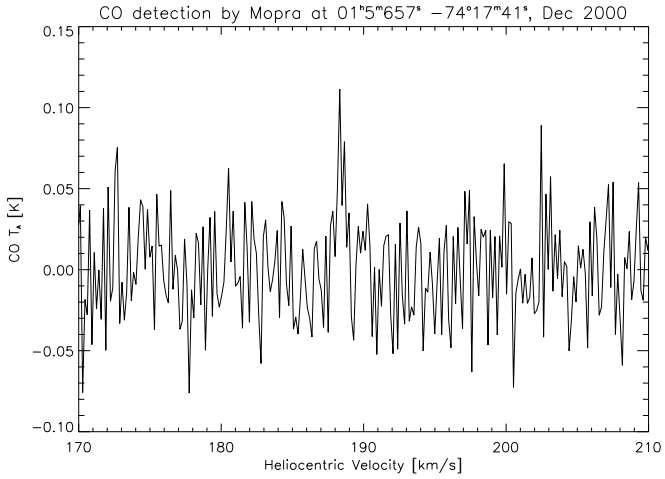

Figure 8.2: Initial ^{12}CO(2-1) detection made with the ATNF Mopra Telescope. These data have been adjusted for the efficiency of the Mopra telescope ($\sim$40%)

Pointing	V_o km s^{-1}	T_{max} mK	ΔV km s^{-1}	I_{CO} K·km s^{-1}
1	189.4	140	1.3	0.19
2	189.5	170	1.7	0.31
4	189.3	90	1.4	0.13

Table 8.2: Parameters of Gaussian fit to smoothed data for pointings 1,2 and 4. Central Velocity is consistent to within $\pm$0.2 km s^{-1}, although line width (ΔV , FWHM) varies by up to $\sim$23%

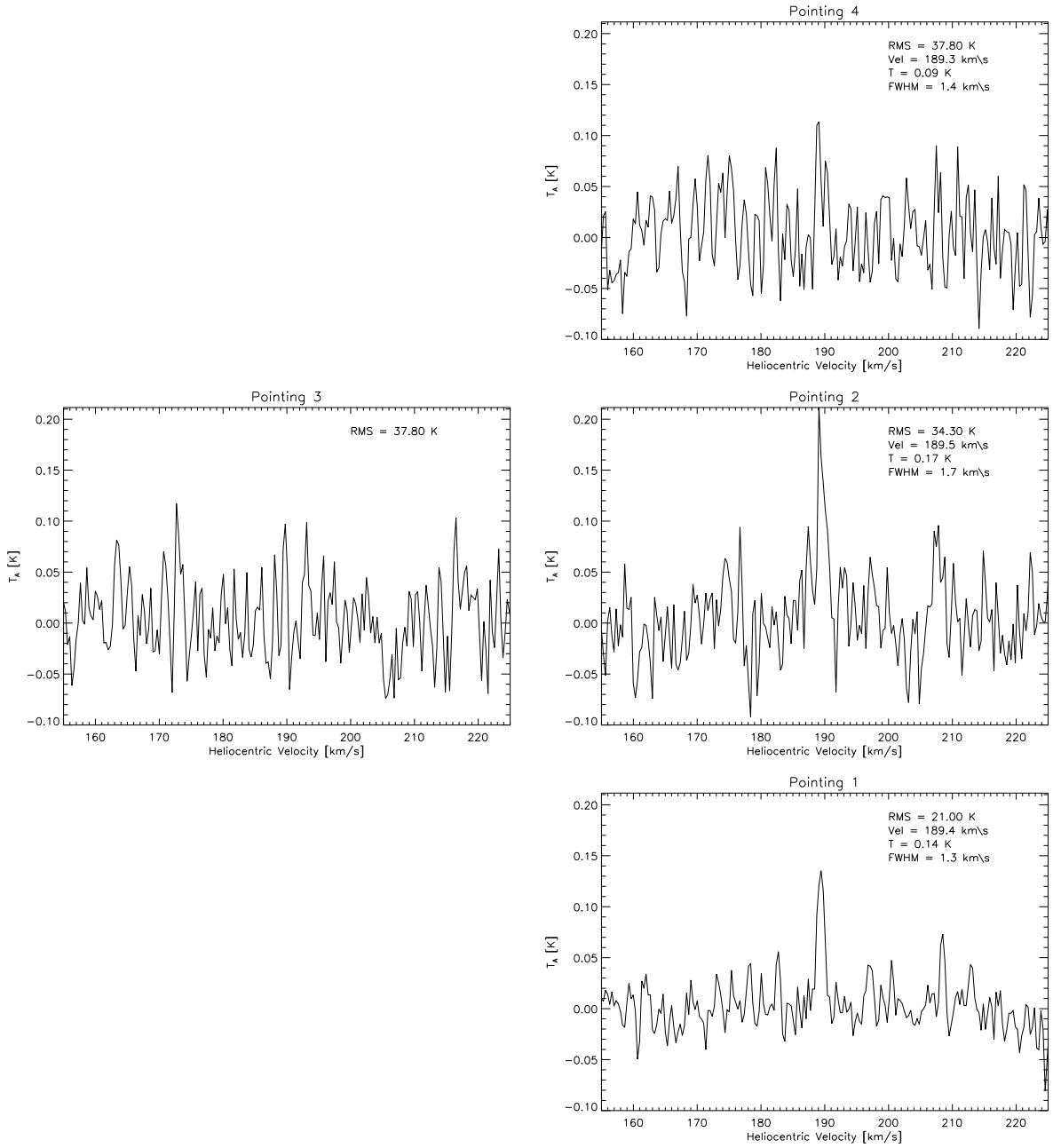

Figure 8.3: Smoothed spectra over velocities $\sim$160 km s^{-1} to 220 km s^{-1} (Heliocentric). Gaussian fit parameters are shown in the top right of each plot. See also Table 8.2.

The detection at Pointing 4 has a S/N of ∼3.1 and is not a significant detection on its own, however positive detections made nearby improve its legitimacy. Pointing 3 did not yield a convincing detection of the ^{12}CO (1-0) line.

We can see from Figure. 8.1 that pointing 1 corresponds to the highest local HI column density. This point appears to be on the rim of an annular, or crescent-shaped HI filament and has a S_{60}/S_{100} =0.18, although this parameter peaks slightly north of the HI integrated intensity maximum at the catalogued object IRAS 0152-7430. Two OB populations are located at almost the same position as the IRAS object, comprising either one association with a more centrally condensed population, or two superimposed OB associations. These associations are labelled BS95 216 and BS95 217 (Bica & Schmitt 1995). A third OB association, WG71 CL 8 is found to the west of pointing 2 (Westerlund & Glaspey, 1971).

The detected CO spectrum from pointing 1 is shown in Figure. 8.4, with the HI spectrum overlaid at the same location. The peak velocity of the CO emission coincides with that of the HI emission, indicating that the CO emission region is enclosed by an HI cloud which may be offering some protection from ambient UV flux. Given the projected proximity of the OB associations BS95 217 and 216 and WG71, we would expect that the UV flux in this region could be quite significant. The IRAS detection for example, indicates significant heating of dust by such sources. The width of the HI line at this location is ∼10 km s^{-1}. More mapping will be required to ascertain the extent of the CO mass and the degree of correlation of the HI and CO emission regions.

We have plotted the integrated CO intensity, L_{CO} as a function of line-width in Figure 8.5, along with those for detections made in the SMC by Israel et al. (1993). This plot highlights the relative weakness and the low velocity dispersion of the CO detection in the Magellanic Bridge. Visually, the plot also suggests that the Bridge detections fit quite well into a correlation between velocity width and I_{CO} for SMC detections. The value of I_{CO} plotted by Israel et al. (1993) is a direct sum, whereas our value of I_{CO} is determined from a gaussian fit. However, since the emission line appears to have no velocity structure, the difference between the methods is considered to be negligible. The errors for this plot were determined using the algorithms developed by Landman, Roussel-Dupré & Tanigawa, (1982) and Barranco & Goodman, (1998).

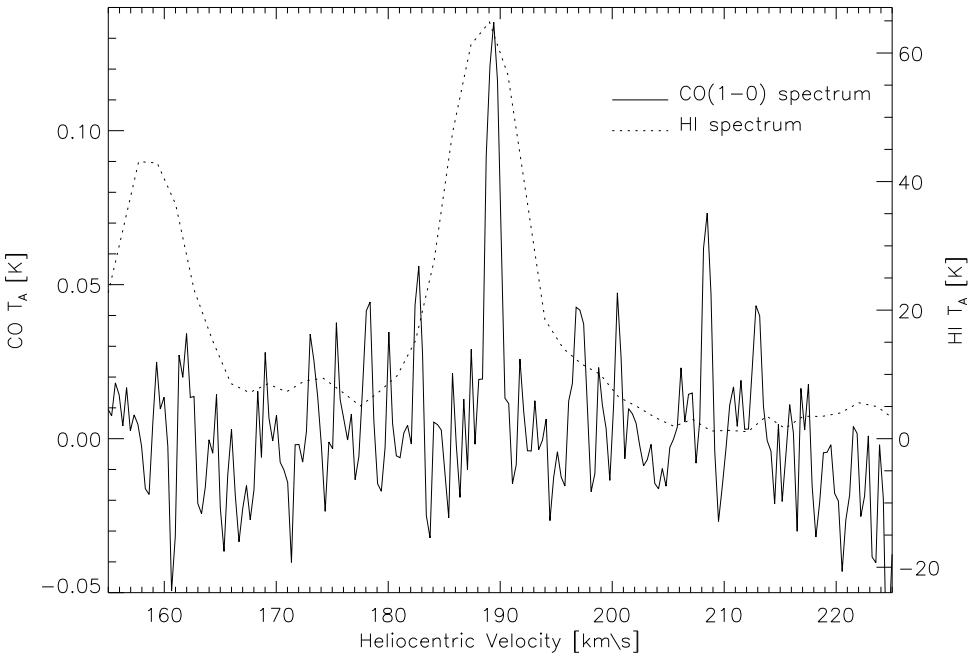

Figure 8.4: Smoothed CO spectrum at pointing 1, overlaid on HI spectra at same location. *Dotted line and right axis:* HI spectrum. *Solid line and left axis:* CO spectrum. This figure shows the excellent match in velocity between the peaks of the spectra, suggesting that the CO cloud is embedded within an HI cloud.

8.5 Discussion

From the observations around RA $01^{\rm h}\,56^{\rm m}\,48^{\rm s}$, Dec. $-74^\circ\,16'56''$(J2000), three separate locations have shown a positive ^{12}CO(1-0) detection. The pointing from which the CO emission is absent does not appear to be significantly different to the other three positions in terms of S_{60}/S_{100} HI integrated intensity or proximity to potential disassociating sources such as the BS95 or WG71 sources.

Rubio et al. (1993) were able to formulate empirical relations from their studies of SMC CO emission regions. These relations allow the velocity dispersion, luminosity, virial mass and H_2/CO factor to be estimated from a measurement of the radius of the CO emission region. We estimate a new fit to only the SMC data from the paper by Rubio et al. (1993) and find a relation of $\log(R) = 0.57\log\Delta{\rm V} + 0.87$. The dataset from Rubio et al. (1993) is shown in Figure. 8.6 along with the fit determined here. We have included an upper limit to the log-log fit, based on the beamsize used for those observations, from which we estimate an upper limit to the radius of the Magellanic Bridge CO emission region of

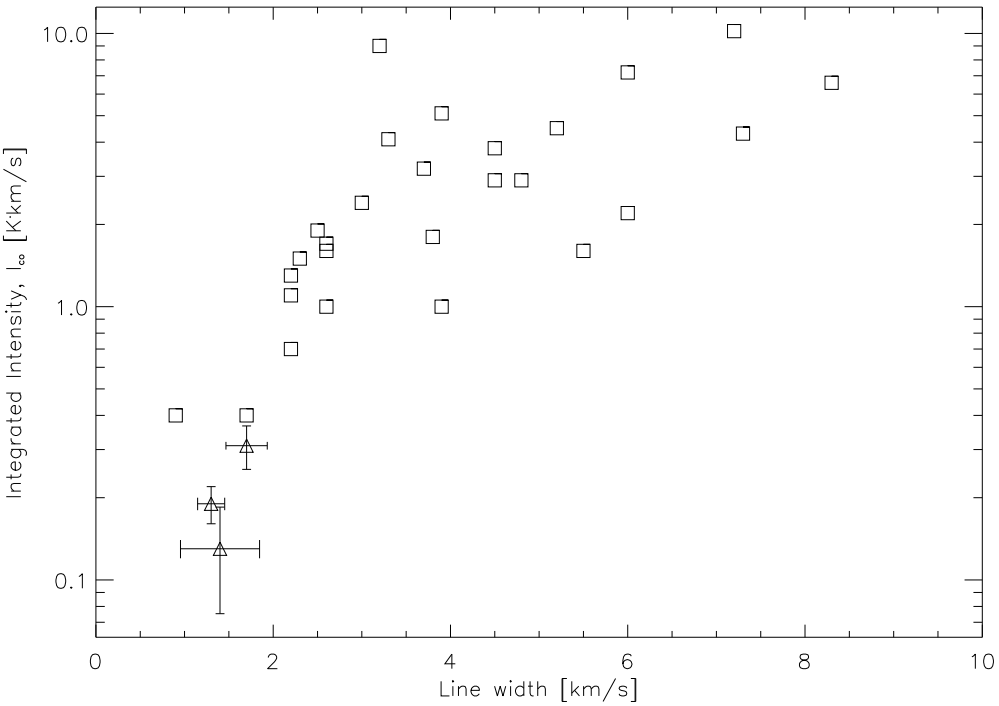

Figure 8.5: Integrated CO intensity against line-width after Israel et al. (1993) (Figure 6b). ^{12}CO detections within the SMC are shown as squares, with data from this work are shown as triangles with error bars. These new detections are consistent with the previous trend between CO line width and CO intensity.

$\sim$16 pc. We see from Figure 8.3 that the emission region extends across multiple beamwidths, where one beamwidth subtends $\sim$10 pc. From the relative amplitudes of each of the positive detections, we suggest that the centre of the CO emission cloud is southwest of pointing 2 and is perhaps co-incident with the association WG71. We should bear in mind that the Magellanic Bridge has a slightly lower metal abundance than the SMC by $\sim$0.5 dex (Rolleston et al. 1993) and we would expect this to reduce the size of the emission region (Rubio et al. 1993).

CO has not been detected in emission for any galaxy having a 12+log(O/H)$\lesssim$7.9 (Taylor, Kobulnicky & Skillman, 1998). Taking a mean value for 12+log(O/H) for the SMC of $\sim$7.98 (Pagel et al. 1978), along with the knowledge that isolated measurements of the Magellanic Bridge show an under-abundance relative to the SMC, we see that this may be the first successful detection of CO in emission where 12+log(O/H)$\lesssim$7.9. We should note that the estimates of 12+log(O/H) by Pagel et al. (1978) were made from studies of HII regions and range between 7.84 and 8.16. More importantly, the estimates of the 12+log(O/H) for the Magellanic Bridge were made at a location a few degrees east from the location of the CO detection and Rolleston et al. (1993) have shown that the metallicity of the SMC is not homogeneous. It is probable then, that the metallicity of the Magellanic Bridge is equally inhomogeneous.

A mean conversion factor for X=$N(H_2)/I_{CO}$=$(120 \pm 20) \times 10^{20}$ cm^{-2} was determined by Israel (1997) from analysis of various CO emission regions in the SMC. It is interesting to apply this factor to the CO emission detected in the Magellanic Bridge. Table 8.3 shows the predictions of the H_2 column densities using this transformation. We also see from this table that the ratio of M(H_2)/M(HI) is significantly larger than the mean M(H_2)/M(HI) for the SMC. To maintain a consistent M(H_2)/M(HI) between the Bridge and SMC, a lower X value is required for the Bridge. This is as we would expect for a lower-metallicity environment.

The Galactic X factor has been recently measured at $\sim 1.8 \times 10^{21}$ (Dame, Hartmann & Thaddeus, 2001). The lower conversion factor implies a higher metallicity, and we therefore look for other processes which may deplete a region of a CO component. Israel (1997) discusses, among other processes, the effects that photodisassociation may have on the measured X conversion factor.

Depletion of the CO component by photoionisation is discussed in Chapter 2 and has

Pointing	N(H_2) $\times 10^{21}$cm^{-2}	M(H_2)/M(HI)
1	2.3	1.7
2	3.7	2.8
4	1.6	1.3
SMC	-	0.2 (Mean)

Table 8.3: Estimates of H_2 column density using the SMC factor $X = N(H_2)/I_{CO} = (120 \pm 20) \times 10^{20} cm^{-2}$. The predicted H_2 column density is comparable to that of the HI column density. This is an interesting result in the context of the SMC, where the M(H_2)/M(HI) ratio is significantly smaller (Israel, 1997).

been addressed in the context of the Magellanic Clouds by Israel (1997). They show a proportional correlation between the measured far infrared brightness and the [O]/[H] (i.e. metallicity) level for the SMC and the LMC. They discuss the effects of shielding for lower metallicity environments: where the dust fraction is relatively low and the absorbed fraction of photoionising radiation is smaller. Lower metallicity environments are therefore expected to be more susceptible to disassociation. Some degree of disassociation by photoionisation is very likely to be occurring at the CO emission region in the Bridge, ultimately depressing the X factor somewhat. However, based on the the linear regression analysis of CO regions in the SMC by Israel (1997), the expected *infrared energy available per nucleon* σ, is approximately σ_{FIR}=0.4 - 0.2$\times 10^{-28}$Wm^{-2} sr^{-1}cm^2. Which is an order of magnitude lower than both the SMC and LMC. Clearly the photodisassocation effects of the infrared radiation is expected to be very low, considering that Israel was able to notice the depletion of the extended and tenuous CO component only for $\sigma_{FIR} > 17 \times 10^{-28}$Wm^{-2}sr^{-1}cm^2.

The general nature of HI within the brightest parts of the Bridge is clearly turbulent (See Chapters 3, 4 and 5) and the HI in the neighbourhood of these detections has a clear bimodal profile (See Chapter 6), and the CO detections made here correspond to the velocity of the receding peak. Rubio et al. (1993) noted that all the CO detections in the SMC were located on the approaching velocity peak, although any reason or significance for a preference is unclear. A more detailed study of this area shows that it cannot be interpreted as an expanding HI shell (See Chapter 4).

Studies of the CO emission from Tidal Dwarf Galaxies and tidal remnants by Braine et al. (2000) and Braine et al. (2001) have shown that molecular gas is observable within the

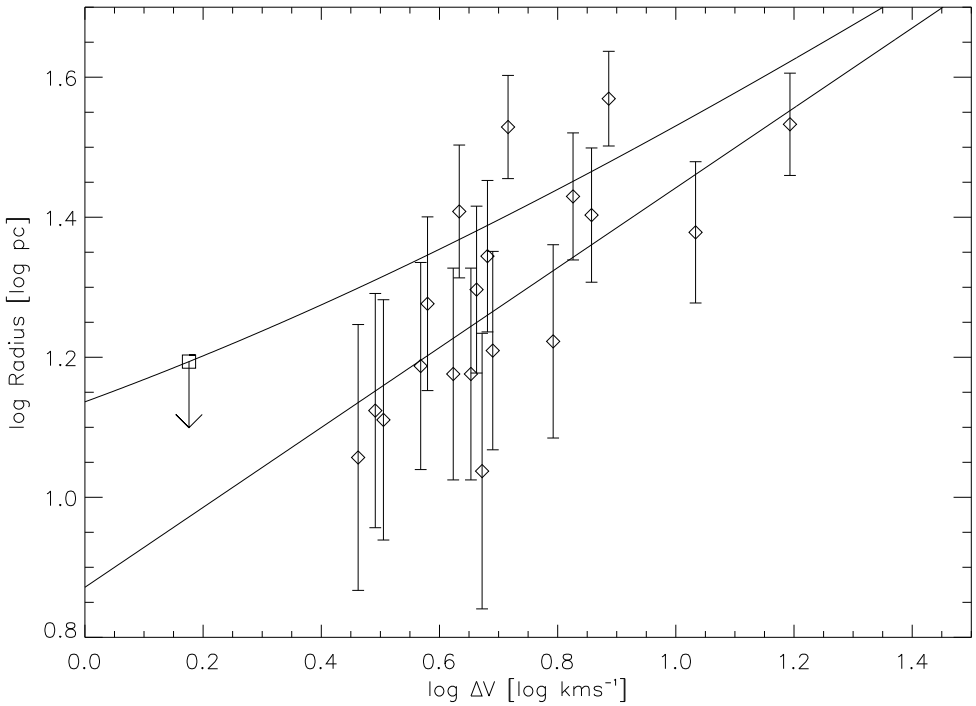

Figure 8.6: Plot of the dependence of CO emission region radius (pc) on velocity width (ΔV) for SMC CO emission regions *(diamonds)*. The straight *lower line* is a fit to the SMC dataset collated by Rubio et al. (1993). This figure differs from that of Figure 1 of that paper, in that the axes are reversed and the radius is treated as the dependent variable. The upper *curved line* represents an upper limit to the log-log fit and is half the size of the beam used in the SMC observations. The square marks the upper radius limit of the Magellanic Bridge detection at pointing 2 (ΔV =1.7 km s^{-1}). Error bars are one half the beamwidth for the observations ($\approx$6.3 pc).

remnants of tidal interactions and these authors suggest that the CO regions form after the tidal stripping event. Typical line-widths and I_{CO} values from these observations of the ^{12}CO (1-0) transition are $\sim$15 - 66 km s^{-1} and 0.1 - 2 K·km s^{-1}. However, that sample has an oxygen abundance range of 12+log(O/H) $\sim$8.2 - 8.6, which is in the upper range of that found from a study of dwarf galaxies including the SMC and the LMC (Israel, Tacconi & Baas, 1995). The high metallicities of these types of galaxies are considered to be the remnants of their original host galaxies. As the SMC is thought to be the original host for the matter drawn out into the Magellanic Bridge, we would expect the line-widths of the Bridge CO emission regions to be similar to those of the SMC and Figure 8.5 shows that this is apparently the case. Braine et al. (2000) selected CO candidate emission regions on the basis of high HI column density. They also concluded that the spatial co-incidence of HI clumps and CO regions suggested that the CO region had formed after the tidal extraction event. From the lack of information of the spatial distribution of the CO emission region in the Bridge, it is difficult to say whether the CO emission region coincides exactly with the nearby HI clump. At this stage however, the spatial and velocity positions of HI clumps and the CO emission region appear to correspond. A future work will examine this aspect in more detail.

At this stage then, it appears then that the narrow CO line-widths as measured in the Magellanic Bridge are not representative of those of observed TDGs, although we should bear in mind the differences in the progenitor galaxy types and we should be careful in drawing parallels in this context.

8.6 Summary

We have detected a ^{12}CO(1-0) emission region within the Magellanic Bridge. The line width and integrated intensity is compatible with other CO detections within the SMC, although it is somewhat weaker and cooler, implying a lower metallicity. The findings at this point appear to be consistent with studies of CO emission regions within the SMC where CO has been found to be associated with high HI integrated intensity and with $S_{60}/S_{100} <$0.2. Estimates made from log-log model fits to SMC CO observations indicate that the Magellanic Bridge CO emission region is spatially small and has a radius of <16 pc. The CO emission region has a narrow line-width compared with observations of the SMC and with other TDGs, lending support to findings that suggest the Bridge has a

lower metallicity than the SMC. At this stage, a reliable estimation of H_2 mass is not really possible from the small amount of spatial information, although these issues will be addressed in a future paper. We have, for the first time, detected the hitherto elusive presence of CO emission regions within the Magellanic Bridge and confirmed that the process of star formation is active in this region.

Chapter 9

Summary and Future work

> *"The purpose of writing is to inflate weak ideas, obscure pure reasoning, and inhibit clarity"* - Calvin, 1996

This thesis has presented results for a number of different studies and discussed the region between the Small and Large Magellanic Clouds known as the Magellanic Bridge.

The bulk of the analyses have centred around an HI dataset, obtained with the Australia Telescope Compact Array and the Parkes Telescope. The observed region spans eastward from the eastern edge of the SMC a projected distance of $\sim$7.7 kpc, halfway across the Bridge. The total observed area is approximately $7^\circ \times 7^\circ$ and has a resolution of $98''$. A complex and filamentary structure is seen across much of the observed region and the HI in the Magellanic Bridge and is shown to be contiguous, geometrically and kinematically, with the SMC.

The HI dataset appears to show a significant number of expanding shells. The survey suggests a poor spatial correlation of the shell population with the OB stellar population within the Magellanic Bridge. Overall, there appears to be a general deficiency of large shells in the Magellanic Bridge relative to the adjacent SMC. The deficiency is due to the rigorous shell-selection criteria and to a tendency for large-scale shells to succumb to fragmentation more easily than small shells. Overall, the distribution of expansion velocities for shells found within the Bridge is a power law with an index similar to that found in the SMC and the Holmberg II galaxy.

A study of the mean distribution of HI around the OB association population showed an apparent *excess* of HI within $\sim$80 pc of the associations. This is an interesting result,

as we would expect the cluster to deplete and ionise the local hydrogen gas during its formation and evolution.

In general, the observed shell population is too young to be easily associated with formation by stellar wind or supernovae. GRBs are not likely to be a significant shell formation mechanism, since these phenomena occur too infrequently to be responsible for a significant fraction of the HI expanding shell population. The population of HVCs at Magellanic distances is rather unknown and impacts by these clouds into the Bridge is one further alternative formation mechanism which now requires a more dedicated study.

There is good agreement of the observed kinematical and spatial distribution of the HI in the Bridge with N-Body numerical simulations. The simulations suggest that parts the SMC have been drawn into the region between the Clouds, and that the lower velocity component may be the nearer arm of the SMC, while the higher velocity part is a more distant arm. The simulations indicate that the near arm is responsible for forming the LMC-SMC link, while the distant arm extends radially away and is less involved in the Bridge. Tidal stretching would therefore be a dominant process for the low velocity arm

Various large scale features in the Magellanic Bridge have shown evidence for large energy deposition events. The prominent bimodal arrangement of HI in the Bridge is shown to be an extension of an existing shell feature SMC. The overall continuity of the bimodal feature into the SMC shell suggests that the shell had formed within the SMC *before* the Bridge developed. Assuming a stellar wind model leads to estimates of the age for the SMC shell which is not compatible with the age of the Bridge.

The mechanism responsible for the formation of a large HI hole off the north-eastern edge of the SMC remains ambiguous. it was shown that processes typically held responsible for forming similar features (e.g. stellar wind, Supernovae, high velocity cloud impacts) could not deposit an amount of energy necessary to form this feature. Numerical simulations are in general unable to satisfactorily reproduce the development of this feature and suggest that the hole is not co-incident with the second Legrange point.

A survey for Hα emission regions has detected emission at many locations across the entire length of the Bridge. In most cases, it was possible to locate catalogued objects which were probable sources for ionising the ISM. In a few instances, the morphology of the Hα was more consistent with shock heating, although further data is required before

is is possible to definitively determine the ionisation process. This part of the thesis now contains a new catalogue for Hα emission regions in the Magellanic Bridge.

A survey for CO in the Magellanic Bridge has detected emission for the first time in the Magellanic Bridge and has consolidated an apparent relationship of 100μ excess with CO emission detected in the SMC. At this stage, only one of up to six candidate CO emission regions have been explored. The velocity dispersion and total brightness of this detection show a consistency with CO detections in the SMC and are strongly consistent with a low metallicity of the Bridge.

9.1 Future work

This thesis has opened up a number of issues which deserve considerable further research. We have shown that the spatial distribution of the OB stellar population of the Bridge does not correlate very well with that of the HI expanding shell population. We must now examine in a more definitive manner, the mechanism responsible for creating these features. As the survey of Chapter 4 considered only *complete* spherical structures, it is now important to re-examine the dataset with a more relaxed criteria, and include partially complete shell-like features. The possibility that HVCs may be responsible for generating the observed structures also calls for more work in this area: a survey focussing on the spatial number density of small tenuous gas clouds within the general region will go some way to helping understand how important this process is to the formation of these shell-like features.

The origins of the large HI hole are not well known. Detailed numerical simulations will allow us to understand if such features can be formed kinematically, or require a different energy input process. Combined with the high resolution HI dataset presented in this thesis, these simulations will help to refine the understanding of the overall radial structure of the Magellanic System.

A continuation of the search for CO emission regions will lead to a more solid understanding of the process and frequency of star formation in the Magellanic Bridge. It will also help us to understand the metallicity variation throughout the Bridge and lead to estimates of the CO-H_2 conversion factor in this region. It will be necessary to map these CO emission regions at higher resolution to learn of the spatial extent and morphology.

The distribution and excitation mechanisms for the observed Hα emission requires considerable further research, in particular, a radio continuum dataset must be examined to enable an understanding of ionisation processes. This will ultimately lead to a better understanding of the processes active in the unique environment of the Magellanic Bridge.

This Thesis has presented the beginnings of an analysis into a unique and diverse region. The Magellanic Bridge is the closest gaseous tidal remnant to our Galaxy, and offers opportunities to study large-scale physical processes at resolutions unmatched elsewhere in the universe.

"So THAT'S *what you have been doing for the last four years!"* - Mum, 2003

Bibliography

Ardeberg,A., Maurice,E.,1977,A&A Sup. Ser. ,V 30,p. 261

Avedisova,V.S.,1972,Soviet. Astr.,V 15,p. 708

Ayal,S., Piran,T., ,2001,ApJ ,V 555,p. 23

Barranco,J.A., Goodman,A.A. ,1998,Apj ,V 504,p. 207

Bica,E. L.D., Schmitt,H.R. ,1995,ApJ Sup. Ser.,V 101,p. 41

Blanco,V.M., Demers,S., Douglass,G.G., Fitzgerald,M.P.,1968,Publ. U.S. Naval Obs.,V 21, 2^{nd} Edition ,

Blinnikov,S.I., Novikov,I.D., Perevodchikova,T.V., Polnarev,A.G.,1984,Soviet. Asrt. Lett ,V 10,p. 177

Bowers, R.L., Deeming, T.,1984,Astrophysics,Jones and Bartlett Publishers,Boston

Bowyer,S., Sasseen,T.P., Wu,X., Lampton,M., 1995,ApJ Sup. Ser.,V 96,p. 461

Brüns, C ,2002,PhD Thesis, University of Bonn

Braine,J., Duc,P.-A., Lisenfeld,U., Charmandaris,V., Vallejo,O., Leon,S., Brinks,E. ,2001,A&A,V 378,p. 51

Braine,J., Lisenfeld,U., Duc,P-A., Leon,S. ,2000,Nat.,V 403,p. 867

Brinks,E., Bajaja,E. ,1986,A&A,V 169,p. 14

Brück,M.T., Hawkins,M.R.S. ,1984,in van den Bergh, S., de Boer, K., S., eds., Structure and evolution of the Magellanic Clouds, Proc. Symp. #108,D. Reidel Publishing Co., Dordrecht, Holland., p. 103

Brück,M.T., Hawkins,M.R.S.,1983,A&A,V 124,p. 216

Bureau,M., Carignan,C.,2002,ApJ ,V 123,p. 1316

Burke B. F., Graham-Smith. F., ,1997,An introduction to radio astronomy. ,Cambridge University Press ,New York

Carozzi,N. ,1971,A&A Sup.,V 4 ,p. 231

Castor,J., McCray,R., Weaver,R. ,1975,ApJ ,V 200,L 107

Chevalier,R.A.,1974,ApJ ,V 188,p. 501

Clarke,B.G. ,1999,in G. B. Taylor, C. L. Carilli, and R. A. Perley, eds, Synthesis Imaging in Radio Astronomy II, A Collection of Lectures from the Sixth NRAO/NMIMT Synthesis Imaging Summer School. ASP Conf. Ser. ,V 180, Astronomical Society of the Pacific, ,San Francisco, USA., I1p. 1

Clementini,G., Held,E.V., Baldacci,L., Rizzi,L.,2003,ApJ ,V 588,L 85

Courtes,G., Viton,M., Sivan,J.P., Dechter,R., Gary,A. ,1984,Sci.,V 225,p. 179

Cox,D.P. ,1972,ApJ ,V 178,p. 159

Crovisier,J., Dickey,J.M.,1983,A&A,V 122,p. 282

Davies,R.D., Elliott,K.H., Meaburn,J. ,1976,RAS. Mem.,V 81,p. 89

deBlok,W.J.G., Walter,F.,2000,ApJ ,V 537,L 95

Demers,S., Battinelli,P. ,1998,ApJ ,V 115,p. 154

Demers,S., Irwin,M.J.,1991,A&A Sup. Ser. ,V 91,p. 171

Demers,S., Irwin,M.J., Kunkel,W.E. ,1993,MNRAS,V 260,p. 103

Demers,S., Kunkel,W.E., Irwin,M.J. ,2000,AJ ,V 119,p. 2789

Dickey,J.M., McClure-Griffiths,N.M., Stanmirović,S., Gaensler,B.M., Green,A.J.,2001,ApJ ,V 561,p. 264

Dickey,J.M., Mebold,U., Stanmirović,S., Staveley-Smith,L.,2000,ApJ ,V 536,p. 756

Dopita, M.A. Mathewson, D.S., Ford, V.L., 1985,ApJ ,V 297, p.599

Dreyer,J.L.E.,1888,RAS. Mem.,V 49,p.1

Dyson,J.E., Williams,D.A.,1997,in Dyson,J. E., Williams., D. A. eds., The Physics of the Interstellar Medium. ,The graduate series in astronomy, Institute of Physics Publishing, ,Bristol

Efremov,Y.N., Elmegreen,B.G., Hodge,P.W. ,1998,ApJ ,V 501,L 163

Ehlerova,S., Palous,J., Theis,Ch., Hensler,G.,1997,A&A,V 328,p. 121

Elmegreen,B.G ,1992,in Burton,W.B., Elmegreen,B.G., Genzel,R. eds., The galactic interstellar medium,Springer-Verlag ,Berlin, Heidelberg, New York

Elmegreen,B.G., Kim,S., Staveley-Smith,L.,2001,ApJ ,V 548,p. 749

Feast,M.W.,1988,in van den Bergh, S., Pritchet, C.J., eds., The Extragalactic Distance Scale. Proc.of the ASP., # 100 ,Astronomical Society of the Pacific, San Francisco, USA., p. 9

Feast,M.W.,1989,in K.S. de Boer, F. Spite, G. Stasinska eds., Recent Developments of Magellanic Cloud Research.,Observatoire de Paris, Section Astrophysique de Meudon, Meudon, ,Meudon France

Field,G.B., Goldsmith,D.W., Habing,H.J.,1969,ApJ ,V 155,L 149

Fujimoto,M.,1979,The large-scale characteristics of the galaxy, Symp. Proc. ,Dordrecht, D. Reidel Publishing Co., p. 557

Galliano,F., Madden,S., Jones,A.P., Wilson,C., Bernard,J.P., LePeintre,F. ,2002,in Giard, M., Bernanrd, J.P., Klotz, A., Ristorcelli I. eds., Proceedings of Infrared and Submillimeter Space Astronomy, EAS Publications Series, V 4, EDP Sciences, ,p. 381

Gardiner,L.T., Noguchi,M.,1996,MNRAS,V 278,p. 191

Gardiner,L.T., Sawa,T., Fujimoto,M. ,1994,MNRAS,V 266,p. 567

Garwood,R.W., Dickey,J.M.,1989,ApJ ,V 338,p. 841

Gibson,B.K., Giroux,M.L., Penton,S.V., Putman,M.E., Stocke,J.T., Shull,J.M. ,2000,AJ ,V 120,p. 1830

Goldman,I. ,2000,ApJ ,V 541,p. 701

Graham,M.F., Smith,R.J., Meaburn,J., Bryce,M. ,2001,MNRAS,V 326,p. 539

Green,D.A.,1993,MNRAS,V 262,p. 327

Grondin,L., Demers,S. ,1993,in Sasselov, D.D., ed., The International Workshop on Luminous High-Latitude Stars.,Astronomical Society of the Pacific, San Francisco, USA., p 380

Grondin,L., Demers,S., Kunkel,W.E., Irwin,M.J.,1990,AJ ,V 100,p. 663

Hambly,N.C., Dufton,P.L., Keenan,F.P., Rolleston,W.R.J., Howarth,I.D., Irwin,M.J. ,1994,A&A,V 285,p. 716

Hindman,J.V. ,1967,Aust. J Phys,V 20,p. 147

Hindman,J.V., Kerr,F.J., McGee,R.X.,1963,Aust. J Phys,V 16,p. 570

Hindman,J.V., McGee,R.X., Carter,A.W.L., Holmes,E.C.J., Beard,M. ,1963,Aust. J Phys,V 16,p. 552

Hindman,J.V., McGee,R.X., Carter,A.W.L., Kerr,F.J. ,1961,AJ ,V 70,p. 45

Hodge,P.,1985,PASP,V 97,p. 530

Holdaway, M.A., ,1999,in G. B. Taylor, C. L. Carilli, and R. A. Perley, eds, Synthesis Imaging in Radio Astronomy II, A Collection of Lectures from the Sixth NRAO/NMIMT Synthesis Imaging Summer School. ASP Conf. Ser. ,V 180, Astronomical Society of the Pacific, ,San Francisco., USA., p. 401

Holmberg,E.B., Lauberts,A., Schuster,H.E., West,R.M. ,1974,A&A,V 18,p. 463

Irwin,M.J., Kunkel,W.E., Demers,S. ,1985,Nat.,V 318,p. 160

Israel,F.P.,1997,A&A,V 328,p. 471

Israel,F.P., Burton,W.B.,1986,A&A,V 168,p. 369

Israel,F.P., Johansson,L.E.B., Lequeux,J., Booth,R.S., Nyman,L.A., Crane,P., Rubio,M., deGraauw,T., Kutner,M.L., Gredel,R., Boulanger,F., Garay,G., Westerlund,B.,1993,A&A,V 278,p. 25

Israel,F.P., Tacconi,L.J., Baas,F. ,1995,A&A,V 295,p. 559

Johnson,P.G., Meaburn,J., Osman,A.M.I.,1982,MNRAS,V 198,p. 985

Kamphuis,J., Sancisi,R., vanderHulst,T.,1991,A&A,V 244,L 29

Kerr, F.,1968,in Barbara M. Middlehurst and Lawrence H. Aller., eds., Nebulae and interstellar matter ,Series: Stars and stellar systems, V 7, Chicago Press. ,Chicago University, USA.,

Kerr,F.J., Hindman,J.V., Robinson,B.J.,1954,Aust. J Phys,V 7 ,p. 297

Kim,S., Staveley-Smith,L., Sault,R.J., Kesteven,M.J., McConnell,D., Dopita,M.A., Bessell,M.,1998,in Breitschwerdt, D. , Freyberg, M. J., Truemper, J., eds., The Local Bubble and Beyond. Lyman-Spitzer Colloquium, IAU sump. Proc. # 166 ,V 506, Springer-Verlag

,Berlin, Heidelberg, New York, p. 521

Kim,S., Staveley-Smith,L., Sault,R.J., Kesteven,M.J., McConnell,D., Freeman,K.C.,1997,PASA,V 14,p. 119

Kleinmann,S.G., Cutri,R.M., Young,E.T., Low,F.J., Gillett,F.C.,1986,IRAS Serendipitous Survey Catalogue ,Tuscon, Univ. of Arzona ,

Kobulnicky,H.A., Dickey,J.M.,1999,AJ ,V 117,p. 908

Kunkel, W.E. in Hesser, J.E., ed. Star Clusters, IAU Symp. 85, 1980, Dordrecht, D. Reidel Publishing Co., p. 353

Kunkel,W.E., Demers,S., Irwin,M.J. ,2000,AJ ,V 119,p. 2789

Landman,D.A., Roussel-Dupre,R., Tanigawa,G. ,1982,ApJ ,V 262,p. 732

Lazarian,A., Pogosyan,D. ,2000,ApJ ,V 537,p. 720

Lee,V.L., Burkhead,M.S. ,1971,AJ ,V 76,p. 467

Lehner,N. ,2002,ApJ ,V 578,p. 126

Lehner,N., Sembach,K.R., Dufton,P.L., Rolleston,W.R.J., Keenan,F.P.,2001,ApJ ,V 551,p. 781

Lequeux, J. ,1983,in Audouze,J., Lequeux,J., Levy,M., Vidal-Madjar,A. eds., Diffuse matter in galaxies,Dordrecht, D. Reidel Publishing Co., Dordrecht, Holland p. 1

Lindsay,E.M. ,1974,MNRAS,V 118,p. 118

Lozinskaia,T.A.,1992,Supernovae and Stellar Wind in the Interstellar Medlium ,American Institute of Physics,New York

Luks,Th., Rohlfs,K.,1992,A&A,V 263,p. 41

Madden,S.C.,2002,A&SS,V 281,p. 247

Maddison,S.T., Kawata,D., Gibson,B.K. ,2002,A&SS,V 281,p. 421

Maloney, P., Black, J.H., 1988, ApJ,V 325,p. 389

Manchester,R.N., Gaensler,B.M., Wheaton,V.C., Staveley-Smith,L., Tzioumis,A.K., Bizunok,N.S., Kesteven,M.J., Reynolds,J.E.,2002,PASA,V 19,p. 207

Marcelin,M., Boulesteix,J., Georgelin,Y. ,1985,Nat.,V 316,p. 705

Mathewson, D.S. ,1976,R.G. Obs Bull. ,V 182,p. 216

Mathewson,D.S.,1984,ASP ,V 13/2 ,p. 57

Mathewson,D.S.,1976,PASA,V 3 ,p. 20

Mathewson,D.S., Cleary,M.N., Murray,J.D. ,1974,ApJ ,V 190,p. 291

Mathewson,D.S., Ford,V.L.,1984,in van den Bergh, S., de Boer, K., S., eds., Structure and evolution of the Magellanic Clouds, Proc. Symp. #108,D. Reidel Publishing Co., Dordrecht, Holland p. 125

Mathewson,D.S., Schwarz,M.P.,1976,MNRAS,V 176,p. 47

Mathewson,D.S., Schwarz,M.P., Murray,J.D. ,1977,ApJ ,V 217,L 5

McClure-Griffiths,N.M., Dickey,J.M., Gaensler,B.M., Green,A.J., Haynes,R.F., Wieringa,M.H. ,2000,AJ ,V 119,p. 2828

McCray,R., Kafatos,M. ,1987,ApJ ,V 317,p. 190

McCray,R., Snow,T.P.,Jr.,1979,ARAA,V 17,p. 213

McGee,R.X., Milton,J.A. ,1966,Aust. J Phys,V 19,p. 343

McGee,R.X., Newton,L.M. ,1986,PASA,V 6 ,p. 471

McKee,C.F., Ostriker,J.P.,1977,ApJ ,V 218,p. 148

Meaburn,J. ,1986,MNRAS,V 223,p. 317

Metzger, P.G.,1975,in Setti,G., ed., Structure and evolution of galaxies, Proc. of the Advanced Study Institute, International School of Astrophysics, D. Reidel Publishing Co., Dordrecht, Holland p. 143

Minter,A. ,2002,in Taylor, A. R. , Landecker, T. L. Willis, A. G., eds., .Seeing Through the Dust: The Detection of HI and the Exploration of the ISM in Galaxies, ASP Conf. Proc. ,#276, Astronomical Society of the Pacific, ,San Francisco, USA., p. 221

Mitchell,R.C., Baron,E., Branch,D., Hauschildt,P.H., Nugent,P.E., Lundqvist,P., Blinnikov,S., Pun,C.S.J.,2002,ApJ ,V 574,p. 293

Mizuno,N., Rubio,M., Mizuno,A., Yamaguchi,R., Onishi,T., Fukui,Y. ,2001,PASJ,V 53,L 45

Mizuno,N., Yamaguchi,R., Mizuno,A., Rubio,M., Abe,R., Saito,H., Onishi,T., Yonekura,Y., Yamaguchi,N.i, Ogawa,H., Fukui,Y.,2002,PASJ,V 53,p. 971

Moore,B., Davis,M.,1994,MNRAS,V 270,p. 209

Morgan,D.H., Hatzidimitriou,D.,1995,A&A Sup. Ser. ,V 113,p. 539

Morras,R. ,1995,AJ ,V 90,p. 1801

Murai,T., Fujimoto,M. ,1980,PASJ,V 32,p. 581

Murali,C. ,2000,ApJ ,V 529,L 81

Napier,P.J. ,1999,in G. B. Taylor, C. L. Carilli, and R. A. Perley, eds, Synthesis Imaging in Radio Astronomy II, A Collection of Lectures from the Sixth NRAO/NMIMT Synthesis Imaging Summer School. ASP Conf. Ser. ,V 180, Astronomical Society of the Pacific, ,San Francisco, USA., p. 37

Oey,M.S., Clarke,C.J.,1997,MNRAS,V 289,p. 570

Olnon,F.M., Raimond,E., Neugebauer,G., vanDuinen,R.J., Habing,H.J., Aumann,H.H., Beintema,D.A., Boggess,N., Borgman,J., Clegg,P.E., Gillett,F.C., Hauser,M.G., Houck,J.R., Jennings,R.E., deJong,T., Low,F.J., Marsden,P.L., Pottasch,S.R., Soifer,B.T., Walker,R.G., Emerson,J.P., Rowan-Robinson,M., Wesselius,P.R., Baud,B., Beichman,C.A., Gautier,T.N., Harris,S., Miley,G.K., Young,E. ,1986,A&A Sup. Ser. ,V 65,p. 607

Olsen,K.A.G., Salyk,C. ,2003,AJ ,V 124,p. 2045

Ott,J., Walter,F., Brinks,E., VanDyk,S.D., Dirsch,B., Klein,U. ,2001,AJ ,V 122,p. 3070

Paczynski,B.,1998,AJ Lett.,V 494,L 45

Padoan,P., Kim,S., Goodman,A., Staveley-Smith,L.,2001,ApJ ,V 555,L 33

Padoan,P., Rosolowsky,E.W., Goodman,A.A.,2001,ApJ ,V 547,p. 862

Pagel,B.E.J., Edmunds,M.G., Fosbury,R.A.E., Webster,B.L. ,1978,MNRAS,V 184,p. 569

Pak,S., Jaffe,D.T.,1999,in Chu, Y.-H. , Suntzeff, N. , Hesser, J. , Bohlender, D., eds., New Views of the Magellanic Clouds, IAU Symp. #190,#190, Astronomical Society of the Pacific ,San Fransisco, USA.,p114

Paolo P., Alyssa G., Mika J.,2002, ,

Parker, Q,1998,AAO Newsletter ,#87,p. 8

Parker,Q.A., Malin,D.,1999,PASA,V 16,p. 288

Paturel,G., Andernach,H., Bottinelli,L., diNella,H., Durand,N., Garnier,R., Gouguen-

heim,L., Lanoix,P., Marthinet,M.C., Petit,C., Rousseau,J., Theureau,G., Vauglin,I.,1997,A&A,V 124,p. 109

Puche,D., Westpfahl,D., Brinks,E., Roy,J-R. ,1992,AJ ,V 103,p. 1841

Putman,M.E.,2000,PASA,V 17,p. 1

Putman,M.E., Gibson,B.K., Staveley-Smith,L.,1999,in Chu, Y.-H. , Suntzeff, N. , Hesser, J. , Bohlender, D., eds., New Views of the Magellanic Clouds, IAU Symp. ,#190, Astronomical Society of the Pacific ,San Fransisco, USA., p. 51

Putman,M.E., Gibson,B.K., Staveley-Smith,L., Banks,G., Barnes,D.G., Bhatal,R., Disney,M.J., Ekers,R.D., Freeman,K.C., Haynes,R.F., Henning,P., Jerjen,H., Kilborn,V., Koribalski,B., Knezek,P., Malin,D.F., Mould,J.R., Oosterloo,T., Price,R.M., Ryder,S.D., Sadler,E.M., Stewart,I., Stootman,F., Vaile,R.A., Webster,R.L., Wright,A.E. ,1998,Nat.,V 394,p. 752

Putman,M.E., Staveley-Smith,L., Freeman,K.C., Gibson,B.K., Barnes,D.G. ,2003,ApJ ,V 586,p. 170

Rhode,K.L., Salzer,J.J., Westpfahl,D.J., Radice,L.A.,1999,ApJ ,V 118,p. 323

Roeser,S., Bastian,U. ,1988,A&A Sup. Ser. ,V 74,p. 449

Rolleston,W.R.J., Dufton,P.L., Fitzsimmons,A., Howarth,I.D., Irwin,M.J.,1993,A&A,V 277,p. 10

Rolleston,W.R.J., Dufton,P.L., McErlean,N.D., Venn,K.A.,1999,A&A,V 348,p. 728

Rosolowsky,E.W., Goodman,A.A., Wilner,D.J., Williams,J.P.,1999,ApJ ,V 524,p. 887

Rubio,M., Cohen,R., Montani,J.,1994,in van den Bergh, S., de Boer, K., S., eds., Structure and evolution of the Magellanic Clouds, Proc. Symp. #108,D. Reidel Publishing Co., Dordrecht, Holland., p. 399

Rubio,M., Garay,G., Montani,J., Thaddeus,P. ,1991,ApJ ,V 368,p. 173

Rubio,M., Lequeux,J., Boulanger,F.,1993,A&A,V 271,p. 9

Rubio,M., Lequeux,J., Boulanger,F., Booth,R.S., Garay,G., deGraauw,Th., Israel,F.P., Johansson,L.E.B., Kutner,M.L., Nyman,L.-A. ,1996,A&A Sup. Ser. ,V 118,p. 263

Ryder,S.D., Staveley-Smith,L., Malin,D., Walsh,W. ,1995,ApJ ,V 109,p. 1592

Sanders,D.B., Scoville,N.Z., Solomon,P.M. ,1985,ApJ ,V 298,p. 373

Sanduleak,N.,1989,AJ ,V 98,p. 835

Sault, R. J., Kileen N. ,1999, ATNF

Sault,R.J., Staveley-Smith,L., Brouw,W.N. ,1996,A&A Sup. Ser. ,V 120,p. 375

Sembach,K.R., Gibson,B.K., Fenner,Y., Putman,M.E.,2002,ApJ ,V 572,p. 178

Shu,F.H. ,1992,Physics of Astrophysics, V II, Published by University Science Books, Mill Valley, USA.

Shull, J.M., Beckwith, S., 1982, ARAA,V 20,p. 163

Shull,J.M., Saken,J.M. ,1995,ApJ ,V 444,p. 663

Smoker,J.V., Keenan,F.P., Polatidis,A.G., Mooney,C.J., Lehner,N., Rolleston,W.R.J. ,2000,A&A,V 363,p. 471

Stanimirović, S. ,1999,PhD Thesis, University of Western Sydney

Stanmirović,S., Dickey,J.M., Krco,M., Brooks,A.M.,2002,ApJ ,V 576,p. 773

Stanmirović,S., Lazarian,A. ,2001,ApJ ,V 551,L 53

Stanmirović,S., Staveley-Smith,L., Dickey,J.M., Sault,R.J., Snowden,S.L. ,1999a,MNRAS,V 302,p. 417

Stanmirović,S., Staveley-Smith,L., Sault,R.J., Dickey,J.M., Snowden,S.L. ,1999b,in Chu, Y.-H. , Suntzeff, N. , Hesser, J. , Bohlender, D., eds., New Views of the Magellanic Clouds, IAU Symp. #190,#190, Astronomical Society of the Pacific ,San Fransisco., USA., p. 103

Staveley-Smith,L., Kim,S., Calabretta,M.R., Haynes,R.F., Kesteven,M.J. ,2003,MNRAS,V 339,p. 87

Staveley-Smith,L., Sault,R.J., Hatzidimitriou,D., Kesteven,M.J., McConnell,D.,1997,MNRAS,V 289, ,p. 225

Stavely-Smith,L., Kim,S., Putman,M., Stanmirović,S.,1998,in Schielicke., R.E., Reviews in Modern Astronomy 11: Stars and Galaxies.,V 11, Astronomische Gesellschaft, Hamburg, Germany, p. 117

Steinberg, J.L., Lequexu, J.,1963,Radio astronomy. Translated by R.N. Bracewell,McGraw-Hill ,New York

Tanaka,K.I., Hamajima,K. ,1982,PASJ,V 34,p. 417

Taylor,C.L., Kobulnicky,H.A., Skillman,E.D.,1998,AJ ,V 116,p. 2749

Taylor,C.L., Walter,F., Yun,M.S.,2001,ApJ ,V 562,L 43

TenorioTagle,G., Bodenheimer,P., Rozyczka,M., Franco,J.,1987,Rev. Mex. Astron. Astrofis. ,V 14,p. 241

Tenorio-Tagle,G, Bodenheimer,P.,1988,in Burbidge, G., Layzer, D., Phillips, J.G., eds., Annual review of astronomy and astrophysics, ,V 26, Annual Reviews, Inc., ,Palo Alto., USA., p. 145

Tenorio-Tagle,G.,1981,A&A,V 94,p. 338

Tenorio-Tagle,G., Bodenheimer,P., Rozyczka,M., Franco,J.,1986,A&A,V 170,p. 107

Testor,G., Rola,C.S., Whiting,A.B. ,1999,in Chu, Y.-H. , Suntzeff, N. , Hesser, J. , Bohlender, D., eds., New Views of the Magellanic Clouds, IAU Symp. ,#190, Astronomical Society of the Pacific ,San Fransisco., USA.,p. 132

Tucholke,H.-J., deBoer,K.S., Seitter,W.C. ,1995,A&A Sup. Ser. ,V 119,p. 91

van Dishoeck, E.F., Black, J.H., 1900, ApJ,V 334,p. 771

van Woerden,H., Peletier,R.F., Schwarz,U.J., Wakker,B.P., Kalberla,P.M.W. ,1999,In Gibson, B.K. & Putman, M.E., eds, Stromlo Workshop on High-Velocity Clouds, ASP Conf. Ser. ,V 166, Astronomical Society of the Pacific ,San Fransisco, USA., p. 1

Verschuur,G.L., Kellermann,K.I., vanBrunt,V. ,1974,Galactic and Extra-Galactic Radio Astronomy ,V 402, Springer-Verlag ,Berlin, Heidelberg, New York

Vishniac,E.T. ,1983,ApJ ,V 274,p. 152

Wakker,B.P.,2001,ApJ Sup. Ser.,V 136,p. 463

Wakker,B.P., Oosterloo,T.A., Putman,M.E. ,2002,ApJ ,V 123,oo 1953

Wayte, S. R.,1990,PhD Thesis, Australian National University

Weaver,R., McCray,R., Castor,J., Shapiro,P., Moore,R. ,1977,ApJ ,V 218,p. 377

Welch,D.L., McLaren,R.A., Madore,B.F., McAlary,C.W. ,1987,ApJ ,V 321,p. 162

Westerlund,B.E.,1990,ARAA,V 2 ,p. 29

Westerlund,B.E., Glaspey,J. ,1971,A&A,V 10,p. 1

Wijers,R.A.M.J., Bloom,J.S., Bagla,J.S., Natarajan,P. ,1998,MNRAS,V 294,L 13

Wilcots,E.M., Miller,B.W.,1998,AJ ,V 116,p. 2363

Yoshizawa,A.M., Noguchi,M.,1999,in Barnes, J. E. , Sanders, D. B., eds., Galaxy Interactions at Low and High Redshift, IAU Symp.,#186, Kluwer Academic Publishers,Dordrecht, Holland., p. 60

Zaritsky,D., Harris,J., Grebel,E.K., Thompson,I.B.,2000,ApJ ,V 534,L 53